8-2019

Preparation and characterization of metal decorated metal oxide materials and study of porous structures

Daniele Paradiso
University of Tennessee, dparadis@vols.utk.edu

To the Graduate Council:

I am submitting herewith a dissertation written by Daniele Paradiso entitled "Preparation and characterization of metal decorated metal oxide materials and study of porous structures." I have examined the final electronic copy of this dissertation for form and content and recommend that it be accepted in partial fulfillment of the requirements for the degree of Doctor of Philosophy, with a major in Chemistry.

John Z. Larese, Major Professor

We have read this dissertation and recommend its acceptance:

Sharani Roy, S. Michael Kilbey, Norman Mannella

Accepted for the Council:

Dixie L. Thompson

Vice Provost and Dean of the Graduate School

(Original signatures are on file with official student records.)

Preparation and characterization of metal decorated metal oxide materials and study of porous structures

A Dissertation Presented for the

Doctor of Philosophy

Degree

The University of Tennessee, Knoxville

Daniele Paradiso

August 2019

To my lovely wife Francesca

To our children, Lorenzo and Tommaso (to be born)

“ Concern for man and his fate must always form the chief interest of all technical endeavors. Never forget this in the midst of your diagrams and equations.”

Albert Einstein

“ E quando miro in cielo arder le stelle;
Dico fra me pensando:
A che tante facelle?
Che fa l’aria infinita, e quel profondo
Infinito seren? che vuol dir questa
Solitudine immensa? ed io che sono?”

Giacomo Leopardi

Acknowledgments

There is a long list of people who have contributed to make this work possible.

First of all, nothing would have begun if Prof. Larese had not asked me, on a day of late February 2013: "Are you interested in pursuing a Ph.D.?" The answer to that question did not come immediately, but it spread throughout the following many months and, eventually, came as a "yes" with the official beginning of my graduate school adventure at the University of Tennessee in August 2014. Since then, I have certainly grown as a person and as a scientist; although, the good thing is that, as Prof. Larese would say, this is only the beginning, just a preparation for an entire career. After five long and challenging years, I believe I need to align with Prof. Larese's statement: he is right, this is just the beginning. Therefore, thank you Prof. Larese for taking care of me, in one way or the other, and always showing me where lies the very interest and passion for doing science. "You should always do your best and see what happens", he would recite. I will thus always try to do my very best, whatever is the endeavor requiring my focus and attention.

Sincere thanks go to Mrs. Larese as well, for having helped with practical aspects of life in Tennessee in several instances.

Very important thanks and great gratitude go to each and every Larese group member whom I have encountered and shared some part of the adventure with, having helped to a lesser or to a greater extent. They are (in chronological order of appearance during my adventure): Andrew Hicks, Christopher Crain, Sourav Adak, Nathaniel Bass, Nicholas Strange, George Rouvelas, Fatema Wahida, Luther Langston, Andrew Pedersen, Zachary Stroupe. Everyone has somehow contributed to the betterment of my personality and actions.

Special thanks go to the machinists who have helped me realizing many of the experimental and technical components I have needed throughout my work at the University:

Tim Free (Chemistry Dept.), Ricky Huffstetler (Physics Dept.) and Randy McMillan (JIAM). Your help has revealed essential in many instances of my work. Technical help and instrumental availability has also come from Josh Moore. Thank you all for your help.

Sincere thanks go to Prof. Mannella and Dr. Vilmercati for useful and insightful discussions.

Sincere thanks also go to Prof. Roy, Prof. Kilbey and Dr. Fernandez-Baca (ORNL) for serving on my doctoral committee from the very beginning.

Thank you to all the American and international friends whom I have met throughout these years, and who made Tennessee a home for me and my family, and have always encouraged me to stay strong and never lose track of the reason why all this adventure had begun.

Very special thanks go to my direct and in-law family for the infinite and loving support provided from overseas at every single step of this very long way, especially when feelings of failure and discouragement were prevailing: my parents Marilena and Giuseppe, my brother Simone; my parents-in-law Patrizia and Michele, my sister-in-law Mariachiara, and my brothers-in-law Gabriele and Guido. Thank you for always believing in me.

A special thank you goes to my brother Simone for great help with all the technical drawings presented in this dissertation.

Last but not least, I wholeheartedly thank the love of my life, my dear sweet wife Francesca, and my adorable son Lorenzo Matthew (and my son-to-be-born Tommaso), for all their support, care and love shown each single day of these long years. Francesca has grown extremely strong and patient in listening to my problems, worries and complaints, and in understanding me, and advising me on anything I was stuck on. And there have been thousands of times when I was literally stuck and unable to get out of muddy waters. Nevertheless, I have always come out of any muddy waters, and I am now sailing toward the next harbor. Still together and ever stronger. Thank you my sweetheart.

Abstract

Today's energy needs are presenting challenges which have to be addressed with novel, as well as sustainable and efficient solutions. Within this context, the family of metal oxide (MO) materials offers a broad diversity of both structural and physicochemical properties, along with great versatility of synthesis. Nanoscale MO particles can be decorated with other nanoparticles, particularly of metals, and new properties may arise from such combinations. The present dissertation work reports the details of the development of an experimental method to accomplish the decoration of MO materials with metal species originated by an effusive source, along with the characterization of the decorated materials' properties. A custom-made vacuum chamber was optimized with several components (e.g. a calibration sensor to measure the effusive beam's flux; a conical vessel to mix and expose the MO powders to such beam) and utilized to produce different decorated materials. The pure MO materials were synthesized as high-quality, size-selected particles with a patented method. Due to their different structure and optoelectronic character, magnesium (MgO) and zinc (ZnO) oxide were chosen as substrates to explore this novel decoration process; while copper, nickel and cobalt were selected as the decorating metal species, offering the opportunity to study not yet fully understood transition metal electronic properties. The several examples of newly formed materials were characterized using different techniques, in particular X-ray diffraction, photoluminescence and diffuse reflectance spectroscopy (reflectance was then converted into absorbance). These techniques revealed trends in some properties of the novel materials, and were paired with more microscopic probes, namely magnetization and electron microscopy measurements. Great emphasis was put on the Cu/MgO system. In particular, Z-contrast scanning transmission electron microscopy has shown clear presence of metal deposits of copper on the MgO surfaces, confirming the results gained with the

previous techniques. Furthermore, a computer code was developed to facilitate the pore size distribution analysis obtained on mesoporous substrates. Several different materials were studied, in order to show the viability of the automated process, and the potential applicability of this method to studying porous structures for the same decoration process described earlier.

Table of Contents

List of Tables

List of Figures

Chapter 1

Introduction

The present work was stimulated by the idea of producing materials at the nanoscale, combining the properties of metals with those of metal oxides (MOs) through a chemical-free deposition methodology. The synthesis of a vast variety of nanoparticles (NPs) via a diversity of methods has reached nowadays numerous examples in the scientific literature, encompassing a plethora of both synthesis and characterization techniques ([32], [18]). Many of these methodologies have also been applied to pursue the deposition of certain species on substrates of different nature, either via chemical methods, e.g. co-precipitation of the two species ([21]), or by use of vapor-based methods to obtain the final product on single-crystal substrates [7].

Differently from most of the reported deposition methodologies, the aim of the present study is to pursue a deposition of NPs on powdered substrates bypassing the use of chemicals, therefore using physical methods. There are certain instances where the material to be deposited (or *decorated*) could lose purity due to chemical agents (e.g. surface etching and contamination with external agents).

The goal, then, is to deposit metal species (metal atoms or clusters) on metal oxide substrates: an example of oxide substrate is magnesium oxide (MgO), which can be prepared with highly clean and pure surfaces by a novel synthetic method that does not make use of any chemical reagent [46]. MO particles with narrow-size distribution can be produced via vapor entrainment in an inert gas atmosphere: this is the case of MgO, and potentially

for other MOs, e.g. zinc oxide (ZnO). Preserving the purity and cleavage of the surfaces is believed to play a key role in how metal particles can be deposited on them.

The technique to be used in order to decorate the surface is physical vapor deposition (PVD), in particular magnetron sputtering deposition, where an effusive beam of particles is generated under vacuum by means of an inert gas plasma, through ejection of particles off of a metal target by pure kinetic energy transfer from the plasma ions. Metal particles are thus generated directly from a pure substrate of the selected metal species without the need for a precursor, as it typically happens in deposition reactions.

The properties of matter at the nanoscale level, as compared to its bulk counterpart, have revolutionized our understanding of nature and opened a lot of new avenues for discovery and potential applications ([31], [63]). Therefore, it is desirable not only to develop a methodology whereby novel materials can be produced, but also to learn what properties these materials might offer. In particular, whether and how the addition of a metal on a MO substrate can modify the properties of the substrate is very intriguing, e.g. tuning the band gap, changing optoelectronic features, conferring catalytic properties, where the reduced size offers maximization of the surface area which is crucial in applications (such as catalysis). Harvesting energy in innovative forms is presenting important challenges to nowadays economy and society, and nanoscale matter might offer a very important contribution to solving this problem.

The choice of the metal species for deposition is important and will determine the final properties of the decorated substrate. Precious metals are a preferred choice as the deposited species due to their remarkable properties, e.g. in catalyzing certain gas-phase reactions [26]. With the intention to develop a viable method, a valid choice is to start with non-precious metals, which yet can offer a great opportunity to combine interesting properties with those of MOs.

Copper (Cu) is a very good example of such metals due to its remarkable electrical and thermal conduction characteristics. The combination of Cu with MgO (a wide band-gap electrical insulator) is very appealing, because of their very different electronic properties. On the same 3d transition metals row, nickel (Ni) and cobalt (Co) are also found, which are

electrically conductive and magnetic, too. The question of whether their magnetism might introduce magnetic character into the oxide substrate is another interesting one.

MOs are a wide class of materials whose properties are very diverse and range from insulator to semiconductor, as well as optoelectronic and catalytic applications of many types. MgO presents surfaces with very specific defects (i.e. color centers), which can give rise to light emission processes [40]. Past work in this research group has shown important expertise in both the synthesis [46] and fundamental studies of MgO(100) surfaces [49]. As aforementioned, the MgO produced by this group is very pure (i.e. with very low contamination from other metal species) and narrow-size distributed: MgO NPs have cubic shape, where the recurring cleavage is along the (100) face. Additionally, the MgO surfaces are purified with heat-treatment at very high temperatures (i.e. 950 °C): heat-treatment principally helps to remove impurities adsorbed from the atmosphere.

The same level of purity via high-temperature treatment might not be always possible due to lower melting point of the metal combined in the metal oxide. This is the case of ZnO, which is a very interesting semiconductor offering a diversity of properties, and it is used in a lot of applications. Despite the breadth of applications, its fundamental properties are still not completely understood [37].

The deposition of Cu on MgO has been explored with physical methods (and magnetron sputtering, in particular) in a variety of cases and thus several examples are reported in the literature. The main interest in many of such examples has been to grow films on single-crystal substrates, not exclusively metallic Cu layers, but also layers of one of its oxides, either Cu_2O or CuO (typically making use of reactive sputtering). One of the earliest examples is the work by He and co-worker, where electron beam evaporation is utilized for the epitaxial deposition and growth of Cu on MgO [27], studying the trapping of Cu in vacancy defects by means of electron energy loss spectroscopy (EELS). The epitaxial growth of Cu(100) on MgO(100) surfaces and the equivalent process between respective (111) surfaces is also investigated with EELS [28].

Later investigations encompass growth of Cu on MgO(001) and on ZnO($10\bar{1}0$) again by EELS [29]; and X-ray photoemission spectroscopy (XPS) studies of Cu on MgO(100) [3]. In the latter work, the authors state at the very beginning that "oxide-supported metal

catalysts have been widely studied in powder form while relatively few studies have been carried out on single crystals". Despite the many examples of powdered oxide-supported metal catalysts preparation even in the recent literature (examples of the Cu/MgO system can be found in [80] and [81]), these typically involve chemical deposition methods, spanning different combinations of metal and metal oxide substrates. In general, a lot of examples of physical vapor deposition of metals on oxide substrates are reported in the literature, regardless their interest as catalysts ([56], [73], [72], [64], [76], [75]); although few encompass physical deposition on powders [2].

After Alstrup and Møller [3], much effort has focused on the deposition of Cu and especially its oxides via both PVD and chemical vapor deposition (CVD). A special interest is devoted to Cu_2O due to its potential applications in the fields of photovoltaic cells, high-T_C superconductors and Bose-Einstein condensation ([56], [66], [11], [64], [55], [110], [71], [35], [34]). Specific use of reactive dc-magnetron sputtering is implemented to intentionally grow the oxides of Cu. Very recent examples of the sputtering of Cu on MgO and other substrates (e.g. glass) are reported here ([10], [33], [51], [90]).

The aim of the present study is to develop an apparatus, as well as a methodology that employs magnetron-based PVD sputtering in order to initially investigate the deposition of Cu on MgO powders, and offer the potential to extend this method to other metal/MO systems. The sputtering apparatus is composed of custom-made components, designed to address the specific purpose that future experimental investigations will require. This setup will be described along with the associated measurements used to characterize the Cu/MgO system as well as other systems that were investigated.

An additional portion of this dissertation study is related to the analysis of the pore size distribution (PSD) of few different porous powder materials. The experimental probe for this purpose are gas adsorption and desorption isotherms, while the data gathered with this technique are analyzed with the standard model of the Kelvin equation to assess pores radii and distribution of volumes in the materials. Such an analysis is facilitated by a code-based script that can take adsorption and desorption data as input, and provide all the relevant quantities for the pore size analysis as output.

Several pore models are considered as a means to evaluate the PSD obtained with the automated calculations [25]. The script is composed specifically for the data produced by computer-controlled volumetric adsorption isotherm apparatuses [59]. A detailed knowledge of the porosity structure in powdered materials of interest can actually help the choice of the substrate for the deposition of alien species, particularly in the fields of heterogeneous catalysis and surface chemistry ([53] and all papers in the same series, [97]), and, more in general, for energy applications.

This dissertation is divided into five additional chapters and four appendices as follows.

Chapter 2 discusses the theoretical background behind synthesis and characterization techniques used to study the decorated powders. The topics are: a presentation of MO materials and their properties, especially when implemented as supports for the deposition of other species; description of sputtering processes for the deposition and synthesis of the decorated materials; background theory for deposition calibration (quartz crystal microbalances); description of structural and optical techniques to study and analyze the properties of the decorated materials; a presentation of other structural and microscopic techniques to perform more fundamental measurements on the same materials; and description of adsorption and desorption phenomena for study of porous structures.

Chapter 3 describes the development of the magnetron sputtering-based system used for materials deposition. Also included is a characterization of the effusive (sputtering) beam used for deposition of metal nanoparticles and the details of the preparation and synthesis method of the decorated materials along with methods used to characterize their properties. Finally, the method used to study porous structures will be described.

Chapter 4 includes a detailed description and analysis of the results of the characterization of the decorated materials.

Chapter 5 describes the investigation of several porous species with gas adsorption and desorption techniques at low temperatures (around 77 K) to illustrate the analysis script developed.

Chapter 6 presents the summary and conclusions on the different areas of investigation contained within this dissertation, as well as perspectives for future work.

Appendix A includes the technical information regarding the experimental apparatus used for the metal deposition and its calibration.

Appendix B includes additional information and tables regarding the decorated materials whose preparation and characterization is described throughout this dissertation.

Appendix C details the code for adsorption/desorption analysis and describes how it can be implemented by a general user.

Appendix D includes additional information regarding the characterization of porous materials.

Chapter 2

Background

This Chapter introduces topics relevant to the experimental and characterization methods described below. First, an overview of the properties of metal oxide materials will be given. Then, a theoretical background of the sputtering process will be given as a foundation for the preparation method used in the PVD process for producing the metal decorated materials. Additional background will also be given of the experimental techniques to study the microscopic properties of such materials.

2.1 Materials: metal oxides

Metal oxides (MOs) are a wide class of materials whose physical properties range from semiconductors to wide-bandgap insulators. MOs exhibit interesting bulk properties and of particular interest here, at the surfaces of nanoparticles. Usually, the exposed faces tend to those that minimize the surface free energy, hence the resulting surface states are generally stable configurations. In cases where the capability to produce particles with surfaces of a desired crystallographic face exists, the results can be dramatic because the physico-chemical properties of nanoparticles are readily linked to the changes in the surface character.

The simplest and most relevant model to describe MO structures is an ionic model, applicable because the relevant interactions in the MO crystal structures are the ones between positively charged metal cations and the negatively charged oxygen anions, O^{2-}. Coordination between cations and anions in the MO structure plays a principal role in

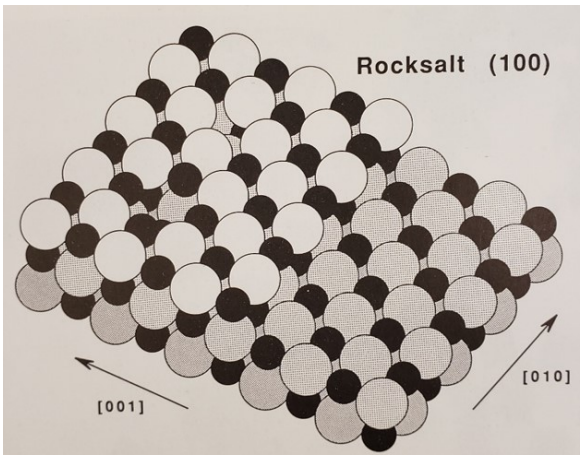

Figure 2.1: Model of the rocksalt (100) surface. Large circles are O anions, small circles are metal cations. A [010] step to another (100) terrace is shown, as are both missing anion and missing cation point defects [30]. Lattice parameter for the MgO simple cubic structure is $a = 4.21$ Å.

the MO bulk, as well as the MO surface. Lowering of the coordination (where either the metal cation or the oxygen anion is taken as the center of coordination) is what typically generates vacancies and defects on the MO surface, reducing the crystallographic perfection and introducing new sites, e.g. F and V centers, i.e. oxygen vacancies and metal ion vacancies, respectively (F centers are also referred to as color centers). Such centers are related to the excitation of unbound outer-shell electrons, possibly resulting in radiative emission in the visible range of the electromagnetic spectrum.

Different crystal structures impose very different properties to MOs. Perfect examples for a comparison are the two MOs which will be of interest to the present study: MgO and ZnO. MgO with its rocksalt structure exhibits six-fold octahedral coordination as do many other in this structure class (see Fig. 2.1). The large Madelung potential between ions results in one of the most stable crystal structures and preferential cleavage along the {100} direction. This remarkable stability, along with the nonpolar nature of the bulk, contributes to the remarkable insulating properties of MgO (bandgap of 7.8 eV).

ZnO, on the other hand, exhibits a wurtzite structure (see Fig. 2.2). This structure class has four-fold tetrahedral coordination, which is *lower* than rocksalt structure coordination and thus leaving more freedom for electrons to move within the crystalline structure. ZnO

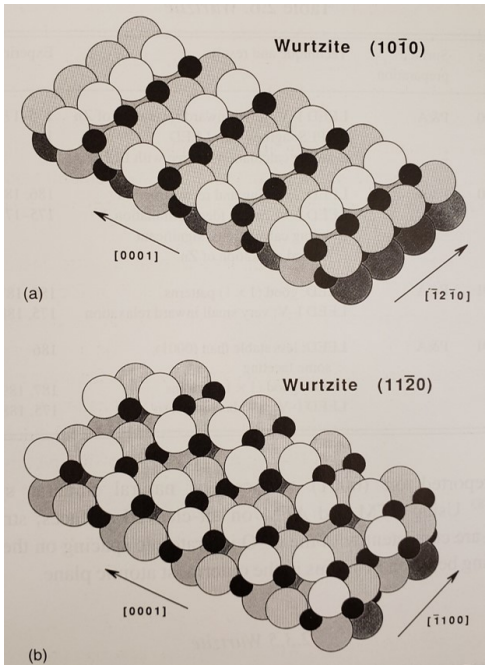

Figure 2.2: Models of wurtzite surfaces: (a) (10$\bar{1}$0) and (b) (11$\bar{2}$0) [30]. Lattice parameters for ZnO wurtzite structure are $a = 3.25$ Å and $c = 5.21$ Å.

is in fact a semiconductor (bandgap of 3.37 eV), leading to a broad variety of appealing properties, from the optoelectronics [37] to the antibacterial [1] and gas-sensing ones [36].

MgO and ZnO appear as two good candidates to attempt the deposition of individual or clusters of metal species on the surface. Both these MOs are well known for applications in the field of heterogeneous catalysis, where the different structural properties may provide different contributions to the interaction with the ad-metal species deposited on the surface and hence opportunities to develop novel materials. A broader discussion of the fundamental properties of MOs, as well as of their technological importance, can be found here [30].

2.2 The sputtering process

Sputtering is a deposition technique that utilizes an ionized gas (*plasma*) under vacuum conditions in order to generate an effusive source of particles from a target. In general, the term *physical vapor deposition* (PVD) refers to several deposition techniques that do not employ a chemical reaction to generate the desired deposited species. Hence, the term

PVD refers to a physical process whereby a species is deposited on a certain substrate material; whereas *chemical vapor deposition* (CVD) refers to a chemical process to facilitate the formation of a deposited layer or film of coating.

Thus in the PVD methods that are used for sputtering metal atoms or clusters from a solid target, the evaporation process usually involves a sublimation of the surface atoms thereby forming a vapor phase by heating the material to be evaporated within a vacuum. Many PVD-based sputtering methods occur via erosion of a solid (target) material when an energetic particle bombards the target in a low pressure (vacuum) environment. A plasma of inert gas (e.g. argon) is generated using an electromagnetic field. For high sputtering efficiency, the ions in the plasma have to be comparable in mass to the atomic mass of the target material. Motion of the ionized particles in the vicinity of the target statistically causes a certain number of them to hit the target's surface (to *impinge* on the surface), transferring kinetic energy to the substrate. When the kinetic energy is sufficient to overcome the binding energy of the target's topmost layer, atoms are released into the gas phase and can travel freely.

The sputtering process can be controlled by tuning the voltage applied to the used sputtering device. The target is mounted on a plate acting as a cathode (attracting positively charged ions) and the substrate acts as the anode. Application of a high voltage (few kV) between cathode and anode generates the electric field to ionize the inert gas, thus generating the plasma for ion cascade on the target, and consequent erosion. Specially designed sputtering guns are constructed such that both cathode and anode are incorporated, with negative voltages applied to the cathode (usually hundreds of volts) to establish the electric field.

A more sophisticated version of a sputtering gun utilizes the *magnetron sputtering* principle: here the head of the gun (the cathode) employs an arrangement of permanent magnets such that the charged particles of the ionized gas move within a confined region in the vicinity of the target. Electrons that are confined along the magnetic field's lines (due to Lorentz's force $\mathbf{F}$, $\mathbf{F} = q\mathbf{v} \times \mathbf{B}$, where q is the electron's charge, $\mathbf{v}$ is its speed and $\mathbf{B}$ the magnetic field generated by the permanent magnet) induce secondary-ionization processes in the vicinity of the target. The magnetic field causes ionized atoms to impinge on the

target and induce an eroding (evaporation) process that is about 100 times higher than regular sputtering. The erosion of the target is somewhat asymmetric, i.e. limited to only certain areas of the target depending on the geometry of the magnetic field (e.g. toroidal). This asymmetry results in only a fraction of a sputtering target to be usable in magnetron sputtering (typically about 30-35%).

The sputtering process can be induced using either a DC (direct current) or AC (alternate current) power. The former is known as dc-magnetron sputtering. Radio-frequency (RF) waves at frequencies in the MHz range are also used to establish the oscillating electric field between electrodes. These RF magnetrons are commonly used when the substrate or the target are insulators.

2.2.1 Principles of sputtering

There are two fundamental parts needed to describe the sputtering process: *erosion of the sputtering target* and *effusion of the ejected particles*. Erosion of the sputtering target occurs when the kinetic energy of the impinging gas ions is much higher than the binding energy of the atoms in the outermost layers. The excess energy will allow an atom in the surface region to travel away from it. The impact of an ion on the target's surface generates a *collision cascade*, such that the initial collision generates a growing sequence of collisions that extends beyond the outermost layer of atoms. This causes multiple atoms to be ejected from the surface region (see Fig. 2.3). The efficiency of this process is called the *sputtering yield*, i.e. the number of atoms ejected per impinging ion.

The various relevant energies involved in this sputtering process are the threshold energy, E_{th}, which is the binding energy of a projectile to the target surface; the surface binding energy, E_{sp}; and the heat of sublimation, E_{sb}. For the sputtering process to occur, E_{th} must meet the following requirement:

$$E_{th} + E_{sp} > E_{sb}/\gamma \tag{2.1}$$

where the factor:

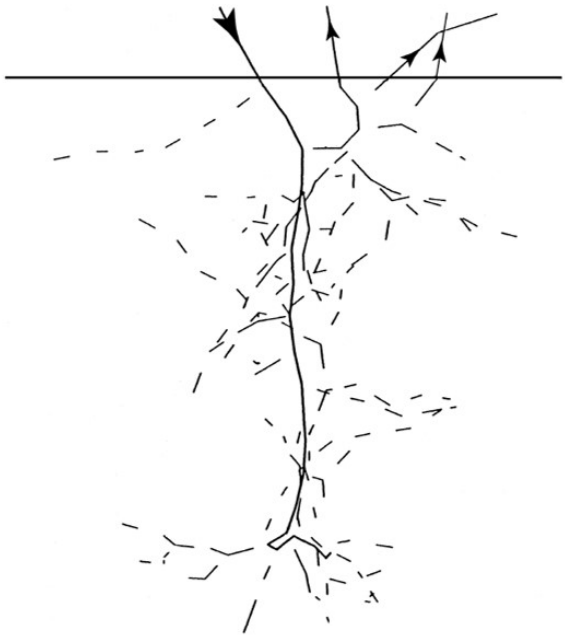

Figure 2.3: Simulation of a collision cascade initiated by a 1 keV Ar ion at 30° incidence on a Ni substrate leading to three sputtered atoms [5].

$$\gamma = 4M_1M_2/(M_1 + M_2)^2 \tag{2.2}$$

in a binary collision is called the *energy transfer factor*. M_1 and M_2 are the masses of the projectile and target, respectively. For noble gas ions, $E_{sp} = 0$, which means that for the typical choice of argon, the threshold energy must be greater than the surface binding energy scaled by γ: $E_{th} > E_{sb}/\gamma$ (γ can be extrapolated from experimental data).

The primary ion's energy, E_n (i.e. the energy of an ion impinging on the target's surface) will determine the effectiveness of the sputtering process. In particular, the number of atoms taking part to the collision cascade will depend upon the fraction of E_n making nuclear collisions. The motion of atoms in the substrate also has an effect on the formation of defects, i.e. how the sputtering target is eroded in the process. The average number of atoms in a cascade with an energy E_i recoiling within the energy interval $[E_i, dE_i]$ can be written as:

$$F(E_n, E_i) \approx \frac{\Gamma E_n}{E_i^2},\ \gamma E_n \gg E_i. \tag{2.3}$$

Γ is (weakly) dependent on the atomic interaction ($\Gamma \approx 0.4 - 0.6$). $F(E_n, E_i)dE_i$ is the *recoil density*, which is of great importance because it ultimately defines the *flux* of atoms moving in the cascade with energy E_i. Therefore, the sputtering yield depends on the energy deposited at or near the surface and the *internal energy distribution* of atoms is proportional to E_i^{-2} ([85], [5]).

Several models have been proposed to describe the collision cascade. The theory by Sigmund considers a *linear collision-cascade regime*, which means that the sputtering yield Y is predicted to scale linearly with the energy deposited in elastic collisions at the surface [84]. Within the same model, given the energy surface barrier U (typically, the sublimation energy of the solid can be used), the probability for an atom to escape from the surface is given by:

$$P(E_i, \theta_i) = \begin{cases} 1, & E_i \cos^2 \theta_i \geq U \\ 0, & E_i \cos^2 \theta_i \leq U \end{cases} \tag{2.4}$$

where E_i and θ_i are, respectively, the energy and the angle (relative to the normal) with which the atom approaches the surface from within the target. In general, the differential sputtering yield can be derived for atoms sputtered with an energy E, into the solid angle Ω around the polar emission angle θ:

$$\frac{d^3Y}{dEd^2\Omega} \propto \frac{E}{(E+U)^{3-2m}} \cos\theta \tag{2.5}$$

where m characterizes the power of the interatomic potential V: $V(r) \propto r^{-1/m}$.

A similar result was derived by Thompson [99], where the monotonically falling recoil spectrum within the target (Eq. 2.3) is transformed into an *energy* spectrum peaking at energy E_{peak}, which is theoretically dependent on the specific target material (via U) only, and not upon the mass and energy of the impinging ion alone:

$$E_{peak} = \frac{U}{2(1-m)}. \tag{2.6}$$

In the case of high emission energies, $E \gg U$, the energy spectrum is predicted to fall off as $1/E^{(2-2m)}$ according to Eq. 2.5. In general, the value of the parameter m depends

on the energy regime of the sputtering process, but in principle it is inappropriate to set it equal to zero: $m = 0$. Independent of the value of m and the energy dependence of the sputtering yield, Eq. 2.5 clearly predicts a *cosine law* or *cosine-like* behavior for the angular (θ) distribution of the sputtering. Such a cosine law is associated with an isotropic distribution of the ejected particles from the target. This dependence can be expressed as:

$$\frac{dY}{d\Omega} \propto \cos^{y}\theta \tag{2.7}$$

where, usually, $y > 1$. In general, the energy and the distribution of the sputtered particles may depend strongly on the solid structure of the target material, i.e. its crystalline or amorphous phase [5].

For the purposes of this discussion, one only needs a brief description of the typical energy regimes for sputtering processes. For very low impact energies (for low-mass projectiles), namely 1 keV or lower, i.e. the so-called *single knockon regime*, a full collision cascade does not evolve and sputtering usually takes place from isolated collisions. In the case of metal and semiconductor targets, where the projectile gas is e.g. argon, the impact energies can be as high as tens of keV; here one has the *linear collision-cascade regime* (see model by Sigmund [84]). The third (and last) regime occurs at high-impact energies, i.e. up to several tens of keV, collisions using heavy projectiles, and where very dense collision cascades may develop involving very high numbers of atoms. This is the *high-density cascade* or *spike regime* [5].

In the studies described herein argon is used as the ionized gas to generate the sputtering collisions; hence the energy range of interest is probably the linear collision-cascade regime, involving energies of about 10 keV or slightly higher. Examples of metals and their respective sublimation energies are: Cu (3.50 eV); Ni (4.45 eV); Co (4.44 eV) [52]. An example of a method used to estimate the surface binding energy can be found in the study by Kudriavtsev and co-workers [44].

2.3 Introduction to quartz crystal microbalance sensors

Relative to the implementation of PVD methods and the generation of effusive beams, characterization of the beam is an important aspect from the experimental perspective. The knowledge of the amount deposited (typically, from a metal target) per unit of mass and time, at a specific distance from the source, is a key factor for deposition purposes. Given certain deposition conditions, the *flux* of ejected atoms (or clusters) will also vary depending upon the nature of the sputtering target. Eq. 2.5 and 2.7 can be used to describe the general behavior of the beam generated by an effusive source, although a quantitative assessment of the flux is preferred.

To satisfy this assessment of the flux, some type of sensor should be used to gauge the beam characteristics for a prescribed set of deposition parameters (e.g. distance from source, power of the source, inert gas pressure). A quartz crystal microbalance (QCM) is a sensor typically used for high-sensitivity deposition measurements. A QCM is constructed using a piezoelectric crystal which vibrates in shear-mode when an AC potential is applied to its electrodes. These shear-mode oscillations occur at a specific frequency (typically in the MHz range), i.e. the resonant frequency for the specific crystal. However, the resonance frequency of the QC is found to diminish proportionally to the deposited amount. The details of using this sensor will be detailed below, along with the necessary equations and principles of operation of a QCM. The work by Lu and Czanderna is followed [54] and references therein are especially relevant.

The theoretical foundation for using quartz crystals as a microbalance can be traced back to Lord Rayleigh, who showed that a small change in the inertia of a mechanically vibrating system perturbs the resonance frequency. It was Sauerbrey who suggested using a quartz crystal oscillator as a sensing device for measuring the thickness of thin films and showed that, by exposing a torsional beam microbalance and a quartz plate to the same depositing flux, the shift in resonance frequency is proportional to the deposited mass to within $\pm 2\%$ [54].

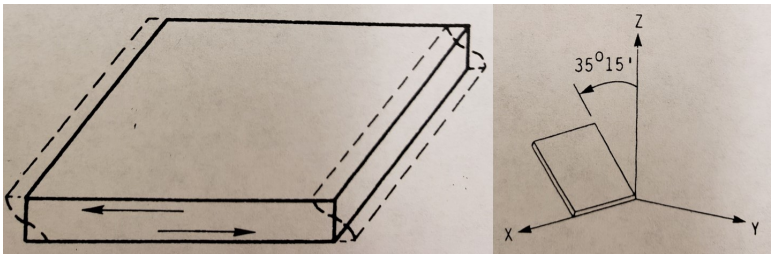

Figure 2.4: *Left*: The fundamental thickness-shear mode of vibration. *Right*: AT-cut quartz crystal plate. From reference [54].

A rapid development of the QCM as a mass balance most likely happened because devices could measure frequencies with a precision of 1 part in 10^{10} (in 1960), and quartz crystals could be produced with frequency stability for weeks of one part per billion (ppb). Hence the resulting QCM device is attractively simple and of outstanding sensitivity to mass change. Warner and Stockbridge ([88], [105]) were the first ones to focus on the development of the same set of parameters still relevant today, and furthermore they identified the promise of an AT-cut vibrating in the thickness-shear mode (Fig. 2.4), writing that "for measurement accuracy of 0.3 ng/cm^2, which can be made near 7 MHz, all that is required is a frequency measurement accuracy in 1 part in 10^8. These measurements can be performed with an electronic counter averaging for 10 s, that is, counting cycles directly for 10 s" [54]. The equivalent circuit of a QCM is shown in Fig. 2.5.

In the first place, a linear frequency-to-mass equation for small loads can be obtained. Considering a quartz crystal and a deposited film of material on it, one defines the areal densities m_f and m_q as the mass per unit area for the deposited film and quartz crystal, respectively. Introducing the resonant frequency of the quartz crystal, f_q, and the resonant frequency of quartz crystal with the deposited material, f_c, the following equation can be derived [54]:

$$\frac{f_c - f_q}{f_q} = -\frac{m_f}{m_q} \tag{2.8}$$

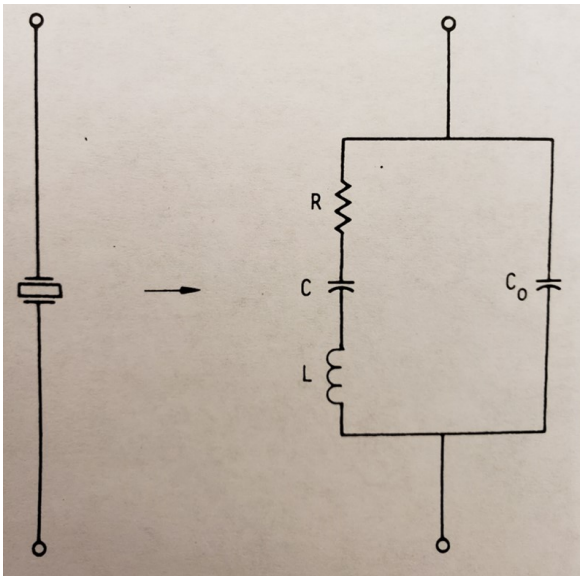

Figure 2.5: The equivalent circuit of a quartz crystal resonator. The motional capacitance C represents the mechanical elasticity of the vibrating body; the motional inductance L is a measure of the vibrating mass; and the equivalent resistance R corresponds to the total loss of mechanical energy due to internal friction and energy dissipated to the surrounding medium and supporting structures. The shunt capacitance C_0 is an actual lump capacitance (i.e. a capacitance model with negligible internal temperature differences) due to the electrodes of the resonator and stray capacitance to the supporting structures [54].

It is important to remember that, for materials with a spatially uniform density, the areal density is also equivalent to the product of thickness and density, thus giving $m_f = t_f \rho_f$ and $m_q = t_q \rho_q$. It can be shown that Eq. 2.8 can be re-written as:

$$m_f = \frac{(f_c - f_q)\rho_q v_q}{2 f_q^2} \tag{2.9}$$

being v_q the shear wave velocity.

The use of areal density rather than mass in Eq. 2.9 is more convenient because the vibrating area of an actual quartz crystal resonator does not necessarily extend to its entire surface and the exact area is hard to define. Eq. 2.9 can be used to determine the areal density of a deposited film as long as the active area of a quartz crystal resonator is completely covered by the deposited film. It is also more meaningful for deposited materials that do not have a well-defined density, such as in the cases of very thin or discontinuous films. Eq. 2.9 is often expressed simply by

$$\Delta f = -C_f m_f \tag{2.10}$$

where $\Delta f = f_c - f_q$ is the frequency shift and

$$C_f = \frac{2 f_q^2}{\rho_q v_q} \tag{2.11}$$

is defined as the mass sensitivity or calibration constant of a QCM.

As an example, for an AT-cut quartz crystal, where $\rho_q = 2650$ kg/m^3 and $v_q = 3340$ m/s, the mass sensitivity for a 5 MHz resonator, obtained from Eq. 2.11, is 5.65 MHz $\cdot$ m^2/kg. This means that the addition of a material with an areal density of 17.7 ng/cm^2 onto such a resonator will cause a frequency shift of 1 Hz. Since a number of frequency measurement techniques can have a resolution of better than 1 Hz at 5 MHz, the detection limit can be even smaller assuming all other factors that may affect the resonant frequency can be properly controlled.

There are two advantages in expressing the deposited mass of the film as $m_f = t_f \rho_f$. First, the mass sensitivity of a QCM can be calculated from its resonant frequency and the intrinsic properties of the quartz crystal. Thus, no individual calibration is required provided

that the deposited material covers one crystal surface (or the active vibrating area) entirely. Secondly, the mass sensitivity is independent of the other physical properties of the deposited material [54].

In the case of extended mass loads, a linear period-to-mass approximation can be developed. This is especially true when a QCM may have already been deposited with mass loads in previous uses, e.g. this could be the case of using a QCM as a film thickness monitor in a vacuum deposition system. Instead of Eq. 2.10, only the frequency shift might be measured and the following equation employed to determine the areal density:

$$\Delta f_c = -C_f m_f \tag{2.12}$$

where Δf_c is the frequency shift induced by the addition of material with an areal density m_f to a quartz resonator which may already have a significant amount of deposited material. One would expect that as more material is accumulated onto the quartz crystal resonator, the use of a constant mass sensitivity would result in an increasingly large error in the areal density determination. In the early 1960s, Behrndt and Love [54] suggested that the mass sensitivity should be defined by

$$C'_f = \frac{2f_c^2}{\rho_q v_q} \tag{2.13}$$

and therefore the equation

$$\Delta f_c = -C'_f m_f \tag{2.14}$$

should be used for determining the areal density of deposited films.

If one considers Eq. 2.14 and differentiates it:

$$dm_f = -\left(\frac{\rho_q v_q}{2f_c^2}\right) df_c \tag{2.15}$$

and performs an integration:

$$\int_0^{m_f} dm_f = -\left(\frac{\rho_q v_q}{2}\right) \int_{f_q}^{f_c} \frac{1}{f_c^2} df_c \tag{2.16}$$

the following equation is obtained:

$$m_f = \rho_f t_f = \frac{\rho_q v_q}{2}\left(\frac{1}{f_c} - \frac{1}{f_q}\right) \tag{2.17}$$

which is expressed in terms of the areal density and also of the film thickness and density.

Since $\frac{1}{f_c}$ and $\frac{1}{f_q}$ are the periods of oscillation for the quartz crystal resonator with and without the deposited material, respectively, Eq. 2.17 implies that the areal density of a deposited film is linearly proportional to the change in period of oscillation. The changing mass sensitivity as defined by Eq. 2.13, and expressed in terms of frequency change per unit areal density, is not explicitly shown in Eq. 2.17, which, instead, shows a proportionality constant $\frac{\rho_q v_q}{2}$. Such a constant is independent of the mass load on the quartz crystal. Thus, Eq. 2.17 can be implemented into an instrument that measures the change in period of oscillation of the quartz crystal.

However, given a quartz crystal resonator, any measurement of the frequency of oscillation can be used to calculate the deposited mass, i.e. the areal density m_f, via Eq. 2.17. It was also confirmed experimentally that Eq. 2.17 could provide better accuracy in mass determination than that given by Eq. 2.9. Eq. 2.17 is independent of any physical properties of the deposited film other than its areal density, and can be accurately applied to measure mass deposits of any material up to frequency shifts of 10% of f_q [54].

2.4 X-ray diffraction

Crystal structures of solid materials are three-dimensional repetitions of atoms generated by a set of unit vectors, $\mathbf{a_1}$, $\mathbf{a_2}$, $\mathbf{a_3}$. The unit vectors follow a scheme of repetition which is described by specific crystallographic planes. Such planes will describe different arrangements depending upon the type of lattice (*Bravais lattice*) used to describe the specific geometry of the particular crystal structure.

Different schemes of repetition of the unit vectors generate a specific Bravais lattice in the so-called *direct space*. The direct space has its counterpart in the *reciprocal space*, being the two related by Fourier transformation. Unit vectors $\mathbf{b_1}$, $\mathbf{b_2}$, $\mathbf{b_3}$ in the reciprocal space can be derived from $\mathbf{a_1}$, $\mathbf{a_2}$, $\mathbf{a_3}$. The advantage of expressing crystalline structures in the reciprocal

space stays in the relationship with the wavevector describing radiation interacting with the crystal. Particular importance resides in the relationship between the radiation wavelength and the separation (i.e. distance) between crystallographic planes.

X-rays can be generated with wavelengths comparable to the typical interatomic distances in crystal structures (order of magnitude of the Å). Bragg's law establishes a relationship between the wavelength of an incident radiation, λ, the angle at which radiation is reflected off of lattice planes, θ, and the distance d between such planes:

$$n\lambda = 2d_{hkl}sin(\theta). \tag{2.18}$$

The subscripts *hkl* are integers and called the Miller indices: *hkl* indicate a set of crystallographic planes, one of which passes through the origin (of the direct space), and the next nearest makes intercepts $\mathbf{a_1}/h$, $\mathbf{a_2}/k$, and $\mathbf{a_3}/l$ on the three crystallographic axes.

Two properties of a set of *hkl* planes as they relate to Bragg's law are: the orientation of the planes and their spacing. A simple representation of both properties is obtained by introducing a vector $\mathbf{H}_{hkl}$, which is perpendicular to the planes *hkl*, and whose magnitude is the reciprocal of the spacing. This latter can be expressed in terms of the reciprocal unit vectors:

$$\mathbf{H}_{hkl} = h\mathbf{b_1} + k\mathbf{b_2} + l\mathbf{b_3}. \tag{2.19}$$

If vectors $\mathbf{H}_{hkl}$ are drawn for all values of *hkl*, the terminal points of these vectors form the reciprocal lattice, whose repetition vectors are in fact $\mathbf{b_1}$, $\mathbf{b_2}$, $\mathbf{b_3}$. The spacing with respect to one of the crystallographic axes $\mathbf{a_i}$, i = 1, 2, 3 is given by the following relationship:

$$d_{hkl} = \frac{\mathbf{a_i}}{h} \cdot \frac{h\mathbf{b_1} + k\mathbf{b_2} + l\mathbf{b_3}}{\|\mathbf{H}_{hkl}\|} \tag{2.20}$$

being each reciprocal vector perpendicular to the plane defined by the two crystal axes with different indices ($\mathbf{a_i} \cdot \mathbf{b_j} = 0$, $i \neq j$).

The measurement of X-ray reflections from crystallographic planes as a function of the reflection angle results in a diffraction pattern for a specific crystalline structure. In fact, only X-ray photons (of a given λ) which satisfy Bragg's law will interfere constructively to

generate a diffraction pattern, because only those are reflected by equivalent lattice planes (see Fig. 2.6). The constructive interference will produce peaks (X-ray counts) for those values of 2θ which satisfy Bragg's law (angle of incidence and of reflection are the same, and their sum yields 2θ). Usual X-ray radiation for diffraction measurements is the copper $K_{\alpha_1\alpha_2}$ doublet ($\lambda = 1.542$ Å).

There is a distinction between diffraction measurements on single-crystal and powdered samples. In the former case, a specific lattice plane can be directly exposed to the incoming beam of X-rays; in the latter case, small (or very small) particles cannot be manually arranged in order to expose a certain set of planes to the incoming beam. For this reason, the sample usually rotates on a stage, in a way such that the grains can be hit by X-rays from all angles over a certain time interval, averaging diffraction signal to build a pattern. In this latter case, two are the most used methods to determine the crystalline phases of a specimen: the so-called Bragg-Brentano method ($\theta - 2\theta$ geometry), and the Debye-Scherrer method. These two methods encompass different geometries of measurement.

For a more detailed presentation of fundamentals and applications of X-ray diffraction, see reference [106].

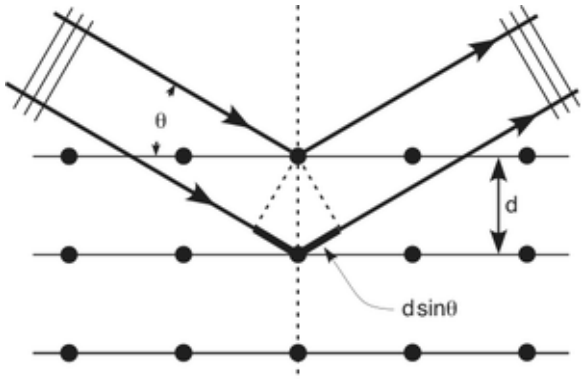

Figure 2.6: A Bragg reflection from a particular family of lattice planes, separated by a distance d. Incident and reflected beams are shown for two neighboring planes. The path difference is $2dsin(\theta)$.

2.5 Optical techniques

The investigation of the optical character of the deposited materials in this dissertation has been carried out primarily by using two techniques: photoluminescence spectroscopy (PL) and diffuse reflectance (DR) spectroscopy. PL takes place when a material absorbs light at certain energy (wavelength) and re-emits it at a lower energy (longer wavelength) after some type of decay process. On the other hand, DR occurs as the measurement of diffused light off of a material sample irradiated with light radiation in a specific wavelength range.

Such techniques can provide complementary types of information regarding a system. In particular, reflectance data can be converted into values of absorbance, therefore one can study where light is absorbed on an energy scale, and compare this to the excitation and emission processes probed by PL. This relationship will be addressed later on in this Section.

2.5.1 Photoluminescence spectroscopy

Photoluminescence is a general term that refers to the emission of light by any type of matter (typically, solid or liquid materials) upon absorption of light by the same. In general, the light radiation involved in PL phenomena spans across the UV-visible range, namely 200-800 nm. Electrons in the constituent atoms, or molecules, of the luminescent material are excited by light with energy (wavelength) that usually falls within the UV, i.e. 200-350 nm; the same electrons undergo a relaxation process during which they release part of the original energy in form of radiation. Therefore, the emitted radiation will have lower energy (longer wavelength) than the incoming one $\lambda_{exc} < \lambda_{emis}$. This can be shown as:

$$E_{exc} = h\nu_{exc} = h\frac{c}{\lambda_{emis}} > h\frac{c}{\lambda_{emis}} = h\nu_{emis} = E_{emis}. \tag{2.21}$$

The wavelength is often expressed in terms of its reciprocal, the wavenumber $\tilde{\nu}$.

A general representation of the light absorption and emission processes can be given by the so-called Jablonski diagram (Fig. 2.7), which illustrates the transitions between atomic/molecular energy levels corresponding to absorption and emission, respectively. After light is absorbed by ground state electrons, some energy is usually released within the material, while the rest of it is emitted upon final relaxation of the excited electrons back to

their ground state. Such a re-emission can happen on different time scales depending on the speed at which energy transfers happen within the substance, and thus the emission rate.

In excited singlet states, where the electron in the excited orbital is paired to an electron in the ground-state orbital (by opposite spin), return to the ground state is allowed and occurs quickly by emission of a photon. This occurrence is named *fluorescence*, and happens with typical rates of 10^8 s^{-1} (with typical lifetimes of about 10 ns). Whereas, in the case of triplet excited states, the electron in the excited orbital has the same spin orientation as the ground-state electron: transitions to the ground state are forbidden and the emission rates are slow, i.e. 10^3 s^{-1} or slower. This is the case of *phosphorescence* whose lifetimes are typically of the order of milliseconds to seconds, because the transitions between triplet excited states and singlet states are forbidden by selection rules for dipole transitions, namely $\Delta L = \pm 1$ and $\Delta S = 0$, being L and S the angular momentum and spin quantum number, respectively [47]. The mechanism whereby phosphorescence takes place is called *intersystem crossing* (IC), because an electron relaxes from a singlet to a triplet state (Fig. 2.7) before final relaxation to singlet ground state with radiation emission. This process is, in fact, forbidden by the aforementioned selection rules, and this is what causes relaxation and emission times to be orders of magnitude larger than those for fluorescence.

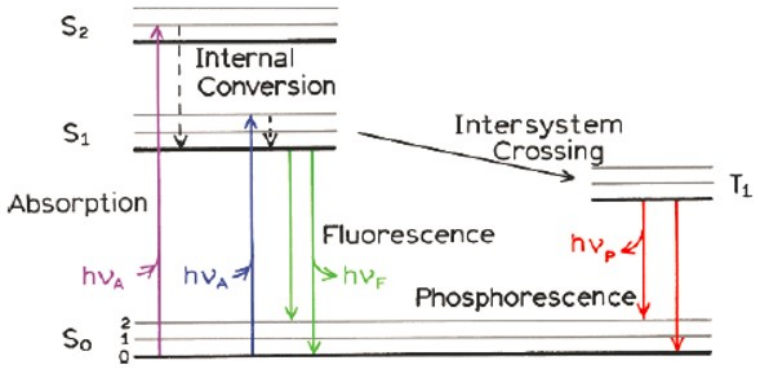

Figure 2.7: Example of Jablonski diagram representing absorption of light from the ground state, and re-emission in the form of fluorescence or phosphorescence [47].

Generally, the term PL describes both fluorescence and phosphorescence, indicating their similar nature as phenomena of light absorption and consequent emission at lower energy. In certain instances, distinguishing between the two might not be easy because ranges of emission rates can overlap. The general description of PL encompasses all the possibilities of absorption and re-emission of light. It is important to note that the terminology photoluminescence is a more appropriate terminology when dealing with solid materials, because it encompasses all the possible phenomena of light absorption and re-emission (at longer wavelength) that can take place in a solid structure, both in the bulk and *at the surface*, taking all the possible relaxation time scales into account.

Absorption and emission of light are measured separately. As noted above, absorption is related to the excitation process in the luminescent material. An *excitation spectrum* measures the intensity of light emitted at a particular wavelength, while excitation wavelength is changed across a certain interval. Thus, one can detect the peak of absorption for a specific emission. On the other hand, an *emission spectrum* measures the intensity of light emitted on a given interval, while excitation occurs at a specific wavelength. One can therefore appreciate the changes in the emission features of a material with constant atomic/molecular excitation (Fig. 2.8). Excitation and emission spectra will overlap on a certain wavelength range: coincidence of the two ideally means that no radiative energy transition is occurring. Such overlapping typically occurs in the case of fluorescence, because timescales of absorption and emission of light are very similar.

Knowledge of excitation and emission features provides information about how a certain species responds to incoming light radiation. In certain instances, one can expect light of a specific energy to be absorbed, e.g. according to the energy band gap of a solid material. In the latter case, the energy difference between valence and conduction energy bands will be enough to excite electrons into a higher energy state, and these will emit light in their relaxation process. Semiconductor materials are broadly studied because their energy band gap falls within few eV, i.e. energy values included in the UV range. This may not be the case for more insulating materials with larger difference between bands in their lattice structure.

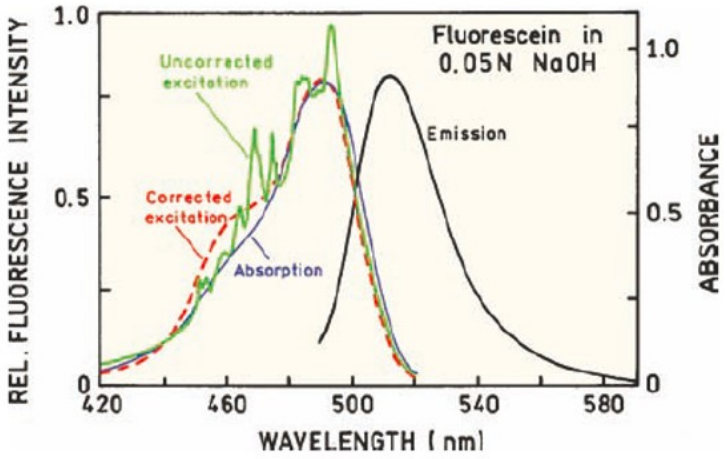

Figure 2.8: Excitation and emission spectra of fluorescein [47].

2.5.2 Diffuse reflectance spectroscopy

DR spectroscopy is a widely used technique with solid samples to measure their absorption properties, e.g. absorbance. In fact, light cannot travel through most solids as readily as it does through liquid solutions. Naturally, the density of most solids is higher and light interacts primarily with the outer surface before undergoing attenuation. For this reason, absorption cannot be measured directly; nevertheless, light is reflected by the outer surface to some extent and thus surface reflectance is typically measured. The term *diffuse* derives from the assumption that the angular distribution of the reflected radiation from a surface is isotropic, therefore the surface brightness is directionally independent [41].

DR can be used to quantify the absorbance of a certain material. In particular, this assumes that the thickness of the surface under investigation, i.e. the thickness of the material sample light is shone upon, is infinite with respect to the penetration depth of impinging radiation. Also, a layer of material is actually composed of tightly packed particles in the case of a powder, which can involve not only absorption, but also scattering of the incident light. The different nature of light interaction with matter in the reflection process is described by means of two different constants, namely the absorption coefficient, or absorption constant, k, and the scattering coefficient, or scattering constant, s.

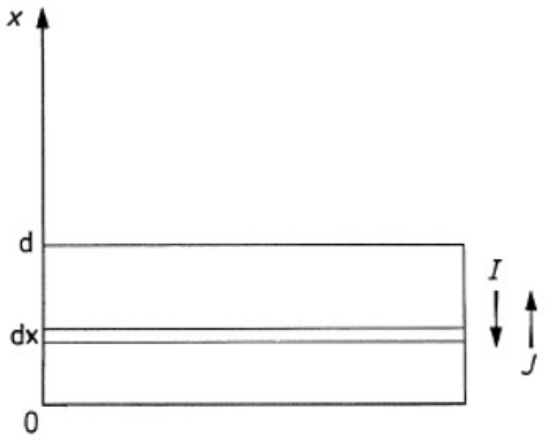

Figure 2.9: Concerning the derivation of the simultaneous differential equations according to Kubelka-Munk [41].

Kubelka and Munk [43] have derived an equation to describe the diffuse reflectance from a surface, which solely depends upon the ratio between absorption and scattering coefficients. The derivation refers to a system as described in Fig. 2.9: let a plane parallel layer of material, with thickness d, be irradiated by a monochromatic diffuse radiation flux I, in the direction x. Considering the example of a solid powder as above, the layer will be given by tightly packed particles of a certain size. The layer d is capable of both absorbing and scattering radiation. (Scattering will certainly depend on the particles' size, although in general it is assumed that the layer is able to scatter incoming radiation.) Edge effects may be ignored because the layer is infinitely greater in the yz-plane than its thickness d. While the incoming flux has intensity I, the reflected one has intensity J, and therefore will be directed along x.

Let an infinitesimal portion of such layer, dx, be now considered, and the intensity of absorbed (by reflection, refraction, or diffraction) and scattered light through it be named i and j, respectively. The intensities i and j will decrease due to radiation absorption and scattering by the amounts $(k + s)idx$ and $(k + s)jdx$, respectively. The intensity lost by scattering (not absorption) in the x direction will add up to the scattered intensity in the x direction, and vice versa. This situation can be described by the following system of differential equations:

$$-di = -(k+s)idx + sjdx \tag{2.22}$$

$$dj = -(k+s)jdx + sidx \tag{2.23}$$

($-di$ means that i increases in the opposite direction to x).

Equations 2.22 and 2.23 can be re-written as two fundamental simultaneous differential equations:

$$-\frac{di}{dx} = -(k+s)i + sj \tag{2.24}$$

$$\frac{dj}{dx} = -(k+s)j + si. \tag{2.25}$$

If one imposes the condition:

$$\frac{s+k}{s} = 1 + \frac{k}{s} \equiv a \tag{2.26}$$

then Equations 2.24 and 2.25 become:

$$-\frac{di}{sdx} = -ai + j \tag{2.27}$$

$$\frac{dj}{sdx} = -aj + i. \tag{2.28}$$

Dividing Eq. 2.27 by i and Eq. 2.28 by j, and adding the two, one can find, after defining $\frac{j}{i} \equiv r$:

$$\frac{dr}{sdx} = r^2 - 2ar + 1 \tag{2.29}$$

or:

$$\int \frac{dr}{r^2 - 2ar + 1} = s \int dx. \tag{2.30}$$

Integration over the whole thickness of the layer with boundaries:

$$x = 0 : (\frac{j}{i})_{x=0} = R_g = \text{reflectance of the background} \tag{2.31}$$

$$x = d : (\frac{j}{i})_{x=d} = R = \text{reflectance of the sample} \tag{2.32}$$

and the approximation $d = \infty$, therefore $R_g = 0$ and $R = R_\infty$, yield:

$$(-a - \sqrt{a^2 - 1})(R_\infty - a + \sqrt{a^2 - 1}) = 0 \tag{2.33}$$

which, solved for R_∞, gives:

$$R_\infty = a - \sqrt{a^2 - 1} = 1 + \frac{k}{s} - \sqrt{\frac{k^2}{s^2} + 2\frac{k}{s}}. \tag{2.34}$$

Therefore, R_∞, the *diffuse reflectance* of the sample, is readily measurable, and is a function of $\frac{k}{s}$ only, so it depends exclusively on the *ratio* of the absorption and scattering coefficients, not upon their absolute value. Solving Eq. 2.34 for $\frac{k}{s}$, one finally obtains:

$$\frac{k}{s} = \frac{(1 - R_\infty)^2}{2R_\infty} \equiv F(R_\infty). \tag{2.35}$$

Equation 2.35 can be used to obtain a quantity of absorbance of the measured sample, reduced by a scattering factor, once the reflectance of the sample has been measured. Reflectance is measured on a scale 0 to 1 (or 0% to 100%) where the two ends of the range correspond to completely absorbing and completely reflecting standards, respectively. Eq. 2.35 is called the *Kubelka-Munk function*, and R_∞ is measured on an infinitely thick sample. A full derivation of the Kubelka-Munk function can be found in Kortüm [41] as well as in Kubelka and Munk [43].

For UV-visible light wavelengths, the depth of a material layer can be considered "infinite" when its thickness exceeds the wavelength (hundreds of nm) by several orders of magnitude. Therefore, a fraction of a mm should already be enough for light to be fully absorbed beyond the first superficial layers, where the reflected light actually comes only from the surface (as compared to the *bulk* of material layer). The compactness of a material's sample will also

be important in creating a homogeneously dense and compact layer. Furthermore, when measuring samples with same composition, scattering can be assumed to occur equivalently, thus the Kubelka-Munk function will be a representation of the absorption power of the material, being F proportional to k in Eq. 2.35. Moreover, the absorption power of the materials depends upon the concentration of the absorbing species. Absorbance is proportional to the concentration of absorbing species too (through Beer-Lambert's law), therefore this is where one can assume the absorption coefficient and absorbance to be equivalent, and the Kubelka-Munk function to yield the absorbance from layers of powdered materials.

It was mentioned at the beginning of this Section how absorption of light can help the interpretation of PL data. A material can luminesce only upon absorption of radiation. For a luminescent process to occur, the radiation released in the electronic relaxation needs to travel away from the excitation sites without being re-absorbed elsewhere in the material. A scenario might present where the absorption properties of the material have changed, and the light emitted in the conditions before such changes is now absorbed by the new structure of the material. Probing the material's reflectance (and thus its absorbance, through the Kubelka-Munk function) can elucidate the range over which absorption occurs, and thus link this to the lack of emission in photoluminescence. This type of phenomenon should be borne in mind when looking at PL and absorbance data.

2.6 Electron microscopy

Electron microscopy has given scientists an unprecedented opportunity to obtain images of materials and surfaces at the nanoscale and below in the past 50 years as had never been possible before. Several techniques have been developed and become available, each of which typically offers a specific method for probing matter. In particular, Z-contrast scanning transmission electron microscopy (STEM) can be used to obtain atomically-resolved elementally specific images directly.

The advantage of taking a direct image of the atomic structure composition relies in the fact that no need for any preconceived model structure is required. Z-contrast STEM

has the capability of revealing unanticipated atomic arrangements, providing a new depth of understanding into the origin of materials properties [69]. The atomic arrangement of a structure depends upon its growth mechanisms, and these two cannot be separated from each other. Growth mechanisms determine how grain boundaries, defects, or interfaces will look like, and Z-contrast STEM is capable of resolving such important features for a bulk material's properties.

The term Z-contrast originates from the technique's high sensitivity to elemental and atomic composition, i.e. the atomic number Z. This is why it becomes possible to resolve differences, defects, transitions and even abrupt changes between different types of ordering in a material. In particular, with reference to Fig. 2.10, a finely focused probe of high-energy electrons is scanned across a thin sample in order to map out the location and scattering power of the atomic columns, thus producing a direct image at atomic resolution, where atomic species will be distinguished on the base of their atomic number Z.

As can be seen in Fig. 2.10, the electrons are collected by an annular detector. This detector will collect those electrons that have undergone Rutherford scattering: unlike diffraction at small angles, Rutherford scattering (i.e. the elastic scattering of charged particles by Coulomb interaction) involves scattering at much larger angles, and its intensity depends strongly upon the sample's composition through the Z^2 dependence of the scattering cross section (where the term Z-contrast comes from). For example, in a crystalline material, a fine enough probe can be scanned through atomic separations, therefore mapping out each single atomic column. Then, the intensity of each column in the image will directly reflect its composition as a function of Z^2. Therefore, the image can be thought of as a simple map revealing the scattering power of the material at atomic resolution [69].

In a conventional image, a broad but highly collimated electron beam is used to illuminate the crystalline sample under study. The transmitted beams, along with a number of diffracted beams generated by the crystal, are collected by an objective aperture and projected onto the microscope screen. The contrast that results from recombining these beams depends on their relative phases after passing through the crystal and the optical system of the microscope. It is because these relative phases are highly sensitive to both the exact crystal thickness and to the exact microscope focus that such phase contrast images

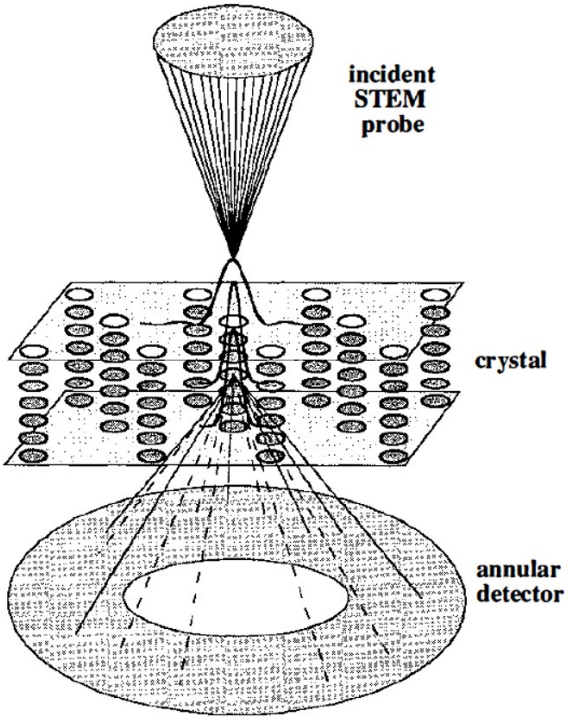

Figure 2.10: Schematic showing the formation of a Z-contrast image in the STEM. A fine electron probe maps out the location and scattering power of the atomic columns, thus producing a direct image at atomic resolution [69].

show a large variety of different possible forms for the same crystal structure. Thus, in general, phase contrast images can only be interpreted by simulating the anticipated image forms for a small set of trial structures, then determining the best fit [69].

In Z-contrast imaging, instead, the relative phases of the incident beam and the scattered beams reaching the annular detector are unimportant. The total intensity reaching the detector depends only on the incident intensity at each atomic site and on the species present, which scatters a small fraction of that intensity to the detector. The inner detector angle must be sufficiently large so that the signal it collects is dominated by thermal diffuse scattering. This is generated very close to the atomic sites, and it is the atomic vibrations themselves that break the coherence of the images process. A typical inner detector angle would be 75 mrad. Nevertheless, a quantum mechanical description of the imaging process has shown in detail how dynamical diffraction effects are reduced to second order in the Z-contrast image. Only one stationary quantum state of the fast electron in the crystal contributes significantly to the image, thus dynamical diffraction effects are effectively avoided [69].

In conclusion, Z-contrast STEM can be used as an effective and reliable means to obtain direct images of crystalline materials samples with atomic resolution.

2.7 Introduction to adsorption phenomena

Among all the microscopic properties that can be found in materials, porosity is a very attractive one. Especially in powdered materials, porosity offers remarkable opportunities in terms of several applications, because pores usually increase the surface area and the empty volume in a material. Porous structures can become important when selecting a substrate for deposition of external species.

Sorption of gases in porous materials has been extensively studied in the last five decades since early experimental works in the field, although theoretical predictions on gas sorption in pores, as well as first comparisons with some experimental data, can be traced back even earlier ([14], [83], [4]). Much of the early work on porous materials was also driven by the interest in catalytically active powders ([53] and all the papers in the same series).

Physisorption of gases on solid substrates is a preferred method to assess porosity, and nitrogen (N_2) is a very common choice of adsorbate gas on an adsorbent substrate to probe the surface structure and capacity. In fact, nitrogen is very affordable, and it condenses (i.e. forms a liquid adsorbate on the surface) at the same temperature of its liquid phase, i.e. 77 K, which can as well be obtained conveniently and used to cool samples down to a required temperature.

Molecular (diatomic) nitrogen has a quadrupole moment, which has an effect on its interaction with surfaces due to enhanced charge configuration. This causes adsorption to commence at lower relative pressures than in the case of absence of such electric moment. For this reason, argon (Ar) has recently become another typical choice of adsorbate gas, due to its zero quadrupole moment, and still boiling point above 77 K [97]. An alternative temperature is 87 K, set slightly below its boiling point. More in general, 77 K sets above nitrogen triple point (about 63 K), while 87 K is just above argon's triple point at 83.8 K. Reference to triple point is very important because the gas can exist in its solid phase, and this will affect the molecules' mobility throughout the pores.

Common porosity assessment encompasses measuring a so-called *volumetric isotherm*, which is a measurement of pressure changes of gas expanded into the solid sample cell, upon addition of the same adsorbate gas in repeated cycles into a given volume. The name *isotherm* refers to the fact that the volumetric pressure measurements are performed at a constant temperature. Moreover, the increasingly additional pressure to the solid sample cell is recorded as equilibration occurs between the sample cell itself, and an initial *dosing volume* (i.e. the initial volume for adsorbate gas addition). Such an equilibration pressure is typically expressed as a reduced (or relative) pressure, p/p_0, with respect to the vapor pressure of saturation (SVP) of the adsorbate gas at that specific temperature, i.e. p_0.

A key aspect of this assessment is to link an experimental isotherm to a model that can quantitatively describe the porosity of the material. The classic approach to this is the so-called *Kelvin equation*, named after Lord Kelvin [25]. Starting from the thermodynamic argument of equilibrium between chemical potentials of a liquid and a gas phase in contact with each other, it is possible to establish a relationship between the radius of curvature of

a liquid meniscus and the relative pressure of the gas at which condensation (thus formation of such a meniscus) occurs in the pores of a solid substrate. In particular:

$$ln\left(\frac{p}{p_0}\right) = \frac{-2\gamma V_L cos\theta}{RT}\frac{1}{r_m} \tag{2.36}$$

where p/p_0 is the relative pressure of the vapor in equilibrium with a meniscus having a radius of curvature r_m; γ and V_L are the surface tension and molar volume of the adsorbate, respectively; R is the universal gas constant, $R = 8.314$ J/(mol·K), while T is the temperature of the isotherm. It is generally assumed that the angle of contact, θ, is zero, and thus $cos\theta = 1$ in Eq. 2.36.

The thermodynamic argument assumes that the equilibrium pressure, p, over a concave meniscus of liquid, must be less than the saturation vapor pressure, p_0, at the same temperature, T; this implies that a vapor will be able to condense to a liquid in the pores of a solid, even when its relative pressure is less than unity. The formation of such meniscus can be described in different manners depending upon the pore geometry. A very common choice for this description are cylindrical pores, usually depicting the (often complex) pores structure reasonably well. Upon formation of an adsorbed liquid meniscus, *desorption* of the adsorbate does not occur as the exact opposite of the *adsorption* of the condensed film of gas. For this reason, the desorption process is actually delayed and quantity of volume adsorbed at a certain relative pressure will be desorbed at a lower relative pressure due to the phenomenon of *capillary condensation*. This difference between adsorption and desorption branch of the isotherm generates hysteresis, and gives rise to the formation of a *hysteresis loop* between these two branches of the isotherm, as can be seen in Fig. 2.11 [25].

The Kelvin equation allows calculation of values of the pore radius for which capillary condensation occurs. In particular, one can find out what is the minimum value of such radius at which to expect capillary condensation to happen. In fact, looking at Fig. 2.11, the merging point of the two branches of the isotherm localizes the pressure where condensation in pores should commence, individuated as the desorption branch closes onto the adsorption one. The validity of the Kelvin equation usually spans pore radius values as low as 1 nm, and up to 25 nm, which is a practical limit due to a relative pressure very close to unity (where

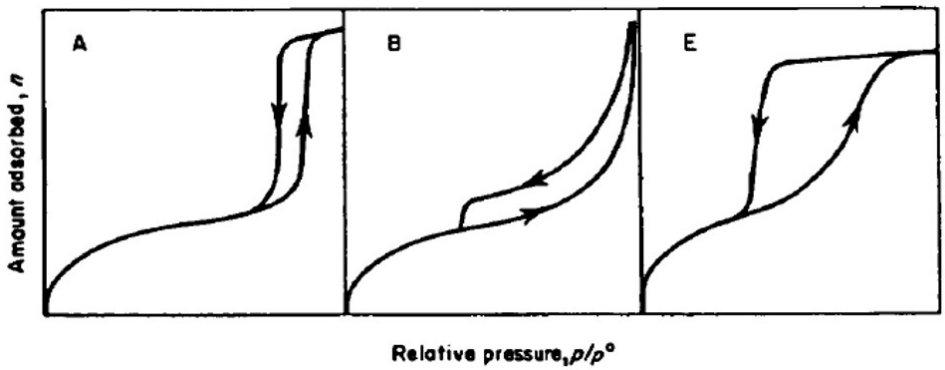

Figure 2.11: Different types of hysteresis loops. The arrows in the plots indicate the upward development of the adsorption isotherm branch, and the downward trend of the desorption branch [25].

it becomes hard to distinguish small variations of p/p_0). Therefore, the Kelvin equation is usually applicable to the *mesoporous* range (pore diameter between 2 and 50 nm), and hardly applicable to the *microporous*, i.e. pore diameter below 2 nm (especially), and the *macroporous* (pore diameter above 50 nm) ranges [25]. In this work, because of the use of the Kelvin equation, it will be natural to discuss results in terms of pore radius, although pore diameter is simply obtained as twice the radius.

So far, the radius of curvature of the meniscus and pore radius have been considered equal. Nevertheless, this is not exactly the case. The reason for this resides in the geometrical description of the meniscus as the interface between a condensed layer of the adsorbate gas, and the same gas in the vapor phase. Looking at Fig. 2.12, r_1 and r_2 fully describe the surface curvature of a concave liquid meniscus. Following a geometrical argument, one can derive the Young-Laplace equation to describe the capillary pressure difference at the interface between the gas and the liquid:

$$p_{gas} - p_{liquid} = \gamma\left(\frac{1}{r_1} + \frac{1}{r_2}\right) = \frac{2\gamma}{r_m}. \tag{2.37}$$

The mean radius of curvature, r_m, is given by:

$$\left(\frac{1}{r_1} + \frac{1}{r_2}\right) = \frac{2}{r_m} \tag{2.38}$$

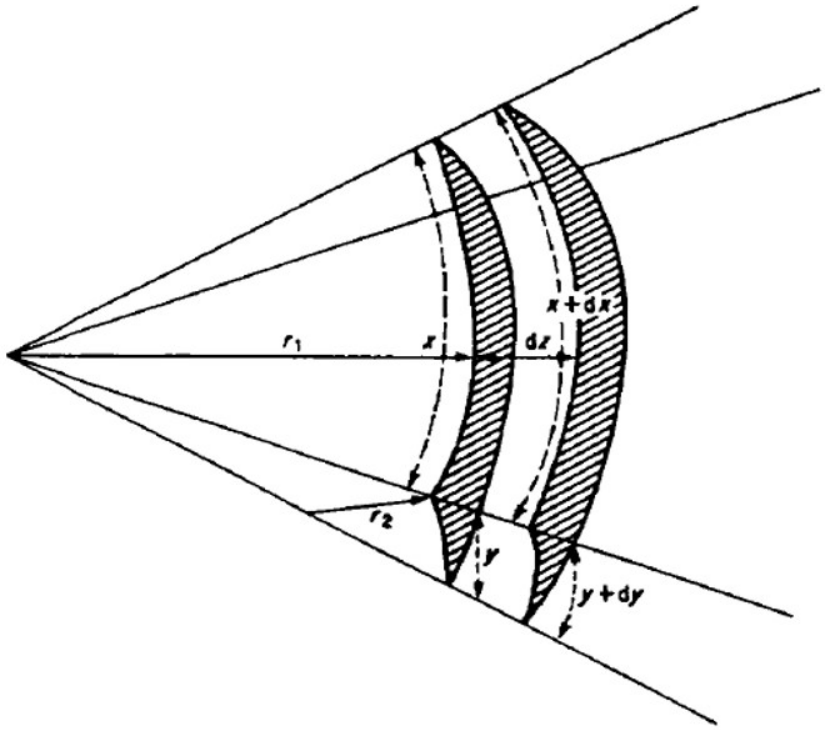

Figure 2.12: Representation of the interface between a liquid and a gas (meniscus), described by the two radii of curvature, r_1 and r_2 [25].

The mean radius of curvature, r_m, therefore, corresponds to a *core* radius more than a *pore* radius, where the core takes into account the adsorbed layer on the surface of the pore (pore walls). The actual pore radius could thus be expressed as $r_p = r_m - t$, being t the *statistical thickness* of the adsorbed layer. The statistical thickness is calculated from the molecular diameter of the adsorbate gas, σ, multiplied by the ratio between the adsorbed quantity of gas, n, and the adsorbed quantity at the monolayer (first step of the isotherm, see Fig. 2.11), n_m:

$$t = \frac{n}{n_m}\sigma. \tag{2.39}$$

As the statistical thickness can be accounted for in the Kelvin equation, the mean radius of curvature gives, in general, a good first representation of the pore radius, and such it has been considered for long time up to recent days [25].

Several methods have been proposed to represent the pore geometry in porous materials. The most common geometrical shape is the cylinder, as it is used when the Kelvin equation is applied to a porous structure; other shapes are wedges and slits; more complicated models try to use ink-bottle necks to represent the pores [25]. Whichever is the pore model one uses to attempt a representation of the experimental data on a particular system, the *distribution of pore sizes*, also called *pore size distribution* (PSD), is expressed as the variation of pore volume with respect to the pore radius. Specifically, variations of the adsorbed volume V (gas adsorbed in the material's pores) in the pore size regions of interest (as given by the Kelvin equation) can be evaluated as the derivative dV/dr_m, and the distribution expressed as dV/dr_m vs. r_m. As explained above, there is no distinction between r_m and r_p in the general case.

Chapter 3

Experimental methods

This Chapter will be dedicated to the description and development of the custom-made magnetron sputtering deposition apparatus used to prepare the decorated metal oxide powders. The apparatus is comprised of a variety of components that have been developed at different times to address specific needs. The final appearance of it is the result of changes and modifications required by continuous instrumental development. Furthermore, the preparation of the pure and decorated MO materials, along with the deposition process, will be presented. Lastly, characterization methods for the decorated materials properties will be illustrated, including the one for pore size analysis.

3.1 Introduction to the deposition method

The systems of interest to this study are powdered materials. Typically, deposition under vacuum is performed on solid non-moving substrates, like pieces of single-crystal or thin films. This is the case of many of the experimental works mentioned in Chapter 1. As it was previously introduced, the idea of depositing alien species on substrate particles is not a common choice when it comes to using chemical-free methods.

Nevertheless, the idea of sputtering deposition on metal oxide particles and, specifically, the use of a powder mixer to agitate the particles, is not new. The earliest work that reports this idea is the U.K. Patent by Cairns, Nelson and Barnfield [9]. Cairns and co-workers proposed powder agitation during deposition as a novel technique to prepare oxide-supported

metal catalysts. The driving motivation for them was the need to deposit selectively small particles of expensive metals (e.g. platinum and palladium) on the surface of metal oxides. Acknowledging the fact that catalysis is a surface phenomenon, they based their invention upon the discovery that, if catalytic material is deposited by sputtering under carefully controlled conditions, it is possible to obtain catalytically active surface coatings for gas phase catalysis applications with very much smaller quantities of catalytic material than is possible by vapor deposition (not sputtering) or deposition from solution. The choice of powders is driven by the enhanced catalytic activity and efficiency due to enlarged surface area (surface-to-volume ratio).

Several authors have later proposed technical expedients to mix the powders in the deposition chamber. These methods, though, are not necessarily related to the preparation of catalytic materials. Examples of these ideas are rotating drums or vibrating cups to mix and agitate powders with or without the purpose of metal surface coatings ([107], [79], [93], [2]). A further development of these is the rotating wing drum presented by Ensiger and Müller for ion beam implantation purposes ([20], [58]). A recent application of the same idea is found in the works by Veith, Lupini and co-workers ([101], [102], [103]). It is important to reiterate that, whatever is the goal for mixing a powdered material sample, such a method appears to be a simple and effective one for a statistically averaged exposure of the particles surfaces to an incoming beam of particles.

Powder mixing with a rotating device is the chosen route to achieve one of this study's goals, i.e. becoming proficient at depositing metal particles on metal oxide substrates. A description of the development of the powder mixer used in the described experiments, as well as of all the parts that comprise the whole deposition system, follows below.

3.2 The sputtering system and its components

The deposition apparatus has been assembled initially as a group effort, and subsequently developed in all its different components as part of the work here presented. It is a custom-made system whose parts have been built and modified as it appeared necessary to achieve a specific goal. In particular, the powder mixer, or cement mixer, or also *tumbler*, is a key

component for the preparation of the decorated materials, hence it received a significant attention and underwent several modifications. A full description of the apparatus follows.

A vacuum chamber is connected to the vacuum system, which is comprised of a turbo molecular pump backed by a rotary vane pump, and allows to establish the needed vacuum in the chamber (base pressure in the 10^{-6} Torr range or lower). Such a chamber is cross-shaped and has six apertures (four on the horizontal plane, two on the vertical one) that fit standard flanges. These serve different functionalities: there is a window in the front to let the experimenter see inside it; the flange opposite to the window connects to the vacuum system through a flexible vacuum-tight hose; the other two apertures in the horizontal plane can host flanges to support the magnetron gun (on one side) and the tumbler for powder mixing (on the opposite side). The last two apertures face one another vertically: one allows insertion of an additional component from the top (which will be described later), and the one at the bottom is closed with a blank for support on a housing cart (see Fig. 3.1).

The implemented dc-magnetron sputtering gun is a SpinTron 2 © manufactured by MicroMagnetics, Inc. which is operated by an Advanced Energy MDX 500 © power supply (Fig. 3.2 reports the sputtering gun). This sputtering gun is designed to house both non-magnetic and magnetic evaporation metal targets. Circular metal targets of 2″ diameter and variable thickness (0.125″ for non-magnetic materials and 0.063″ for magnetic ones) are mounted on the front of the gun according to which metal species is desired for the deposition process. Once base pressure has been established, the gun can be operated upon introduction of argon (Ar) gas in the chamber directly from a gas supply tank through stainless steel and Teflon tubing connections. Argon supply is controlled using an MKS © Mass Flow Controller (Model 247C, 4-channel readout, connected to a MKS © Flow Meter, Model 1759) to determine the gas flow, and monitored by an MKS © pressure readout, Model PDR-C-1C (see Section 2.2 for an explanation of how a magnetron sputtering gun works, and for a discussion of the sputtering process in general).

Opposite to the magnetron gun, a tumbler is supported on a rotary shaft through a vacuum flange. This shaft allows rotation of the tumbler from the outside driven by a DC (direct current) motor, or dc-motor (that usually operates at 5.0 V). The rotary shaft was built assembling different parts. A bored cylinder made of aluminum is house for two linear

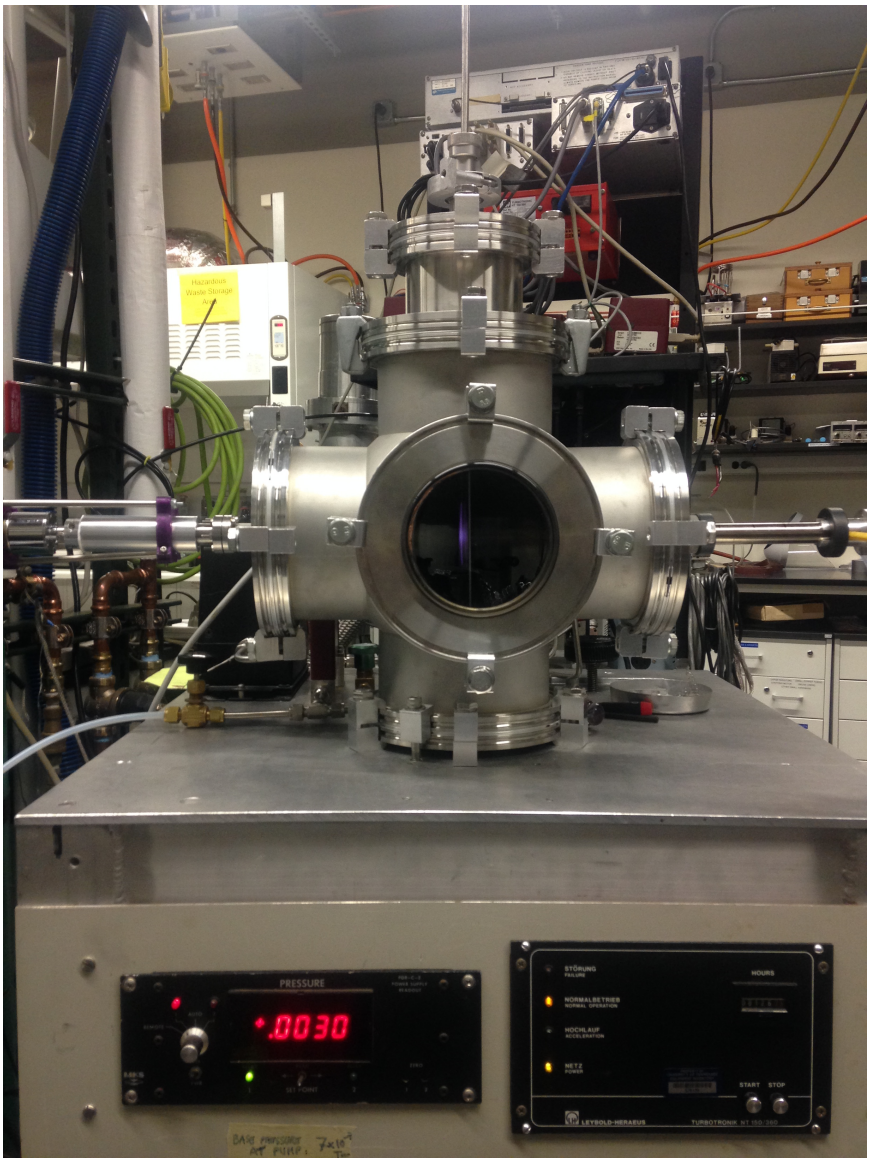

Figure 3.1: The sputtering apparatus comprised of the parts described in the text: magnetron gun (*right*), rotary shaft for tumbler and dc-motor support (*left*), argon supply (*bottom left*), vacuum insert (*from the top*), and readout displays and controllers (*bottom*).

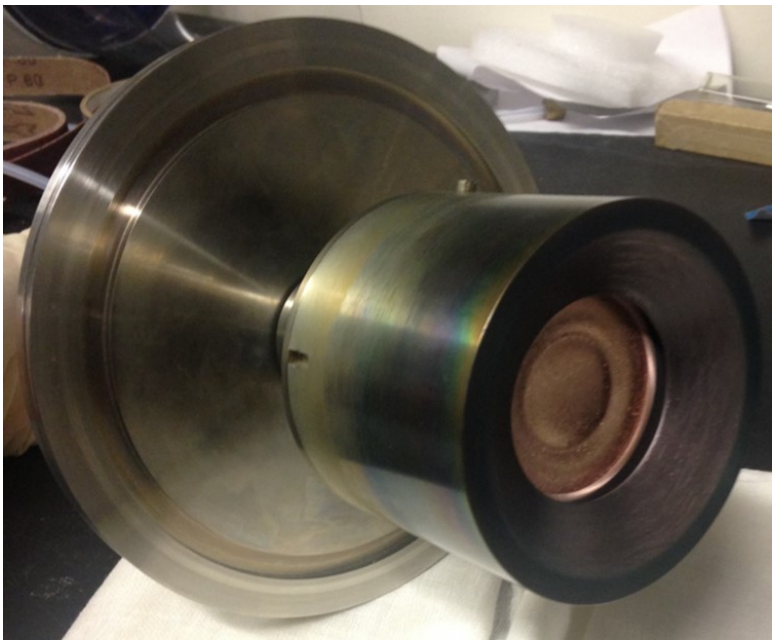

Figure 3.2: The magnetron gun, inserted on a vacuum flange (Cu target mounted on it).

bearings, which support an aluminum rod that is longer than the cylinder, and couples to the dc-motor on one side, while it slides into a vacuum fitting on the other (in order to couple with the tumbler inside the vacuum chamber). Such a fitting is a quick-connect (QC) whose cap was glued with epoxy into the aluminum cylinder, while its thread adapts on the vacuum flange (that latches onto the chamber) through a 1.33″ diameter conflat flange (CF), also called a mini-conflat. The O-ring seal inside the QC allows free spinning of the aluminum rod while maintaining proper vacuum inside the chamber. Fig. 3.3 reports a picture of the shaft assembly, while Fig. A.1 in Appendix A represents a schematic drawing of the same. The tumbler and its modifications will be described in Section 3.2.1.

The top aperture of the chamber holds an assembly for a quartz crystal microbalance (QCM), a very common device used to measure the deposition rate as mass of metal (or any other measurable species) added on the crystal, as a function of time. A QCM resonates at a specific frequency (typically in the MHz range) and addition of mass on it causes the resonance frequency to diminish proportionally to the same addition. The principles of operation of a QCM have been described in Section 2.3.

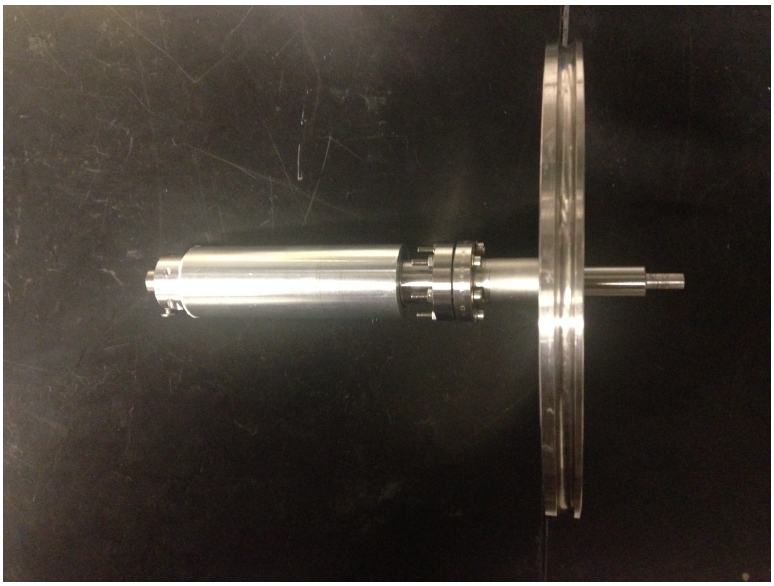

Figure 3.3: Rotary shaft assembly to support the tumbler, mounted on a vacuum flange. An aluminum rod is supported by two linear bearings, encased in a cylinder that couples to a mini-conflat flange. Shaft couples to dc-motor for spinning on the left, and to tumbler on the right.

This assembly is comprised of a flange with QC fitting that allows insertion of 0.750″ stainless steel (SS) tubing from the top. The two ends of such a tube are comprised as follows. An electrical feedthrough connects on one end to circuit board that drives the QCM (Teensy board [89] encased in an aluminum box and connected to laptop computer via cable for data collection - see Section 3.3 for full description of data collection). The other end has a CF jointed with SS tube where two insulated copper wires run all inside the tube to a custom-made Teflon support for holding the crystal. The crystal is cradled within a SS frame (originally manufactured for an Inficon © vacuum insert) and connections to copper wires are made through soldered pins. The QCM is surrounded by a SS cylinder (that can be shifted upward and downward) that has a circular window meant to allow exposure of the crystal's surface only, and is positioned on the SS tubing by means of two set screws. The whole assembly can be moved at convenience according to the region of effusive beam needed to be calibrated (Fig. 3.4 shows the QCM assembly; Fig. 3.5 shows the QCM shield in detail; Fig. A.2 in Appendix A is a schematic drawing of QCM shield).

At the bottom of the SS cylinder that shields the QCM, an aluminum plate is installed for the purpose of removing impurities from the target without exposing the powders to it. This is put between the magnetron gun and the tumbler before sputtering operations in order to be stage of deposition for the first round of metal particles ejected from the gun target. The sputtering chamber has to be opened to air for transferring powders in and out, and exposure of the target to atmosphere (even if minimal) certainly generates some oxidation of the surface. This can thus help to clean the target (remove the impurities from its topmost surfaces) before actually using the sputtered metal particles for deposition on the oxide powders.

Alternatively, a thin sheet of aluminum foil can be wrapped and flattened on a bent piece of SS tubing, and this can be used as screen between tumbler and gun for cleaning purposes (Fig. 3.6 and 3.7 show the two types of screen). In such a configuration, a thin aluminum plate is slid inside the chamber between magnetron gun and tumbler, where a large enough hole was bored in the center. The hole is as large as the front aperture of the tumbler (about 2.5″ - 6.35 cm) and opens the tumbler only to the target on magnetron gun: the goal for

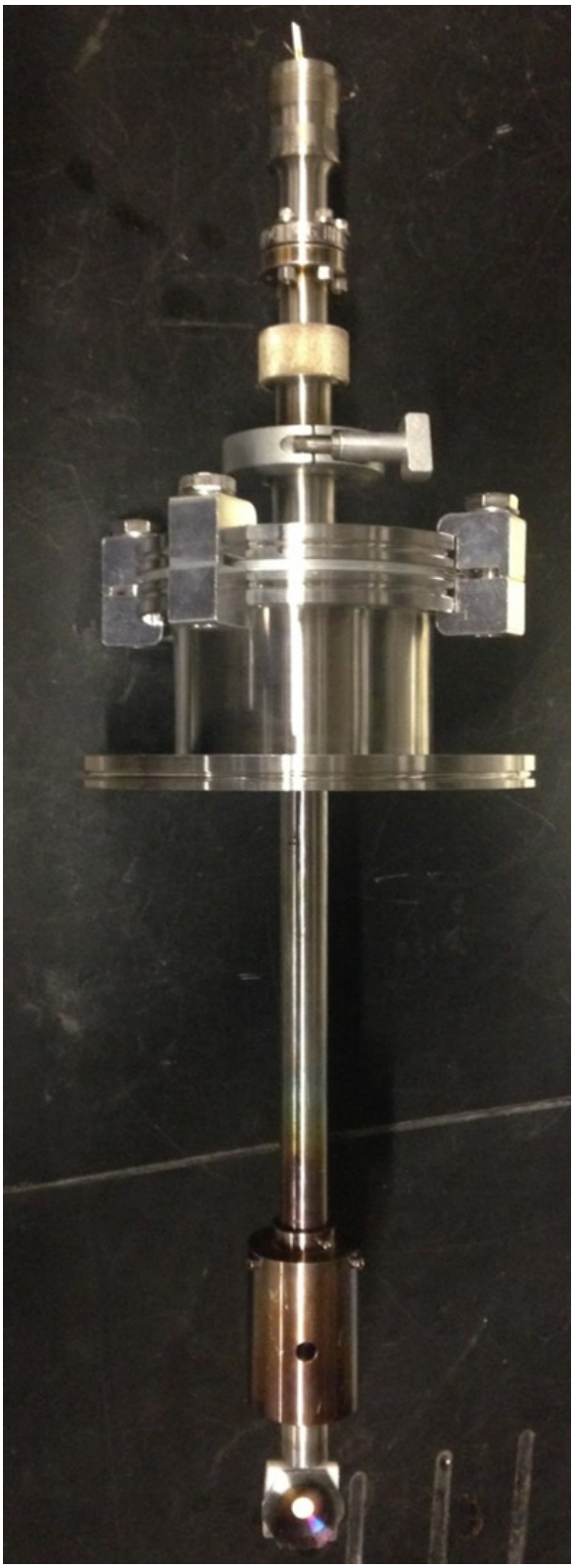

Figure 3.4: QCM assembly from electrical feedthrough (*top*) to the actual crystal (*bottom*).

Figure 3.5: Detail of the QCM Teflon holder with shield to allow exposure of crystal only (shield slid upward).

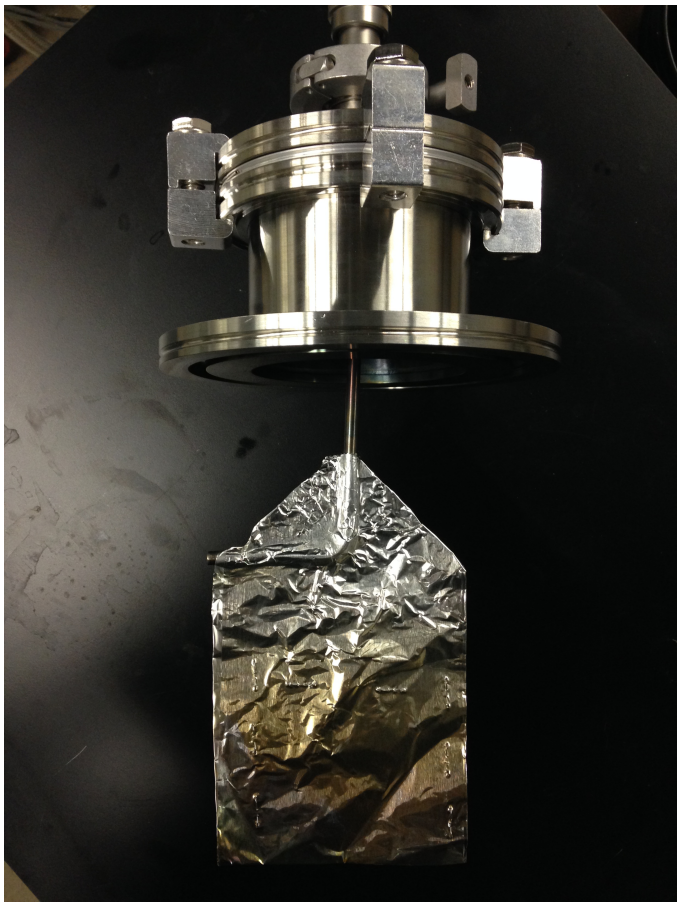

Figure 3.6: Aluminum screen for "target cleaning" as described in the text. This version of the screen is supported by SS tubing.

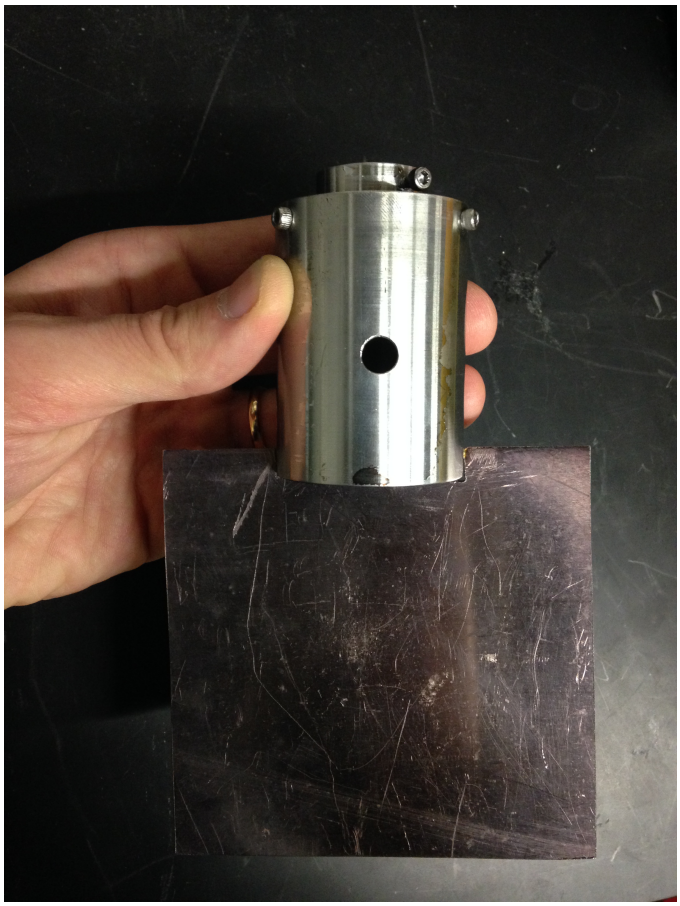

Figure 3.7: Aluminum screen for "target cleaning" as described in the text. This plate can hang right underneath the QCM shield.

this configuration is to let only the most intense region of effusive beam reach the end of the tumbler, where the powders move, and therefore to screen out the peripheral regions of it.

3.2.1 Development of the tumbler

As it is discussed in Chapter 1, the deposition of copper on MgO has attracted the interest and focused the attention of this study, being a valid case of deposition to show a proof of principle for this tumbler and sputtering system in general. This proof-of-principle endeavor has helped the development of several technical details of the experimental setup. Agitation of the powders is a key factor in the method which is being developed, and thus different configurations of the rotating tumbler were tried.

A first version of the tumbler was 3D-printed with PLA polymer: CAD design allowed the construction of a cylindrically shaped drum with multiple fins to generate powder falls, and narrower diameter of the cylinder on the open side of it than the rest of its body (Fig. 3.8). A technical issue had to do with the high temperatures when sputtering at high power (100 W or more): exposure to beam would fairly soon (a matter of minutes) melt the plastic and the tumbler would bend on itself. This soon caused the tumbler to lose stability in its spinning. The agitation of the powders was good, but the constituent material must withstand the sputtering conditions. High temperatures could be related to high sputtering power, but also to extended periods of sputtering time (extended exposure to the beam).

A more robust option encompasses the use of SS, both in terms of melting point and of inertness to the surrounding atmosphere. The simplest design was first pursued, with a cylindrical shape and two straight fins (not curve-shaped) in order to make the machining process easier. A following development of this has been a front cover to enclose the powders: a small lid could be opened and closed and be held in position by magnets (see Fig. 3.9 for tumbler, and Fig. A.3, A.4, and A.5 in Appendix A for schematic drawings of cover with lid). Using such a cover, the material could be heat-treated and then transferred from a quartz tube into the tumbler in an inert atmosphere (e.g. glove bag filled with argon). Then, the cover would be put on the tumbler using four screws. The tumbler would then be transferred into the chamber, and after establishing an inert atmosphere, the lid would be opened by means of a SS tubing arm from the top (in place of the QCM assembly).

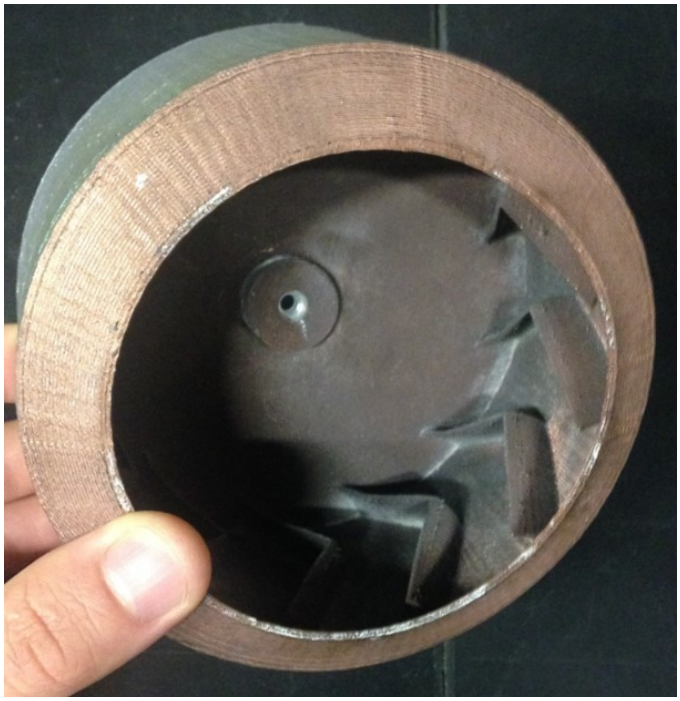

Figure 3.8: The first version of the tumbler (3D-printed).

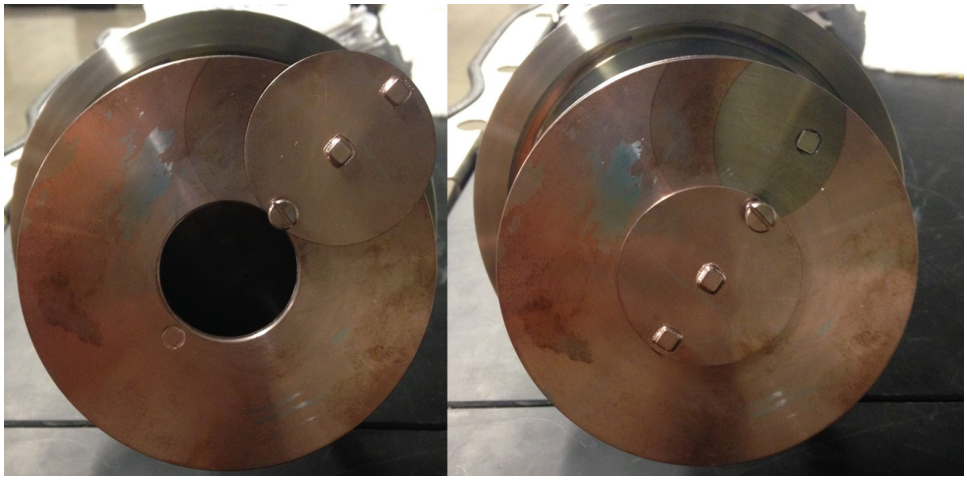

Figure 3.9: First version of the SS tumbler with cylindrical body. Here it is shown with the cover with lid described in the text (*left*: open lid; *right*: closed lid).

Part of the materials preparation before deposition can, in fact, be heat-treatment of the powders. The main issue with dry heat-treated powders is their stickiness, and this is particularly true with MgO (due to its insulating character). The free tumbling of the powders is prevented if they remain stuck on the inner walls of the tumbler. This is not only the case of MgO, as other substrate materials (e.g. Al_2O_3, SiO_2) have presented the same problem. However, the cover on the tumbler would help preventing loss of powder from the inside that would otherwise fall off and get lost during deposition.

In order to overcome the problem of losing material, the cylindrical shape was converted into conical, very much like the rotating wing drum proposed by Ensiger and Müller ([20], [58]). In addition to this, curved fins were machined and welded on the SS body for better powder collection during rotation, in particular, to actually keep the powders up to the topmost position before falling to the bottom of the tumbler. This new version of the tumbler is separable in two pieces: the bottom plate and the conical body with the four fins welded on it at even distances. The cone is fixed on the bottom plate by use of four screws. The issue of the stickiness of the tumbling powders, instead, has been addressed with the construction of four small cylindrical masses (also called *tapping weights* or *tapping devices*). These masses are attached to long screws (fixed into the plate) such that they are made spin around the tumbler and hit ("tap") the outer walls of the cone, causing the powders to be shaken off of the inner walls of the tumbler (Fig. 3.10). The cone is 4.5″ in length and its base measures 4.5″ in diameter. This version of tumbler has been used for all the most relevant cases of deposition presented throughout this study.

Additional modification of the conical-shaped tumbler was attempted in order to reduce the shortest physical distance between the target in use on the sputtering gun and the powders inside the tumbler. The magnetron gun cannot be too close to the SS tumbler (contact between gun and tumbler could cause grounding of the gun, preventing it from regular operation), therefore the length of the tumbler is what determines the minimum distance between target and powdered material. Thus, the tumbler was cut in half, obtaining a shorter version of it, whose length is circa 2.25″. No results obtained with this newer part are going to be presented in this study, but the modification itself proves that continuous upgrade of the experimental apparatus is the key toward perfecting its functionality. There

Figure 3.10: Tumbler with conical shape, having curved fins inside and four tapping weights around to shake powders inside.

is no reason why the system should not be modified again if steps for further amelioration will be deemed necessary.

3.3 Calibration of the sputtering beam

Fundamental part of the experimental methodology developed in the present study is the characterization of the effusive beam of metal particles from the sputtering target. The QCM assembly described in Section 3.2 was used for this characterization. Eq. 2.17 was used in order to calculate the deposited amount of metal particles on the QCM from frequency change measurements, due to its general validity and applicability to this particular case.

Some external factors, e.g. pressure changes on the crystal or temperature changes of the crystal due to ongoing deposition, can affect the stability of the crystal's resonance frequency. As far as pressure is concerned, no appreciable change in the resonance frequency was measured in the range of operating pressures of the magnetron gun, i.e. from base pressure in the chamber (nominally 0 mTorr) up to 40 mTorr. There are examples of studies

of QCM stability as a function of the external pressure, where the authors have even proposed a modified versions of Sauerbrey's original equation (Eq. 2.8) that accounts for changes in the resonance frequency of the resonator as a function of the external pressure [100]. The situation of the present study does not need that particular treatment, because no noticeable change in the measured frequency change was observed upon the pressure variations involved in the beam characterization. Additionally, the herein presented measurements have been carried out consistently recording the oscillation frequency after each deposition run in conditions of base pressure.

Temperature of the resonator in operational conditions (i.e. when exposed to an effusive beam) can rise significantly according to the operating power of the magnetron gun, and therefore its energy flux. A consistent behavior of the QCM system has been noticed even when exposed to the highest power experimented (i.e. 100 W). As a precaution, the resonator's frequency was measured at the end of each deposition process, when the crystal was no longer in the path of the beam, and the temperature was supposedly already lower than operational conditions. Nevertheless, tests revealed that a measure of the changing frequency of the crystal as deposition occurs is possible, when the sputtering power (and so the energy flux the crystal is exposed to) is low enough, namely 10 W.

The resonance frequency of a quartz crystal was measured before any deposition would occur on it. The QCM was driven by a Teensy [89] board-based integrated circuit interfaced to the acquisition software OpenQCM [62]. The use of the open software OpenQCM allowed for very accurate measurements of the frequency change on the QCM: as it will be explained later on, accuracy of the measurement could be as low as fractions of ng. The resonance frequency of the QCM was measured before starting any new series of depositions, especially because the different sets of measurements showed that the resonance frequency the QCM can slightly change between different sets of experimental conditions. The frequency of oscillation was measured at the end of each deposition cycle, and the deposited mass was then obtained as areal density using Eq. 2.17: the difference between periods of oscillation was calculated using a measured frequency, f_c, and the frequency measured upon completion of the preceding deposition cycle, f_q. In this way, all the deposited masses up to the very first deposition on a particular quartz crystal could be taken into account. When a deposition

cycle was the very first one on a new crystal (i.e. free from any previous deposit), f_c was actually the actual resonance frequency of the crystal.

Sets of depositions for fixed time intervals (6 minutes) were run at a specific target-QCM distance (4.5″, about 11.5 cm, i.e. realistic distance target-powder when powder is in the tumbler), varying pressure and power in order to study trends in deposition. Pressure was set at fixed values (3, 7.5 or 15 mTorr) and deposition was measured for three indicative values of sputtering power (10, 50 and 100 W). It was then possible to obtain deposition rate trends at fixed argon pressure and fixed sputtering power, as a function of the sputtering power and pressure in chamber, respectively. It is also interesting to notice that deposition rates in the high end of sputtering pressure range (namely, 40 mTorr) were found to be almost negligible. This suggests that an effective metal deposition should stay away from the higher limit in the range of allowed sputtering pressures.

The results of these measurements show increasing trends with power having constant pressure, which can be logically expected. Conversely, the trend with pressure keeping sputtering power constant appears decreasing, suggesting that the higher the pressure in the vacuum chamber, the lower will be the mean free path of sputtered particles. Cu is the metal with the highest deposition rate, that turns out to be about twice as much as both Ni and Co rates in the same deposition conditions (see Table 3.1 for comparisons; see Fig. A.6 to A.23 in Appendix A for sputtering rate trends with sputtering power and pressure, for the three metals Cu, Ni, Co).

It was also important to treat the accuracy of these measurements. The resolution of the QCM crystals that was used is 0.124 ng/(mm^2·Hz), as consistently measured in all the deposition runs. Most of the measurements showed an uncertainty of circa ±4 Hz in the acquired signal, which would determine an uncertainty on the single measurement of circa 0.500 ng/mm^2 (using Eq. 2.17). This result actually needs to take into account the deposition time, i.e. the time over which the deposited mass caused a change in the QCM frequency of oscillation. Such a deposition time equaled 6 minutes (360 s) in all cases. The uncertainty on the single measurement would then become less than 0.002 ng/(mm^2·s), which appears very small and unrealistic compared to most results reported in Table 3.1. Propagation of the

Table 3.1: Sputtering rates (ng/(mm^2·s)) for the three different metals (Cu, Ni and Co) as measured over 360-second time periods at a target-QCM distance equal to 4.5″ (11.43 cm), keeping target and QCM on the same horizontal axis. Rates are enlisted below each of the three representative Ar pressure values at which data were collected: 3 mTorr, 7.5 mTorr, 15 mTorr.

Deposited metal	**Power [W]**	**3 mTorr Ar**	**7.5 mTorr Ar**	**15 mTorr Ar**
Copper	10	0.231	0.108	0.041
	50	1.395	0.676	0.122
	100	3.065	1.213	0.578
Nickel	10	0.091	0.048	0.020
	50	0.576	0.262	0.097
	100	1.130	0.629	0.197
Cobalt	10	0.075	0.036	0.014
	50	0.450	0.226	0.085
	100	1.067	0.531	0.094

error from Eq. 2.17, instead, provides an uncertainty equal to 0.700 ng/mm^2, that reduces to circa 0.002 ng/(mm^2·s) on the 6-minute period.

Both methods for error determination on the measured sputtering rates yield very small values. Thus, it was decided to take a percentage value of the measured sputtering rate as the error value displayed on the linear fit plot of the data. This appeared a more appropriate method to take into account the differences in the uncertainty due to the variation in the deposited mass, therefore the variation in sputtering rate for different sputtering conditions. In fact, sources of error can be: small variations in flux during sputtering; fluctuations in tenths of mTorr on the argon pressure; efficiency of sputtering for a given combination of sputtering power and pressure. The percentage for the error bars in all the sputtering rate plots (Fig. A.6 to A.23 in Appendix A) was set at ±5%.

In general, there is good agreement between data obtained on different days (i.e. different experimental conditions). With respect to the trends, behavior of sputtering rates with power at fixed pressure shows a linear increase, which can be logically expected (e.g. the rate is doubled when the power is doubled). The case of Co rates at 15 mTorr (Fig. A.20 in Appendix A) seems to be an exception, where the value at 100 W is just barely higher

than the value for 50 W, instead of being twice as much (the value for 50 W, instead, is about 5 times greater than that for 10 W - see Table 3.1). When it comes to behavior of sputtering rates with argon pressure, not only the rates decrease with increasing pressure, but the decrease could be described with a different function from the linear one, such as a decreasing exponential.

The QCM was also used to determine the experimental shape of the effusive beam. In fact, theory predicts a cosine-like distribution of the ejected particles from the sputtering target (see Section 2.2.1). It was decided to measure such a distribution using Cu, setting the Ar pressure at 3 mTorr, which is found to be the value of Ar pressure associated to the highest sputtering rates (Table 3.1); 10 W was chosen for the power, because this value was deemed to yield sufficient deposition on the QCM to appreciate differences in rate over the chosen period of time (namely, 3 minutes). Measurements of the sputtering rate were taken at 5 different distances target-QCM, namely 2.5″ (6.35 cm), 3.5″ (8.89 cm), 4.5″ (11.43 cm), 5.5″ (13.97 cm), and 6.5″ (16.51 cm); in combination with positions of the QCM on the beam axis and at a distance from it equal to 1 cm, 2 cm, 3 cm, 4 cm, 5 cm, and 6 cm. The distance target-QCM was measured in inches because it was more convenient to equally span the length of the magnetron gun, as the gun was moved away from the QCM for each different distance of the QCM from the beam axis. Due to the circular geometry of the sputtering process on the magnetron gun (impinging of the Ar ions and secondary-ionization electrons confined by the gun's magnetic field), there is radial symmetry around the beam axis and therefore any point on a circle around the same axis is equivalent to study this problem.

Results from characterization of the beam's shape are reported in Fig. 3.11. The first observation is related to the decrease in flux as the distance from the source increases: it is reasonable that the farther from the target, the less atoms will travel and reach a certain distance from their point of ejection. Secondly, 6 cm from the beam axis is already enough to appreciate the outermost wing of the beam profile with respect to its axis: the flux here (i.e. at 6 cm away from the axis) at 2.5″ distance from the source, is actually lower than any other farther away distance, confirming that the cosine-like beam shape predicted by theory is interested by the highest sputtering rates in the forward direction (with a maximum in

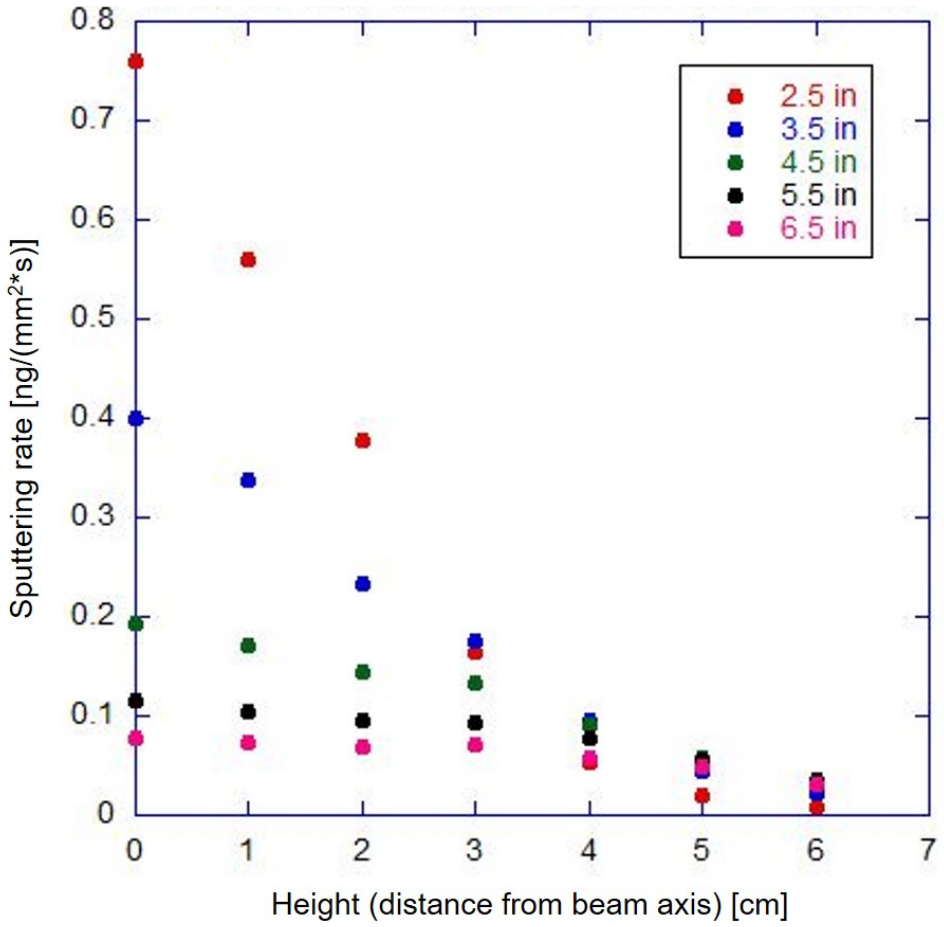

Figure 3.11: Sputtering rates for Cu at 3 mTorr Ar and 10 W power reported as a function of the distance QCM-beam axis (called "Height" on the plot's x-axis), for several different values of the distance target-QCM (expressed in inches and represented by a different color as indicated by the inset chart).

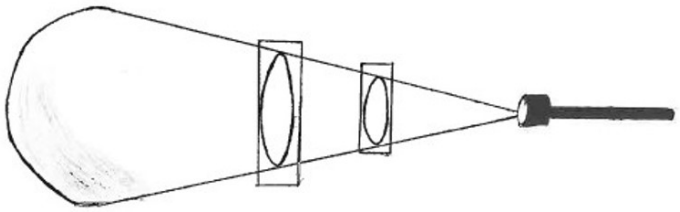

Figure 3.12: Schematic representation of the effusive beam generated by argon plasma impinging on a magnetron gun.

proximity to the source, i.e. the target), while the intensity goes progressively to zero moving away from the source and from its axis, especially at the 90° position from the axis.

A third observation has to do with the shape itself of the beam. Figure 3.12 ideally represents the cosine-like distribution of a sputtering effusive beam, with particular reference to the magnetron gun implemented in this study. If one looks at the data for values of the target-QCM distance equal to 5.5″ and 6.5″, in particular, one will notice that the flux is very similar over a cross section spanning the radius that connects the beam axis and its boundaries. This clearly shows how the beam flux diminishes as metal particles get farther away from the target, until the far most cross section where there will barely be flux. This confirms what the theory predicts and that one should expect due to the nature of the sputtering phenomenon. This whole description demonstrates a very useful application of a QCM.

From the data in Table 3.1 one can learn that it would need twice as long deposition time with Ni or Co as with Cu in order to achieve the same amount of deposition per unit area. This is an important piece of information when exploring deposition of each of the metals on different metal oxide substrates. It is also interesting to notice that knowledge of the deposition rates can help to determine the most appropriate set of power and pressure values so as to achieve the desired deposition in a specific instance. Moreover, values of the sputtering flux can be used to estimate how much mass of a metal can be expected to impinge onto the MO NPs.

For example, if one assumes a powder fall (i.e. a downward stream of MO powders in the tumbler) every second with an initial amount of powder equal to 1 g, one can (reasonably) estimate about 0.2 g of MO material falling in a 1 cm^2 area. This calculation assumes that all powders from the hypothetical 1-g mass are freely tumbling (in the reality of an experiment, there is always a fraction of the initial mass that does not move freely over the deposition time after sticking to the SS walls of the tumbler). In the case of 3 mTorr of Ar pressure at 10 W sputtering power, the deposition rate of Cu is about 23 ng/cm^2 every second, which yields a metal/MO wt% of about $1.2 \cdot 10^{-7}$ every second (23 ng of Cu divided by 0.2 g of MO on the same area). Then, for instance, multiplication by a sputtering time of 10 minutes (i.e. 600 s) yields a metal/MO wt% of about $0.7 \cdot 10^{-4}$, indicating a ratio of almost 1:1000 of Cu metal deposited on the unit amount of MO (for example, the single NP). This calculation should be taken as a possible example of the decoration process, but certainly the calculated weight percentage value will increase with increasing deposition time.

3.4 Preparation of the decorated materials

The experimental setup with all its parts and the characterization of effusive beam (*sputtering flux*) from the source have helped to develop a methodology to prepare the MO powders decorated with metal species. As a general consideration, different choices of sputtering target (i.e. deposited metal) and substrate (i.e. the MO) do not affect the experimental approach to obtain the material with deposit.

3.4.1 Synthesis and characterization of the bare MO

The MO powders used in this work were synthesized using the same vapor-entrainment method, which is described elsewhere [46]. A quartz chimney was house for a coil connected to an induction furnace, surrounding a stage for a graphite crucible containing the reagents, i.e. chunks of the metal and graphite chips. The chimney was flushed twice with argon in order to form an inert atmosphere for the reaction to occur. RF power applied to the coil heated up the load, i.e. the crucible with reagents in it, in order to start melting the metal chunks. As heat was provided to the reagents, an intermediate step with formation of a

carbide would happen; afterwards, with temperatures above 1000 °C, metal vapors would be made react with pure oxygen injected onto the reaction stage, still maintaining a constant flux of argon. The heat ramp and the time at which oxygen was supplied to the reaction batch mostly determined size and shape of the particles, and thus their quality. Fig. 3.13 and 3.14 represent the chimney and reaction environment for the above described vapor-entrainment synthesis method, and a schematic diagram of the same reaction environment, respectively.

The role of argon is to promote the mixing of metal vapors and pure oxygen, as well as the transport of the newly formed oxide particles upward onto the inner walls of the chimney, from which the powders could be scraped and collected. All the powders have been stored under argon until use, in order to maintain their original morphology and purity as much as possible. In fact, the action of air and moisture on the newly synthesized particles (e.g. hydroxylation) can be even detrimental in certain cases: MgO is the best example of this "degradation" phenomenon, which can lead the NPs to change from perfect cubes, exposing the (100) facets primarily, to cubes with smoothed edges. This is what typically leads to formation of multiple steps in place of one single edge on the nanocubes [48].

The problem of MgO sensitivity to external agents is wider in nature: in Chapter 1, it was mentioned how chemical agents, e.g. acetone, can etch the surfaces of metal oxides, and this holds particularly true for MgO [77]. Acetone can ruin and damage the MgO surfaces, permanently altering its original morphology and purity. In the perspective of the whole study presented in this dissertation, preserving the original quality of the material from synthesis has been one of the main reasons for choosing a chemical-free deposition technique to decorate the MO materials of interest.

A particular aspect of this synthesis method is that the heating ramp, combined with flux of argon, can be tuned in order to select the particle size. Additionally, particles can be produced in a narrow size distribution. In the particular case of MgO, there is a very viable way to assess the quality of the material. A sample from the reaction batch was typically heat-treated at the temperature of 950 °C and then gas adsorption was measured at the temperature of 77 K (liquid nitrogen temperature) using methane (CH_4) expansion in a custom-made volumetric adsorption apparatus [59].

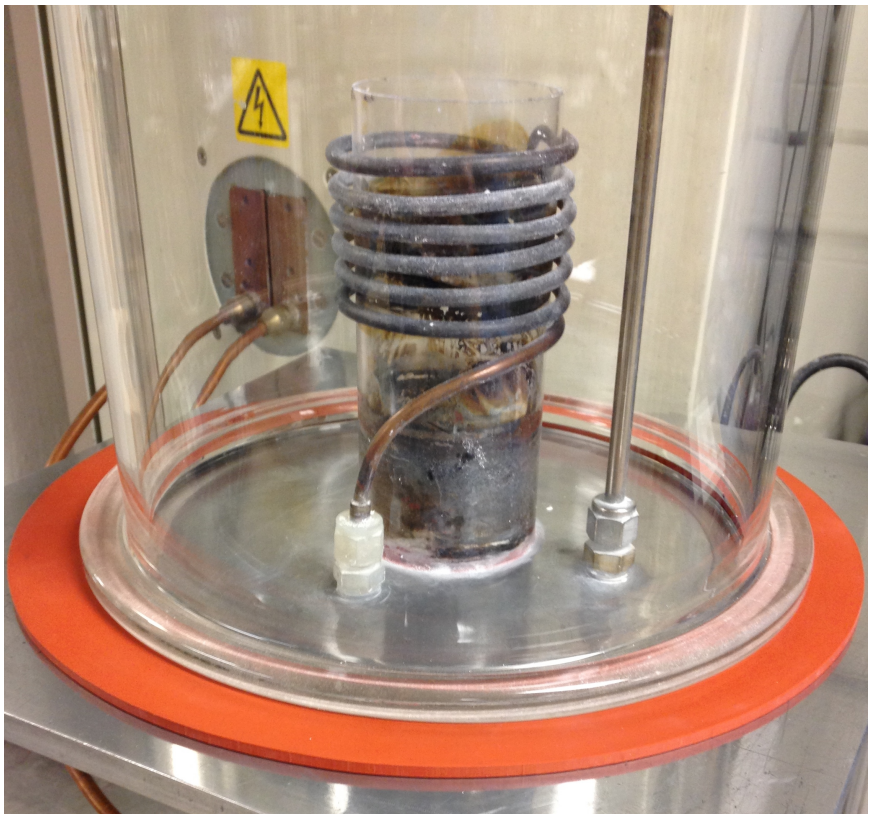

Figure 3.13: The induction furnace-based apparatus for the MO synthesis described in the text.

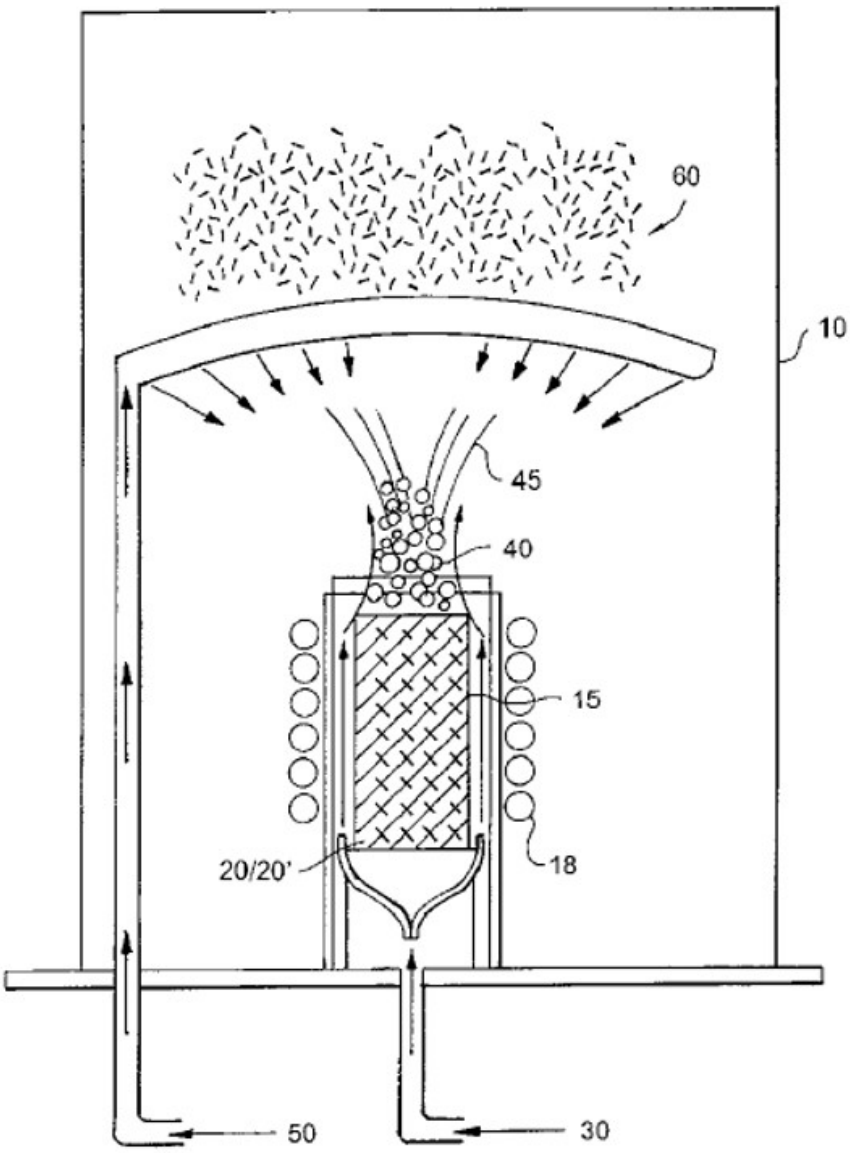

Figure 3.14: The induction furnace-based apparatus for the MO synthesis described in the text (schematic) [46].

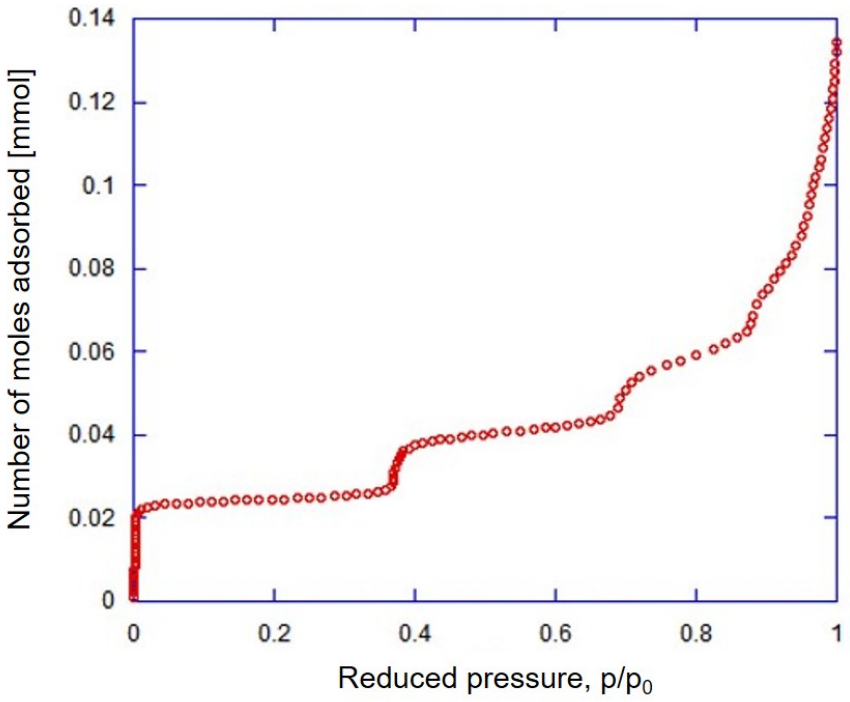

Figure 3.15: Adsorption isotherm of CH_4/MgO at 77 K (batch M0715A).

Fig. 3.15 reports an example of CH_4/MgO adsorption isotherm at 77 K: the adsorption steps correspond to the formation of gas ad-layers on the material's surfaces, where a higher number of steps (typically 4-5) should indicate a higher quality of cleaved facets of the material.

3.4.2 Metal deposition methodology

The MO materials were typically prepared with heat-treatment before being put in the deposition chamber. Heat-treatment has not been a standard step in the preparation process since the very beginning of this investigation, neither throughout; although, certain characterization results on the decorated materials have indicated the importance of considering heat-treatment as an important part of the preparation process.

Moreover, the stickiness of the MO powders is a major problem that halts their free movement in the tumbler. This issue can be at least partially overcome by use of the tapping weights (described in Section 3.2.1), which can help to unstick the material from the

tumbler's inner walls. This problem holds particularly true for the insulator MgO, which tends to accumulate electric charge on its external surfaces, especially when it is very dry after heat-treatment. MgO was typically heat-treated at 950 °C for at least 10 hours *in vacuo* (base pressure of at least 10^{-6} Torr). A similar procedure was used for heat-treatment of ZnO, with much lower temperature, i.e. 250 °C, due to the reduced thermal stability of this compound.

The powders were transferred from their original batch into the clean tumbler. If heat-treatment under vacuum had occurred keeping the sample in a quartz tube, the sample was then transferred quickly into the tumbler to minimize exposure to air. Transfer in argon atmosphere was used in some cases where the version of tumbler with cover was implemented; although, the powders would hardly move inside the tumbler due to really inert and dry conditions.

With the powders in the tumbler, their free movement and the aid from using the tapping weights to shake the stuck portion of the material (when applicable) were checked before deposition. The tumbler was thus mounted on its shaft that is part of the appropriate vacuum flange (see Section 3.2). A vacuum was established inside the deposition chamber until the lowest pressure reading on the gauge mounted on the chamber. Typically, the lowest pressure values on the gauge, i.e. nominally the "zero" pressure, are associated with a base pressure on the turbomolecular pump in the 10^{-6} Torr range (measured via ion gauge). Once base pressure was checked, the operation of impurity removal from the target in use was performed using one of the aluminum screens described in Section 3.2: sputtering was enabled and continued for at least 7-10 minutes, after which oxidation and contamination of the sputtering target after exposure to air in the chamber was expected to be completely removed from its surface.

After purification of the target, the screen was removed and gun and tumbler were brought to the closest distance (avoiding direct contact) such that the actual distance between the powders (at the back of the tumbler) and the target was about 4.5″. Such a distance was a usual choice also with older versions of the tumbler, and revealed to be the closest effective distance target-powders allowed by the parts involved in the deposition process.

During deposition, the main valve connecting the sputtering chamber to the pumping system was kept open, in order to maintain the highest purity of the atmosphere inside the chamber. In fact, plasma and the generated effusive beam, especially in the vicinity of other metal and SS parts, e.g. tumbler, might cause the local temperature to rise and the pressure of the inert gas to rise as well, or even to fluctuate. It was previously reported that this type of solution helped maintaining the set pressure of inert gas inside the deposition chamber [90]; this revealed true also in the specific case of the present work. The mass flow controller also helped to regulate the pressure inside the chamber: the typical pressure of 3 mTorr corresponded to a flow of about 1.5 sccm (standard cubic centimeters per minute).

Deposition occurred as the tumbler spun on its shaft. The revolution speed was usually set at 0.25 Hz (corresponding to 5.0 V dc-voltage) in the direction that allowed the fins in the tumbler to collect the powders and cause their fall. These revolution conditions revealed to be the most effective ones by observation: a lower voltage would cause less revolutions in the unit time, and therefore less powder falls in the unit time. On the other hand, faster spinning could cause the QC on the shaft to leak, as well as the powders might stick more easily due to centripetal force toward the tumbler's inner walls. 5.0 V is thus a reasonable value in the middle of this range, allowing the most effective particle motion and simultaneous exposure to the effusive beam.

Calibration of the beam suggested to utilize low values of the argon pressure in the operational range of the magnetron gun. Sputtering rate (flux) is higher for lower Ar pressure (for given power), as seen in Table 3.1. 3 mTorr is a good choice at the lower end of the gun's operational range, being also the pressure value that maximizes the flux. Thus, this value was preferred for all decoration processes. With respect to the sputtering power, instead, it has been preferred to keep it low as well within its operational range, varying the sputtering time to increase the total deposited amount on a certain sample. 10 W and 30 W have been used the most, but also higher values have been considered in certain instances. Once a certain effectiveness of the process was established (rotation of powders and their exposure to the beam), then the choice of different sputtering power, and consequently deposition time, was ultimately reflected on the results from characterization measurements obtained on the decorated materials.

There is another aspect that should be considered at this point. Given different choices of sputtering power and time, the *exposure amount* might be defined as the product *sputtering power* $\cdot$ *sputtering time*. This value will be the same for cases with different values of power and time such that their product yields an equal number for the exposure. For example:

$$10\ W \cdot 180\ minutes = 1800\ W \cdot minutes = 30\ W \cdot 60\ minutes. \tag{3.1}$$

When the exposure amount is the same between two different sets of sputtering power and time, one could expect equal (or comparable) total amounts of metal deposit on the MO powders. Nevertheless, the total number of revolutions in a sputtering run actually depends upon the total time of deposition: therefore, given the same exposure amount, powders will experience a higher number of powder falls when the deposition time is longer, as compared to a higher sputtering power. It is also important to say, in general, that the MO material in the tumbler is somehow exposed to the beam of metal particles at all times, even if the MO NPs do not move through the center of the tumbler, i.e. through the beam axis, while falling from top to the bottom of the tumbler.

For a given exposure amount, the use of tapping weights to shake powders inside the tumbler showed potential improvement in powders agitation. In particular, when the exposure amount was the same, and with the same mobility conditions of the powders at commencement of the decoration process, it was observed that the amount of retrieved material was usually higher when the tapping weights were in use. A typical example could be that an initial amount of 1 g of material (MgO) reduces to about 0.25 g after 3 hours of deposition at 10 W, but the final mass of retrieved material can be as high as 0.5 g (improvement from 25% to 50%) when tapping weights were used. Usually, the material that could not be retrieved after deposition was severely stuck to the inner walls of the tumbler, posing a limitation on the efficiency of the method when MOs with insulating character were involved. The situation happened to be very different with MO materials as ZnO, whose semiconductor character allowed a much better mobility and consequent higher yield of decorated material. Whether tapping weights were or were not used, yields for ZnO

could be as high as 0.6-0.7 g, with a starting amount of 1 g. In general, better mixing of powders in the tumbler should sustain a better particle surface exposure.

The efficiency of the sputtering process depends on another factor, too: the sticking coefficient (or sticking probability) of a particular metal onto a specific MO. This quantity assesses how efficiently an alien species can adhere to a certain substrate (or, two species can join at the interface). Sticking coefficients can be measured with temperature programmed desorption, which helps to assess how strongly a species was bound to another one as a deposited sample is heated up [108]. The sticking coefficient of the sputtered materials could not be measured *in situ* within the context of the present work. Nonetheless, Table 3.1 provides an idea of the flux of metal particles at a distance of interest, and the sticking coefficient will certainly depend upon the energy of the incoming particles, which is determined by the sputtering power. This could help assess the sticking coefficient, even though it would not be a precise measure of it.

3.4.3 Characterization techniques for the decorated materials

Powder materials were heat-treated after deposition in the same conditions as the bare MgO or ZnO before deposition, although not necessarily at the same temperature (particularly, in the case of MgO). Post-deposition heat-treatment is meant to remove additional impurities from the as-deposited materials and potentially induce reduction of the metal on the oxide surface (driving away excess oxygen species). The decorated materials were then characterized with several techniques. These encompass structural, optical, magnetic, and microscopic probes. A sample of bare MO material was measured along with the decorated material for comparison, when possible. While the focus of the present study has been put on the system Cu/MgO, the deposition of other metals on MgO, as well as deposition on ZnO, was studied.

Powder X-ray diffraction (PXRD) patterns were measured using a Panalytical Empyrean © diffractometer in a Bragg-Brentano $\theta - 2\theta$ geometry by means of the Cu K_{α_1} radiation at 1.5406 Å. The measured patterns span a $2theta$ range 30°-100°. In order to perform measurements, powders were placed on a zero background plate, and the signal from the same plate was subtracted from measured patterns.

Photoluminescence (PL) spectra were obtained on an Agilent Cary Eclipse © fluorescence spectrophotometer using the appropriate solid sample holder for powdered samples. PL emission spectra were measured with different emission and excitation wavelengths (energies) depending on the MO. For MgO, sample materials were excited with UV light at 220 nm, collecting data in phosphorescence mode (usually, in the window 285-600 nm), in order to allow optimal detection of the long-lived electronic transitions on the MgO surfaces. For ZnO, instead, excitation of electrons across the band gap is possible (being ZnO a semiconductor, band gap equals 3.37 eV, corresponding to 368 nm): emission is already present in the green-to-blue portion of the spectrum (below 400 nm), therefore excitation was set at 325 nm [48]. Background signal was measured from a non-emissive substrate (Teflon) in order to be subtracted from the measured emission spectra. This was meant to help eliminating contributions to the signal that do not belong to emission phenomena, e.g. background light from the source (Xe flash lamp). Background subtraction was especially used with MgO PL, because PL is a weaker phenomenon (limited to surface excitations) and background effects become important toward the overall emission intensity.

Diffuse reflectance (DR) spectra were obtained on a Cary 5000 © UV-Vis-NIR spectrophotometer in the range 200-800 nm. The Kubelka-Munk function (see Eq. 2.35) was derived from the experimental data in order to obtain the absorbance of the decorated materials. A high-reflectivity Teflon disk and a black substrate were used to identify the 100% and 0% reflectivity baselines for the instrument. The instrument then applies a correction to the measured signal with reference to the baselines values, and reflectivity can then be expressed as R_∞, being the reflectivity from an infinitely thick material sample with reference to a fully reflecting and a non-reflecting substrates. It is important to remember that MgO is also used as a totally reflecting standard material (instead of, for example, Teflon), and thus its starting reflectivity is actually very high [8]. Furthermore, scattering from the same type of material (e.g. MgO or ZnO particles) can be assumed equivalent, therefore the Kubelka-Munk function is equal to the absorption coefficient, and this is where absorbance is obtained from reflectance spectra. Absorption and absorbance are both assumed to be proportional to concentration of the same species of interest in the measurement, and thus proportional to each other.

All PXRD, PL and DR, thus absorbance, measurements were performed at room temperature and in air, keeping the powdered samples in the appropriate solid sample holders (for PL and DR measurements).

Magnetic measurements on several decorated materials were performed with a Quantum Design © SQUID vibrating sample magnetometer (VSM). The measurements were carried out in the two portions of zero-field cooled (ZFC) and field cooled (FC) modes, spanning a temperature range 5-300 K. In particular, the magnetic moment of the materials as a function of temperature was recorded.

Microscopy images were obtained using a Z-contrast STEM machine, in particular an aberration-corrected Nion UltraSTEM200 © system, operating at 200 kV.

All the characterization measurements were performed with the same degree of carefulness with respect to handling the materials (both pure and decorated), thus everything was stored under argon except for the time of performing such measurements. All the characterization methods described herein were used for the system Cu/MgO, while the other MgO- and ZnO-supported materials were mainly characterized with PXRD, PL and DR spectroscopy.

3.5 A method for pore size calculation

Pore size analysis of a material can be conducted on the base of isothermal experimental data. The Kelvin equation is a very common means to gain a good estimate of the pore radius distribution in a porous material. Experimental investigations on a particular substrate might be initiated after prior pore characterization, e.g. electron microscopy measurements to visualize the structure, or they might be the first piece of data on that system. In the latter case, no prior investigation determines whether or not there is porosity in the material, and thus isothermal adsorption/desorption can be used for an initial assessment. The occurrence of hysteresis between the two branches of an isotherm (see Section 2.7) is in most cases indication of porosity in the material, and its absence usually signals a nonporous structure.

Custom-made experimental apparatuses are available in this research group's laboratory for the measurement of high-precision volumetric adsorption isotherms [59], and were used to perform all the measurements further described in this study (see Fig. 3.16 for a picture

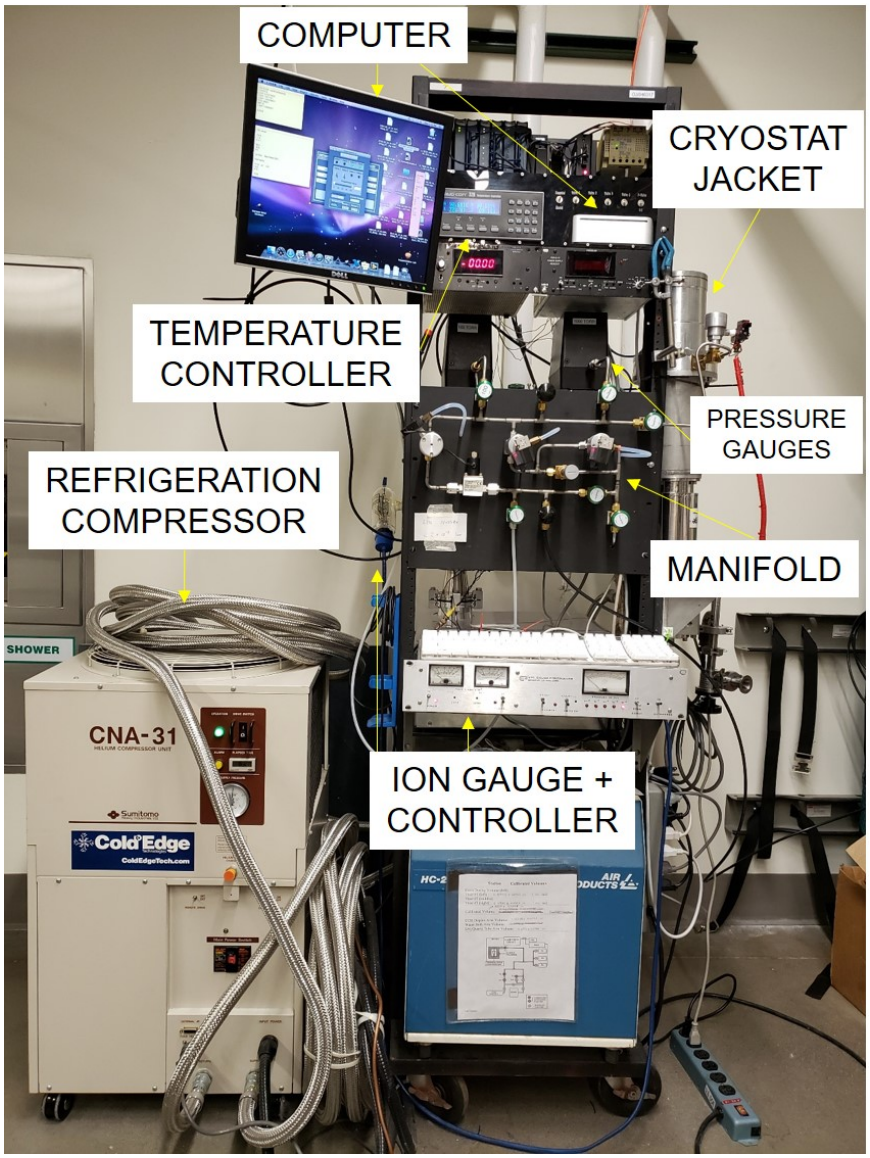

Figure 3.16: The custom-made volumetric adsorption apparatus that was used for the adsorption and desorption measurements described in the text.

of the experimental apparatus). Each apparatus is comprised of a gas-handling manifold connected to an evacuation system, pressure gauges and a sample cell which is part of a cryostat, allowing measurements at temperatures as low as 7-10 K. Moreover, the cryogenic system permits a temperature control on the sample cell as low as 2.5 mK. A LabView © program performs the automated acquisition of adsorption and desorption isotherms: dosing of the desired gas into the main manifold, and its expansion into the sample cell are repeated in multiple cycles, as the pressure of final equilibration of gas aliquots is measured, and the running sum of the pressures is calculated and plotted (as a function of equilibrium pressure). Such an automated process helps the achievement of a pressure accuracy as low as the resolution of the pressure gauge in use, according to the parameters set by the user. Output files can be retrieved from the computer that runs the LabView © program to perform the measurements.

A programmed script was composed using the MATLAB © programming language, which takes the files generated from LabView © as inputs, and generates output files containing all the intermediate and final quantities for PSD analysis (one file for the adsorption and one for the desorption branch of the isotherm). The input quantities that the script needs are the final pressure of equilibration and the running sum of pressures for each measuring cycle (called p_f and $SumdP$, respectively, both expressed in Torr); as part of the output, the script produces plots in MATLAB © to give the user an immediate sense of the PSD without need of further manual data reduction. The script only requires a few values as input from the user, which are specific to the experimental apparatus and sample, namely: the dosing volume of the gas-handling manifold; the volume of the deadspace in the sample cell (i.e. empty space not occupied by the sample); the experimental temperature of the isotherm; the sample's mass; the type of pressure gauge used for the measurement.

The volume of the manifold is known from previous calibration by means of a standard volume. The deadspace volume in the sample cell can be measured by repeated expansions of gas from the manifold into the sample cell performed at room temperature: pressure is measured before and after the expansion, the volume of the manifold is known, therefore the deadspace volume is determined using Boyle's law: $P_{initial}V_{initial} = P_{final}V_{final}$. The experimental temperature can be assessed by the user taking into account the readings from

the two sensors, one on the so-called *cold finger* that supports the sample cell, and the other one on the top of the cell itself (with a typical temperature difference between the two of about 150-200 mK). Lastly, sample's mass is determined by weighing the sample itself before its preparation in the cell (which is performed within an inert environment to preserve the purity of the sample after heat-treatment purification, e.g. in a glove box).

The value of the deadspace volume is used by the script to correct the amount adsorbed, as calculated from *SumdP*, with the pressure (amount adsorbed) taken up during previous cycles. The following formula describes this correction:

$$n_{ads,i} = \frac{\Sigma\Delta p_i \cdot V_{dose}}{RT_{room}} - \frac{(p_{f,i} - p_{f,i-1}) \cdot V_{deadspace}}{RT_{isotherm}} \tag{3.2}$$

where $n_{ads,i}$ is the amount adsorbed at cycle i (in mmol); $\Sigma\Delta p_i$ is the *SumdP* up to i-th cycle, $p_{f,i}$ and $p_{f,i-1}$ are the final pressure of equilibration at the i-th and (i-1)-th cycles (in Torr); V_{dose} and $V_{deadspace}$ are the volumes of the dosing manifold and of the deadspace, respectively (in cm^3); R is the universal gas constant (8.314 J/(mol·K)); and T_{room} and $T_{isotherm}$ are ambient temperature and temperature of the isotherm, respectively (in K). Eq. 3.2 can be used similarly when the desorption branch is considered, although it is used backwards, because desorption measurements commence from SVP.

Eq. 3.3 is the Kelvin equation with modified pore radius, i.e. pore radius minus the statistical thickness. The script generates a plot of the PSD based on Eq. 3.3, the *modified Kelvin equation*:

$$ln\frac{p}{p_0} = \frac{-2\gamma M}{RT\Delta\rho}\frac{1}{(r_m - t)} \tag{3.3}$$

with t statistical thickness of the specific adsorbate gas, and the molar volume is re-written as: $V_L = M/\Delta\rho$, being M the molar mass of the gas and $\Delta\rho$ the difference between orthobaric liquid density and gas density. The liquid density, ρ_l, is typically almost 3 orders of magnitude larger than the gas density, ρ_g; therefore, $\Delta\rho \approx \rho_l$. Use of the liquid density also simplifies implementation of the code for a variety of gases (which the user has to specify when launching the script), because the molar volume has not been measured and tabulated for gases of interest for different values of temperature. This is the case of both N_2 and Ar,

whereas the molar volume of CH_4 (another nonpolar gas of interest to this study, nonetheless an atypical choice as adsorbate for pore size analysis) has been measured and reported as a function of temperature [22].

Table 3.2 reports relevant quantities in Eq. 3.3 for the three gases as implemented in the script code, namely surface tension γ (more precisely, the parameters for its functional form, a and b), molar mass M, orthobaric liquid density ρ_l, and the atomic/molecular diameter σ, from which the statistical thickness t can be derived (see Eq. 2.39).

The output files contain results for the PSD obtained with two different methods for the calculation of the adsorbed volume. The standard version uses values of volume adsorbed (in cm^3 STP/g) calculated from the amount adsorbed, and calculates dV/dr_m as a numerical derivative. A second version, instead, implements the so-called BJH method [4], which attempts to describe desorption as successive removal of adsorbed layers of volume, V, with the composite formula:

$$V_i = \frac{r_{p_i}^2}{(r_{k_i} + \Delta t_i)^2} \cdot \Delta V_i - \frac{r_{p_i}^2}{(r_{k_i} + \Delta t_i)^2} \cdot \Delta t_i \cdot \sum_{j=1}^{i-1} c_j A_j \tag{3.4}$$

$$c_j A_j = \frac{r_{p_i} - t_i}{r_{p_i}} \cdot 2 \cdot \frac{V_i}{r_{p_i}} \tag{3.5}$$

being $r_k = r_p - t$, $\Delta t = t_i - t_{i-1}$, $\Delta V = V_i - V_{i-1}$, with cycles indexed by i.

Table 3.2: Summary of the relevant values as implemented in the script code described in the text, listed for the three adsorbates under study. The functional form for the surface tension γ, as a function of the temperature, T, is the following: $\gamma = a - b \cdot T$. Values for the parameters a and b were obtained from [38] for N_2 and Ar, and from [50] for CH_4.

	Nitrogen	**Argon**	**Methane**
a [mN/m]	26.42	34.28	33.99
b [mN/(m·K)]	0.2265	0.2493	0.1893
M [g/mol]	28.013	39.948	16.043
ρ_l [g/cm^3]	0.808	1.395	0.423
σ [nm]	0.36	0.40	0.40

Two aspects need to be taken into account while using Eq. 3.4: first, it is best applied to the desorption branch of the isotherm due to its own nature of assessing the volume as molecular layers are removed from the surface; second, and this holds true for the general Kelvin equation (as aforementioned), its validity is confined in the mesoporous range. In general, there are two underline assumptions to the use of this method: 1) the pores have cylindrical shape (choice of a specific geometry) and 2) the amount of the adsorbate in equilibrium with the gas phase is retained by the adsorbent by means of two mechanisms, namely physical adsorption *on* the pore walls and capillary condensation *in* the inner capillary volume.

A final, although important, remark has to do with the form of the Kelvin equation, and the factor "-2" that compares in it. The factor "-2" should be included in Eq. 3.3 (and Eq. 2.36) only in the case of desorption, when capillary condensation is assumed to occur in a cylindrical geometry. In the case of adsorption, such a factor does not compare in the Kelvin equation. The automated code considers this difference when performing PSD calculations.

The PSD calculation script was used to assess the pore structure of some materials of interest, upon measurement of adsorption and desorption isotherms. An analysis of the results was performed for each of such materials: the collection of the chosen materials represents a set of examples of how this methodology could be used to assess porosity in a general material. The script code and detailed information on how to use it are reported in Appendix C.

Chapter 4

Characterization of the decorated materials

This Chapter illustrates the characterization measurements, as well as their respective analysis and discussion, obtained on the metal/MO decorated materials. The background description of the characterization measurements can be found in Sections 2.4, 2.5, and 2.6, while description of how these measurements were performed is given in Section 3.4.3. Furthermore, a complete overview of all the relevant decorated materials is given in Appendix B, especially in Tables B.1 to B.6.

4.1 The deposition of copper on MgO

The deposition of copper (Cu) on MgO occupies a major position in this study. As pointed out in Chapter 1, there is a particular interest to study the deposition of Cu on the surfaces of MgO; at the same time, the choice of Cu appears interesting due to its electronic, thermal and catalytic properties, and the properties of its oxides likewise (especially the one of lowest oxidation, namely copper(I) oxide, or Cu_2O). The Cu/MgO system has therefore been used in this study as the example to investigate the efficiency of the deposition process, as well as to carry out a comprehensive study of the properties of the decorated materials.

The initial investigations on the deposition of Cu on MgO were short trials (about 10-12 minutes long), performed at moderate power values (around 50 W). The usual value for

Ar pressure, instead, was set at 3 mTorr, which maximizes the beam flux, as explained in Section 3.3.

As experimentation moved on, it was deemed useful to pursue longer deposition runs (up to hours long), to possibly allow a more uniform decoration of the metal oxide powders. Lower values of the sputtering power were preferred (10 W and 30 W). A focus was kept on studying the evolution of the new materials' properties as a function of the deposition time (i.e. with increasing exposure amount). Additionally, part of the post-deposition study has become heat-treatment of the decorated materials at different temperatures. This method has revealed to be an interesting (and useful) means to observe changes in the color of the decorated powders. This aspect will be touched upon later in this Chapter.

4.1.1 Investigation with X-ray diffraction

PXRD was used since early investigations on the decorated materials as a first characterization method to observe structural changes between pure and decorated MgO. Diffraction of X-rays and the condition imposed by Bragg's law (see Eq. 2.18) can provide a fingerprint of the crystalline structure in a material. In this specific case, comparison of patterns between a sample of pure MgO and one of Cu/MgO would show if any additional crystalline phases (i.e. peaks in the diffraction pattern) arise in the new material with respect to the pure one. What will be done for the Cu/MgO system can be repeated for all other systems under study.

It is interesting to compare diffraction patterns of decorated materials that were prepared at different times, using different versions of the tumbler (3D-printed vs. SS conical): the decorated materials considered here are comparable due to same exposure amount, namely 1800 W·minute (Fig. 4.1 for materials produced with the 3D-printed tumbler; Fig. 4.2 and 4.3 for materials produced with the SS conical tumbler). Despite the different experimental conditions, this comparison illustrates how the same exposure amount to the effusive beam yields comparable structural fingerprints, and in particular the emergence of crystalline phases that do not belong to the MgO structure. Such additional phases in the diffraction patterns are mostly recognized as Cu crystalline phases; only one of them, which is typically barely visible, can be attributed to copper oxide (Cu_2O). The observed crystalline phases

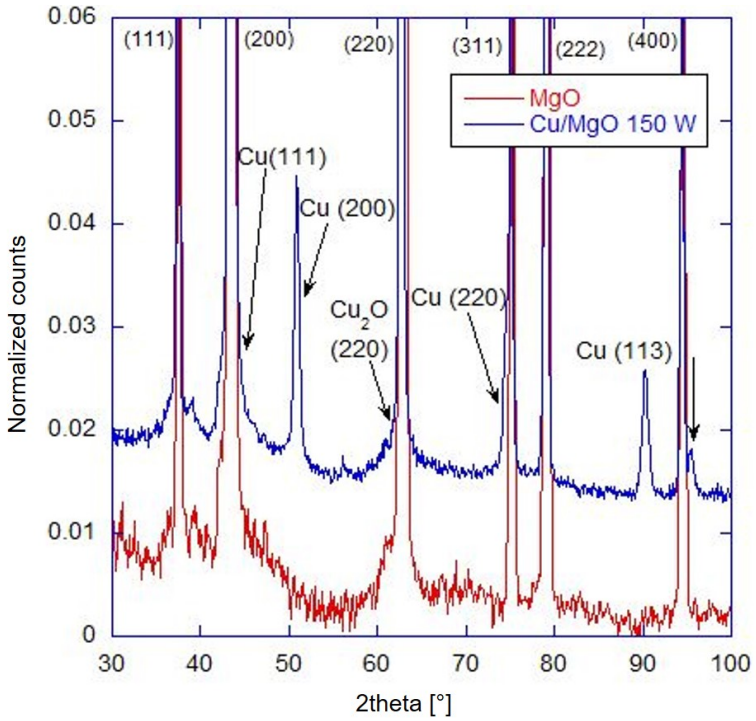

Figure 4.1: Diffraction patterns of bare and Cu-decorated MgO for a sample exposed to 150 W beam for 12 minutes (no heat-treatment before deposition; heat-treatment after deposition at 500 °C). The Miller indices sets (111), (200), (220), (311), (222), and (400) with no further specification represent crystalline phases of the bare MgO structure.

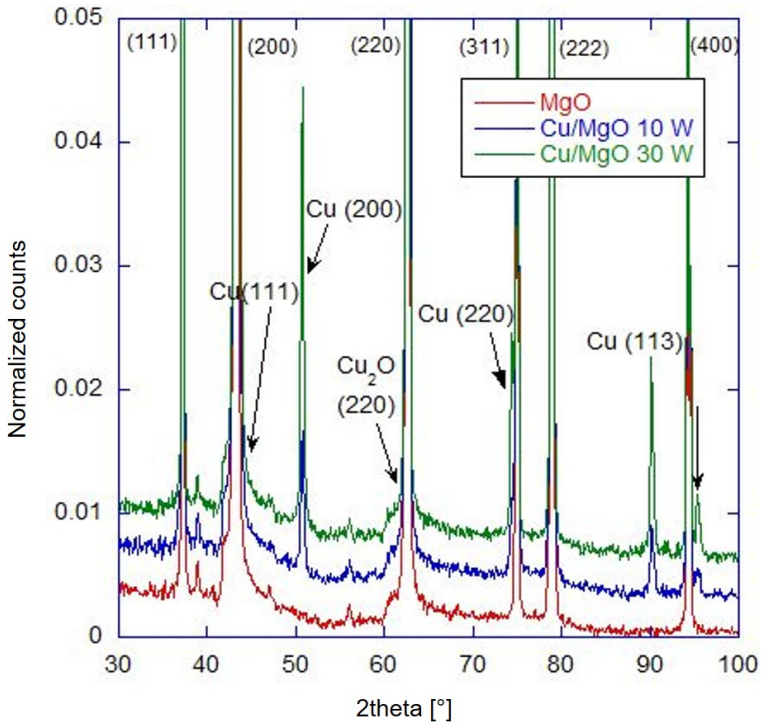

Figure 4.2: Diffraction patterns of bare and Cu-decorated MgO for samples exposed to 10 W and 30 W beam (respectively) for 180 minutes (heat-treatment before deposition at 950 °C; heat-treatment after deposition at 500 °C). The Miller indices sets (111), (200), (220), (311), (222), and (400) with no further specification represent crystalline phases of the bare MgO structure.

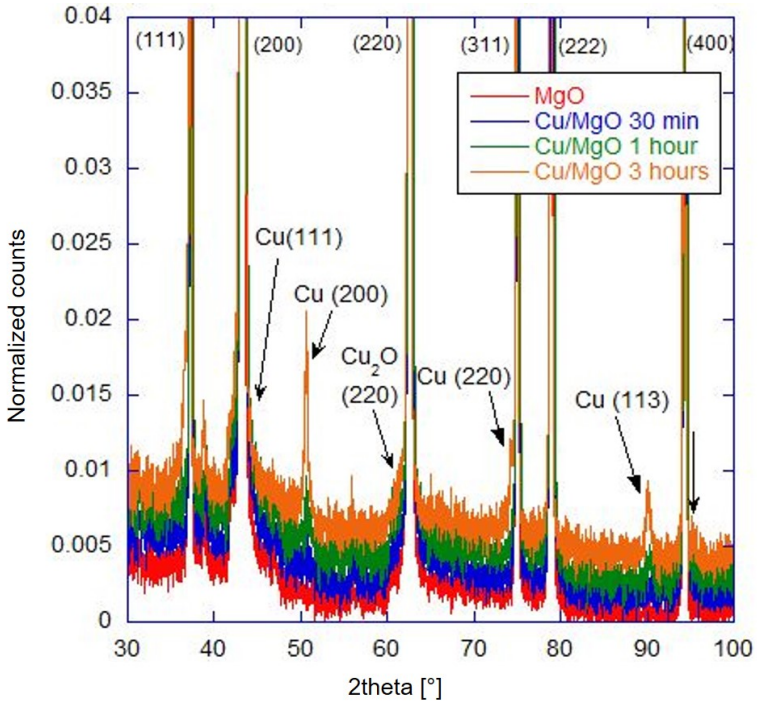

Figure 4.3: Diffraction patterns of bare and Cu-decorated MgO for samples exposed to 10 W beam for different time intervals, namely 30, 60 and 180 minutes (heat-treatment before deposition at 950 °C; heat-treatment after deposition at 500 °C). Tapping weights were used to improve powders mixing in the tumbler. The Miller indices sets (111), (200), (220), (311), (222), and (400) with no further specification represent crystalline phases of the bare MgO structure.

are the following (with positions in $2theta$ [°]): Cu(111) at 43.5°; Cu(200) at 50.6°; Cu(220) at 74.4°; Cu(113) at 89.9°; Cu_2O(220) at 61.5°. These crystalline phases are observed in all Cu/MgO patterns reported in Fig. 4.1, 4.2, and 4.3, especially the (200), (220) and (113) phases of Cu. Cu(111) almost coincides with MgO(200) at 43°, and therefore is better visible in cases of higher exposure amount (e.g. 30 W flux instead of 10 W, see Fig. 4.2). A similar argument is valid for the only copper-oxide phase, Cu_2O(220), which results more intense when the power of the beam (and, consequently, the exposure amount) were higher.

Fig. 4.1 reports a particular case of short, although high-power deposition of Cu on MgO. In particular, Cu crystalline phases in this plot appear more intense (by about 75%) than the ones shown in Fig. 4.2 and 4.3 for the same exposure amount (1800 W·minute, 10 W for 180 minutes in the latter case instead of 150 W for 12 minutes in the former). The reason for this could be a much higher flux the MgO NP were exposed to, still with NP agitation in the tumbler (number of powder falls per unit of time) reduced due to reduced deposition time. As a result, growth of crystalline structures might have taken place on a limited portion of the NP surface area. For this reason, exposure of particles to much lower flux (typically 10 W) on a longer period of time has been preferred throughout this study, as compared to a high-flux, short-time exposure as in the case represented in Fig. 4.1: a longer exposure with much smaller flux should favor a more homogeneous decoration of the MgO NPs surfaces, as compared to formation of larger agglomerates in localized area of these surfaces.

Another aspect of the diffraction results that is worth attention, can be found in Fig. 4.2. In this figure, a comparison between exposure amounts 1800 W·minute and 5400 W·minute (corresponding to 10 W and 30 W at 180 minutes deposition time, respectively) is proposed: clearly, three times as much flux (in the same deposition conditions) generates about as large of an increase in diffraction peaks intensity. Additionally, one can notice an increased background (also observed in the pattern of Fig. 4.1), showing how higher flux (independently from the deposition time) adds metal deposits on the MgO surface, that act as scatterers for the X-ray radiation, and do not necessarily contribute to formation of a crystalline structure.

Fig. 4.3 and 4.4 report patterns of Cu/MgO materials with different deposition times. One can clearly notice how the signatures of Cu crystalline phases emerge after at least

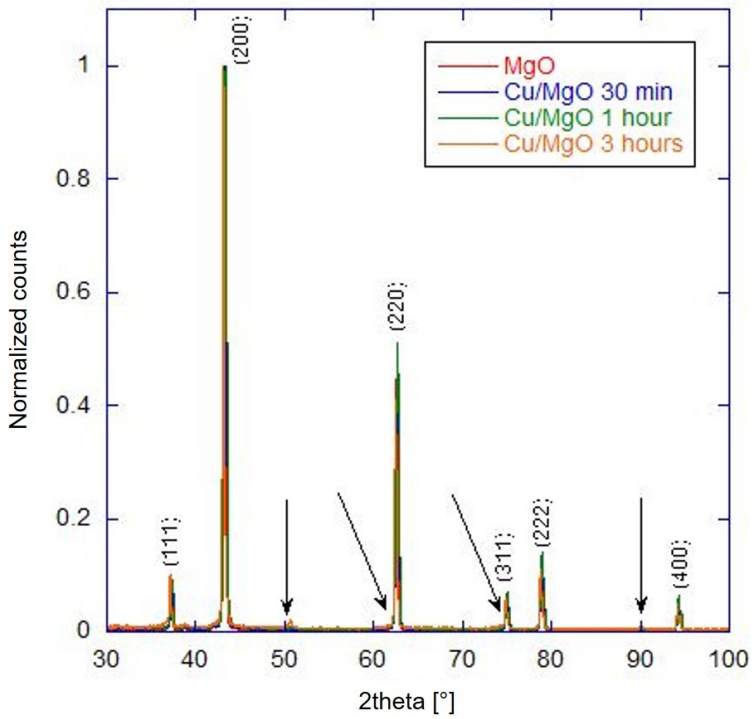

Figure 4.4: Same diffraction patterns as Fig. 4.3, where peaks for MgO crystalline phases are shown in full. The Miller indices sets (111), (200), (220), (311), (222), and (400) with no further specification represent crystalline phases of the bare MgO structure.

one hour of deposition (10 W power in all cases). This confirms what stated above, and sets a minimum value of exposure amount below which the emergence of a new structure is not observed. Such a value can be reasonably set between 200 and 300 W·minute, that corresponds to 20-30 minutes of exposures of the particles to 10 W beam. This means that a structured formation of deposits on the MgO surface, or the formation of a new, additional structure besides the one of MgO, begins to occur after a certain deposition time is reached, i.e. 20-30 minutes. This dependence of changes in the Cu/MgO materials (in general, of the decorated MgO materials) on the deposition time (i.e. exposure amount) is a key factor that will be considered throughout the materials characterization.

Along with the structural modifications, the decorated powders also show a coloration that changes from gray/black in the as-deposited powders, toward green and then pink/red for increasingly high temperatures of heat-treatment after deposition, as high as 950 °C (Fig. 4.5). The Cu crystalline phases appear only when the as-deposited powders are heat-treated after deposition; otherwise, such diffraction peaks appear broader and much shallower. This suggests that a reduction process might occur upon heat-treatment of the as-deposited materials, in possible conjunction with sintering of the deposited species. In both cases of post-deposition heat-treatment that were considered in this work, namely 500 °C and 950 °C, the observed peaks of the Cu crystalline phases do not change their position in $2theta$, neither they present different intensities for different temperature of treatment. If heat-treatment of the bare MgO materials does not have any influence on the diffraction patterns (full patterns of bare and Cu-decorated MgO are reported in Fig. 4.4), it will instead have an influence on other characterization measurements following X-ray diffraction, in particular the optical ones.

4.1.2 Investigation with optical probes: PL

Photoluminescence (PL) spectra were first obtained for bare MgO. It was found that maximum emission intensity occurs at 375 nm (3.31 eV) upon excitation at 220 nm (5.64 eV). Luminescence from MgO powders has been determined for long time to be related to surface energy states emission ([15], [87]), being the energy band gap situated at about 7.8 eV (therefore far off a possible excitation with UV light). The excitation energy of 5.64 eV

Figure 4.5: Cu/MgO powdered materials showing changes in coloration from deposition up to the highest post-deposition heat-treatment temperature. *Top left*: Cu/MgO right after deposition. *Top right*: Cu/MgO after heat-treatment at 500 °C (tapping devices in use). *Bottom left*: Cu/MgO after heat-treatment at 950 °C (tapping devices not in use). *Bottom right*: Cu/MgO after heat-treatment at 950 °C (tapping devices in use). Cu/MgO shows a black/gray color after deposition, and heat-treatment changes its color into shades of green (500 °C) and eventually pink/red (950 °C).

well aligns with the one theoretically calculated for 4-coordinated sites on the MgO surfaces ([82], [92]). Pure and almost defect-free MgO surfaces are most likely obtained with the synthesis, purification and characterization method described in Section 3.4.1: this implies that the majority of the 4-coordinated sites on the MgO surfaces are most likely to be the edge sites. It appears thus reasonable to assign luminescence emission at 3.31 eV mostly to the excitation of electronic surface states on the edges of the almost perfect MgO nanocubes. A minor contribution could also come from the corners of the MgO nanocubes, which are the primary 3-coordinated surface sites on a defect-free surface. In these regards, there may be emission at longer wavelengths (energy below 2 eV) but this is very weak and it is difficult to understand its nature, as well as to establish the association to specific coordination sites on the surface.

The excitation and emission bands with peaks located at 5.64 eV and 3.31 eV, respectively, are reported in Fig. 4.6: the interest in such bands is due to the association with 4-coordinated sites. The spectra of Fig. 4.6 were measured on MgO powders previously heat-treated at 950 °C: typically, this type of treatment on MgO powders synthesized according to Section 3.4.1 is associated with a low density of defects on the surface. This role of heat-treatment strengthens the association between 4-coordinated sites and edge sites, being lower-coordination (e.g. 4- and 3-coordination) reduced on the MgO(100) surfaces. Furthermore, the slightly asymmetric shape of the emission band peaked at 375 nm (3.31 eV) indicates the possibility of emission processes related to a multiplicity of smaller energy states, e.g. relaxations occurring from multiple triplet energy state to a singlet state (which is the typical mechanism of phosphorescence). The long tail can also be associated to transfer of the excitation to sites of lower-coordination and, thus, lower Madelung constant and binding energy (e.g. a multiplicity of triplet-singlet transition energies).

Moreover, a much broader and shallower emission feature seems to appear at even longer wavelengths, peaked around 680 nm (circa 2 eV): further excitation of lower-coordination sites might be the answer explaining such a phenomenon. A profound explanation of luminescent emission from low-coordination surface sites remains difficult. A full and clear description of the excitation and emission energies related to the luminescent processes on the MgO surfaces is still under debate, too ([13], [12]). It is not the intent of this work

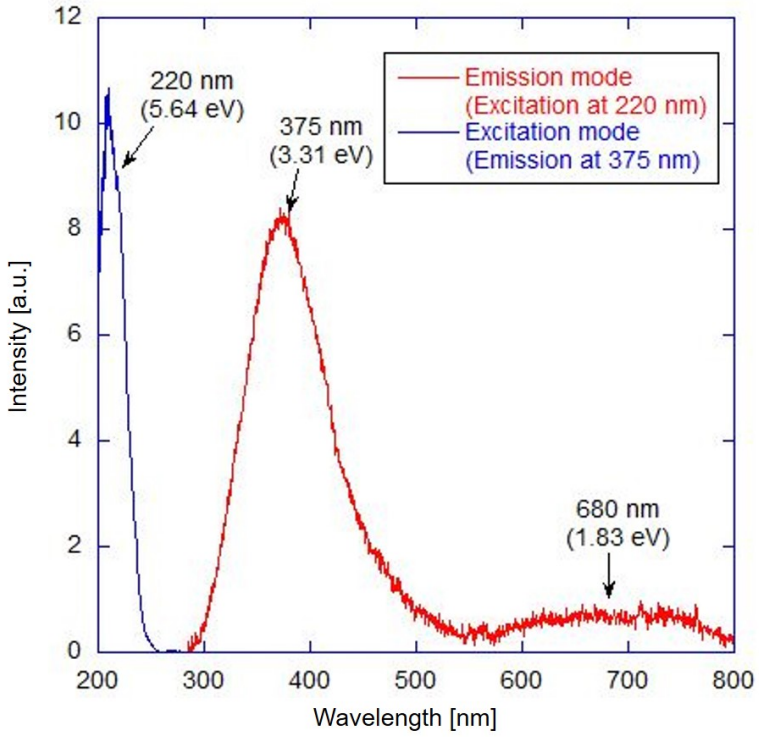

Figure 4.6: PL excitation (blue) and emission (red) spectra of MgO powder after heat-treatment at 950 °C. Background signal was subtracted.

to help the clarification of this problem, rather it is the interest to understand the surface luminescent emission and study its behavior before and after surface metal decoration.

Once Cu species are deposited on the MgO powders, the PL emission studied for pure MgO clearly changes: even a small amount of exposure of the pure MgO species to the effusive beam can cause the PL intensity to quench considerably (Fig. 4.7). This happens consistently from very small deposition times (1 minute) up to long exposures (3 hours), suggesting that the emitting sites mainly contributing to the emission band peaking at 375 nm are prevented from undergoing such a radiative transition. As illustrated above, the major emitting sites are associated to the edges of the MgO nanocubes.

Two possible explanations for the quenching of the PL signal might be the following. First, excitation of 4-coordinated sites occurs on the MgO surface, but the emitted radiation is further absorbed by the deposited species and emission of light cannot be appreciated. An example would be a modified electronic structure where excited electrons eventually

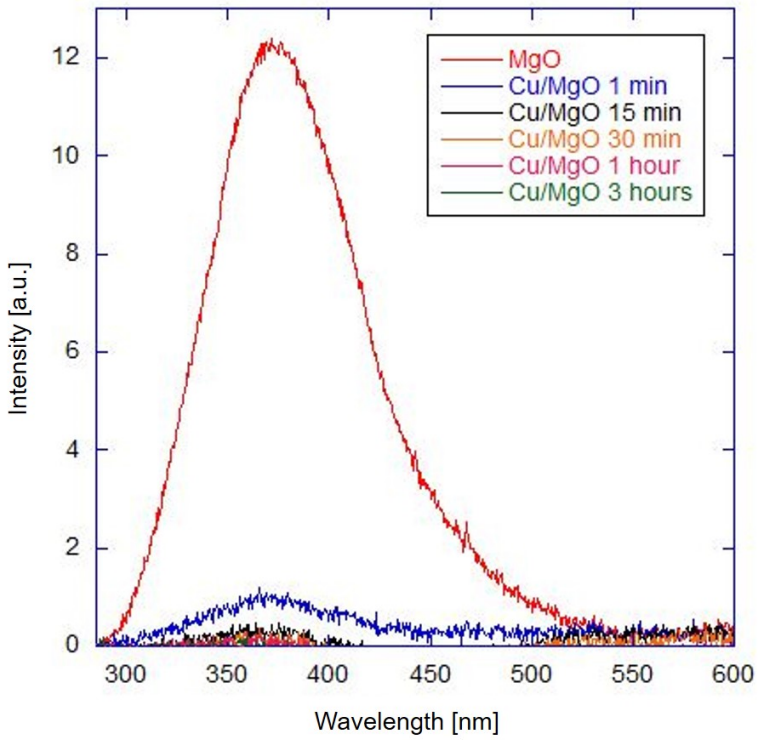

Figure 4.7: PL spectra of pure and Cu-decorated MgO as a function of deposition time. Heat-treatment before deposition at 950 °C; heat-treatment after deposition at 500 °C. Tapping weights were used during the deposition process.

occupy energy levels that were not part of the original structure (due to new electronic states introduced by Cu on the surface). On the other hand, excitation of the MgO surface sites is completely hampered by the deposited species, and all those emitting sites interested by metal species deposition do not undergo excitation at all (all the energy of excitation is absorbed by other species - the metal deposits). In both cases, estimating what fraction of the emitting sites is interested by metal deposition remains difficult, because it depends not only on the several deposition conditions, i.e. exposure amount, but also on the effectiveness of mobility of the powders in the tumbler, and therefore on the degree of homogeneity of metal deposition. When different Cu/MgO materials are produced, the sticking coefficient will be the same due to nature of the system, thus it will not play a role in determining the final configuration of the metal/MO interface.

The use of the tapping weights around the tumbler should improve powders agitation and therefore favor a statistically better exposure of all the MgO particles to the effusive beam of Cu metal. The observation comes from comparing the fractions of PL signal intensity to the intensity of pure MgO of Cu/MgO materials prepared in the same experimental conditions (with heat-treatment after deposition at 950 °C), only differing in the use of the tapping weights. The signal is less quenched (i.e. it is a larger fraction of the PL signal for pure MgO) when the latter were not used during the deposition process. In fact, PL intensity with no use of tapping devices is about 15-20% of the pure MgO PL intensity, as compared to less than 10% when the weights were used. It is although difficult to establish a proportionality relationship between exposure amount and luminescence intensity, because small exposure amounts can already reduce the PL intensity of the original MgO significantly (see Fig. 4.7).

Post-deposition heat-treatment temperature does not have an influence on the degree of quenching of the PL intensity (a similar observation was proposed for the diffraction results). In fact, when MgO materials were decorated with Cu in the same conditions, e.g. 3-hour deposition, and underwent heat-treatment at different temperatures (namely, 500 °C and 950 °C), the two materials ultimately possess almost the same PL behavior, provided that tapping devices were (or were not) used in both cases. Thus, post-deposition heat-treatment temperature does not affect PL behavior of Cu-decorated MgO materials.

It comes natural to observe that, if post-deposition heat-treatment temperature does not affect PL intensity, then the metal deposits are the cause of PL quenching, independently from their chemical state (a reduction process possibly takes place with increasingly higher heat-treatment temperatures), which strengthens the hypothesis of atoms, or clusters, on the surface emitting sites that hamper the light absorption, excitation and luminescence process. However, there remains a question about size, morphology and actual position of the metal deposits, i.e. whether Cu (or any Cu-related species) sits atop, on the bridge, or in the hollow between atomic species (Mg and O) of the MgO surface structure.

4.1.3 Investigation with optical probes: DR

Absorbance of the decorated materials was obtained along with PL spectra, measuring DR spectroscopy. The Kubelka-Munk function, Eq. 2.35, was derived from reflectance data, and represents the absorbance of the pure and decorated powders, as discussed in Section 3.4.3. The absorbance of pure MgO is at least as low as other reflectance standard materials used as references in diffuse reflectance measurements, e.g. Teflon (that was used for these measurements as well): the absolute reflectivity and therefore diffuse reflectance of a light source off of such materials is among the highest, and the one of MgO is comparable to these. Absorbance of MgO is non-negligible in the neighborhood of 230 nm toward lower wavelengths (Fig. 4.8), which is also the region of highest absorption as measured in the PL excitation spectrum (Fig. 4.6).

Fig. 4.8 reports absorbance spectra for pure and Cu-decorated MgO materials: the absorbance of the decorated MgO materials increases as a function of the deposition time. The trend of the Cu/MgO absorbance spectra with the deposited amount is reversed as compared to the observed trend in the PL spectra of Cu/MgO for different deposition times. The increase in absorbance seems logical upon visual inspection of the decorated materials: the white pure MgO powders look darker in the shades of gray and black right after deposition, and then change their color progressively into shades of green and pink/red with higher temperature heat-treatment after deposition (500 °C and 950 °C), as one can see in Fig. 4.5. This was observed in the discussion on the diffraction patterns.

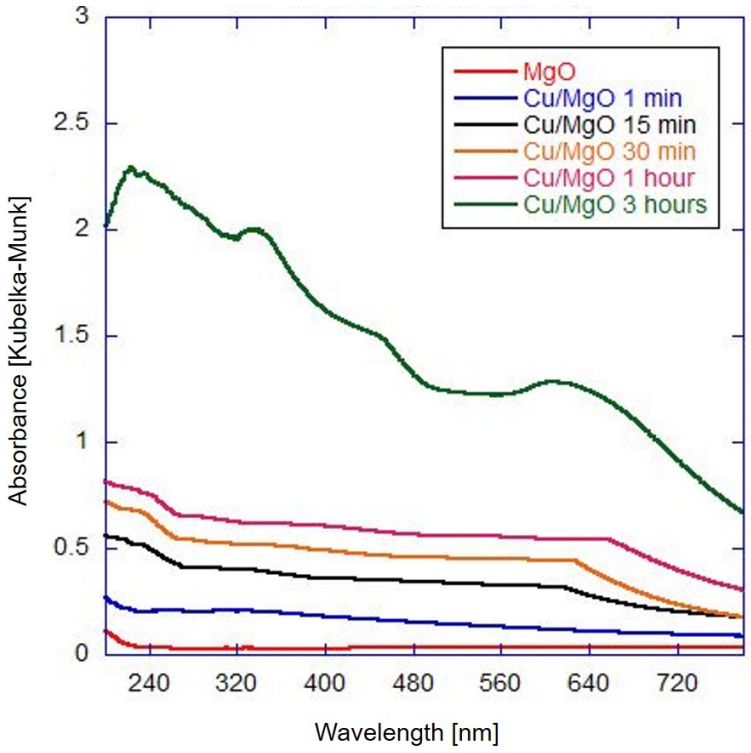

Figure 4.8: Absorbance spectra of pure and Cu-decorated MgO as a function of deposition time, corresponding to PL spectra in Fig. 4.7.

Absorbance actually decreases in intensity in a case of Cu/MgO material prepared in the same experimental conditions (3-hour deposition) with post-deposition heat-treatment at 950 °C as compared to treatment at 500 °C, still maintaining absorbance features mostly unchanged (Fig. 4.9). Some features in these absorbance spectra can be associated with similar measurements obtained on Cu nanocrystals in the same wavelength range: the comparison with the work by Pestryakov and co-workers is interesting, because they studied the optical and electronic properties of supported Cu species [70].

When Cu/MgO was prepared without the use of tapping weights (decorated for 3 hours in the same conditions as above), the absorbance of the resulting material is reduced drastically, in parallel with reduced quenching of PL intensity, and with less pronounced crystalline phase peaks in the diffraction pattern. In particular, the absorbance spectrum loses all the features present in the absorbance of Cu/MgO prepared with tapping devices, while maintaining a (weak) feature between 540-580 nm (Fig. 4.9): this is the typical signature of Cu NPs plasmon resonances, as discussed by Pestryakov and co-workers [70]. In a later discussion, an assignment of all these absorbance features will be proposed.

4.1.4 Magnetic measurements on Cu/MgO

SQUID VSM data were obtained for Cu/MgO material prepared for 3 hours, with no tapping weights, both at 10 W and at 30 W. The specimen prepared at 10 W is the same as the one discussed at the end of Section 4.1.3. Magnetic susceptibility (magnetic moment) was measured as a function of temperature, both in the ZFC and in the FC mode (Fig. 4.10). At low temperatures, i.e. at and below 50 K, the results are intriguing. Especially in the FC portion of the data, the magnetic response of the material significantly increases in the low temperature region: a similar behavior was measured by Wu and co-workers on Cu_2O NPs with diameter smaller than 10 nm, indicating a potential existence of such species on the MgO surface [109]. Interesting is also the comparison between the two Cu/MgO materials, prepared with exposure amounts differing by a factor of 3 (10 W vs. 30 W): lower flux (lower exposure amount) yields a more pronounced feature at low temperature, as well as higher magnetic susceptibility overall. This behavior should be kept in mind while analyzing the characterization results as a whole.

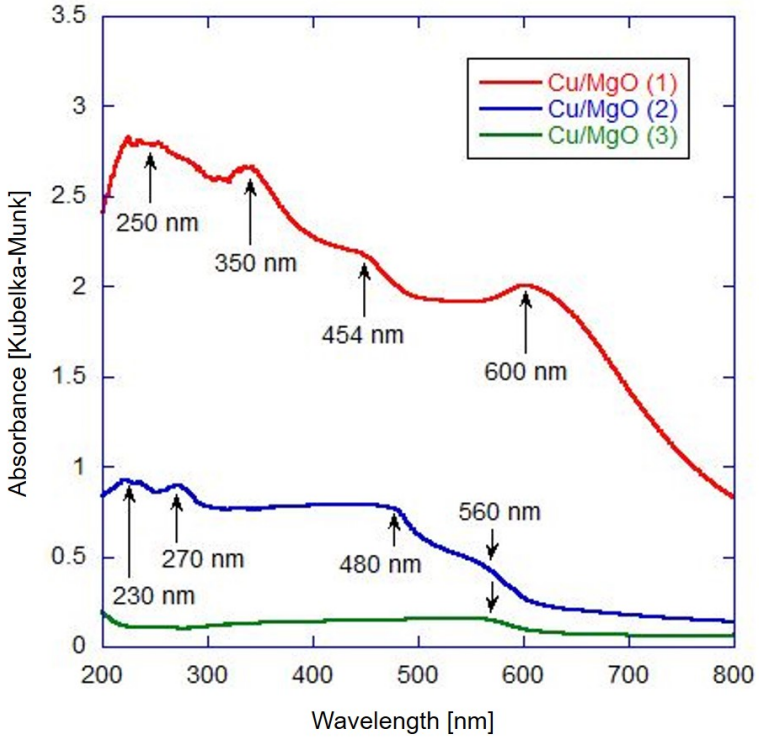

Figure 4.9: Absorbance spectra of (1) Cu/MgO heat-treated after deposition at 500 °C (tapping weights used); (2) Cu/MgO heat-treated after deposition at 950 °C (tapping weights used); (3) Cu/MgO heat-treated after deposition at 950 °C (no tapping weights used).

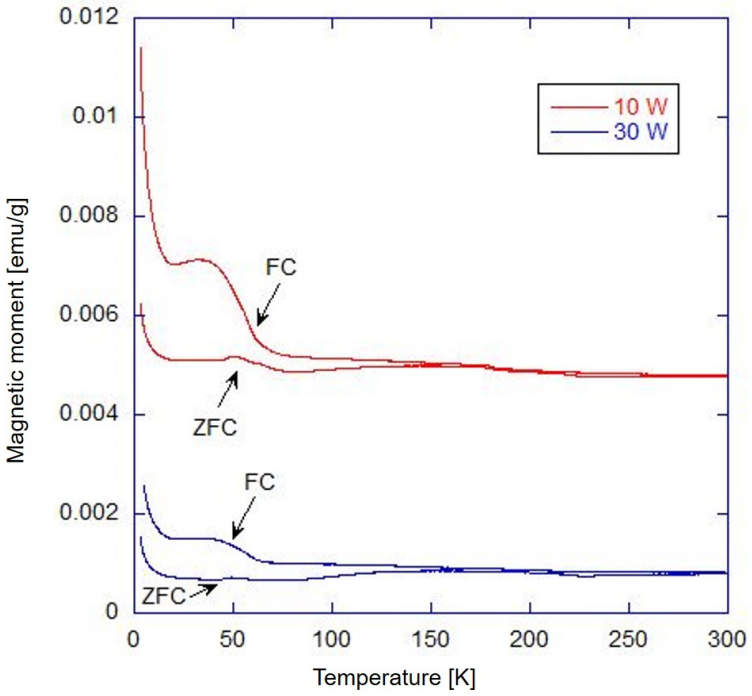

Figure 4.10: SQUID VSM plots in zero-field cooled (ZFC) and field-cooled (FC) modes for the magnetic susceptibility of Cu/MgO (3-hour deposition, heat-treatment after deposition at 950 °C, no tapping weights used during deposition).

4.1.5 Electron microscopy on Cu/MgO

Evidence for the presence of atomically-resolved nanoparticles of metallic Cu comes from Z-contrast STEM images, showing atomic deposits of elemental Cu on the MgO(100) surfaces and especially on the MgO nanocubes edges (Fig. 4.11). This strengthens the hypothesis of quenched PL from edge sites due to a (potentially) new electronic structure, which impedes the excited state decay that causes luminescence from pure MgO particles. This electron microscopy image also stands in accord with the results from the other characterization measurements on the Cu/MgO powders, e.g. X-ray diffraction.

4.1.6 Cu/MgO: discussion

The formation of a new structure in addition to the MgO crystalline structure is very clear from Fig. 4.1, 4.2, and 4.3. The first important observation is that all the major phases of crystalline Cu [78] appear for long enough deposition time, indicating that some type of long-range order is forming. The fact that all the major phases are present might represent a growth process without a particularly preferred orientation. This could correspond to growth of large enough metallic clusters on the MgO particles surface (or clusters forming adjacently to it); on the other hand, long-range order could also be originated by a pattern of atoms (or small clusters) orderly spaced on the MgO particles. With reference to the microscopy image on the left-hand side of Fig. 4.11, formation of clusters can possibly correspond to the region A, as compared to patterned atoms of Cu on the MgO(100) surface possibly corresponding to region B.

If deposition was taking place on a non-moving substrate, growth should probably be expected to occur much more quickly (few minutes of sputtering deposition in the same conditions could possibly produce nanometer-thick layers of Cu). Considering that the substrates of this study are moving, the effective surface area where deposition can take place will be significantly reduced, therefore the appearance of phases other than the MgO crystalline phases comes with longer deposition time.

The trends in quenched PL intensity and increasing absorbance with deposition time help to strengthen the argument in favor of Cu structures formation (Fig. 4.7 and 4.8). The

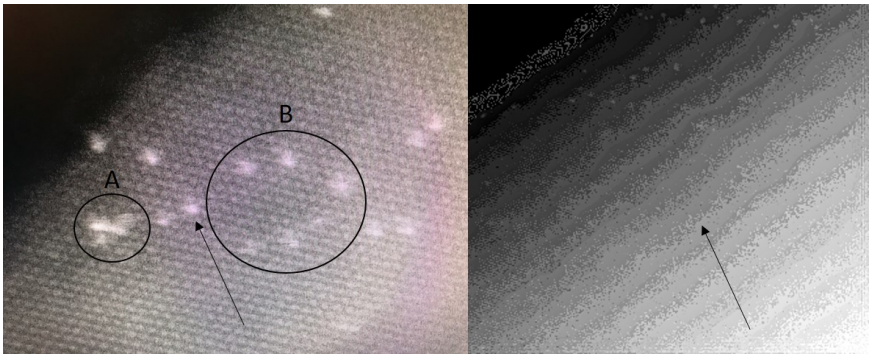

Figure 4.11: Z-contrast STEM images of Cu/MgO (3-hour deposition, heat-treatment after deposition at 950 °C, no tapping weights used during deposition). *Left*: atomic resolution of the MgO(100) surface shows presence of atomic Cu species. See text for explanations about the circled regions A and B. *Right*: step edges of MgO nanocubes are decorated with Cu species as well. Arrows point at Cu species.

electronic excitations giving rise to PL emission only happen at the surface, therefore new species formed on the surface (or in its close vicinity) are the only possible cause for formation of new bonds, preventing the emitting sites of pure MgO from experiencing radiative decay. Quenching has been associated with a reduced ability of the 4-coordinated sites to re-emit light, and 4-coordinated sites are principally located on the edges of the MgO nanocubes. Nevertheless, in case there were defects on the surface, there would be another possibility of 4-coordinated sites, e.g. vacancies: even in such a case, formation of a new bond and electronic structure principally at the surface would explain why PL intensity decreases with respect to the one of pure MgO.

These same species are also responsible for an increased absorbance of light (reduced reflectivity of pure MgO) in the whole visible spectrum (Fig. 4.8 and 4.9). This suggests that the very low absorbance of pure MgO (except for the ultra-violet region, in accord with the excitation spectrum of Fig. 4.6) is drastically changed due to metallic deposits throughout the surface of these MO particles. The change in color of the MgO powders (Fig. 4.5) is the first logical explanation for this. Moreover, the presence of Cu (or any related species) probably introduces a new electronic configuration of surface sites, where more electrons are available for excitation, but also for absorption of photons.

The features in the absorbance plots (Fig. 4.9) have some similarities with already reported results. Features in the region between 200-300 nm can be associated with transitions in Cu_2O (copper(I) oxide) powders [96]. This is valid for Cu/MgO produced with tapping weights, and heat-treated after deposition at both 500 °C and 950 °C. In the case of 500 °C heat-treatment (red line in Fig. 4.5), the mid-region of the spectrum (300-500 nm) contains features at 350 nm (attributed to Cu-O-Cu bonds by Pestryakov and co-workers [70]) and at 454 nm (measured on Cu_2O powders by Tandon and Gupta [96]). In the case of 950 °C heat-treatment (blue line in Fig. 4.9), instead, such features are lost, but a shoulder remains at 480 nm, which seems the same shoulder at 454 nm in the previous case, just shifted to higher wavelengths. The only contribution to the absorbance spectrum in the case of Cu/MgO produced without tapping devices (and heat-treated at 950 °C after deposition - green line in Fig. 4.9) appears around 560 nm and, according to Pestryakov and co-workers [70], it is the signature of Cu NPs plasmon resonance (usually located between 540-580 nm). This is valid for both cases of post-deposition heat-treatment at 950 °C (blue and green lines in Fig. 4.9). The feature at 600 nm in the first case (500 °C treatment after deposition, with tapping devices - red line in Fig. 4.9) might be augmentation of the same plasmon resonance signal at slightly higher wavelengths.

Clearly, results from absorbance can help to provide a better picture of the nature of the deposits on the surface. After 500 °C heat-treatment, the evidence is for a majority of copper-oxygen bonds. After 950 °C treatment, instead, the signature of Cu NPs appears and all the other features are less pronounced, and even have disappeared when the deposit on the surface is nominally lower (case of no tapping devices used). It seems that a reduction process is happening due to increasingly higher temperature heat-treatment of the materials, simultaneously with loss of deposited amount. In fact, an observation comes to help at this point: after heat-treating the material *in vacuo* at 950 °C in usual quartz tubes utilized for MgO heat-treatment, Cu residues are observed stuck on the inside of the tube as a red-colored halo. Despite the fact that metallic Cu has its boiling point above 2500 °C, some Cu deposits might as well be loosely bound to the MgO and be driven away during heat-treatment (this was observed consistently when heating Cu/MgO materials in quartz tubes up to 950 °C).

The absorbance characters are coupled to macroscopic observations about the colors of the decorated Cu/MgO materials (Fig. 4.5). Pure Cu atoms and clusters can be reasonably expected to reach the MgO NPs in the tumbler, considering the fact that pure Cu species are ejected from the sputtering source (e.g. the color of the Cu layer on the QCM surface after beam calibration, along with the very high purity of the Cu targets in use - see Section 3.3 for calibration of the beam). At the same time, oxygen species that are part of the MgO structure, as well as residual O_2 in the high-vacuum deposition chamber, can play a role and participate to the binding of Cu to the MgO NPs. All materials right after deposition appear, in fact, black or, at least, in some shades of gray (Fig. 4.5). (Black is the usual color of CuO, namely copper(II) oxide, powders). Then, heat-treatment of the powders *in vacuo* possibly induces a reduction process, where the color changes from dark (e.g. black and gray) into shades of dark green, and then pink (or red). O is driven away in the treatment, as well as Cu (at least to some extent, as explained above). The argument of Cu reduction taking place upon heating the decorated materials is also strengthened by the intensity of Cu crystalline phases in the diffraction patterns before and after heat-treatment following the deposition process (see Section 4.1.1).

Evidence for such interpretation of the structural and optical characterization results is provided by the STEM images (Fig. 4.11). The Z-contrast STEM images reveal presence of atomic Cu deposited on the MgO surface, and they should be representative of how the entire sample would statistically appear; nonetheless, it is important to remember that deposition on the surface is possibly not homogeneous (as macroscopic color shades in some powders indicate), and that the examined sample by STEM probably represents one of the lowest quantity of deposited Cu species. The fact that single Cu atoms are positioned just a few lattice constants apart (Fig. 4.11) could be in accord with both explanations of a long-range order structure for Cu, namely large enough clusters of atoms (when many atoms are located very close to each other, circle A in left-hand side of Fig. 11), or groups of evenly spaced atoms on the MgO surface, possibly at different surface levels (circle B in left-hand side of Fig. 4.11). The optical measurements would well align with the electron microscopy results as well, in terms of binding both to edge sites (right-hand side of Fig. 4.11) and to other sites

on the (100) surfaces. This would offer an explanation for the modified electronic structure giving rise to quenched PL and increased absorbance.

Lastly, evidences for presence of cuprous oxide, Cu_2O, come from absorbance (Cu-O bonds), PXRD (peak corresponding to the $Cu_2O(200)$ phase) and SQUID VSM results. In particular, the change in magnetic moment below 50 K (especially for the FC portion of the measurement) clearly resembles the one for Cu_2O powders with grain size less than 10 nm. The magnetic susceptibility measured on the same material that underwent Z-contrast STEM measurements (10 W flux for 180 minutes) is significantly lower than the one measured by Wu and co-workers [109] (about 20 times smaller at the peak, resulting from the ratio 0.007 (emu/g)/0.14 (emu/g)), indicating that Cu_2O NPs, if present, are highly dispersed in the MgO matrix. It is reasonable to think, then, that the amount of Cu_2O present in solution with MgO diminishes proportionally with decreasing susceptibility signal. A similar consideration has been proposed about the extent to which the absorbance (and therefore the composition of Cu on MgO) can change with a step from 500 °C to 950 °C post-deposition heat-treatment. However, as pointed out before, it remains very difficult to quantify the amount of Cu (or Cu-related) deposits without having a more elemental survey on the decorated materials.

4.2 The deposition of nickel and cobalt on MgO

After learning properties and trends in the deposition of Cu on MgO (Section 4.1), the deposition of Ni and Co on MgO was explored. These cases of deposition on MgO have not been studied as much in detail, although interesting results were obtained, which reasonably align with the results on the Cu/MgO characterization. The main difference that needs to be kept in mind is the reduced sputtering flux for the same deposition conditions (see Table 3.1), which will be reflected on the variations of the structural and optical properties of the decorated materials.

4.2.1 PXRD on Ni/MgO and Co/MgO

Diffraction results for Ni/MgO and Co/MgO (Fig. B.24 and B.25 in Appendix B) resemble what was observed for the Cu/MgO system (Fig. 4.3). Additional crystalline phases associated to the two metals are present besides the characteristic peaks of pure MgO. The reduced flux for Ni and Co (about half of the one for Cu) explains why the Ni and Co crystalline phases appear only after long exposure to the sputtering beam: deposition for less than 3 hours does not yield any appreciable peaks in the diffraction patterns. For this reason, it was interesting to compare the patterns obtained from the decorated materials with post-deposition heat-treatment at the two different temperature values already discussed for the Cu/MgO system, namely 500 °C and 950 °C.

For Ni/MgO, heat-treatment after deposition at 500 °C does not reveal any structure of the metal, whereas the same treatment at 950 °C results in visible peaks with positions in $2theta$ [°] as follows: Ni(111) at 44°; Ni(200) at 52°; Ni(220) at 76.5°; Ni(311) at 93.5°. Except for the Ni(111) phase peak (about 1% on the normalized counts scale - comparable to the intensities of some of the peaks for metallic Cu in the Cu/MgO diffraction patterns), all the other phases are barely visible above the signal background.

For Co/MgO, metallic phases can be appreciated in both cases of heat-treatment after deposition, but still peaks are more visible for the higher temperature case (i.e. 950 °C). In this latter case, crystalline phases with their $2theta$ [°] positions are: Co(111) at 44°; Co(200) at 52°; Co(220) at 75°; Co(311) at 92°. All such phases are visible, although slightly distinct from the background.

No phases related to oxides of the two metals are noticeable in the analyzed patterns. This appears to be consistent with observations proposed above about Fig. 4.3: mostly metallic Cu must be part of the decorated MgO. Also, the factor 2 of difference in flux between Cu and these two metals (Ni and Co) seems to reflect very faithfully in the diffraction patterns. Less intense crystalline features for Co than for Ni could be explained with differences in sputtering flux as well, because flux for Co is smaller than that for Ni (see Table 3.1). The formation of a new crystalline structure appears consistent for all the decorated materials Cu/MgO, Ni/MgO and Co/MgO, in particular with the use of tapping weights in all cases

(Fig. 4.3 for Cu/MgO; Fig. B.24 and B.25 in Appendix B for Ni/MgO and Co/MgO, respectively).

4.2.2 PL and DR spectroscopy on Ni/MgO and Co/MgO

Fig. B.26, B.27, B.28, and B.29 in Appendix B report compilations of spectra obtained on different deposition time cases of the decorated materials, respectively, PL for Ni/MgO, absorbance for Ni/MgO, PL for Co/MgO, and absorbance for Co/MgO. In all these measurements, similar trends in the quenching of the PL intensity and increase of absorbance are observed similarly to what was observed in Sections 4.1.2 and 4.1.3 for Cu/MgO. Quenching of the PL is not as drastic, with the main emission signal at 375 nm still greater than zero even for several-hour deposition cases (Fig. B.26 and B.28). Whereas, absorbance increases with increasing deposition time, as can be seen in Fig. B.27 and B.29. Strong absorbance signal is present in the UV region of the spectrum in both cases of Ni/MgO and Co/MgO.

As it was noticed for the Cu/MgO PL, it is difficult to quantify the relationship between exposure amount for the deposition process and the extent of PL intensity quenching. However, it was noticed there (Section Cu/MgO PL) that quenching happens in a proportional manner with increasing deposition time. In fact, PL signal intensity is at least twice as much for Ni/MgO (Fig. B.26) and Co/MgO (Fig. B.28) than for Cu/MgO (Fig. 4.7) in the 1-minute deposition case, and appears to be reduced accordingly with increasing deposition time. For Ni/MgO, there is clear distinction between the shortest (1 minute) and the longest (3 hours) deposition cases, while there is overlapping between the intermediate cases (15, 30, 60 minutes). On the other hand, no drastic changes occur between different deposition time cases for Co/MgO, instead quenching occurs progressively from the 1-minute deposition case toward almost zero intensity for the 3-hour deposition case.

Along with consistent PL quenching, increase of absorbance from the decorated materials is observed as well, again proportionally to the exposure amount (deposition time). A significant step is observed between the 1-hour and the 3-hour deposition cases, for both systems. Additionally, a strong feature located in the range 200-400 nm (UV portion of the spectrum) is common to both Ni/MgO (Fig. B.27) and Co/MgO (Fig. B.29), and is

probably associated to the spectral features of the two metals. Again, there is overlapping of the spectra for intermediate deposition times in Ni/MgO, while the increase in absorbance for Co/MgO is progressive from lowest to highest deposition time. This point will be touched upon in the following discussion.

4.2.3 Discussion on Ni/MgO and Co/MgO

After studying the Cu/MgO system with a certain degree of detail (see Section 4.1), some conclusions can be drawn on the Ni/MgO and Co/MgO systems by comparison with the Cu/MgO case study. It is clear that formation of a new structure is taking place on the MgO, indicated by the growth of crystalline phases of metallic Ni and Co. As aforementioned, this happens according to the differences in sputtering flux for the metals. In general, it has been observed that heat-treatment of the powders before deposition does not really influence the growth of an additional crystalline structure on the MgO substrates; whereas, heat-treatment after deposition is critical to make it possible to detect long-range order. Again, this strengthens the hypothesis of a reduction process taking place for the deposited species as heat-treatment temperature increases up to the highest value of 950 °C.

Similar observations to those proposed for Cu/MgO are reiterated for Ni/MgO and Co/MgO: metallic species are driven away while heat-treating the decorated materials *in vacuo*. A similar deposit as a halo inside the quartz tubes used for treatment of the decorated powders could be noticed in the cases of Ni and Co depositions, too. It was also noticed that Cu boiling point (2562 °C) is much higher than the heat-treatment temperature (950 °C); it is not different in the cases of Ni (2730 °C) and Co (2927 °C), for which a similar process is probably taking place.

The characteristic PL band peaking at 375 nm is only measured when the powders have undergone heat-treatment at 950 °C at least once, either before or after deposition. This is true in general for the deposition on MgO. As it was pointed out in the discussion for Cu/MgO, the degree of PL quenching does not change as a function of post-deposition heat-treatment. Likewise, it can be said here that quenching of the luminescence signal probably occurs because of the deposited species on the MgO surface. Considering that quenching

occurs in the same exact way (e.g. the main peak does not shift), a similar explanation can be expected as the one for the case Cu/MgO.

The presence of deposited species interfere with the original electronic structure, and this happens especially in those sites that are the most responsible for light emission. Given that the MgO was prepared and treated throughout the deposition process in the same exact manner for all cases shown in Fig. 4.7, B.26, and B.28, quenching of the original excitation (5.64 eV) is most likely to occur in the same way for Cu, Ni, and Co depositions. Relaxation of the excited electrons does not yield emission of radiation, or radiative emission may occur for a different range of excitation and emission energies (wavelengths). Furthermore, it is interesting to compare PL quenching between Ni/MgO (Fig. B.26) and Co/MgO (Fig. B.28): in the latter, PL signal appears systematically lower (i.e. more quenched) than in the former, suggesting that Co might experience better deposition efficiency, e.g. a higher sticking coefficient of Co on MgO, than Ni on MgO, while the sputtering fluxes for the two metals are very similar.

Absorbance results support PL quenching, as well as formation of new metal-based crystalline structures on the MgO surfaces. In particular, the case of longest deposition (i.e. 3 hours) is interested both by diffraction peaks from the crystalline metal (Ni or Co) and by strong light absorption in the UV range, which is typical of both metals. This is a clear sign of the presence of metal species bound to the MgO surface, probably in a similar manner as the metal species of the Cu/MgO system. Moreover, intensity of absorbance from both Ni/MgO and Co/MgO is much higher for 3-hour deposition than for 1-hour deposition in the interval 200-300 nm, with a feature peaking at about 240 nm having a ratio (3-hour):(1-hour) = 3:1 or higher. Presence of metal species on the MgO surfaces is distinct for the longest deposition case, either in the hypothesis that the deposits form agglomerates, or that they experience higher dispersity still acquiring long-range order on the surface (as it was pointed out for Cu/MgO - Section 4.1.6).

The magnetic behavior of Ni/MgO and Co/MgO materials that were prepared with 30 W beam for 3 hours (in this case, no tapping devices were used) was also investigated. Fig. B.30 in Appendix B reports the magnetic susceptibility as a function of temperature for these materials, along with the case of Cu/MgO (30 W, 3 hours) already reported in Fig. 4.10.

The magnetic moment of both Ni/MgO and Co/MgO is 2 to 3 orders of magnitude higher than the one of Cu/MgO (see logarithmic scale for the magnetic moment in Fig. B.30). This could have been expected, because both Ni and Co are magnetic in their bulk form. Then, it should be noticed that, although the overall susceptibility is higher for Ni/MgO and Co/MgO than for Cu/MgO, no appreciable features are observed in their behavior as a function of temperature, especially in the low temperature range (as it was observed for Cu/MgO, Fig. 4.10). The inset of Fig. B.30 shows this (also, Co/MgO has about 50% higher susceptibility than Ni/MgO).

In conclusion, what can be understood from these latter results is that metallic Ni and Co species have become part of the MgO substrate, and they contribute to improve the overall magnetic character of the new decorated material. These same species contribute to the structural and optical properties as well, as it has been illustrated above.

4.3 Metal deposition on ZnO

The same three metal species (Cu, Ni, and Co) were deposited on ZnO with different deposition times. ZnO is a semiconductor with a plethora of optoelectronic, anti-bacterial/fungal and gas sensing properties, as it was pointed out in Section 2.1 ([37], [1], [36]). The focus on ZnO metal deposition has not been as extensive as the one on MgO. However, it was possible to draw some useful conclusions in the comparison with the deposition on MgO. Standard powders preparation is described in Section 3.4.1: there, it is described why lower temperatures for heat-treatment were considered, i.e. 250 °C.

Deposition on ZnO was carried out mimicking what had been done with MgO: the purpose was to implement the same methodology, and then to be able to establish a comparison between substrates with different crystalline structure and optoelectronic properties. The results for the structural properties did not confirm, while similar results were obtained for the optical measurements.

The crystalline structure of ZnO is not simple cubic, and no preferential plane orientations, e.g. (100) facets, occur in ZnO NPs. This could be one of the reasons why no additional crystalline phases (peaks) appear in the diffraction patterns. In particular,

Cu/ZnO (Fig. B.31 in Appendix B) and Co/ZnO (Fig. B.33 in Appendix B) appear exactly the same as pure ZnO, except for a slightly enhanced background, which (as it was observed in Section 4.1.1) could correspond to deposited species not contributing to an ordered structure (and randomly scattering X-ray radiation). Unlike these two cases, Ni/ZnO (Fig. B.32 in Appendix B) possesses two small signatures of metallic Ni, namely Ni(111) at 44.5°, and Ni(200) at 52.5°.

An exhaustive and coherent explanation of the diffraction patterns measured on the decorated materials appears difficult. In fact, the origin of structure growth of metal species on the MO could be found in a potential match between the metal's and the MO's structures. For example, MgO has a simple cubic structure, and both metallic Cu and Ni have face-centered cubic structures. The only match in geometry between ZnO (wurtzite, hexagonal structure) and one of the three metals is with the hexagonal structure of metallic Co. Despite these potential matches between metal and MO structures, all decorated MgO materials possess phases that belong to the metals (Cu, Ni, and Co), although only Ni/ZnO shows signs of a metal structure among the decorated ZnO materials. A possible (and exhaustive) explanation for these results may not be found in a lattice match between metal and MO, with the respective structures being in register with each other. It is also true that the microscopic evidence of Cu atoms on MgO (Fig. 4.11) suggests a crystalline growth on the surface that does not involve extended lattice formation of the metal on the MO.

PL quenching can be noticed for all three materials Cu/ZnO (Fig. B.34 in Appendix B), Ni/ZnO (Fig. B.35 in Appendix B), and Co/ZnO (Fig. B.36 in Appendix B), and reduction of PL intensity appears consistent in all three, with the exceptions that, for Ni/ZnO (Fig. B.35), there seems to be overlapping in the intermediate deposition length cases, similarly to what was noticed with the same metal on MgO (Fig. B.35). The case Co/ZnO appears to show some overlapping as well (Fig. B.36). In general, the very fact of PL quenching induces to think that there must be some metal deposits on ZnO that generate a decrease in PL emission. Unlike luminescence for MgO, excitation at 325 nm corresponds to 3.82 eV, an energy that is very close to the band gap energy (3.37 eV).

Whatever is the phenomenon taking place at the ZnO NPs surface, this property is enough to prevent the faster excitation and emission processes (than the ones in MgO) from

occurring, and thus from being detectable. The PL phenomena measured on ZnO in this study align with typical luminescence properties of ZnO NPs, in particular with two main emission bands peaked in the neighborhood of 400 nm and between 400-500 nm, respectively ([17], [19]). Furthermore, within this scenario, a contribution might be played by plasmon resonances of the deposited NPs (or particle agglomerates): the metal deposits could drive energy transfers through surface plasmon modes, and this might lead to a route for exploiting a more efficient surface recombination in wide bandgap semiconductors [111].

Absorbance spectra increase in intensity as a function of the deposition time, as illustrated by Fig. B.37, B.38 and B.39 in Appendix B for Cu/ZnO, Ni/ZnO and Co/ZnO, respectively. ZnO is mostly transparent for wavelengths above 400 nm, and experiences an abrupt increase in absorbance in the region 375-400 nm [45]. The decorated ZnO materials of the present study follow the same pattern, indicating that the absorption properties of these material do not change substantially. What can be noticed is an increase of absorbance in both regions of the spectrum (i.e. below and above 400 nm), especially for the 3-hour deposition case. These results suggest a similar interpretation of the deposition as the one suggested by diffraction results, i.e. a randomly dispersed population of deposited species contributing to the background signal, also contributing to the overall absorbance of the surface.

Overall, the information provided by the PXRD, PL and absorbance characterization is clearly not enough to attempt an explanation of the changes in properties of the pure ZnO upon deposition of Cu, Ni and Co. Nevertheless, trends are similar when it comes to optical properties. There are no other results available, e.g. magnetic susceptibility, microscopy, which could help to further describe the properties of the ZnO decorated materials. The optoelectronic properties of ZnO (and of ZnO NPs) are very much dependent on structural and surface defects, and also on the particle morphology (e.g. rods, tetrapods, platelets among the others). This fact is well documented, as well as it has attracted considerable attention, especially the addition of dopants to the structure is of interest ([67], [57]). The herein proposed deposition methodology should be further applied to the synthesis and study of novel ZnO-based structures, in order to understand more deeply how metal deposits can possibly induce modification of the original optoelectronic properties.

Chapter 5

Determination of pore volumes in mesoporous materials

The script that was composed in MATLAB © and described in Section 3.5 was used to calculate adsorption and desorption quantities, as well as to perform PSD analysis, on experiments performed with different gases (methane, argon, nitrogen) on a set of adsorbents with different nature and porous properties. This Chapter includes the results and discussions concerning such experiments.

5.1 First case: silica spheres

Silica powders were investigated as the first adsorbent material in this work. These powders were obtained from Superior Silica © [91] in different sizes, namely 100 nm and 600 nm, and were prepared for adsorption studies with heat-treatment at 350 °C *in vacuo*. The specificity of such powders is their particles narrow size distribution as compared to other commercial silica spheres. These materials do not possess intrinsic porosity as some other carbon or silica-based materials, whose study will follow later in this Chapter. Although, their spherical character represents a very interesting case of gas adsorption in the interstitials between the spheres, as shown in Fig. 5.1.

According to Gregg and Sing [25], porosity in systems of spherical particles should be assessed by means of the adsorption branch of an experimental isotherm. In fact, once the

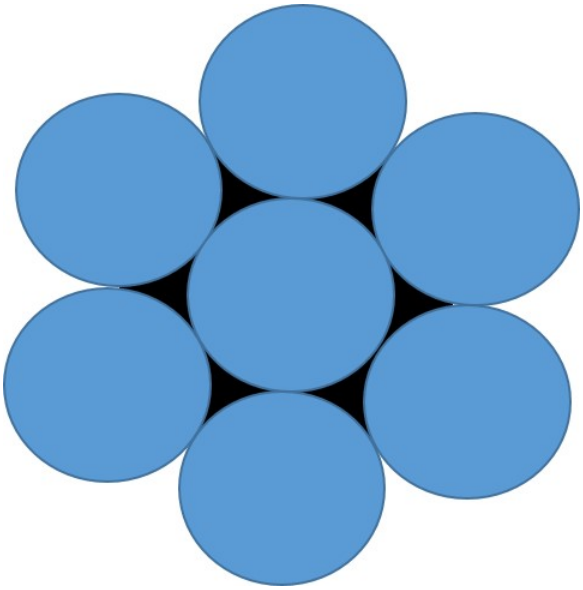

Figure 5.1: Pictorial representation of silica spheres (in blue color), where the inter-particle interstitials are colored in black for easiness of visualization.

adsorbate gas has been trapped between the particles interstitials (Fig. 5.1), the desorption process will occur as if the gas molecules had experienced capillary condensation, especially if the interstitials are narrow enough to offer a cradle for such molecules. The resulting feature in the desorption isotherm would appear as the closure of a hysteresis loop, very much like the ones associated with capillary condensation (see Fig. 2.11).

Despite the absence of intrinsic porosity in these systems of spheres, it is still of great value and interest to utilize gas sorption in order to gain an idea of how large the interstitial spaces between the spheres are. This type of systems usually gives rise to the so-called *pore network effects*, where the interconnected interstitials between particles act as if they were a network of pores, which are able to retain gas molecules, until the relative pressure has become low enough for them to empty the interstitial cavities. Therefore, this phenomenon can be studied with adsorption and desorption of a gas onto the silica spheres.

Another interesting aspect is related to the size of the spherical particles. The larger particles (600 nm) will certainly offer a smaller surface area than the one of smaller particles (100 nm), due to a decreased surface-to-volume ratio; furthermore, the larger radius of curvature of the larger particles will also result in an increased interstitials space between

them, transforming a fine pore network into a coarser one. Therefore, the effect of the interstitials acting as capillaries for guest molecules will be reduced as well, and this should be reflected in the isotherm (particularly, in the desorption branch).

The most successful and meaningful measurements on the silica spheres were achieved with CH_4, which, as aforementioned, is a nonpolar gas, usually not a preferred choice for pore size analysis (see Section 2.7). Nevertheless, radius and molecular size of CH_4 are comparable to those of Ar and N_2, becoming a suitable choice for the typical mesoporous sizes. Hence, the silica spheres were probed with CH_4 at several different temperatures to study the behavior of pore networks in different conditions.

5.1.1 Methane/Silica 100 nm size at 77 K

CH_4 sorption on silica spheres at 77 K is the best example of pore network effect. In fact, with respect to Fig. 5.2, the adsorption branch of a methane isotherm at 77 K clearly resembles surface monolayer coverage followed by an increasing curve toward saturation at $p = p_0$; whereas, the desorption branch draws a loop which closes onto the adsorption branch at $p/p_0 \approx 0.8$. Such value of relative pressure corresponds to the higher portion of the mesoporous range, i.e. in the vicinity of 20 nm, and it is the first indication of a less structured pore array than other silica-based porous materials that will be presented later on (the example is SBA-15, with pores typically smaller than 10 nm).

Figures 5.3 and 5.4 are a representation of the PSD for this adsorbed system, from which further information can be gained. Fig. 5.3 shows PSD as function of the modified Kelvin (pore) radius, Eq. 3.3, indicating a distribution of the pore volume that spans almost 10 nm, namely between 12 and 22 nm. This is the signature of a significantly less ordered pore structure as compared to intrinsically porous materials. Fig. 5.4, on the other hand, helps the determination of a peak for the distribution, due to point of highest inflection in the desorption branch of the isotherm. Such a peak is located at about 18.2 nm.

As aforementioned, the adsorption branch does not usually bear any signature of a pore network generated by the inter-particle interstitials. It is only in the desorption process that one can realize how adsorbate molecules have possibly been trapped between spheres. In particular, it is interesting to notice the relative pressure at which gas evaporation from the

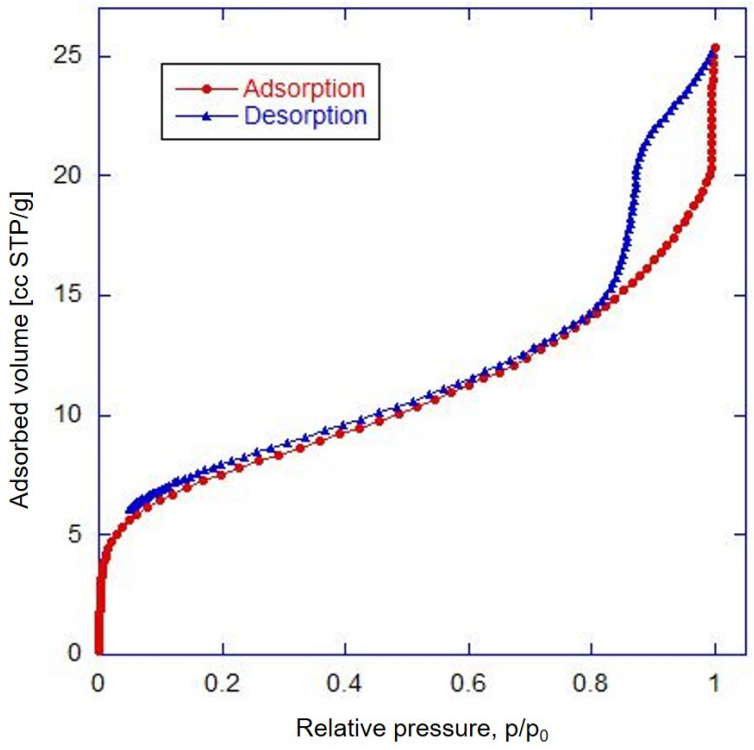

Figure 5.2: Adsorption and desorption isotherms of CH_4 on silica spheres expressed in equivalent STP volume as a function of the relative pressure.

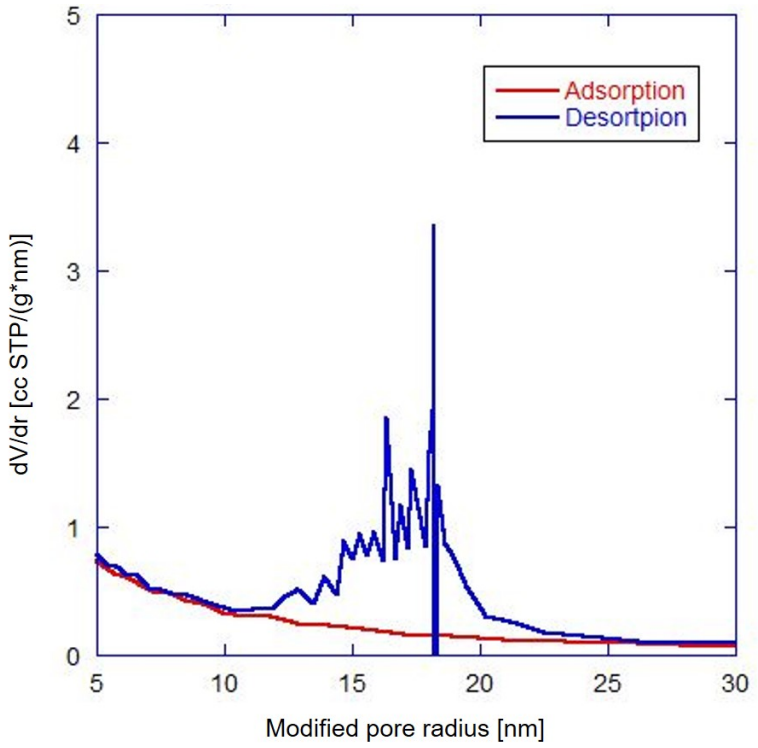

Figure 5.3: Pore size distribution for both branches of the isotherm in Fig. 5.2, expressed as a function of the modified pore radius, Eq. 3.3.

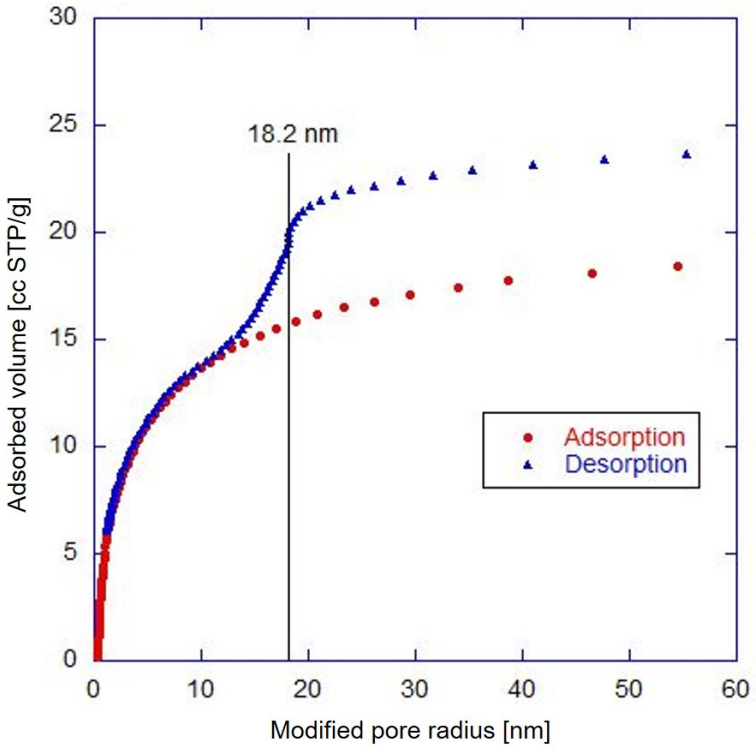

Figure 5.4: Adsorption and desorption isotherms from Fig. 5.2 expressed as a function of the modified pore radius, Eq. 3.3.

pore network occurs, $p/p_0 \approx 0.8$, is a higher fraction of p_0 than the typical relative pressure of evaporation in more ordered pore structures (typical range within 0.4-0.6). This means that CH_4 molecules can start filling the interstitials (the "pores") only when the relative pressure is significantly high, and one can recognize this phenomenon just by looking at how desorption occurs, precisely with an inflection in the curve of adsorbed volume (in the desorption branch of the isotherm) at $p/p_0 \approx 0.8$. Therefore, 0.8 is the value of relative pressure required to fill the interstitials ("pore" volume) by formation of a liquid meniscus: once p/p_0 is lowered below this critical value, evaporation and emptying of the interstitials occurs.

5.1.2 Methane/Silica 100 nm size for other temperatures

Isotherms were measured for the same system, namely CH_4 adsorbed on 100 nm size silica spheres, at several other temperatures. A compilation of the most significant results are reported in Fig. D.40 in Appendix D. The reported temperatures are 70.5 K, 72.5 K and 85 K. A few observations are useful at this point.

First of all, closure of the hysteresis loop is not complete for the temperature value above the 77 K case (i.e. 85 K), while the desorption branch completely closes onto the adsorption branch for temperatures below 77 K, namely 70.5 K and 72.5 K. It should also be observed that the total adsorbed volume significantly increases for the 85 K case. The reason why this happens might be related to molecules mobility and retention in the interstitials: 85 K is a larger fraction of the triple point temperature of CH_4, i.e. about 90 K, than 77 K or all the other lower temperature values. This means that CH_4 molecules will be more free to move at 85 K, while, at the same time, they could reach smaller cradles in the complicated pore network between the spheres. As the desorption process takes place, the molecules retained in smaller cradles will be less likely to move away from them, as compared to a scenario of less movable molecules, which instead have dwelt in larger apertures among spheres and are more prone to move away from them. Furthermore, more mobility for CH_4 molecules could also explain an increased uptake of equivalent STP volume on the adsorbent, because an equal number of molecules will take up a larger space, due to a reduced density.

Pore size distributions shown in Fig. D.41 in Appendix D confirm this interpretation: the PSD plots reflect the experimental isotherms, in particular their desorption branches. At 70.5 K and 72.5 K the PSD is very similar to the 77 K case (shown in Fig. 5.3), i.e. most of the pore volume is distributed between 12 nm and 22 nm (see Section 5.1.1). Differently from these two cases, at 85 K the distribution appears significantly shallower and shifted toward higher values for the radius. In line with the explanation above, a smaller number of molecules will be released from the interstitials, and the majority of them will actually be desorbed at a slightly higher relative pressure. These latter molecules will be likely to occupy larger apertures, where the filling pressure will be higher than the pressure required to fill most interstitials.

The temperature plays a role not only with respect to the phase of the adsorbate, but also for the adsorbent. The spheres will tend to compress against each other more as the temperature lowers, and, vice versa, to create larger interstitial apertures as the temperature rises: this could explain the change in adsorption and pore volume behavior going from 77 K to 85 K. Among the two effects of temperature on the adsorbate and the adsorbent, the strongest one is probably on the adsorbate and its phase changes with respect to its triple point.

5.1.3 Methane/Silica 600 nm size for multiple temperatures

Similar measurements have been performed on a sample of 600 nm size silica spheres, where the chosen experimental temperatures were 65 K, 70 K and 77 K. Fig. D.42 reports a compilation of the experimental isotherms, while Fig. D.43 shows the pore volume distributions obtained from these isotherms (both these figures can be found in Appendix D). The isotherms (both in adsorption and in desorption) and relative PSD can be accounted for in a similar way as the case of 100 nm size spheres. Larger spheres will create larger interstitials, and this explains less defined desorption branches (Fig. D.42) and PSDs (Fig. D.43) as well.

Considering Fig. D.42, narrower loops appear for isotherms at 65 K and 70 K: the two branches are almost indistinguishable for the 65 K case, even though this is the only case presenting some evidence of volume change in the PSD between 10 nm and 60 nm (Fig.

D.43). With respect to the 70 K case, instead, the hysteresis loop stays wider and actually results in an almost flat distribution (except for a small peak at about 50 nm). The 77 K case presents an even wider loop than at 70 K, and closure does not actually occur onto the adsorption branch. The resulting pore volume distribution is free of distinct features (see Fig. D.43).

The larger interstitial apertures play an effect on molecules retention at a lower temperature for this case (600 nm size) than it was for the previous one (100 nm size). In particular, the scenario at 77 K appears similar in the isothermal features as the one at 85 K for smaller particles. In the case of 600 nm size particles at 77 K (Fig. D.42), the non-closure of the hysteresis loop can be ascribed to retention of more mobile molecules in reduced spaces between the spheres, similarly to what was said for 100 nm size particles at lower temperature (77 K vs. 85 K). This can be associated with an enhanced width of the interstitials between spheres for 600 nm size particles.

In the comparison between the 100 nm and 600 nm size spheres, it is also worth comparing the surface areas as they were calculated by the script code from the experimental isotherms. As it should be expected, the larger particles possess a smaller overall surface area, and this is consistently measured across different temperatures as shown in Table 5.1. Within the same comparison, additional information is provided by X-ray diffraction patterns of the silica spheres (Fig. D.44 in Appendix D): a very broad peak between 15° and 30° on the *2theta* scale (and absence of other features) is indicative of an amorphous, rather than crystalline, structure for the spheres. In addition, signs of a periodic porous structure are missing in the region of small-angle scattering (below 2°), confirming the absence of intrinsic porosity.

5.2 Second case: carbon nanotubes

Carbon nanotubes (CNT) were obtained from NanoLab [60], and were prepared for adsorption studies with heat-treatment at 500 °C *in vacuo*. Carbon nanotubes are obtained by wrapping single graphite sheets and they are classified as single-walled, double-walled or multi-walled, whether single tubes (single graphene sheet wraps) are bundled together, or bundles are formed by tubes including one or multiple tubes i.e. one or multiple

Table 5.1: Summary table of amounts adsorbed at monolayer (ML) and surface areas (SA) obtained at several experimental temperature values with silica spheres samples of different size (diameter d): d = 100 nm (mass = 0.2895 g); d = 600 nm (mass = 0.3224 g).

Diameter (nm)	Temperature (K)	ML amount (mmol)	SA (m^2/g)
100	70.5	0.0617	22.7978
100	72.5	0.0681	22.6774
100	77	0.0723	24.0594
100	85	0.0707	23.5349
600	65	0.0108	3.2295
600	70	0.0121	3.6134
600	77	0.0129	3.8441

concentric graphene sheet wraps. Many are the properties and potential applications of carbon nanotubes bundles [39]. In particular, interest of the present study is to characterize their adsorption sites, and thus their associated pore volume, with different adsorbates. The chosen adsorbate gases CH_4, Ar and N_2, for the reasons illustrated in Sections 2.7 and 3.5.

The adsorption properties of carbon nanotubes have been widely studied and reported, along with explanation of what the potential adsorption sites might be ([86], [23], [94]). In particular, there are three main sites available for adsorption in bundles of carbon nanotubes: external sites, interstitial channel (IC) sites and tube sites [86]. Talapatra and Migone [94] also mention the possibility of grooves between tubes (i.e. the insert between two outer, i.e. external, sites) as adsorption sites for adsorbate molecules. A depiction of carbon nanotubes forming a bundle is reported in Fig. 5.5.

There is an interesting discussion about if and where adsorbate molecules tend to adsorb on the available sites of carbon nanotube bundles. First of all, the possibility of adsorption inside the tubes is typically common to most gases, whose atomic or molecular size does not exceed 10-12 Å [23]. Secondly, adsorption sites available around the nanotubes are not always accessible to adsorbates. In particular, if most adsorbates are likely to bind the surfaces of carbon sheets at outer (external) sites and in the grooves, there is debate on whether the IC sites are really available to any adsorbate ([95], [94]). Such a debate is focused on CH_4, Xe and Ne, as a group of atoms and molecules whose size is larger than the

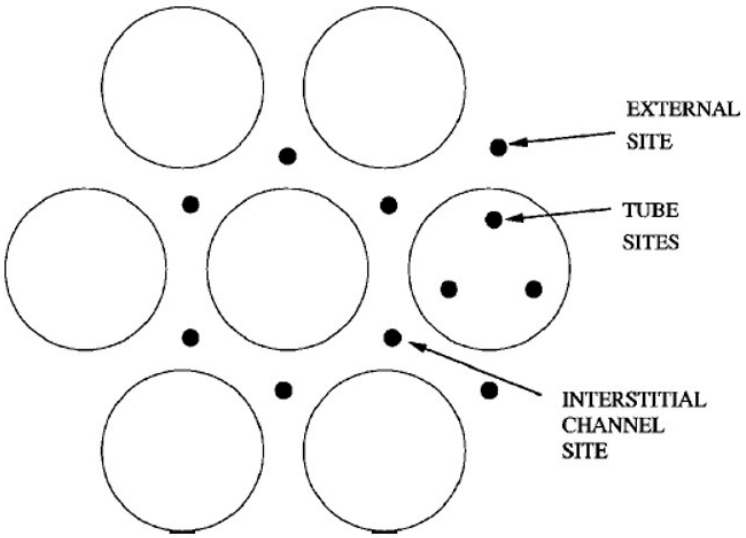

Figure 5.5: Schematic picture of adsorption sites within and outside a nanotube bundle. For the external surface, the most attractive site, located at equal distance from two nanotubes, is shown here. Adsorbed atoms or molecules are represented by dots [86].

smallest among atoms and molecules, namely H_2, He and possibly N_2. It was then suggested that larger atoms and molecules can hardly (or absolutely cannot) reach the IC sites moving through the narrow spaces between tubes.

The reason for the debate finds its reasons in the interesting and attractive structure of carbon nanotube bundles. In fact, nanotube bundles offer a large empty volume not just within the tubes, but also considering all the surface area around the tubes and between them (i.e. outer, groove and IC sites). This represents a great opportunity, for example, in gas storage applications even at room temperature, and the fact that some adsorption sites may or may not be available outside of the tubes could significantly change the overall available surface area. Therefore, studying the adsorption (and desorption) of different size adsorbates at and around their triple points can yield valuable information to a more fundamental understanding of the surface-adsorbate interaction.

Table 5.2 is an overview of some important properties of the adsorbates involved in the measurements presented in this work, namely CH_4, Ar and N_2. Emphasis is given to relevant temperature values (e.g. triple point and boiling point temperatures) and to variations in density of the adsorbed volumes. Volume of liquid adsorbate is particularly used in some PSD

Table 5.2: Relevant temperature and density values for the adsorbates of interest to this work, namely CH_4, Ar and N_2.

	CH_4	**Ar**	**N_2**
Triple point (K)	90.67	83.80	63.14
Boiling point (BP) (K)	111.65	87.35	77.35
Density of gas at STP (g/cc)	0.000761	0.001784	0.001251
Density of liquid at BP (g/cc)	0.422	1.395	0.807
Conversion factor (gas/liquid density)	0.0018	0.0013	0.0016

calculations, e.g. the BJH volume in Eq. 3.4 and 3.5, which is meant to be a more precise method for pore volume determination than simply calculating dV/dr vs. pore radius, as it takes into account pore condensation of the adsorbate and, thus, its retention as a liquid before desorption may occur. It is in fact important to point out where one should assume that the adsorbate species forms liquid layers as the adsorption process occurs.

5.2.1 Isothermal and pore volume analysis of CNT results

Adsorption and desorption isotherms on CNT (sample mass = 0.060 g) were measured with CH_4, Ar and N_2 at 77 K (Fig. D.45, D.47, and D.49 in Appendix D, respectively). The measurements reveal similar characters in the adsorption steps and, thus, in the pore volume distribution. With respect to Fig. D.46, D.48, and D.50 in Appendix D, at least two peaks can be recognized in PSD plots for all three gases below a radius value of 5-6 nm. In particular, Fig. D.50 reports the pore volume distribution for N_2, which actually seems to show three features in this same range (in the adsorption branch). The simplest explanation for this could be ascribed to the size of the N_2 molecules: the smaller size than CH_4 and Ar could make it possible for N_2 molecules to reach narrower sites (probably IC sites) than those sites larger molecules (e.g. CH_4 and Ar) can reach. For such larger molecules, the grooves between tubes in the bundles, as well as the outer (external) sites of the bundles themselves, are preferred binding sites.

Besides the peculiarity of the N_2 case, which, in fact, should be explained by its molecular size, all three isotherms have characteristic monolayer sub-steps in common ([94], [6]).

Following Talapatra and Migone's explanation [94] of monolayer (ML) adsorption sub-steps, what one can appreciate even in the adsorption isotherms in Fig. D.45, D.47, and D.49, is that the main ML step (at almost zero relative pressure) is followed by at least two sub-steps of smaller extent, one of which occurs at still relatively low pressures (0.2-0.3 p/p_0). In that explanation, the authors stressed the fact that such sub-steps represent filling of adsorption sites characterized by a reduced binding energy (outer sites), as compared to sites of greater binding energy, e.g. grooves, due to vicinity of a higher number of carbon atoms on external surfaces of nanotubes.

Therefore, it is reasonable to associate ML step and first following sub-step to filling of the grooves between tubes and formation of a second layer of molecules adjacently to the groove sites. Then, the second sub-step occurring at relative pressures 0.4-0.6 p/p_0 can be reasonably associated to layer formation on the outer sites, where a lower binding energy is compensated by a higher relative pressure. Finally, the case of IC sites has been considered above for N_2 molecules: considering the CH_4 and Ar adsorption particular to this study, if adsorption on the IC sites occurs, it is hard to appreciate the resulting feature between the ML at almost zero pressure and the first sub-step feature. Therefore, an argument of adsorption and pore volume distributions on the CNT materials based on molecular size can reasonably explain these results.

Adsorption within the tubes is not often mentioned in the literature. With respect to the present study, it appears that subsequent adsorption features could explain motion of the molecules through the nanotubes, which requires a higher relative pressure. The fact that such a phenomenon might take place will depend on the composition of the tubes as well, i.e. either single-wall or multi-wall, introducing another element of discrimination for the adsorbate based on molecular size.

If the adsorption branch of the isotherm can provide the information described above, the desorption branch should indicate where adsorbate condensation has occurred. The formation of a liquid meniscus on cylindrical-like pore apertures is the simplest case where the Kelvin equation, Eq. 3.3, can help to assess the width of such apertures. At this point, it is useful to take a closer look to the PSD plots for the three gases.

Considering the CH_4 case, Fig. D.45 shows an almost complete closure of the hysteresis loop, indicating, in the first place, release of adsorbate molecules from larger apertures, as can be appreciated in Fig. D.46 (i.e. the related PSD plot). Such a feature could be associated with accumulation of the CH_4 molecules on the outer surfaces of the nanotube bundles: a PSD peak spread between 6 and 11 nm modified pore radius can possibly indicate it, considering that typical nanotube bundle size ranges 10-15 nm in diameter [23], or larger. Furthermore, adsorption and desorption both show pore volume variation in the PSD at approximately 3 nm: this is likely the case of second layers of molecules formed on the top of groove sites. Desorption from groove sites is probably retarded, and this is shown by a clear peak in PSD for adsorption in the window 1.5-2 nm, which does not appear in the desorption case in the same position, and is likely to overlap with the ML main step feature at almost zero pressure (Fig. D.45).

In both the Ar and N_2 cases, Fig. D.47, D.48, D.49, and D.50, the desorption branch tends to close at low relative pressures, indicating adsorbate retention in possibly all adsorption sites, with a milder molecules release in the regions corresponding to gas uptake on groove and outer sites, as one can see in the PSD graphs, Fig. D.48 and D.50 for Ar and N_2, respectively. The PSD plots show at least one common feature between adsorption and desorption branches, at about 2-2.5 nm, possibly indicating facilitated molecular release from the outer sites. Molecular (for N_2) and atomic (for Ar) desorption seems not to be as spontaneous, requiring relative pressure to be lower than during adsorption in order to have molecules from groove sites moved away in the gas phase.

Despite some spikes for N_2 and some shallower peaks for Ar in the region of modified pore radii greater than 10 nm, the PSD for desorption is mostly localized below 6 nm in both cases. Fewer features in the PSD for desorption than for adsorption (happening for both adsorbates) are probably due to diffusion and binding to the IC sites for N_2, as mentioned above. The quadrupole moment of N_2 molecule certainly plays a role, favoring the binding to the surface of coordinated carbon atoms in a stronger fashion. In the Ar case, instead, there is no characteristic multipole configuration involved; nevertheless, 77 K is situated below both triple and boiling point for this adsorbate (see Table 5.2), favoring its retention over a spontaneous release as the relative pressure decreases.

In conclusion, N_2 shows the strongest binding to the nanotube substrate due to its quadrupole moment, and such effect is important even being N_2 the smallest molecule among the investigated adsorbates: admittance of molecules to the narrowest sites (IC) between nanotubes can then become confinement due to the enhanced effect with the surface. Ar is nonpolar and this explains an adsorbed volume which decreases more quickly (than N_2) with the decrease in relative pressure (see Fig. D.47). CH_4 represents the most interesting case, because it is a nonpolar molecule with comparable size to Ar, but its PSD clearly shows emptying of larger adsorption sites, followed by distinct molecular desorption in the vicinity of the most strongly binding sites (toward the grooves). This latter phenomenon is accompanied by an almost complete closure of the desorption branch, indicating full release of the adsorbate from all adsorption sites. This result is very interesting, because 77 K is situated significantly below both triple and boiling point of CH_4 (see Table 5.2). A comparison between low-pressure surface areas might also contribute to the understanding of such different behavior across the three adsorbates: adsorption with CH_4 yields a surface area of 223 m^2/g, as compared to 288 m^2/g for Ar and 281 m^2/g for N_2. Possibly, more surface area is available for the two adsorbates (Ar and N_2) which show molecular retention down to the lowest relative pressures.

5.3 Third case: SBA-15

SBA-15 (Santa Barbara Amorphous, No. 15) is one example of mesoporous silica-based materials that possess a very specific porous structure. The porous structure in SBA-15 and other similar silica-based mesoporous materials (also called *molecular sieves*) is synthesized in the laboratory (i.e. it is not a naturally occurring porosity): its pores are arranged in hexagonal arrays ([112], [113]). The choice and use of surfactants and the choice of certain reaction parameters, e.g. temperature, and conditions, determines the formation of such arrays, and the resultant pore structure appears to be very homogeneous, with a very well defined pore size. For this reason, these molecular sieves have been studied extensively in the past 20 years since they were first synthesized, in order to characterize and understand their

novel porosity, with a focus on the potential applications in fields as molecular separations and catalysis ([98], [74]).

The structure of SBA-15 materials has been determined in the past, and a structural investigation remains a good first approach to assessing their hexagonal pore arrays. In particular, X-ray diffraction and scattering at low angles (both with X-rays and with neutrons) can provide with information about the spacing between pores and their size, respectively ([42], [98]). An example of structure obtained from the SBA-15 materials used in these studies is reported in Fig. 5.6: the only peak that appears in the diffraction pattern is the one corresponding to the crystalline phase (100) [42]. The spacing d between lattice planes corresponding to this reflection at $2theta = 0.66\ ^\circ$ is equal to 133.7 Å (see Eq. 2.18), approximately 13.3 nm. Being this a reflection from planes (100), the lattice parameters a and c ($a = b$ in a hexagonal lattice) are such that $c = 0$ and $a = d$, therefore yielding $a =$ 13.3 nm. With reference to Fig. 5.7, then, a is the distance between two adjacent pores, as one of the equivalent sides of the rhombus drawn therein.

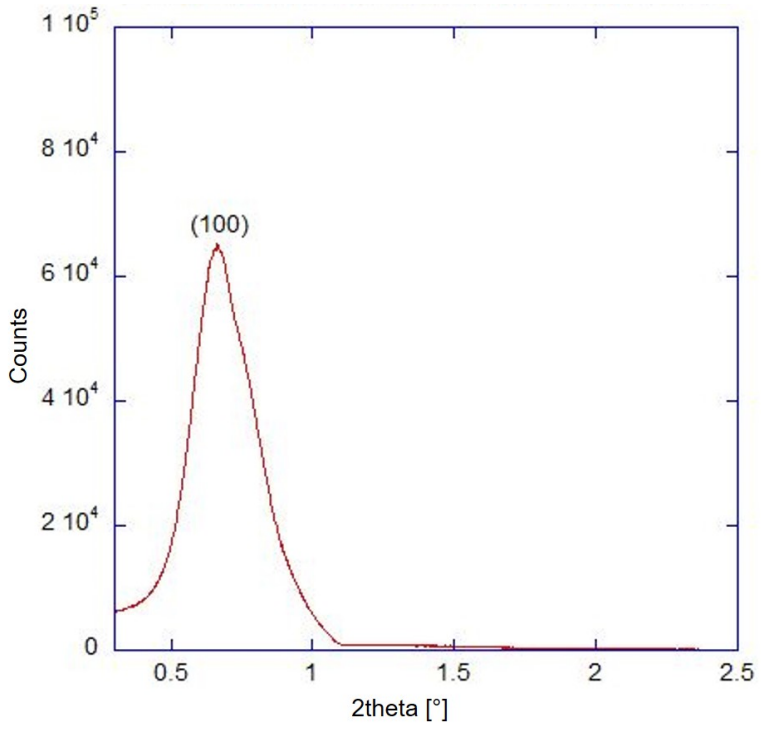

Figure 5.6: Small angle diffraction pattern of SBA-15 powders used in this study.

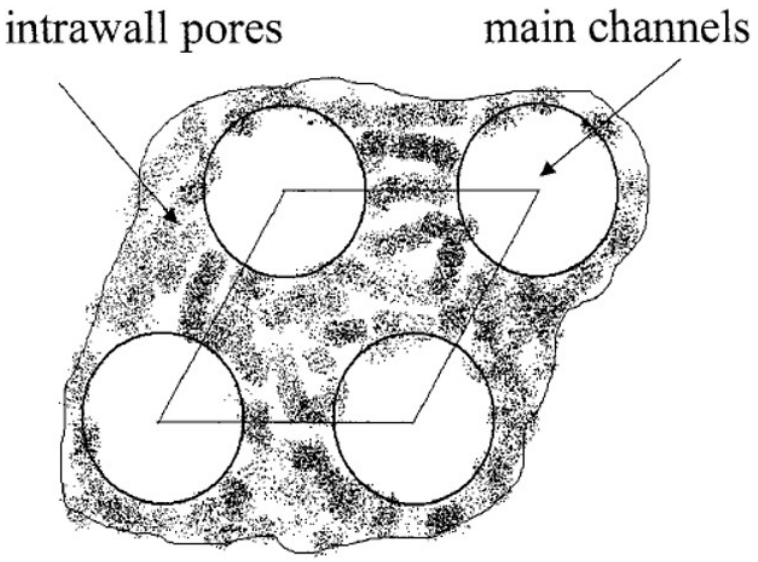

Figure 5.7: Schematic representation of SBA-15 structure [74].

The SBA-15 powders used for adsorption characterization were heat treated at 200 °C *in vacuo* for several hours. Adsorption and desorption measurements were performed with N_2, Ar and CH_4, at 77 K for the first two adsorbates, while at 93 K for the latter. The choice of the temperature for measurements with CH_4 was dictated by vicinity to its triple point. The interest in comparing adsorption and desorption of different adsorbates on silica molecular sieves is related to the different interactions each of these has with the substrate: thus, one should expect different behaviors for N_2, Ar and CH_4 in terms of relative pressures at which condensation in pores and their filling take place.

The very structured pore arrays offer one of the best opportunities to test methods for pore size distribution analysis, and in particular the Kelvin model (Eq. 3.3), due to the cylindrical shape of pores and therefore the match with liquid condensation meniscus in cylindrical apertures assumed by the same Kelvin model. The remarkable porosity of SBA-15 molecular sieves also offers one of the best examples of a neat determination of pore size distribution both from the adsorption and the desorption branch of the isotherm. Both branches show a very steep feature usually between 0.6-0.8 p/p_0, depending on the pore diameter. Another similar example of this phenomenon are MCM-41 (Mobil Composition of Matter, No. 41) molecular sieves [61].

5.3.1 Isothermal and pore volume analysis of SBA-15 results

The adsorption and desorption isotherms for the three systems are reported in Fig. D.51, D.53, and D.54 in Appendix D for the N_2/SBA-15, Ar/SBA-15 and CH_4/SBA-15 systems, respectively. Fig. D.52 in Appendix D is an example of how gas volume uptake can be estimated from the adsorption isotherm for certain points of inflection. The same sample of SBA-15 was used for these measurements (mass = 0.090 g).

First of all, it is interesting to compare volume uptakes across the three different adsorbates. In order to do this, one can mark relevant inflection steps on the adsorption isotherms as it is shown in Fig. D.52. In that plot, a horizontal line parallel to the x-axis determines the adsorbed volume at the commencement and end of pore filling, and at beginning of saturation, i.e. when p reaches p_0. As it was said before, molecular sieves as SBA-15 are great examples of very well defined porous structures, where commencement of pore filling is denoted by rising of an adsorption step in an intermediate region between low relative pressures and saturation. Fig. D.52 shows the type of analysis performed for the other isotherms as well.

The difference between the two marks at commencement and end of pore filling adsorption step can provide with a good estimate of the pore volume in the material (Fig. D.52). Such differences are: 145 cc STP/g for N_2, 175 cc STP/g for Ar, and 127 cc STP/g for CH_4, while the steps are located at relative pressures 0.71, 0.78 and 0.66 p/p_0, respectively. It is also interesting to compare these values to the total volume uptakes as determined by a mark cutting across the very top of the isotherm plots, as saturation is achieved (i.e. volume uptake starts to diverge because $p/p_0 \approx 1$, see Fig. D.52). The total adsorbed volumes are: 527 cc STP/g, 422 cc STP/g and 327 cc STP/g, for N_2, Ar and CH_4, respectively. In parallel to this, it is worth listing the surface areas for the three adsorbates: 345.92 m^2/g for N_2, 360.85 m^2/g for Ar, 290.76 m^2/g for CH_4.

The case of CH_4 shows the lowest values both for pore volume and total volume. CH_4 is a nonpolar molecule and thus no particular interaction with the silica substrate should be expected. Also, CH_4 vapor pressures at the experimental temperature of the measurements, i.e. 93 K, are significantly lower than the vapor pressures of both N_2 and Ar at 77 K. SVP

for CH_4 at 93 K is circa 110 Torr, while SVP values for N_2 and Ar at 77 K are 690 Torr and 180 Torr, respectively. Higher pressures of equilibration will imply a greater uptake of adsorbate volume for comparable relative pressures, and this can be verified just by looking at the volume uptake at which pore filling begins in the three cases: 310 cc STP/g for N_2 (Fig. D.52), 222 cc STP/g for Ar, and 165 cc STP/g for CH_4. For CH_4, therefore, the adsorbed volume is determined by a reduced molecule-substrate interaction as compared to the other two adsorbates under study.

Despite the fact that the N_2 molecule and the Ar atom have comparable sizes (3.6 Å vs. 4 Å), the effective cross-sectional area onto an adsorbent substrate may vary. As it was mentioned in Section 2.7, the quadrupole moment of molecular N_2 influences the adsorption behavior of the molecule, as compared to nonpolar atomic Ar. This is especially true in the case of an insulating substrate as silica (SiO_2): the N_2 quadrupole moment introduces a strong charge character, absent for other adsorbates. Comparing pore volumes for the two adsorbents, the value for Ar is larger (175 cc STP/g) than the one for N_2 (145 cc STP/g), although it has been noticed that pore filling for N_2 commences at 310 cc STP/g as compared to 222 cc STP/g for Ar. The adsorption isotherm for N_2 also shows a small feature at about 0.5 p/p_0, indicating that a stage of pre-filling of the pores might be taking place. The enhanced interaction of N_2 with the silica substrate is likely to cause this, hindering the diffusion process into the pores.

Another interesting term of comparison between the N_2 and Ar data is the relationship between the temperature of the measurements and the triple point (Table 5.2). This holds true for CH_4 as well. In fact, CH_4 at 93 K is above its triple point (situated just above 90 K), thus one could expect more mobility of the adsorbent: the beginning of pore filling in the CH_4 adsorption isotherm (Fig. D.54) is set at 0.66 p/p_0. Such a value is smaller than 0.71 for N_2 and 0.78 for Ar: these two adsorbates are above and below their respective triple points when measured at 77 K. This might explain a lesser mobility of Ar within the pores, needing a slightly higher relative pressure to actually diffuse into the pores. On the other hand, this effect should be counterbalanced by a reduced adsorbate-adsorbent interaction as compared to N_2.

The desorption branch of the isotherms was chosen to assess pore size distribution. More than in the previous cases under analysis (silica spheres and carbon nanotubes), SBA-15 materials represent the cylindrical pore model in the best way, and evaporation from a liquid meniscus is considered a more appropriate option for pore size determination [25]. The PSD plots seem to reflect the same trend. PSD plots from the adsorbed volume and the BJH volume (Eq. 3.4 and 3.5) as calculated by the MATLAB © script are reported in Fig. D.55, D.56, and D.57 in Appendix D for N_2, Ar and CH_4, respectively, highlighting the pore volume feature (peak) related to pore filling from the desorption branch. The mean values and standard deviations of such features as calculated by the script are (location of the peak on the scale of modified pore radius): 3.87±0.33 nm (N_2), 5.10±0.70 nm (Ar), 4.09±0.35 nm (CH_4). These results align with values of SBA-15 pore size reported in the literature, showing pore diameter values between 6 and 9 nm [65]. The smallest value was measured for N_2, and this is in accord with the strongest interaction to the substrate among the three adsorbates, and thus the strongest molecular retention to the substrate. Release of molecules in the gas phase to empty the pores occurs at higher p/p_0 for Ar, yielding higher values of pore size according to Kelvin equation (Eq. 3.3). Only, as pointed out above, 77 K is a lower temperature than Ar triple point, therefore Ar experiences less mobility than it would at a higher temperature than 87 K. The expected value for pore size in that scenario would probably be in line with the one of CH_4.

Desorption of CH_4 molecules actually occurs at lower p/p_0 than N_2, although a larger molecular diameter is attributed to CH_4 and this results in a greater effect of the statistical thickness t on the evaluation of pore radius (Eq. 3.3), which turns out to be slightly larger. While a stronger interaction of N_2 to the substrate logically supports a smaller pore radius (therefore diameter) due to evaporation from the pores at smaller p/p_0, it is also important to remember that the cross-sectional area of adsorbed CH_4 may not be consistent on different substrates, as it is instead for N_2 and Ar [25]. This is also related to the state of the adsorbate, which will be different above or below the triple point. Therefore, a consistent comparison between N_2 and Ar is usually always possible; for other molecules as in the case of alkanes (CH_4 is the simplest alkane), the cross-sectional area on different substrates

may not be equivalent, thus making it more difficult to compare adsorption results to the standard adsorbates N_2 and Ar.

A final consideration is related to the relationship between the adsorption and desorption branches of the isotherms. In all the results presented for adsorption and desorption on SBA-15, the two branches of the isotherms merge after hysteresis at very low relative pressure. Usually, one would expect a closure of the loop at the end of pore emptying. A cause for the retardation of the hysteresis loop closure may be found in the hydroxylation of the silica surfaces, effecting the interaction between substrate and molecule, and retarding full molecular release to much lower relative pressure values. This explanation would particularly well suit the case of N_2 adsorption on SBA-15, if the silica-based substrate had hydrophilic character, thus exerting attraction on the quadrupolar molecule [104].

5.4 Fourth case: dipeptides

Dipeptides are a class of biological materials that exhibit porosity inherently to their crystalline structure. These pores develop as quasi one-dimensional channels within the structure. These materials do not occur naturally, and are obtained by laboratory synthesis [24]. Their adsorption capabilities have been previously studied in this research group, in concert with an interest in the microscopic behavior of certain molecules. In particular, the adsorption properties of CH_4 were determined together with the study of the quantum rotational tunneling phenomenon of CH_4 on dipeptides substrates [68]. In that work, the most interesting system among four different types of dipeptide-based materials was reported, namely IV dipeptide. Following up on the same interest, adsorption and desorption isotherms of CH_4 on IV at 90 K were measured, in the attempt to pursue a pore size analysis of the structure.

The experimental isotherms are reported in Fig. 5.8. The pore volume is analyzed by plotting the adsorbed volume as a function of the modified pore radius, in the attempt to determine the position of points of inflection, associated with possible pore size features.

The adsorption branch of the isotherm compares to the one reported in the work by Paradiso and co-workers [68]: no noticeable features appear in this branch between very low

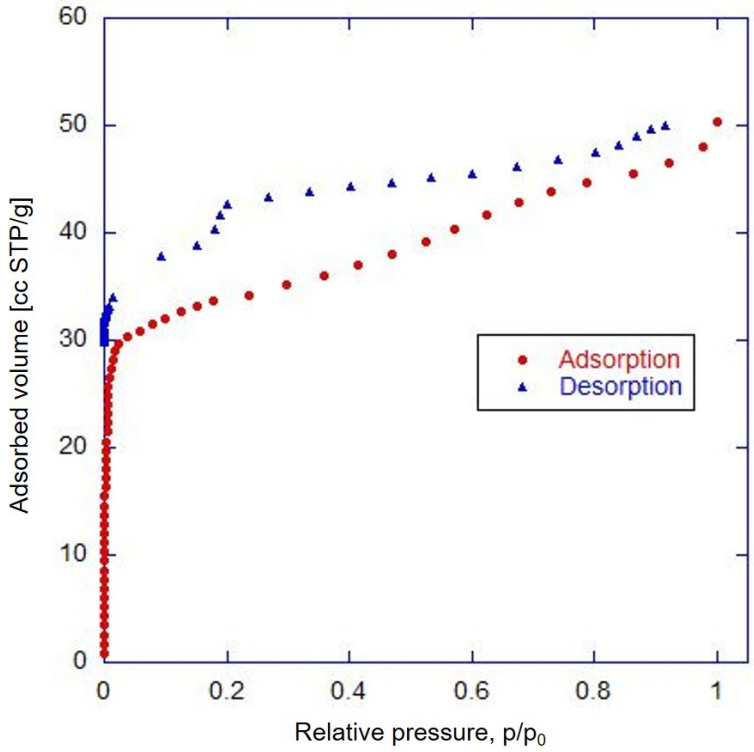

Figure 5.8: Adsorption and desorption isotherms of CH_4/IV dipeptide at 90 K. The adsorption curve has the characteristic shape which is common to the other dipeptide-based materials.

relative pressures and SVP. In contrast, the desorption branch shows a point of inflection at about 0.2 p/p_0, while another steep descend appears in proximity to the zero. This second step does not occur at zero p/p_0, rather it seems to follow a similar inflection observed in the adsorption branch, as can be seen in Fig. D.58 in Appendix D. There, marking lines indicate a first point of inflection in desorption, namely at 1.56 nm, and a second one, corresponding to the step shared by adsorption and desorption branches, located at 0.61 nm.

According to Comotti and co-workers, the pore diameter of the one-dimensional channels in IV is 3.7 Å [16]. In order to establish a comparison to the results in Fig. D.58, pore radii have to be doubled to obtain diameters. The pore diameters corresponding to the two features in Fig. D.58 are 12.2 Å (radius 0.61 nm) and 31.2 Å (radius 1.56 nm). At a first glance, none of the two values can be compared to the literature value of 3.7 Å. An explanation is proposed below.

The step corresponding to 31.2 Å is small in height in comparison with the whole volume uptake in the material. This must be related to adsorption to larger sites than the single channel aperture, where condensation of the adsorbate occurs on an area equivalent to multiple single sites, i.e. one-dimensional channel apertures. It must be remembered that the crystal structure of dipeptides is very complex, and that the channels are densely interconnected. Cradles for molecules may not just be the single channels, but macro areas may act as large hollows to host layers of molecules. The height of such a step is 5 cc STP/g, compared to a total volume uptake (on the desorption branch) of approximately 40 cc STP/g. The ratio between these two values is 1:8. This might represent the extent to which the large hollow effect occurs.

Something similar is likely to take place in the inflection point at 12.2 Å. This feature is shared by both branches of the isotherm. This probably signifies that the same process is happening reversibly at the same relative pressure, and it is likely to correspond to a similar effect as the one described above (large hollows), although on a smaller number of channels. According to the Kelvin equation (Eq. 3.3), when the hollow cradles are smaller, pore filling occurs at smaller relative pressures. In particular, the case 12.2 Å is closer to a single-channel diameter (3.9 Å) than the case 31.2 Å, therefore comparable to filling of the single pore channel. This would explain why a step is present in both branches at the same

relative pressure at 12.2 Å. The feature at 31.2 Å, instead, might have its counterpart in a mild adsorption step stretching between about 0.6-0.7 p/p_0. As discussed above, condensed molecular layers in large hollows would start to evaporate at lower pressures, namely 0.2 p/p_0.

As possible explanations of adsorption and desorption mechanisms of CH_4 on IV dipeptide are discussed, one must remember the flexible nature of the channels, whose inside structure is made up of methyl groups (CH_4). Their motion certainly influences the diffusion of CH_4 molecules through the channels (and, more in general, the motion of any other diffusing molecule), and still it has not been determined exhaustively to what extent guest molecules can move through the channels. Moreover, the aperture of the channels is defined by the hexagonal crystal structure, and the spacing between channel apertures is such that the area of these apertures only accounts for a fraction of the available surface area for physical adsorption of guest molecules (see representation of a channel aperture defined by hexagonal unit cells, Fig. 5.9). This is very likely to be reflected in the data for CH_4/IV, therefore making it difficult to discriminate the different contributions to the adsorption (and desorption) process from molecule/adsorbent interactions at different sites.

The same volumetric adsorption (and desorption) isotherms and pore analysis calculation script could be used further to analyze the adsorption of CH_4 (and possibly other adsorbates, e.g. H_2) on other dipeptides (and at different temperatures) to obtain more elements and evaluate how many points of inflection occur, and where they are located with respect to the nominal channel aperture of each dipeptide. This would definitely help to draw more complete conclusions on the sorption behavior of these biological materials.

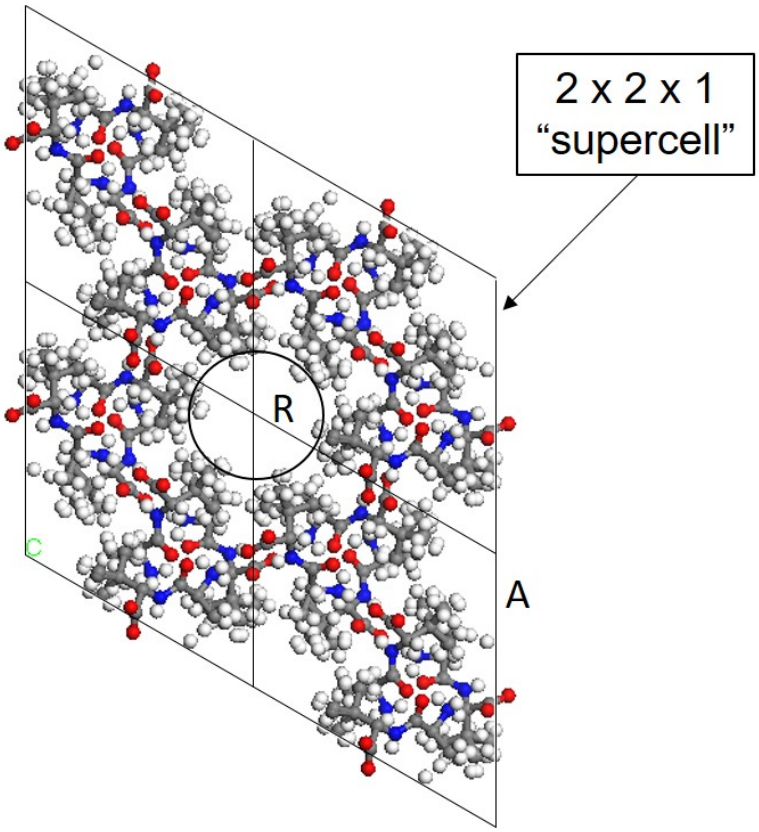

Figure 5.9: Representation of dipeptide crystal structure in the form of a 2 x 2 x 1 “supercell”, constituted by a total of 4 unit cells. R is the radius of the channel aperture, A is the lattice vector a of the hexagonal structure ($a = b$). The lattice vector c is perpendicular to A.

Chapter 6

Conclusions

In order to conclude the work presented in this dissertation, it is deemed important to highlight what are the main results obtained and how these can be interpreted as a whole.

A custom-made vacuum apparatus designed for metal decoration of MO materials has been shown as a viable instrument to decorate NPs of interest. Determination of the flux from a sputtering effusive source has revealed necessary to understand the amount of metal atoms (or clusters of atoms) that can reach the MO powders mixed in a conical vessel called tumbler. The sputtering parameters, such as the power of the source and the pressure of inert gas, and the length of deposition time (i.e. exposure of MO powders to incoming metal beam of particles), could be adjusted to a set of effective values which have rendered the metal deposition of MO materials not just possible, but also repeatable. In particular, argon pressure revealed to maximize the flux of incoming metal particles at the low value of 3 mTorr, while lower sputtering power values, i.e. 10 or 30 W as compared to 100 W or higher, have been preferred in order to more uniformly decorate the surfaces of MOs (especially in the case of MgO). The use of tapping weights around the conical vessel could improve the agitation of the inside powdered materials, especially when the MO experiences static charge build-up (e.g. MgO).

Most effort of this work has concentrated on the Cu/MgO system, which has yielded very interesting results. First, the study and characterization of Cu/MgO materials has shown that a long enough deposition time favors formation of long-range ordered structures primarily of the crystalline metal, i.e. Cu. All the major crystalline phases belonging to the

crystalline structure of fully reduced (metallic) Cu appear along with the phases of MgO in diffraction patterns. Then, optical measurements have provided clear indication of how the electronic states at the surface are modified by the presence of metal deposits. Both PL and absorbance spectroscopy have revealed the characteristics of this phenomenon, in terms of reduction of the emission signal from surface electronic states (PL) and of increase in the absorbance of UV-visible light by macroscopic layers of powders. Difficult remains to determine a proportionality relationship between the deposited amount and the variations of these spectroscopic quantities. A very interesting feature of the Cu/MgO powders is their change in color upon *in vacuo* heat-treatment after the decoration process at increasingly higher temperatures. Such a color change is associated with the occurrence of a reduction process of the metal deposited at the surface.

Very similar results were obtained on MgO powders decorated with Ni and Co. The reduced sputtering flux of these two metal species as compared to Cu (reduced by approximately a factor of 2) is reflected in reduced (to about half) counts in the diffraction peaks belonging to Ni and Co crystalline phases, as well as in a less significant reduction of the PL signal intensity and a less pronounced absorbance from the decorated powders.

A more microscopic character of the studied systems has come from magnetic and electron microscopy measurements. In particular, while the magnetic susceptibility of Ni/MgO and Co/MgO was measured to be much higher than the one of Cu/MgO materials, the Cu/MgO system possesses a peculiar behavior at low temperatures (below 50 K) that was associated with potential ferromagnetic properties of copper oxide (Cu_2O) NPs. The study of this oxide of Cu's could contribute to improve the understanding of superconductive phenomena in materials at high critical temperatures. Moreover, atomic resolution microscopy has confirmed size and disposition of the metal deposits on the surface, showing single Cu atoms deposited on the MgO(100) surfaces and on the MgO nanocubes edge steps. Especially the presence of these deposits on the 4-coordinated edge sites explains the reduction in PL intensity, which is mostly associated to such coordination energy on the MgO surface.

The metal decoration of ZnO, in addition to the one of MgO, has been explored. Metal/ZnO appears to be a different system: in particular, it is hard to appreciate the formation of a new metal structure. Generally, ZnO has different structural and

optoelectronic properties from MgO, and it is reasonable to think that different trends in the effects introduced by the metal deposits could be related to different original properties of the two MO materials.

Additional microscopic information is currently sought after in investigations carried out with X-ray photoemission spectroscopy. This further probe should be able to reveal the chemical character of the metal deposits, i.e. their oxidation state, and should (hopefully) complete an exhaustive characterization of the decorated materials, confirming the validity of the whole decoration and characterization process.

Another portion of the present work has dealt with the development and automation of pore size analysis of porous materials through the use of computer code. The interest in porous materials is originated from their potential use in energy conversion; porous structures have since long ago been considered and studied as solid catalysts in heterogeneous catalysis, and could, more in general, offer a suitable structure for an optimal deposition of metal species. Several nonporous and porous materials, different in nature, have been analyzed to show the applicability of the analysis method to any other structure (either porous or non-porous) and the type of information that one can gain from this analysis, e.g. the distribution of porous volume in terms of pore size.

The MATLAB © code could possibly be coupled with the LabView © program that operates the volumetric adsorption systems, in order to generate live-time volume distribution plots of isotherms as these are measured. Other analysis capabilities could be implemented.

Both the metal decoration and pore analysis methods for nanomaterials should be considered as viable tools to advance the understanding of new composite materials in the powdered form, where a plethora of combinations metal/MO could be attempted, in order to find appropriate systems to address today's challenges in energy storage and conversion.

Bibliography

[1] Aditya, A., Chattopadhyay, S., Jha, D., Gautam, H. K., Maiti, S., and Gnaguli, M. (2018). Zinc Oxide Nanoparticles Dispersed in Ionic Liquids Show High Antimicrobial Efficacy to Skin-Specific Bacteria. *ACS Applied Materials and Interfaces*, 10(18):15401–15411.

[2] Albers, P., Seibold, K., McEvoy, A. J., and Kiwi, J. (1989). High-Dispersion Direct Current Sputtered Platinum-TiO_2 Powder Catalyst Active in Ethane Hydrogenolysis. *The Journal of Physical Chemistry*, 93(4):1510–1515.

[3] Alstrup, I. and Møller, P. J. (1988). X-ray photoelectron spectroscopy study of the vapor deposition of copper onto a MgO(100) surfaces. *Applied Surface Science*, 33/34:143–151.

[4] Barrett, E. P., Joyner, L. G., and Halenda, P. P. (1951). The Determination of Pore Volume and Area Distributions in Porous Substances. I. Computations from Nitrogen Isotherms. *Journal of the American Chemical Society*, 73:373–380.

[5] Behrisch, R. and Eckstein, W., editors (2007). *Sputtering by Particle Bombardment*, volume 110 of *Topics in Applied Physics*. Springer.

[6] Bienfait, M., Zeppenfeld, P., Dupont-Pavlovsky, N., Muris, M., Johnson, M. R., Wilson, T., DePies, M., and Vilches, O. E. (2004). Thermodynamics and structure of hydrogen, methane, argon, oxygen, and carbon dioxide adsorbed on single-wall carbon nanotube bundles. *Physical Review B*, 70:035410.

[7] Bruix, A., Rodriguez, J. A., Ramírez, P. J., Senanayake, S. D., Evans, J., Park, J. B., Stacchiola, D., Liu, P., Hrbek, J., and Illas, F. (2012). A New Type of Strong Metal-Support Interaction and the Production of H_2 through the Transformation of Water on $Pt/CeO_2(111)$ and $Pt/CeO_x/TiO_2(110)$ Catalysts. *Journal of the American Chemical Society*, 134:8968–8974.

[8] Budde, W. (1976). Calibration of Reflectance Standards. *Journal of Research of the National Bureau of Standards - A. Physics and Chemistry*, 80A(4):585–595.

[9] Cairns, J. A., Nelson, R. S., and Barnfield, R. W. (1979). Improvements in or relating to catalysts comprising a particulate substrate with a sputtered deposit of catalytic material. *UK Patent No. 1,537,839*.

[10] Cazottes, S., Zhang, Z. L., Daniel, R., Chawla, J. S., Gall, D., and Dehm, G. (2010). Structural characterization of a Cu/MgO(001) interface using C_S-corrected HRTEM. *Thin Solid Films*, 519:1662–1667.

[11] Chandra, R., Taneja, P., and Ayyub, P. (1999). Optical properties of transparent nanocrystalline Cu_2O thin films synthesized by high pressure gas sputtering. *NanoStructured Materials*, 11(4):505–512.

[12] Chizallet, C., Costentin, G., Lauron-Pernot, H., Krafft, J.-M., Che, M., Delbecq, F., and Sautet, P. (2008a). Assignment of Photoluminescence Spectra of MgO Powders: TD-DFT Cluster Calculations Combined to Experiments. Part I: Hydroxylation Effects. *Journal of Physical Chemistry C*, 112:19710–19717.

[13] Chizallet, C., Costentin, G., Lauron-Pernot, H., Krafft, J.-M., Che, M., Delbecq, F., and Sautet, P. (2008b). Assignment of Photoluminescence Spectra of MgO Powders: TD-DFT Cluster Calculations Combined to Experiments. Part I: Structure Effects on Dehydroxylated Surfaces. *Journal of Physical Chemistry C*, 112:16629–16637.

[14] Cohan, L. H. (1938). Sorption Hysteresis and the Vapor Pressure of Concave Surfaces. *Journal of the American Chemical Society*, 60:433–435.

[15] Coluccia, S., Tench, A. J., and Segall, R. L. (1979). Surface Structure and Surface States in Magnesium Oxide Powders. *Journal of the Chemical Society, Faraday Transactions 1*, 75:1769–1779.

[16] Comotti, A., Bracco, S., Distefano, G., and Sozzani, P. (2009). Methane, carbon dioxide and hydrogen storage in nanoporous dipeptide-based materials. *Chemical Communications*, pages 284–286.

[17] Dai, Y., Zhang, Y., Li, Q. K., and Nan, C. W. (2002). Synthesis and optical properties of tetrapod-like zinc oxide nanorods. *Chemical Physics Letters*, 358:83–86.

[18] Di Bartolo, B., Collins, J., and Silvestri, L., editors (2013). *Nano-Structures for Optics and Photonics*, volume B: Physics and Biophysics of *NATO Science for Peace and Security Series*. Springer.

[19] Djurišić, A. B. and Leung, Y. H. (2006). Optical Properties of ZnO Nanostructures. *Small*, 2(8-9):944–961.

[20] Ensiger, W. and Múller, H. R. (1994). The rotating wing drum: An apparatus for ion beam treatment of powders. *Review of Scientific Instruments*, 65(9):2963–2967.

[21] Fujitani, T., Saito, M., Kanai, Y., Watanabe, T., Nakamura, J., and Uchijima, T. (1994). Effect of Support on Methanol Synthesis over Cu Catalyst. *Chemistry Letters*, 23(10):1877–1880.

[22] Fuks, S., Legros, J.-C., and Bellemans, A. (1965). The molar volumes of liquid methane and deuteromethane. *Physica*, 31:606–612.

[23] Gatica, S. M., Bojan, M. J., Stan, G., and Cole, M. W. (2001). Quasi-one- and two-dimensional transitions of gases adsorbed on nanotube bundles. *Journal of Chemical Physics*, 114(8):3765–3769.

[24] Görbitz, C. H. (2003). Nanotubes from hydrofobic dipeptides: pore size regulation through side chain substitution. *New Journal of Chemistry*, 27:1789–1793.

[25] Gregg, S. J. and Sing, K. S. W. (1982). *Adsorption, Surface Area and Porosity*. Academic Press.

[26] Haruta, M. (1997). Novel catalysis of gold deposited on metal oxides. *Catalysis Surveys of Japan*, 1:61–73.

[27] He, J.-W. and Møller, P. J. (1986a). Epitaxial and electronic structures of ultra-thin copper films on MgO crystal surfaces. *Surface Science*, 178:934–942.

[28] He, J.-W. and Møller, P. J. (1986b). On the defect center electron energy loss structures from MgO surfaces. *Chemical Physics Letters*, 129(1):13–16.

[29] He, J.-W. and Møller, P. J. (1987). The initial stages of deposition of Cu on ZnO($10\bar{1}0$) and MgO(001) surfaces studied by electron energy loss spectroscopy. *Surface Science*, 180:411–420.

[30] Henrich, V. E. and Cox, P. A. (1994). *The Surface Science of Metal Oxides*. Cambridge University Press.

[31] Hofmann, H., Rahmann, Z., and Schubert, U., editors (2002). *Nanostructured Materials*. Springer-Verlag Wien.

[32] Hosokawa, M., Nogi, K., Naito, M., and Yokoyama, T., editors (2007). *Nanoparticle Technology Handbook*. Elsevier.

[33] Hulstrøm, J. D. (2014). Production and Deposition of Copper Clusters Using Magnetron Sputtering. Master's thesis, Aalborg University.

[34] Itoh, T. and Maki, K. (2007a). Growth process of CuO(111) and Cu_2O(001) thin films on MgO(001) substrate under metal-mode condition by reactive dc-magnetron sputtering. *Vacuum*, 81:1068–1076.

[35] Itoh, T. and Maki, K. (2007b). Preferentially oriented thin-film growth of CuO(111) and Cu_2O(001) on MgO(001) substrate by reactive dc-magnetron sputtering. *Vacuum*, 81:904–910.

[36] Jacobs, C. B., Maksov, A. B., Muckley, E. S., Collins, L., Mahjouri-Samani, M., Ievlev, A., Rouleau, C. M., Moon, J.-W., Graham, D. E., Sumpter, B. G., and Ivanov, I. N. (2017). UV-activated ZnO films on a flexible substrate for room temperature O_2 and H_2O sensing. *Scientific Reports*, 7:6053.

[37] Janotti, A. (2009). Fundamentals of zinc oxide as a semiconductor. *Reports on Progress in Physics*, 72:126501.

[38] Jasper, J. J. (1972). The Surface Tension of Pure Liquid Compounds. *Journal of Physical and Chemical Reference Data*, 1(4):841–1009.

[39] Jorio, A., Dresselhaus, M. S., and Dresselhaus, G., editors (2008). *Carbon Nanotubes*, volume 111 of *Topics in Applied Physics*. Springer.

[40] Kappers, L. A., Kroes, R. L., and Hensley, E. B. (1970). F^+ and F' Centers in Magnesium Oxide. *Physical Review B*, 1(10):4151–4157.

[41] Kortüm, G. (1969). *Reflectance Spectroscopy*. Springer-Verlag.

[42] Kruk, M. and Jaroniec, M. (2000). Characterization of the Porous Structure of SBA-15. *Chemistry of Materials*, 12:1961–1968.

[43] Kubelka, P. and Munk, F. (1931). An Article on Optics of Paint Layers. *Translated from the original version in German.*

[44] Kudriavtsev, Y., Villegas, A., Godines, A., and Asomoza, R. (2005). Calculation on the surface binding energy for ion sputtered particles. *Applied Surface Science*, 239:273–278.

[45] Kumar, S. S., Venkateswarlu, P., Rao, V. R., and Rao, G. N. (2013). Synthesis, characterization and optical properties of zinc oxide nanoparticles. *International Nano Letters*, 3:30.

[46] Kunnmann, W. and Larese, J. Z. (2001). Method for the generation of variable density metal vapors which bypasses the liquidus phase. *US Patent No. 6,179,897 B1.*

[47] Lakowicz, J. R. (2006). *Principles of Fluorescence Spectroscopy*. Springer.

[48] Landry, P. (2011). *Adsorption of Hydrogen onto Bare and Metal Decorated Metal Oxides*. PhD thesis, University of Tennessee.

[49] Larese, J. Z. (1998). Neutron scattering studies of the structure and dynamics of methane adsorbed on MgO(100) surfaces. *Physica B*, 248:297–303.

[50] Lecher, M. D., editor (2015). *Landolt-Börnstein IV/24*. Group IV Physical Chemistry. Springer.

[51] Lee, S., Kim, J. Y., Lee, T.-W., Kim, W.-K., Kim, B.-S., Park, J. H., Bae, J.-S., Cho, Y. C., Kim, J., Oh, M.-W., Hwang, C.-S., and Jeong, S.-W. (2014). Fabrication of high-quality sing;e-crystal Cu thin films using radio-frequency sputtering. *Scientific Reports*, 4:6230.

[52] Lide, D. R., editor (1997). *CRC Handbook of Chemistry and Physics, 77th Edition*. CRC Press.

[53] Lippens, B. C., Linsen, B. G., and De Boer, J. H. (1964). Studies on Pore Systems in Catalysts I. The Adsorption of Nitrogen; Apparatus and Calculation. *Journal of Catalysis*, 3:32–37.

[54] Lu, C. and Czanderna, A. W., editors (1984). *Applications of piezoelectric quartz crystal microbalances*, volume 7 of *Methods and Phenomena: Their Applications in Science and Technology*. Elsevier.

[55] Markworth, P. R., Liu, X., Dai, J. Y., Fan, W., Marks, T. J., and Chang, R. P. H. (2001). Coherent island formation of Cu_2O films grown by chemical vapor deposition on MgO(110). *Journal of Materials Research*, 16(8):2408–2414.

[56] Miller, D. J., Hettinger, J. D., Chiarello, R. P., and Kim, H. K. (1992). Epitaxial growth of Cu_2O films on MgO by sputtering. *Journal of Materials Research*, 7(10):2828–2832.

[57] Moezzi, A., McDonagh, A. M., and Cortie, M. B. (2012). Zinc oxide particles: Synthesis, properties and applications. *Chemical Engineering Journal*, 185-186:1–22.

[58] Müller, H. R., Ensiger, W., Frech, G., and Wolf, G. K. (1994). A new approach to ion beam modification of powders. *Nuclear Instruments and Methods in Physics Research B*, 89:357–361.

[59] Mursic, Z., Lee, M. Y. M., Johnson, D. E., and Larese, J. Z. (1996). A computer-controlled apparatus for performing high-resolution adsorption isotherms. *Review of Scientific Instruments*, 67:1886–1890.

[60] NanoLab, Inc. (2018). NanoLab website. https://www.nano-lab.com/.

[61] Neimark, A. V., Ravikovitch, P. I., Grün, M., and Schüth, F. (1998). Pore size Analysis of MCM-41 Type Adsorbents by Means of Nitrogen and Argon Adsorption. *Journal of Colloid and Interface Science*, 207:159–169.

[62] Novaetech Srl (2018). OpenQCM. https://openqcm.com/.

[63] Öchsner, A., da Silva, L. F. M., and Altenbach, H., editors (2013). *New Frontiers of Nanoparticles and Nanocomposite Materials*, volume 4 of *Advanced Structured Materials*. Springer.

[64] Ogawa, K., Itoh, T., and Maki, K. (2000). Charge transfer from Cu in Cu_2O epitaxially grown on MgO(001) by dc-reactive magnetron sputtering. *Physical Review B*, 62(7):4269–4272.

[65] Ojeda, M. L., Esparza, J. M., Campero, A., Cordero, S., Kornhauser, I., and Rojas, F. (2003). On comparing BJH and NLDFT pore-size distributions determined from N_2 sorption on SBA-15 substrata. *Physical Chemistry Chemical Physics*, 5:1859–1866.

[66] Ottosson, M., Lu, J., and Carlsson, J.-O. (1995). Chemical vapour deposition of Cu_2O on MgO(100) from CuI and N_2O: aspects of epitaxy. *Journal of Crystal Growth*, 151:305–311.

[67] Özgür, Ü., Alivov, Y., Liu, C., Teke, A., Reshchikov, M. A., Doğan, S., Avrutin, V., Cho, S.-J., and Morkoç, H. (2005). A comprehensive review of ZnO materials and devices. *Journal of Applied Physics*, 98:041301.

[68] Paradiso, D., Perelli Cippo, E., Gorini, G., Rossi, G., and Larese, J. Z. (2015). Characterization of Dipeptide-based Sorbent Materials using Combined Thermodynamic and Inelastic Neutron Scattering Techniques. *MRS Proceedings*, 1793:47–52.

[69] Pennycook, S. J. (1992). Z-Contrast Transmission Electron Microscopy: Direct Imaging of Materials. *Annual Reviews of Materials Science*, 22:171–195.

[70] Pestryakov, A. N., Petranovskii, V. P., Kryazhov, A., Ozhereliev, O., Pfänder, N., and Knop-Gericke, A. (2004). Study of copper nanoparticles formation on supports of different nature by UV-Vis diffuse reflectance spectroscopy. *Chemical Physics Letters*, 385:173–176.

[71] Purswani, J. M., Spila, T., and Gall, D. (2006). Growth of epitaxial Cu on MgO(001) by magnetron sputter deposition. *Thin Solid Films*, 515:1166–1170.

[72] Qiu, H., Hashimoto, M., Barna, A., and Barna, P. B. (1996). Structural and electrical properties of Ni-Cu films deposited onto MgO(001) by d.c. biased sputter deposition. *Thin Solid Films*, 288:171–175.

[73] Qiu, H., Kosuge, A., Maruyama, H., Adamik, M., Safran, G., Barna, P. B., and Hashimoto, M. (1994). Epitaxial growth, structure and properties of Ni films grown on MgO(100) by d.c. bias sputter deposition. *Thin Solid Films*, 241:9–11.

[74] Ravikovitch, P. I. and Neimark, A. V. (2001). Characterization of Micro- and Mesoporosity in SBA-15 Materials from Adsorption Data by the NLDFT Method. *Journal of Physical Chemistry B*, 105:6817–6823.

[75] Rodriguez, J. A., Liu, P., Pérez, M., Liu, G., and Hrbek, J. (2010). Destruction of SO_2 on Au and Cu nanoparticles Dispersed on MgO(100) and CeO_2(111). *Journal of Physical Chemistry A*, 114:3802–3810.

[76] Rodriguez, J. A., Liu, P., Wang, X., Wen, W., Hanson, J., Hrbek, J., Pérez, M., , and Evans, J. (2009). Water-gas shift activity of Cu surfaces and Cu nanoparticles supported on metal oxides. *Catalysis Today*, 143:45–50.

[77] Ross, M., Beach, D., and Larese, J. Z. (2005). Synthesis and characterization of MgO and ZnO particles. In *2005 APS March Meeting*. American Physical Society. Conference Abstract.

[78] Sabbe, P.-J., Dowsett, M. G., De Keersmaecker, M., Hand, M., Thompson, P., and Adriaens, A. (2015). Synthesis and surface characterization of patterned cuprite sample: Preparatory step in the evaluation scheme of an x-ray-excited optical microscopy system. *Applied Surface Science*, 332:657–664.

[79] Sellschop, J. P. F., Prins, J. F., Wimmersperg, U. v., Tredoux, M., and Rebak, M. (1983). Ion beam analysis of powdered samples. *Nuclear Instruments and Methods in Physics Research*, 218:593–597.

[80] Shi, R., Wang, F., Mu, X., Li, Y., Huang, X., and Shen, W. (2009). MgO-supported Cu nanoparticles for efficient transfer dehydrogenation of primary aluphatic alcohols. *Catalysis Communications*, 11:306–309.

[81] Shi, R., Wang, F., Mu, X., Ta, N., Li, Y., Huang, X., and Shen, W. (2010). Transfer Dehydrogenation of 1-Octanol to 1-Octanal over Cu/MgO catalysts: Effect of Cu Particle Size. *Chinese Journal of Catalysis*, 31(6):626–630.

[82] Shluger, A. L., Sushko, P. V., and Kantorovich, L. N. (1999). Spectroscopy of low-coordinated surface sites: Theoretical study of MgO. *Physical Review B*, 59(3):2417–2430.

[83] Shull, C. G. (1948). The Determination of Pore Size Distribution from Gas Adsorption Data. *Journal of American Chemical Society*, 70:1405–1410.

[84] Sigmund, P. (1969). Theory of Sputtering. I. Sputtering Yield of Amorphous and Polycrystalline Targets. *Physical Review*, 184(2):383–416.

[85] Sigmund, P. (1981). *Sputtering by Particle Bombardment I. Physical Sputtering of Single-Element: Solids (Behrisch, R. editor)*, volume 47 of *Topics in Applied Physics*. Springer-Berlin-Heidelberg.

[86] Stan, G., Bojan, M. J., Curtarolo, S., Gatica, S. M., and Cole, M. W. (2000). Uptake of gases in bundles of carbon nanotubes. *Physical Review B*, 62(3):2173–2180.

[87] Stankic, S., Müller, M., Diwald, O., Sterrer, M., Knözinger, E., and Bernardi, J. (2005). Size-Dependent Optical Properties of MgO Nanocubes. *Angewandte Chemie International Edition*, 44:4917–4920.

[88] Stockbridge, C. D. and Warner, A. W. (1962). *Vacuum Microbalance Techniques (Walker, R. F. editor)*, volume 2. Plenum, NY.

[89] Stoffregen, P. (2018). Teensy USB Development Board. https://www.pjrc.com/teensy/.

[90] Su, J., Liu, Y., Jiang, M., and Zhu, X. (2016). Oxidation of copper during physical sputtering deposition: mechanism, avoidance and utilization. *Science China Materials*, 59:144–150.

[91] Superior Silica LLC (2018). Superior Silica: Our Technology. http://superiorsilica.com/our-technology/.

[92] Sushko, P. V. and Shluger, A. L. (1999). Electronic structure of excited states at low-coordinated surface sites of MgO. *Surface Science*, 421:L157–L165.

[93] Takeuchi, A. and Wise, H. (1983). High Dispersion Platinum Catalyst by RF Sputtering. *Journal of Catalysis*, 83:477–479.

[94] Talapatra, S. and Migone, A. D. (2002). Adsorption of methane on bundles of closed-ended single-wall carbon nanotubes. *Physical Review B*, 65:045416.

[95] Talapatra, S., Zambano, A. Z., Weber, S. E., and Migone, A. D. (2000). Gases Do Not Adsorb on the Interstitial Channels of Closed-Ended Single-Walled Carbon Nanotube Bundles. *Physical Review Letters*, 85(1):138 – 141.

[96] Tandon, S. P. and Gupta, J. P. (1970). Diffuse Reflectance Spectrum of Cuprous Oxide. *Physica Status Solidi*, 37:43–45.

[97] Thommes, M. (2010). Physical Adsorption Characterization of Nanoporous Materials. *Chemie Ingenieur Technik*, 82(7):1059–1073.

[98] Thommes, M., Smarsly, B., Groenewolt, M., Ravikovitch, P. I., and Neimark, A. V. (2006). Adsorption Hysteresis of Nitrogen and Argon in Pore Networks and Characterization of Novel Micro- and Mesoporous Silicas. *Langmuir*, 22:756–764.

[99] Thompson, M. W. (1968). The energy spectrum of ejected atoms during the high energy sputtering of gold. *The Philosophical Magazine: A Journal of Theoretical Experimental and Applied Physics*, 18(152):377–414.

[100] Tsionsky, V. and Gileadi, E. (1994). Use of the Quartz Crystal Microbalance for the Study of Adsorption from the Gas Phase. *Langmuir*, 10:2830–2835.

[101] Veith, G. M., Lupini, A. R., Pennycook, S. J., Ownby, G. W., and Dudney, N. J. (2005). Nanoparticles of gold on γ-Al_2O_3 produced by dc magnetron sputtering. *Journal of Catalysis*, 231:151–158.

[102] Veith, G. M., Lupini, A. R., Pennycook, S. J., Villa, A., Prati, L., and Dudney, N. J. (2007). Magnetron sputtering of gold nanoparticles onto WO_3 and activated carbon. *Catalysis Today*, 122:248–253.

[103] Veith, G. M., Lupini, A. R., Rashkeev, S., Pennycook, S. J., Mullins, D. R., Schwartz, V., Bridges, C. A., and Dudney, N. J. (2009). Thermal stability and catalytic activity of gold nanoparticles supported on silica. *Journal of Catalysis*, 262:92–101.

[104] Vigil, G., Xu, Z., Steinberg, S., and Israelachvili, J. (1994). Interactions of Silica Surfaces. *Journal of Colloid and Interface Science*, 165:367–385.

[105] Warner, A. W. and Stockbridge, C. D. (1963). *Vacuum Microbalance Techniques (Behrndt, K. H. editor)*, volume 3. Plenum, NY.

[106] Warren, B. E. (1990). *X-Ray Diffraction*. Dover Publications.

[107] Wimmersperg, U. v., Prins, J. F., and Derry, T. E. (1982). Rotating powder target for ion implantation. *Nuclear Instruments and Methods*, 197:597–598.

[108] Wu, M.-C., Oh, W. S., and Goodman, D. W. (1995). Initial sticking probabilities of cu vacuum deposited on ordered Al_2O_3 and MgO. *Surface Science*, 330:61–66.

[109] Wu, S. Y., Ji, J.-Y., and Shih, P. H. (2008). Surface Magnetic Anisotropic Energy Gap in Cu_2O Nanoparticles. *Japanese Journal of Applied Physics*, 47:706–711.

[110] Yin, Z. G., Zhang, H. T., Goodner, D. M., Bedzyk, M. J., CHang, R. P. H., Sun, Y., and Ketterson, J. B. (2005). Two-dimensional growth of continuous Cu_2O thin films by magnetron sputtering. *Applied Physics Letters*, 86:061901.

[111] Zhao, B., Jiang, M.-M., Zhao, D.-X., Li, Y., Wang, F., and Shen, D.-Z. (2015). Electrically driven plasmon mediated energy transfer between ZnO microwires and Au nanoparticles. *Nanoscale*, 7:1081–1089.

[112] Zhao, D., Feng, J., Huo, Q., Melosh, N., Fredrickson, G. H., Chmelka, B. F., and Stucky, G. D. (1998a). Triblock Copolymer Syntheses of Mesoporous Silica with Periodic 50 to 300 Angstrom Pores. *Science*, 279:548–552.

[113] Zhao, D., Huo, Q., Feng, J., Chmelka, B. F., and Stucky, G. (1998b). Nonionic Triblock and Star Diblock Copolymer and Oligomeric Surfactant Syntheses of Highly Ordered, Hydrothermally Stable, Mesoporous Silica Structures. *Journal of the American Chemical Society*, 120:6024–6036.

Appendices

A Supplemental information on the experimental apparatus and sputtering beam characterization

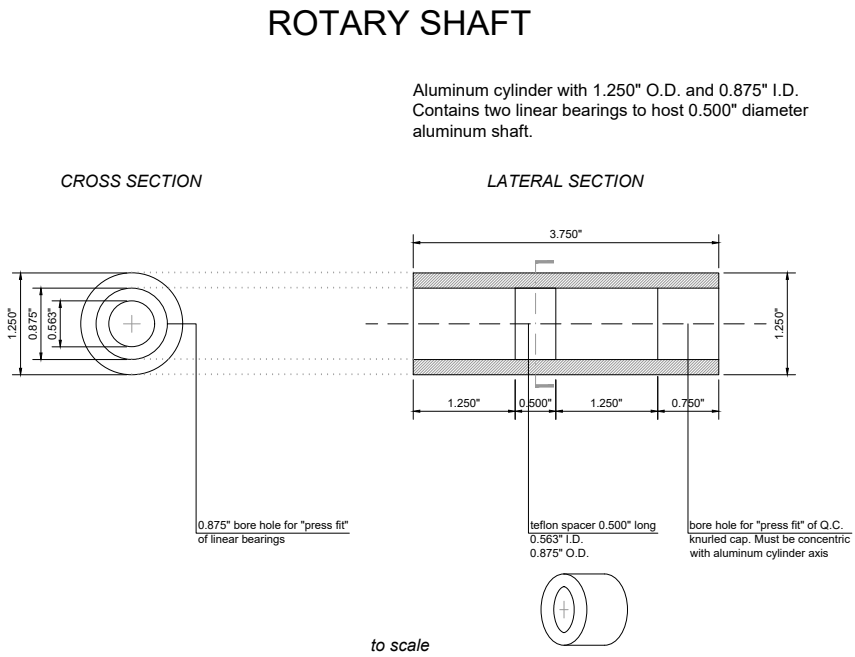

Figure A.1: Schematic drawing of the rotary shaft assembly to house the aluminum shaft that connects dc-motor for spinning of the SS tumbler.

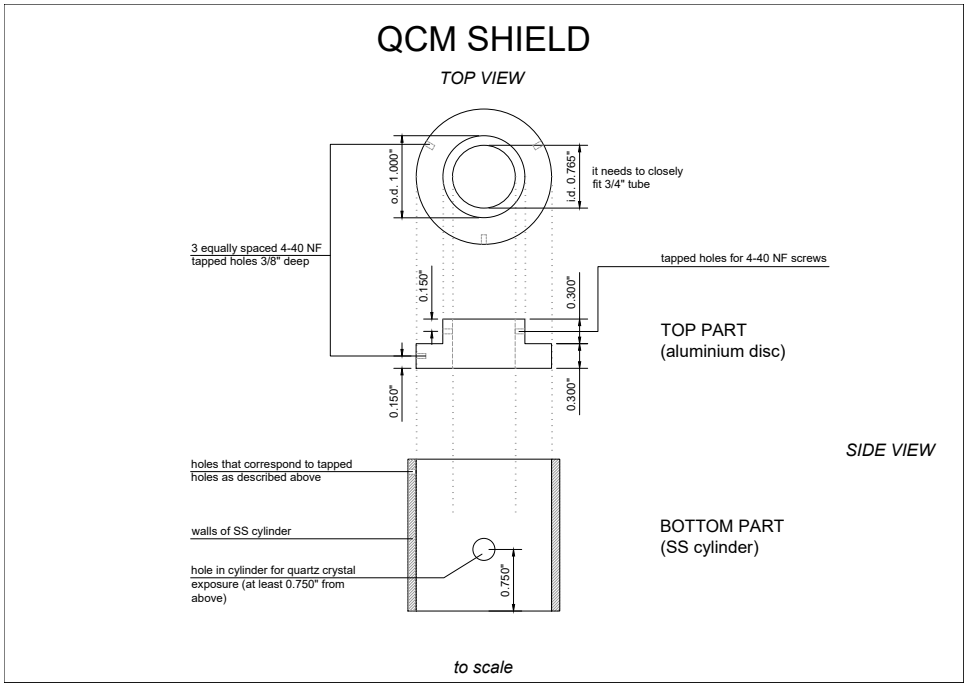

Figure A.2: Schematic representation of the QCM shield in its two separate parts.

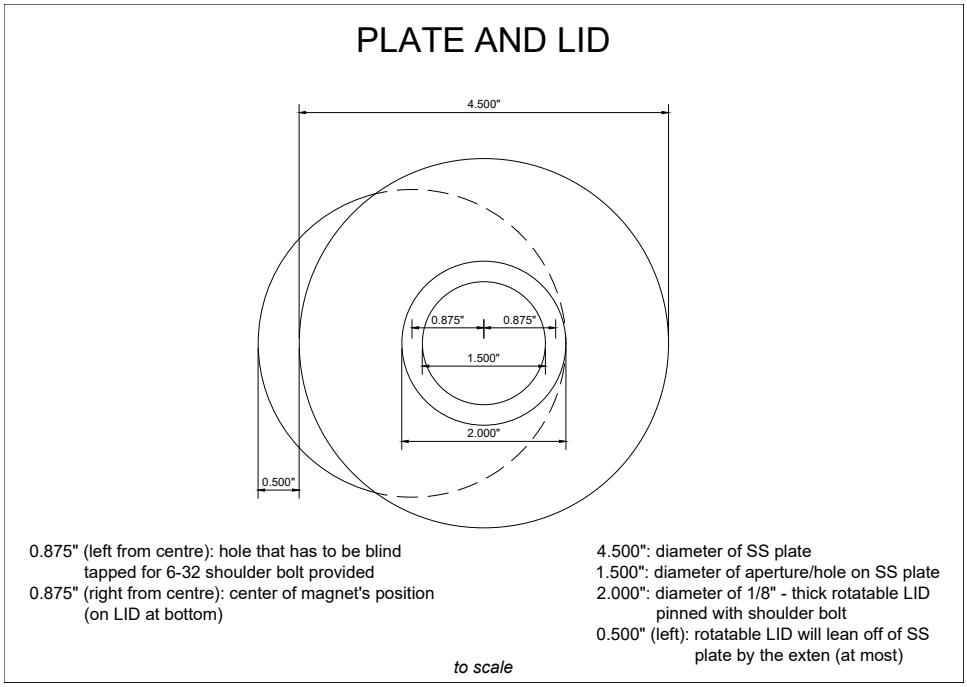

Figure A.3: Schematic representation of cover with lid for tumbler (overview).

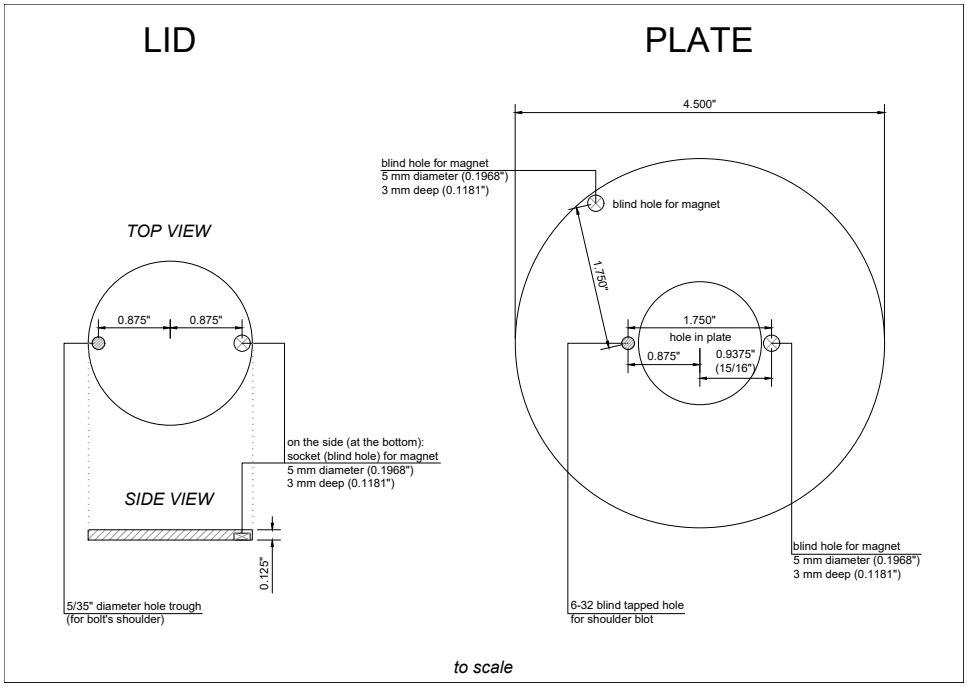

Figure A.4: Schematic representation of cover (plate) and its lid separately.

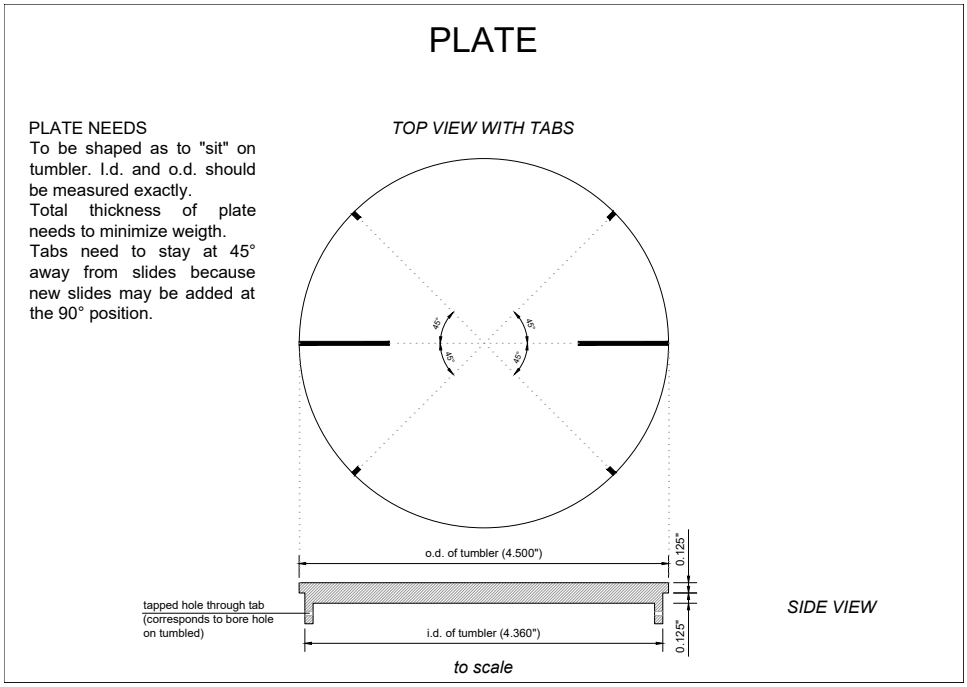

Figure A.5: Schematic representation of cover (plate) with side view.

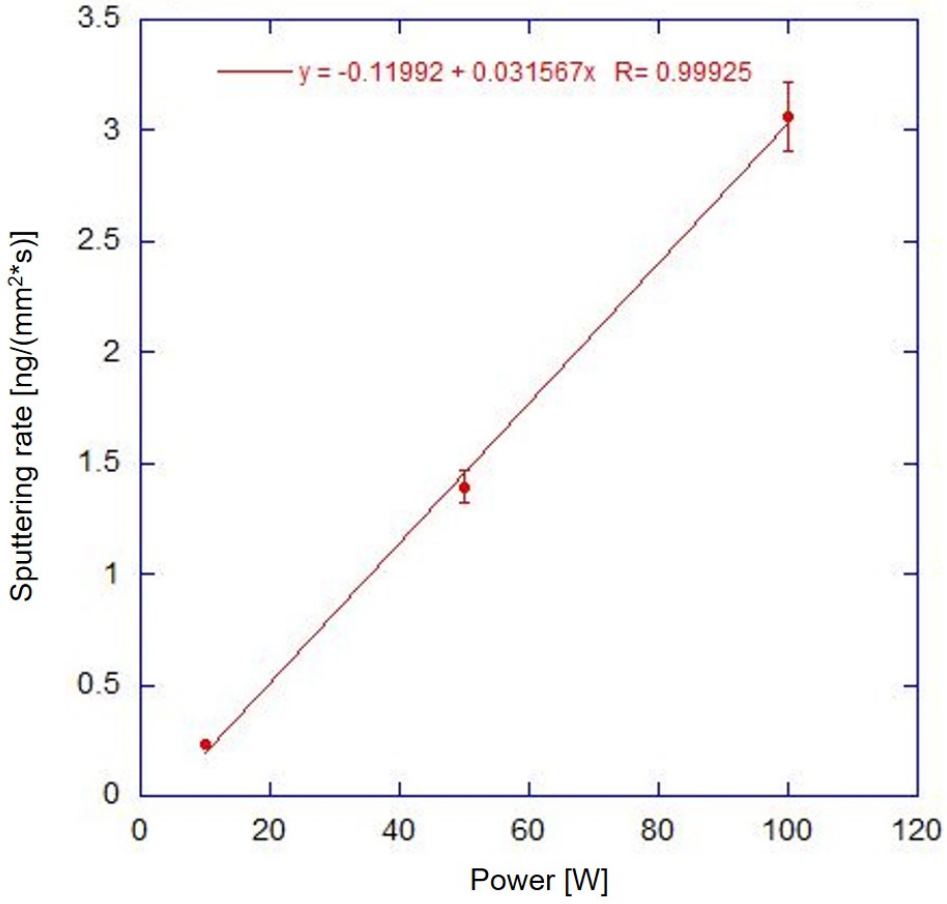

Figure A.6: Sputtering rate as a function of power at 3 mTorr for Cu.

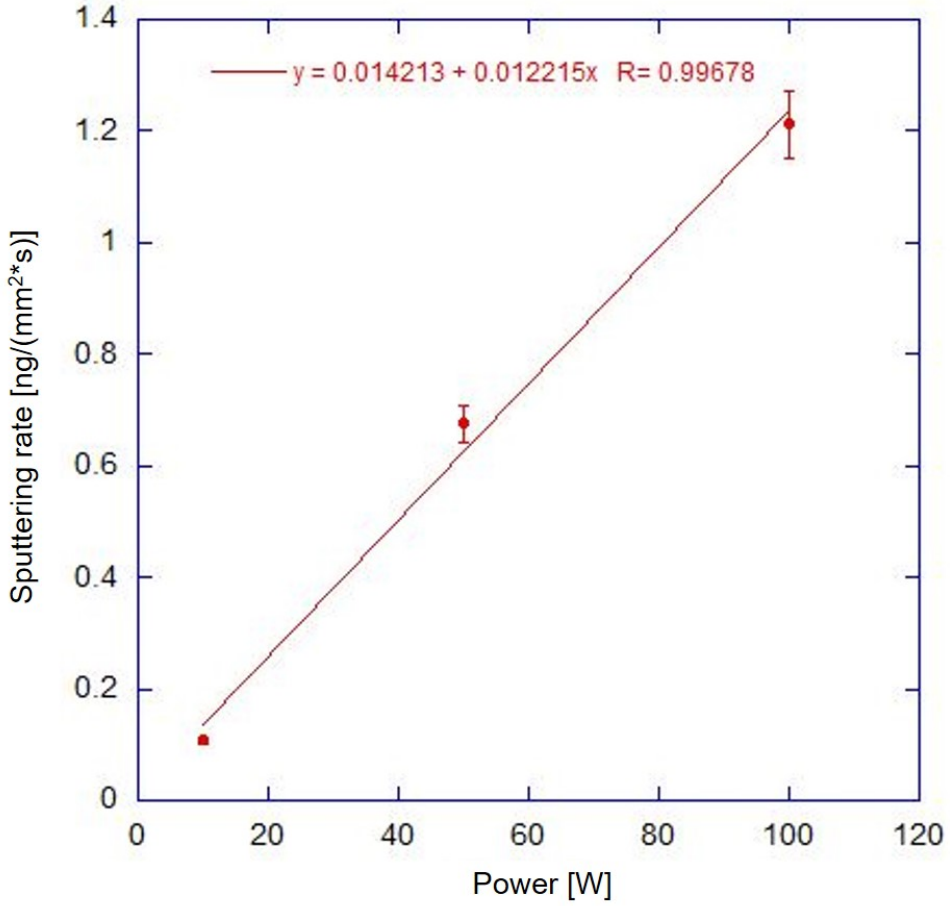

Figure A.7: Sputtering rate as a function of power at 7.5 mTorr for Cu.

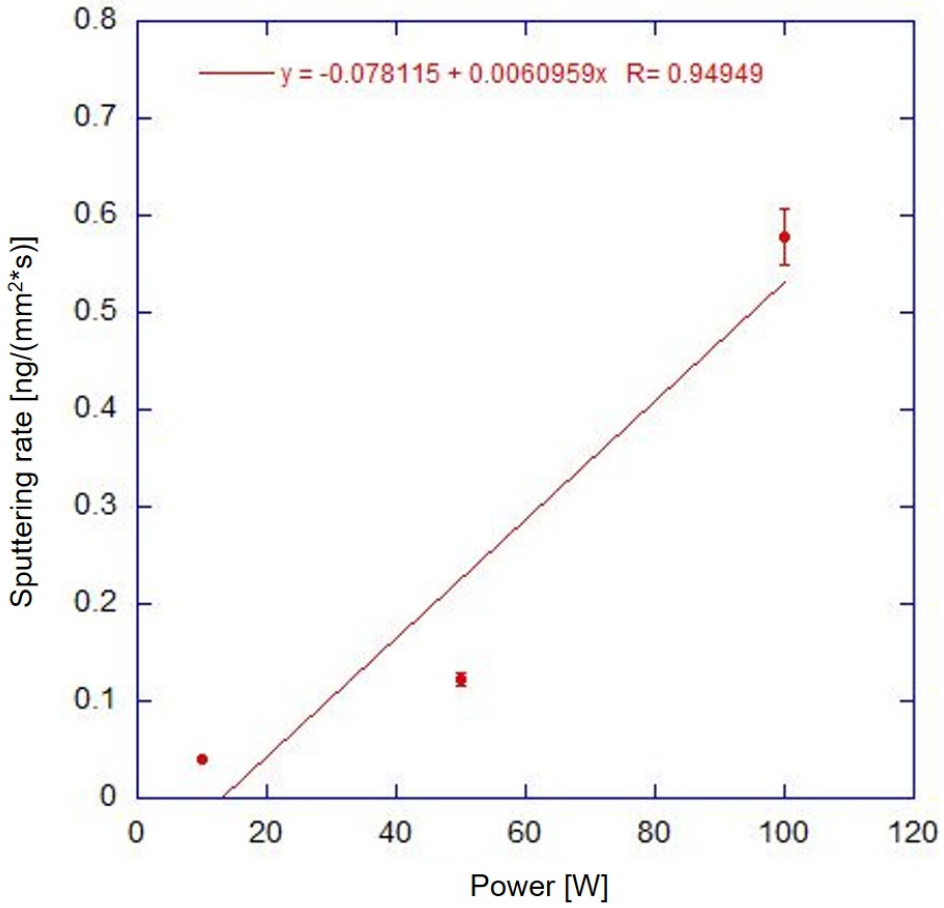

Figure A.8: Sputtering rate as a function of power at 15 mTorr for Cu.

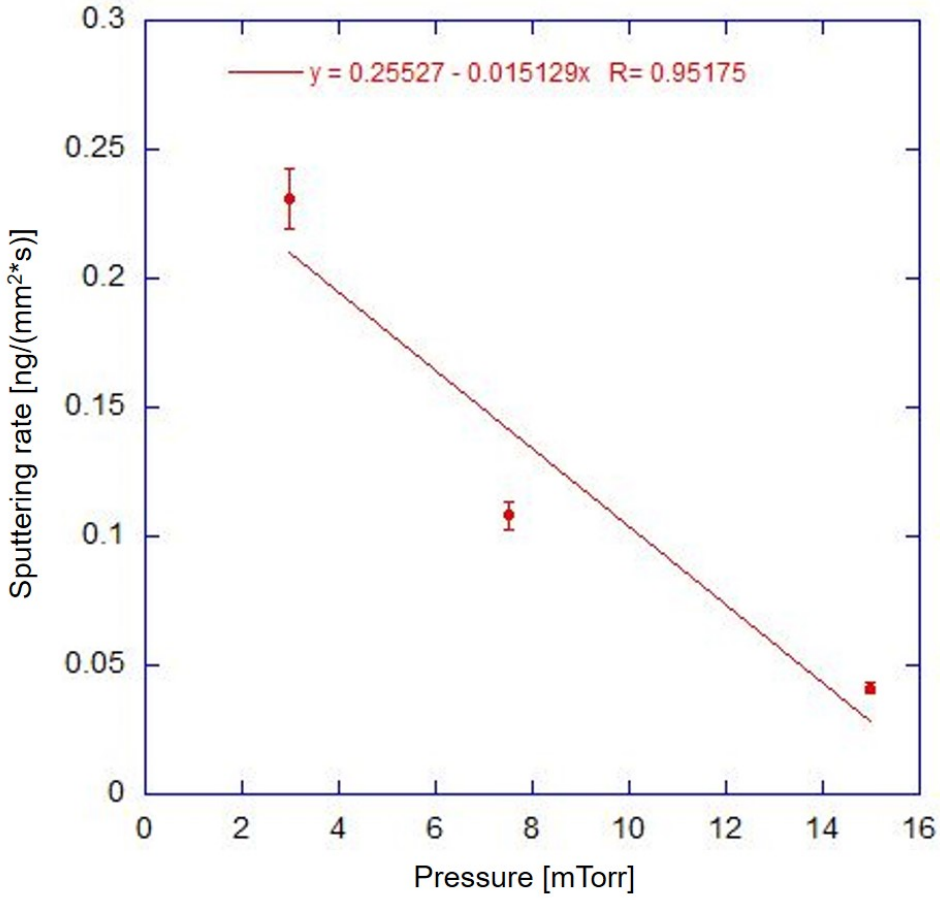

Figure A.9: Sputtering rate as a function of pressure at 10 W for Cu.

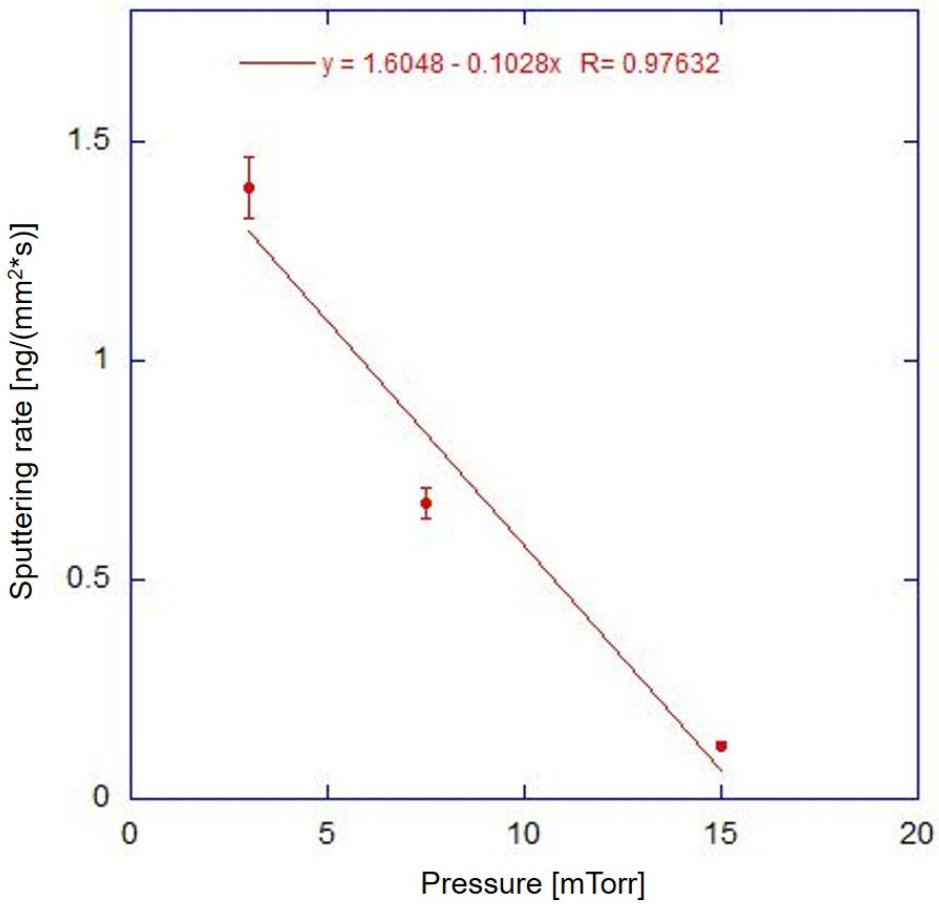

Figure A.10: Sputtering rate as a function of pressure at 50 W for Cu.

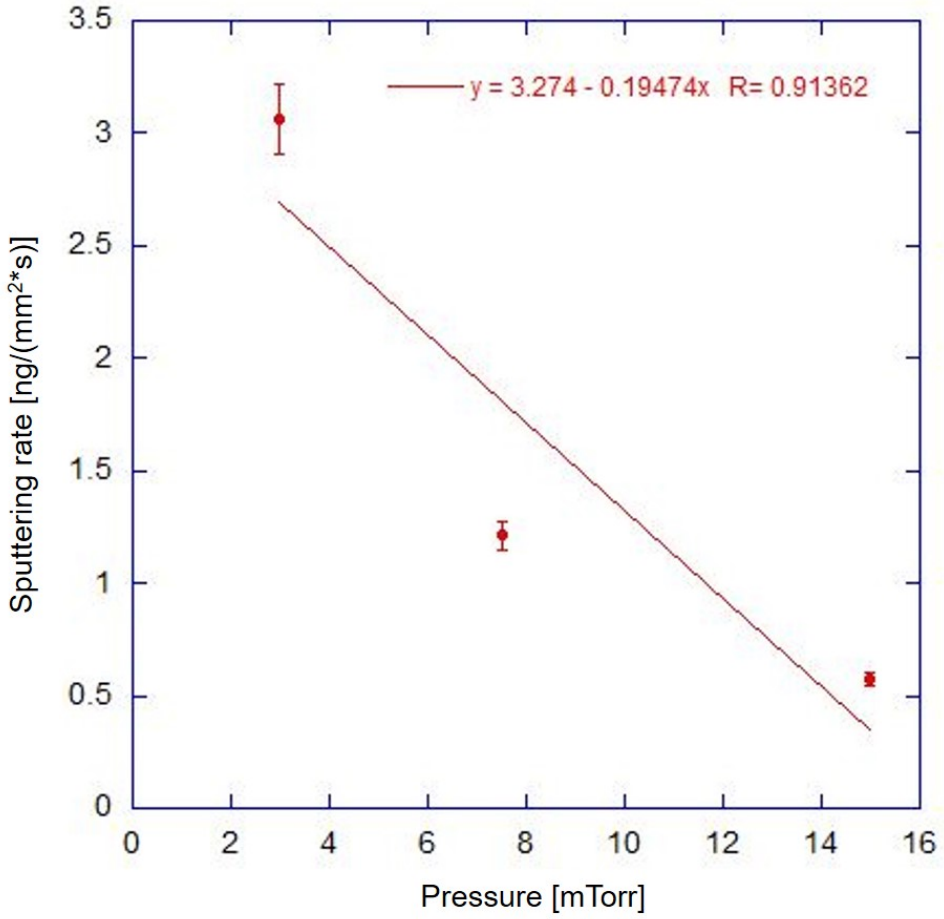

Figure A.11: Sputtering rate as a function of pressure at 100 W for Cu.

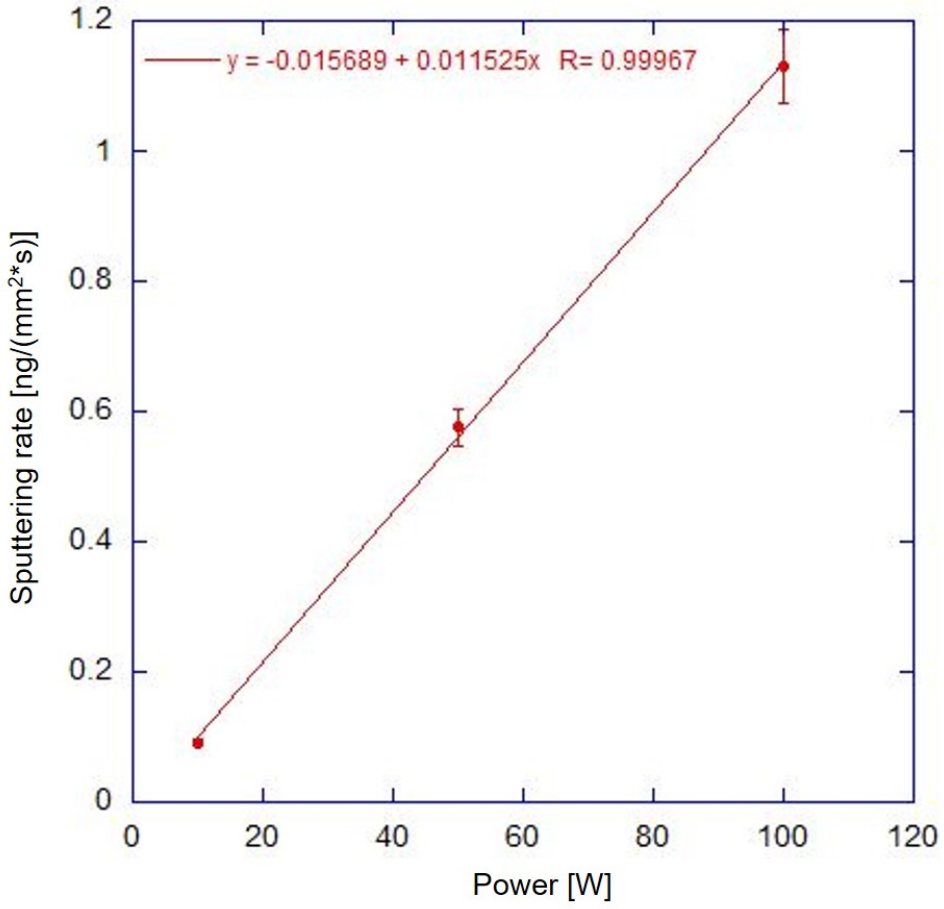

Figure A.12: Sputtering rate as a function of power at 3 mTorr for Ni.

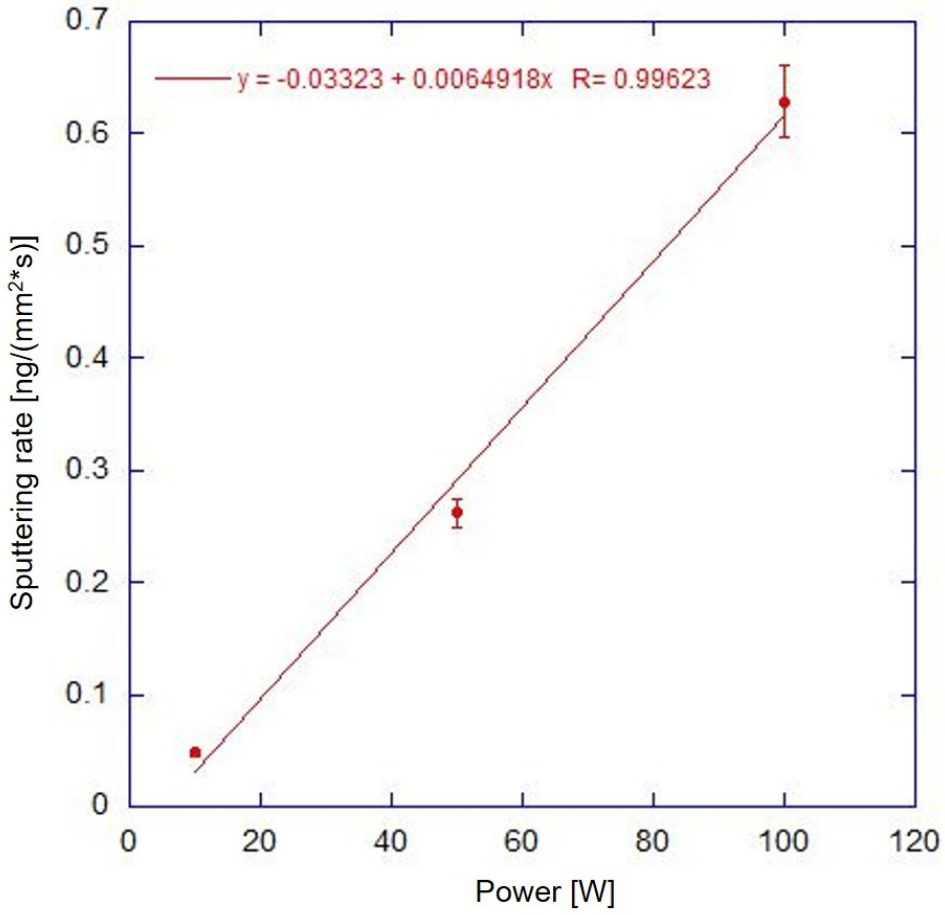

Figure A.13: Sputtering rate as a function of power at 7.5 mTorr for Ni.

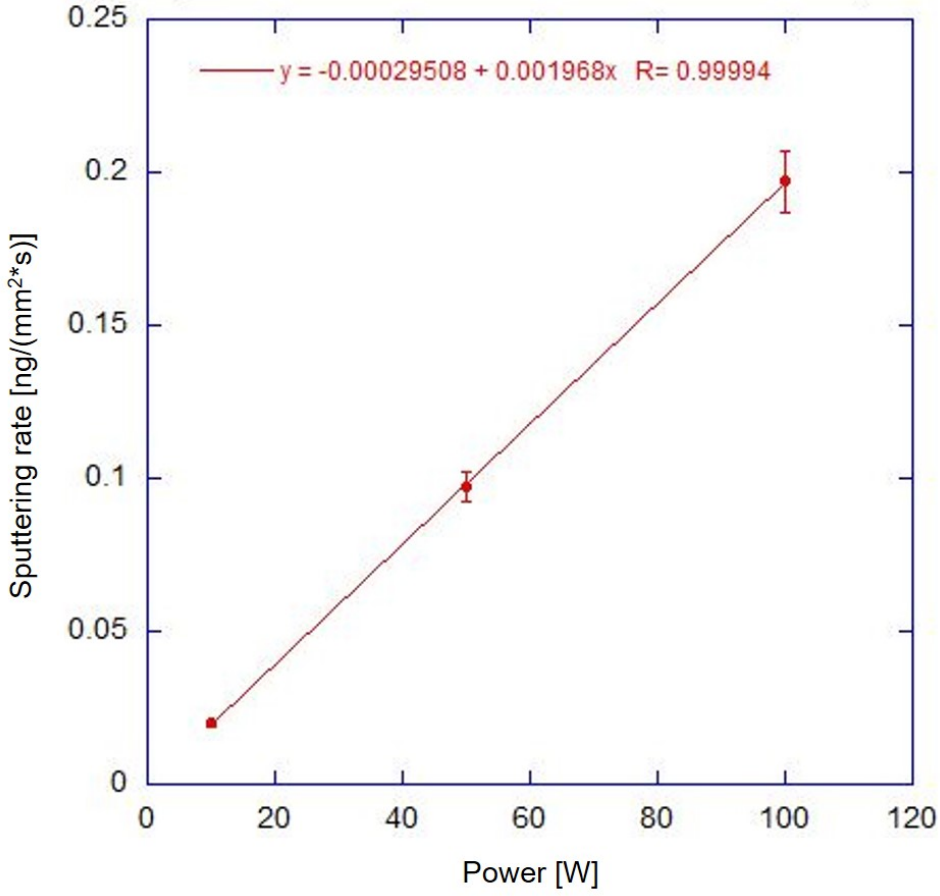

Figure A.14: Sputtering rate as a function of power at 15 mTorr for Ni.

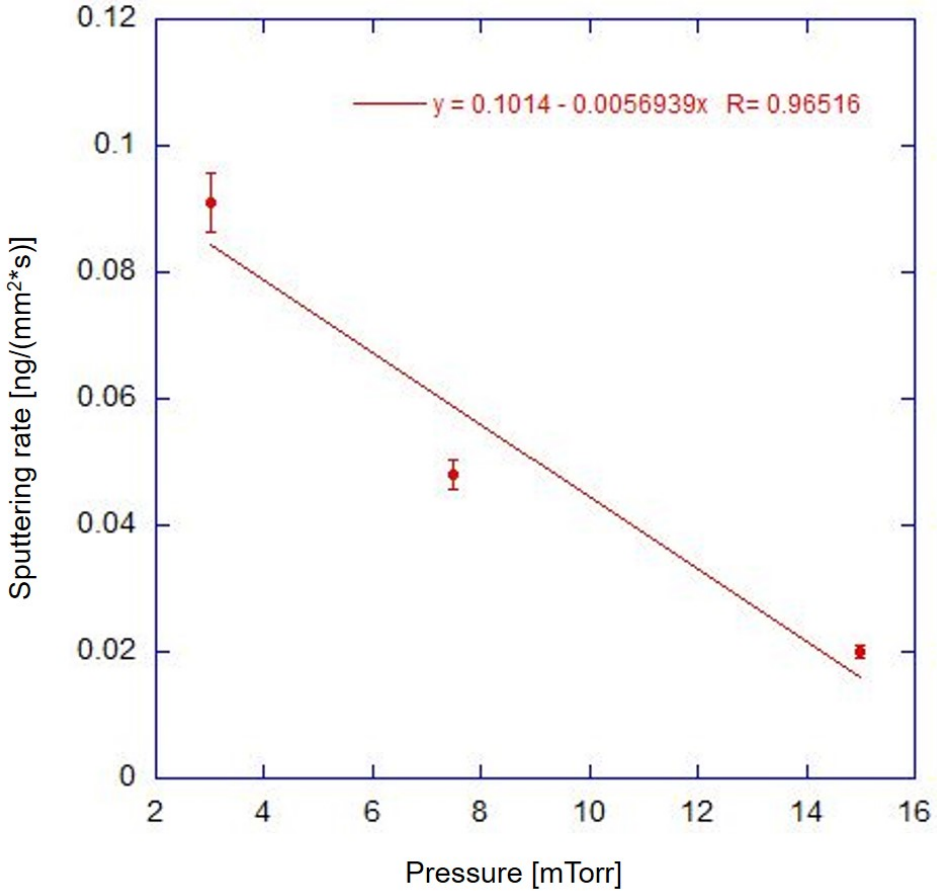

Figure A.15: Sputtering rate as a function of pressure at 10 W for Ni.

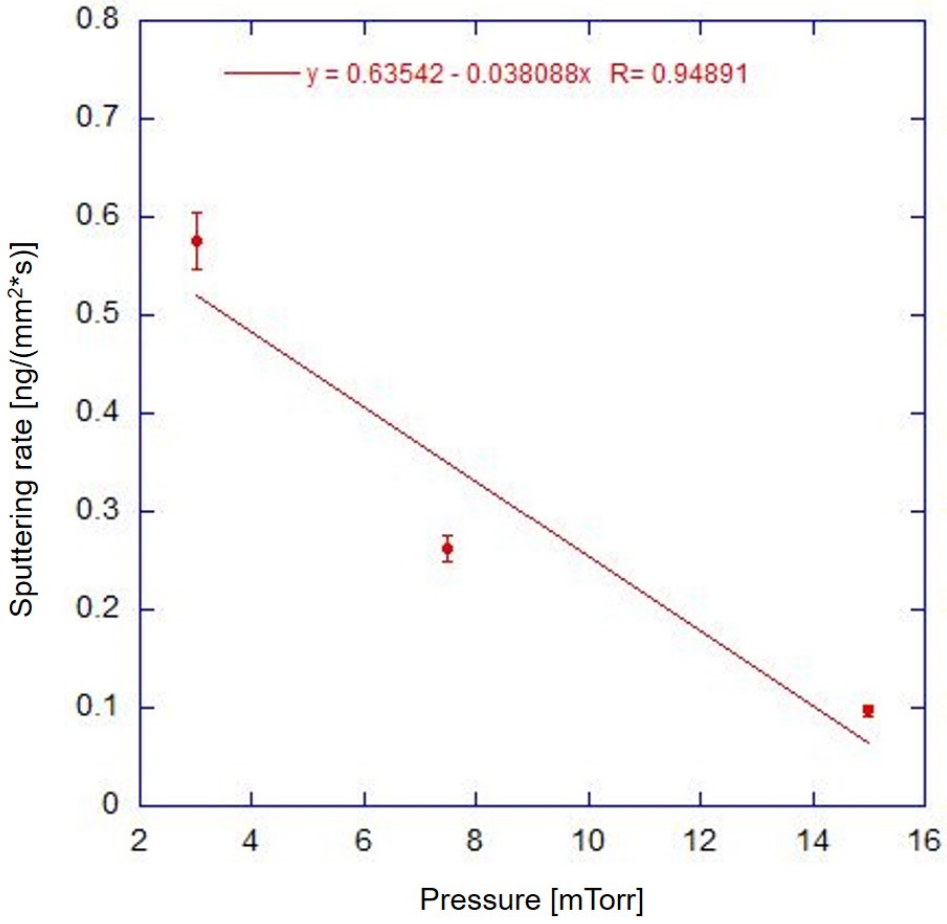

Figure A.16: Sputtering rate as a function of pressure at 50 W for Ni.

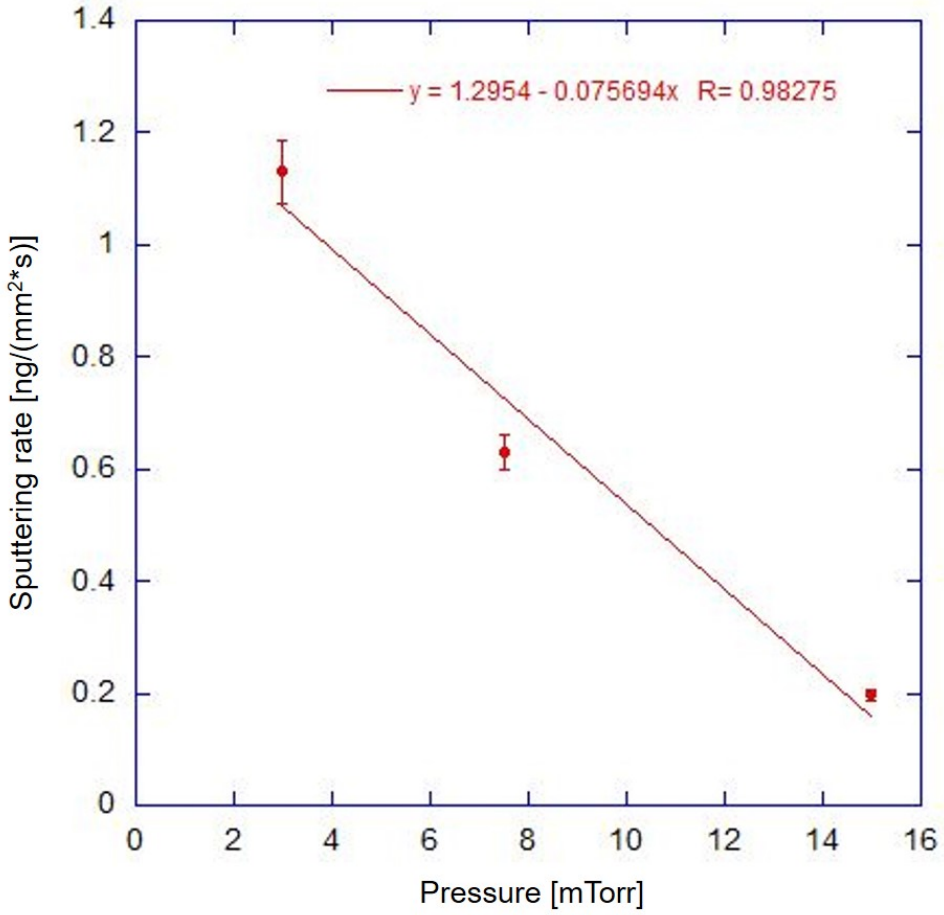

Figure A.17: Sputtering rate as a function of pressure at 100 W for Ni.

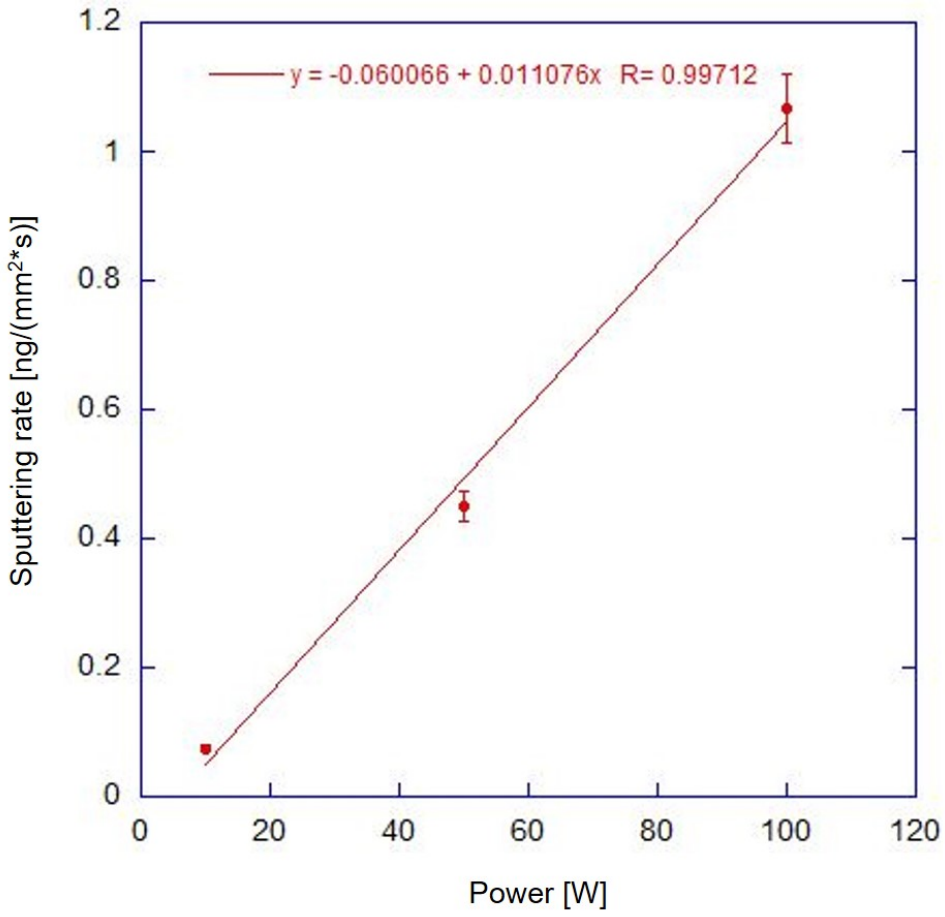

Figure A.18: Sputtering rate as a function of power at 3 mTorr for Co.

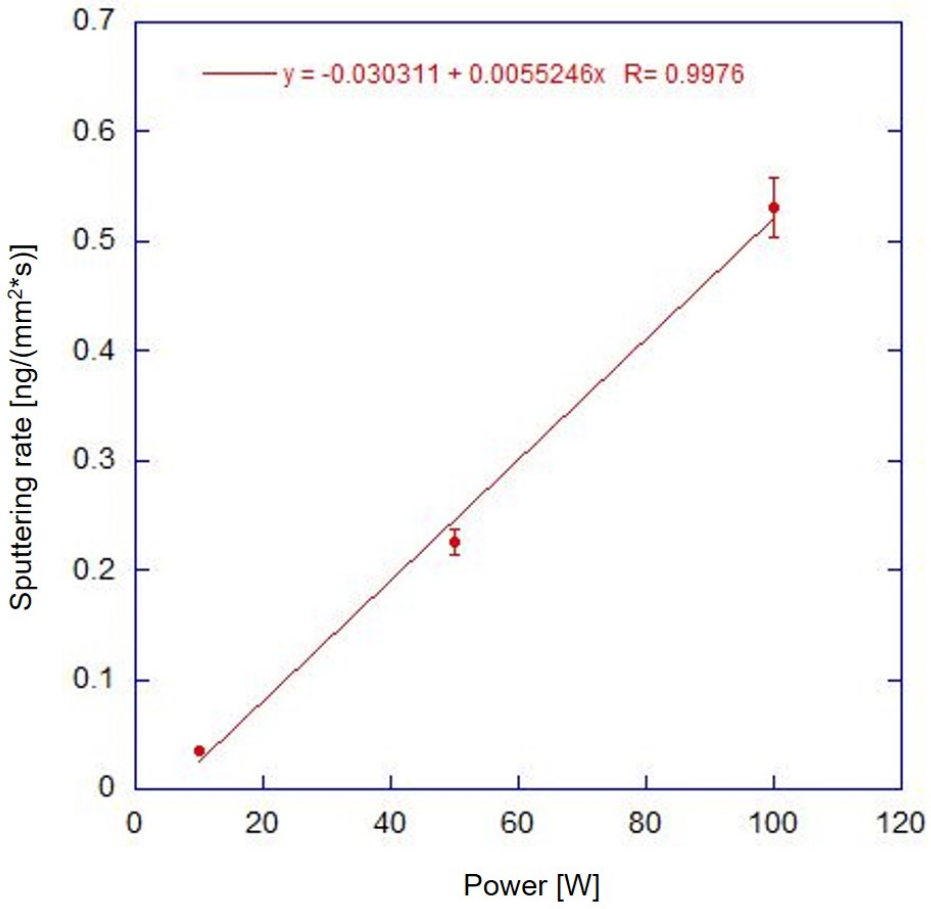

Figure A.19: Sputtering rate as a function of power at 7.5 mTorr for Co.

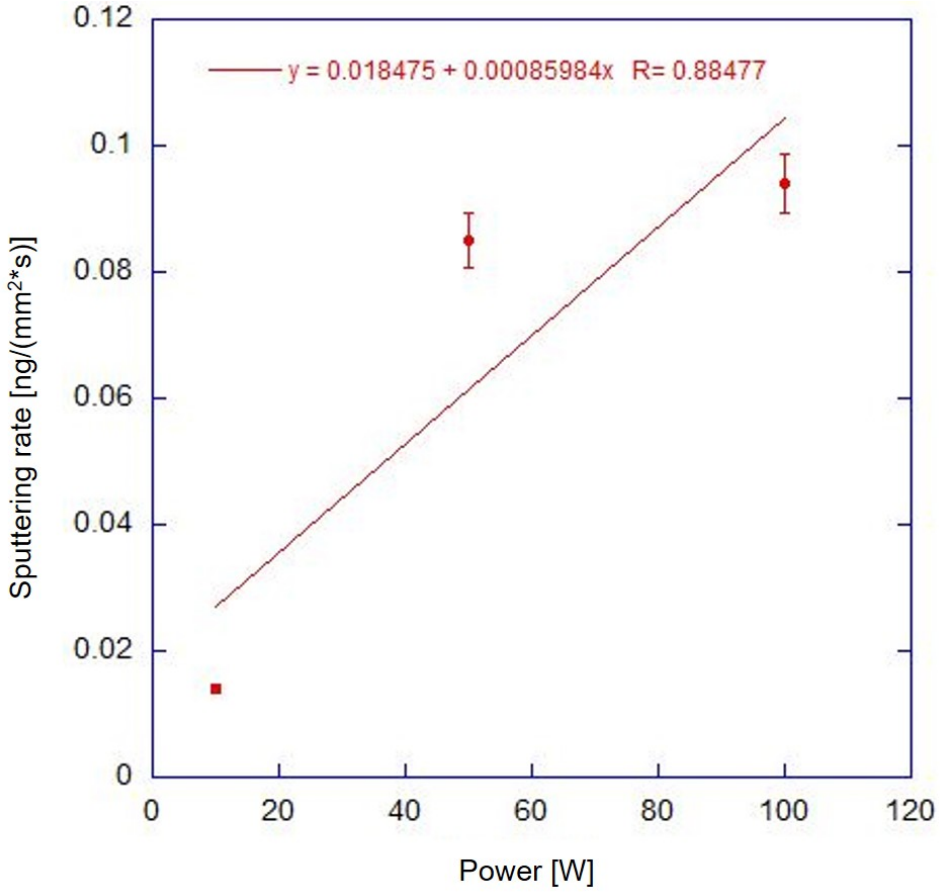

Figure A.20: Sputtering rate as a function of power at 15 mTorr for Co.

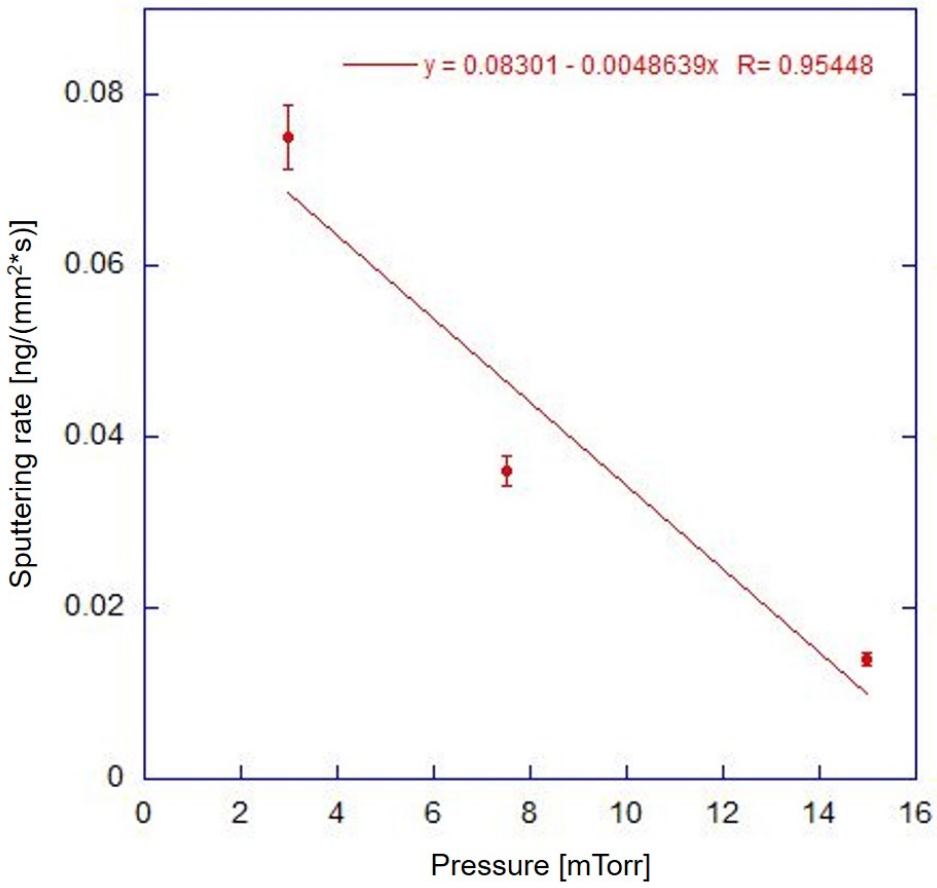

Figure A.21: Sputtering rate as a function of pressure at 10 W for Co.

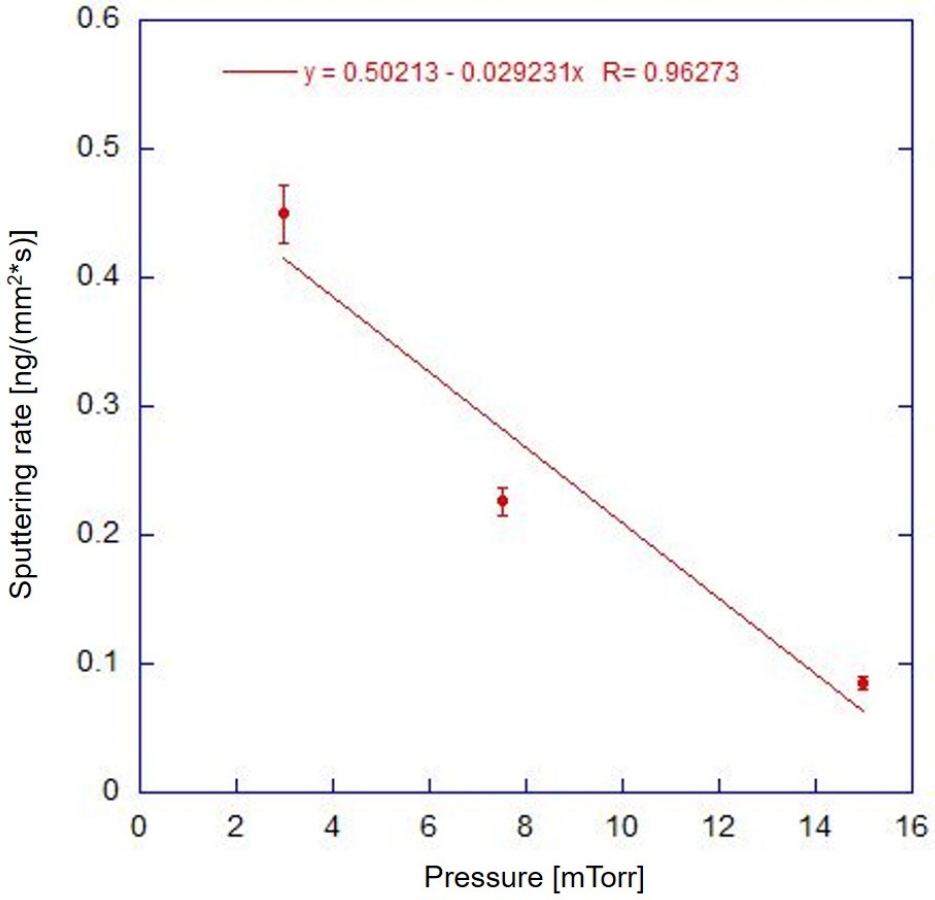

Figure A.22: Sputtering rate as a function of pressure at 50 W for Co.

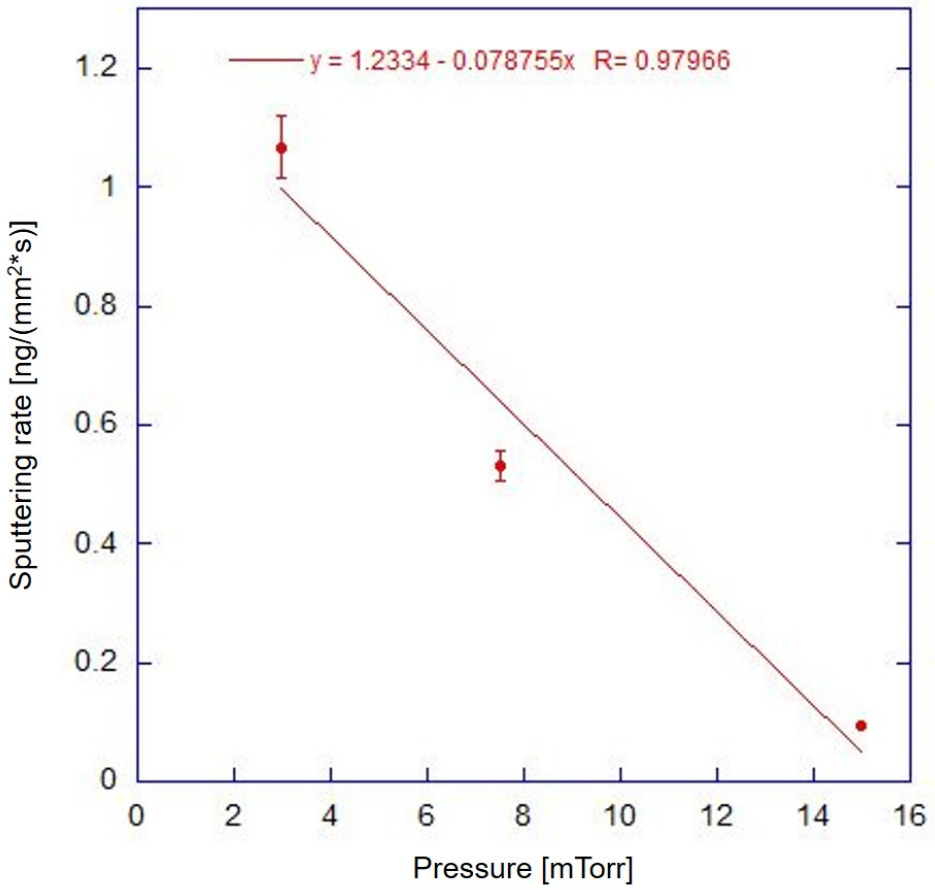

Figure A.23: Sputtering rate as a function of pressure at 100 W for Co.

B Supplemental information on decorated materials and their characterization

This Appendix reports additional information about the decorated materials whose preparation and characterization has been described in this dissertation work. When heat-treatment processes have been involved in the preparation of the materials (before or after the decoration process), duration of such treatments was typically 10-12 hours *in vacuo*.

Original batches of MgO material used for the decorated species reported in this Appendix: M0816C, M0318A, M0218F, M0218B, M0218C.

Original batches of ZnO material used for the decorated species reported in this Appendix: Z0918A, Z0219A.

How to read tables in this Appendix:

Batches of decorated materials are reported by date of preparation. All decorated materials were prepared with Ar pressure of 3 mTorr; the deposition time length and power of the sputtering effusive source are indicated in the columns "**t [min]**" and "**P [W]**", respectively. If heat-treatment of the pure MO powders was performed before deposition, this will be indicated in the column "**Pre-HT**" with a "Yes" or a "No" (if "Yes", temperature of treatment was 950 °C for MgO and 250 °C for ZnO). Whereas, the temperature of heat-treatment after deposition (if applicable) is indicated in the column "**Post-HT**", expressed in [°C]. Two values for "**Post-HT**" indicate two separate heat-treatment processes performed on two samples of the same decorated material at those temperature values. The column "**Mass [g]**" reports the amount of material currently available, and, if two separate values are reported, these correspond to the two separate heat-treatment temperatures. The column "**Notes**" reports whether the tapping weights were used ("Taps") or not ("No taps") during the decoration process; the term "SQUID", if present, denotes that SQUID vibrating sample magnetometer measurements were performed on the material in order to determine its response to an external applied magnetic field as a function of temperature; finally, the term "CYL", if present, denotes the use of the SS cylindrical tumbler for the decoration process, i.e. the version of tumbler preceding the conical one.

Table B.1: Overview of the most relevant Cu/MgO materials studied in this dissertation work.

Date	**t [min]**	**P [W]**	**Pre-HT**	**Post-HT**	**Mass [g]**	**Notes**
3/31/2017	240	30	No	950	0.10	No taps
5/11/2018	180	10	No	950	0.10	No taps; CYL
5/15/2018	180	30	No	950	0.15	No taps; SQUID
6/6/2018	180	10	Yes	950	0.20	No taps; SQUID
8/17/2018	120	10	Yes	500	0.15	Taps
8/20/2018	180	10	Yes	500	0.15	Taps
8/21/2018	180	10	Yes	500; 950	0.10; 0.10	Taps
8/23/2018	180	10	Yes	500	0.10	Taps
8/24/2018	60	10	Yes	500	0.30	Taps
9/3/2018	60	10	Yes	500	0.20	Taps
9/4/2018	30	10	Yes	500	0.20	Taps
9/5/2018	15	10	Yes	500	0.50	Taps
12/20/2018	1	10	Yes	500	0.50	Taps
5/10/2019	240	30	No	950	0.15	No taps

Table B.2: Overview of the most relevant Ni/MgO materials studied in this dissertation work.

Date	t [min]	P [W]	Pre-HT	Post-HT	Mass [g]	Notes
5/21/2018	180	10	No	950	0.10	No taps
5/22/2018	180	30	No	950	0.10	No taps; SQUID
10/11/2018	180	10	Yes	500; 950	0.10; 0.10	Taps
2/5/2019	60	10	Yes	500	0.20	Taps
2/6/2019	30	10	Yes	500	0.20	Taps
2/7/2019	15	10	Yes	500	0.30	Taps
2/8/2019	1	10	Yes	500	0.40	Taps

Table B.3: Overview of the most relevant Co/MgO materials studied in this dissertation work.

Date	t [min]	P [W]	Pre-HT	Post-HT	Mass [g]	Notes
5/23/2018	180	30	No	950	0.10	No taps; SQUID
5/24/2018	180	10	No	950	0.10	No taps
10/18/2018	180	10	Yes	500; 950	0.10; 0.10	Taps
2/9/2019	1	10	Yes	500	0.40	Taps
2/11/2019	15	10	Yes	500	0.20	Taps
2/12/2019	30	10	Yes	500	0.10	Taps
2/13/2019	60	10	Yes	500	0.10	Taps

Table B.4: Overview of the most relevant Cu/ZnO materials studied in this dissertation work.

Date	t [min]	P [W]	Pre-HT	Post-HT	Mass [g]	Notes
10/9/2018	180	10	Yes	250	0.30	Taps
2/25/2019	60	10	Yes	250	0.30	Taps
2/26/2019	15	10	Yes	250	0.50	Taps
2/27/2019	1	10	Yes	250	0.50	Taps

Table B.5: Overview of the most relevant Ni/ZnO materials studied in this dissertation work.

Date	t [min]	P [W]	Pre-HT	Post-HT	Mass [g]	Notes
10/10/2018	180	10	Yes	250	0.30	Taps
2/20/2019	1	10	Yes	250	0.30	Taps
2/21/2019	15	10	Yes	250	0.30	Taps
2/22/2019	60	10	Yes	250	0.30	Taps

Table B.6: Overview of the most relevant Co/ZnO materials studied in this dissertation work.

Date	**t [min]**	**P [W]**	**Pre-HT**	**Post-HT**	**Mass [g]**	**Notes**
10/17/2018	180	10	Yes	250	0.30	Taps
2/14/2019	60	10	Yes	250	0.30	Taps
2/15/2019	15	10	Yes	250	0.50	Taps
2/18/2019	1	10	Yes	250	0.50	Taps

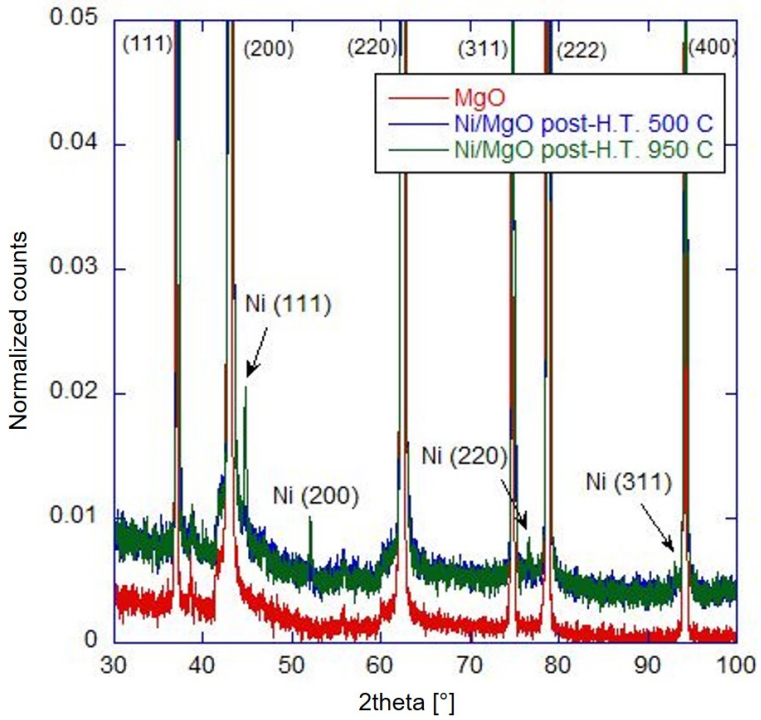

Figure B.24: Diffraction patterns of Ni/MgO prepared at 10 W power for 3 hours (heat-treatment before deposition at 950 °C, after deposition at 500 °C, tapping weights were used). The Miller indices sets (111), (200), (220), (311), (222), and (400) with no further specification represent crystalline phases of the bare MgO structure.

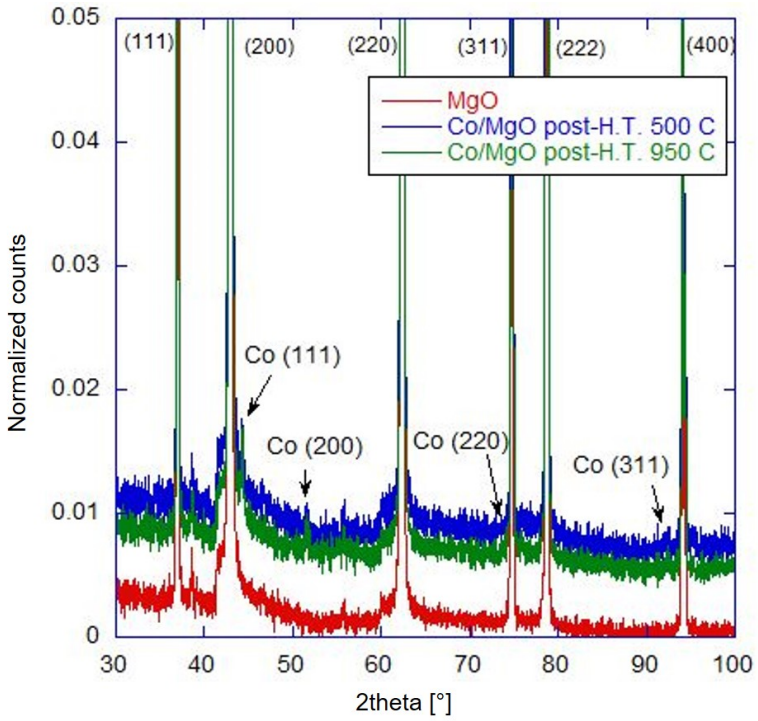

Figure B.25: Diffraction patterns of Co/MgO prepared at 10 W power for 3 hours (heat-treatment before deposition at 950 °C, after deposition at 500 °C, tapping weights were used). The Miller indices sets (111), (200), (220), (311), (222), and (400) with no further specification represent crystalline phases of the bare MgO structure.

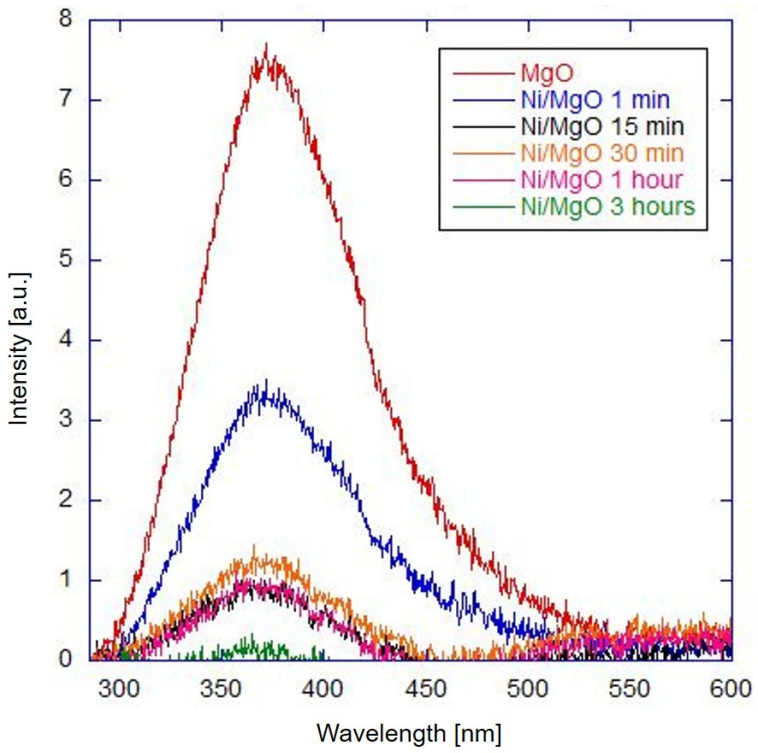

Figure B.26: PL spectra of Ni/MgO prepared at 10 W for different deposition times hours (heat-treatment before deposition at 950 °C, after deposition at 500 °C, tapping weights were used).

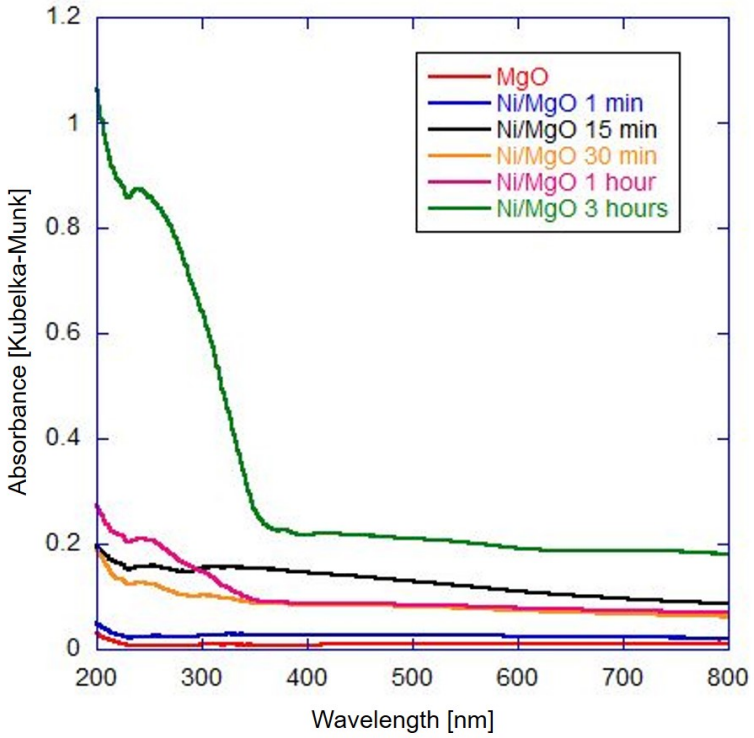

Figure B.27: Absorbance spectra of Ni/MgO prepared at 10 W for different deposition times hours (heat-treatment before deposition at 950 °C, after deposition at 500 °C, tapping weights were used).

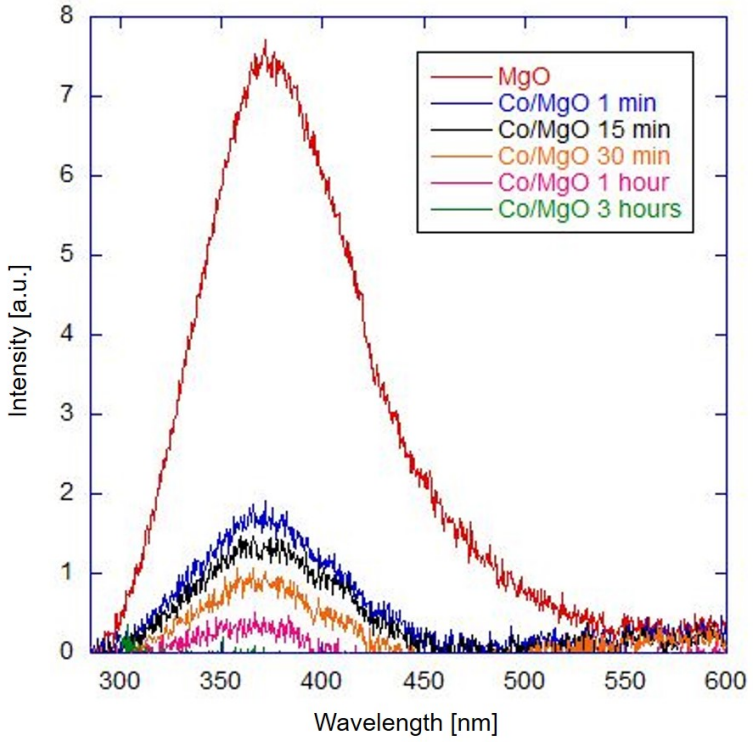

Figure B.28: PL spectra of Co/MgO prepared at 10 W for different deposition times hours (heat-treatment before deposition at 950 °C, after deposition at 500 °C, tapping weights were used).

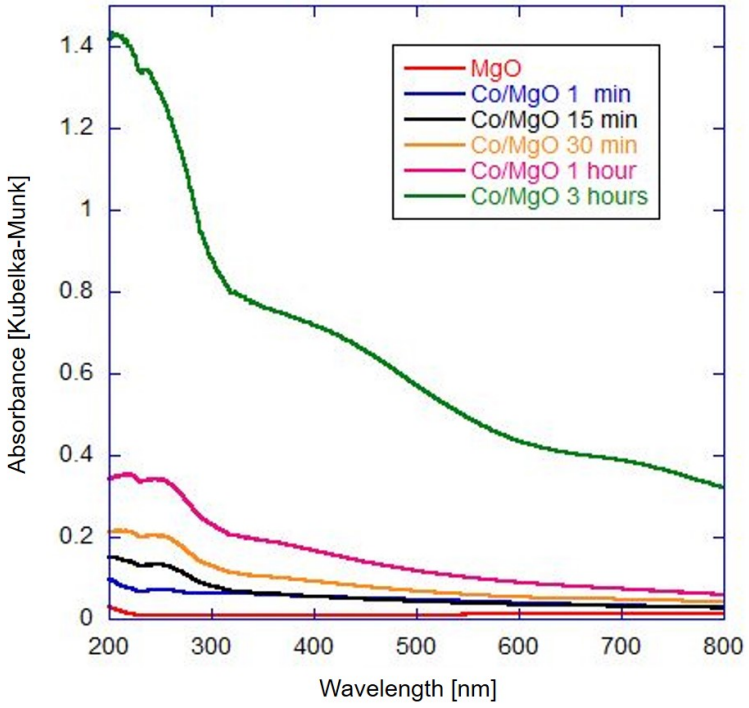

Figure B.29: Absorbance spectra of Co/MgO prepared at 10 W for different deposition times hours (heat-treatment before deposition at 950 °C, after deposition at 500 °C, tapping weights were used).

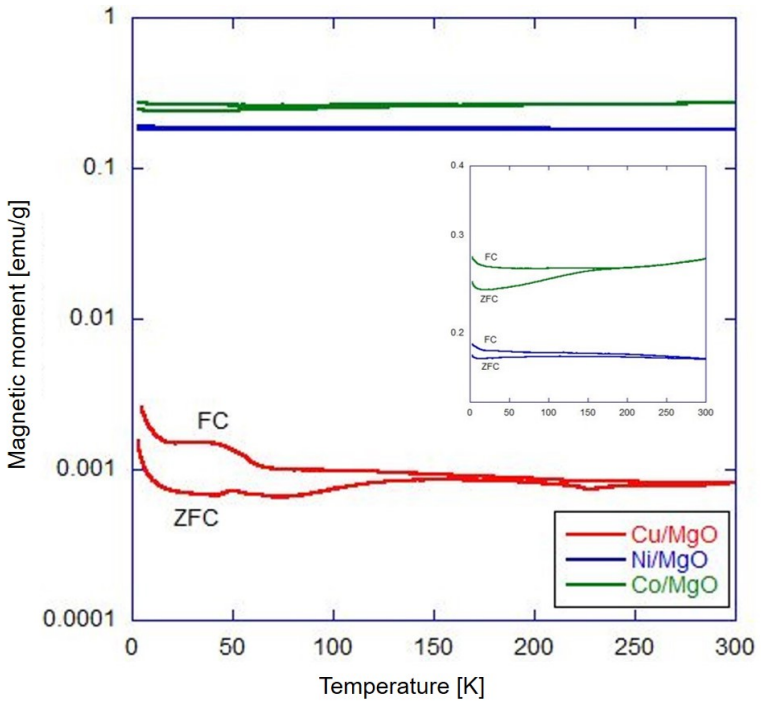

Figure B.30: SQUID VSM plots in zero-field cooled (ZFC) and field-cooled (FC) modes for the magnetic susceptibility of Cu/MgO, Ni/MgO and Co/MgO (30 W, 3-hour deposition, heat-treatment after deposition at 950 °C, no tapping weights used during deposition). Inset shows features of magnetic susceptibility for Ni/MgO and Co/MgO.

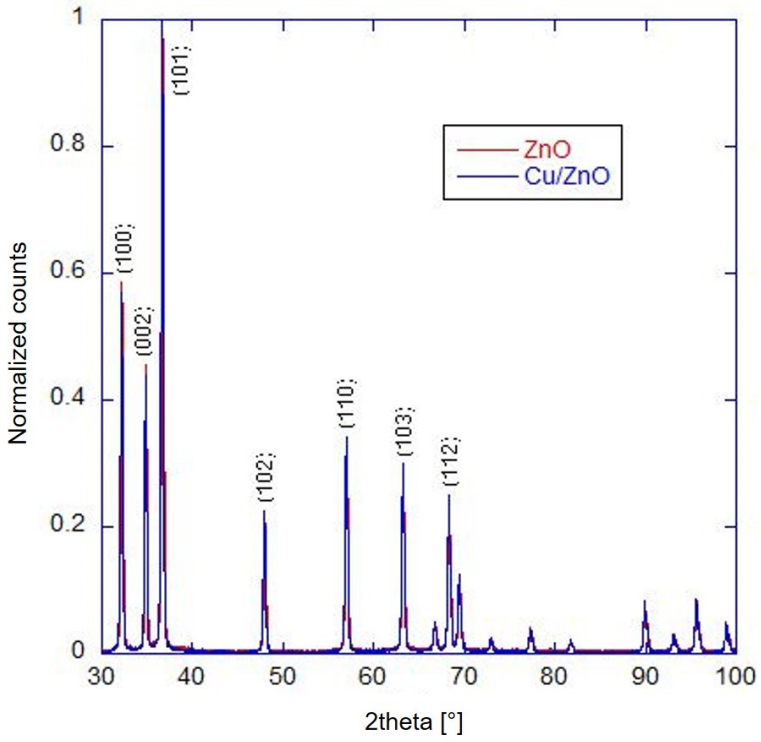

Figure B.31: Diffraction pattern of Cu/ZnO exposed to 10 W beam for 3 hours (heat-treatment before and after deposition at 250 °C). The Miller indices sets displayed on the pattern represent crystalline phases of the bare ZnO structure.

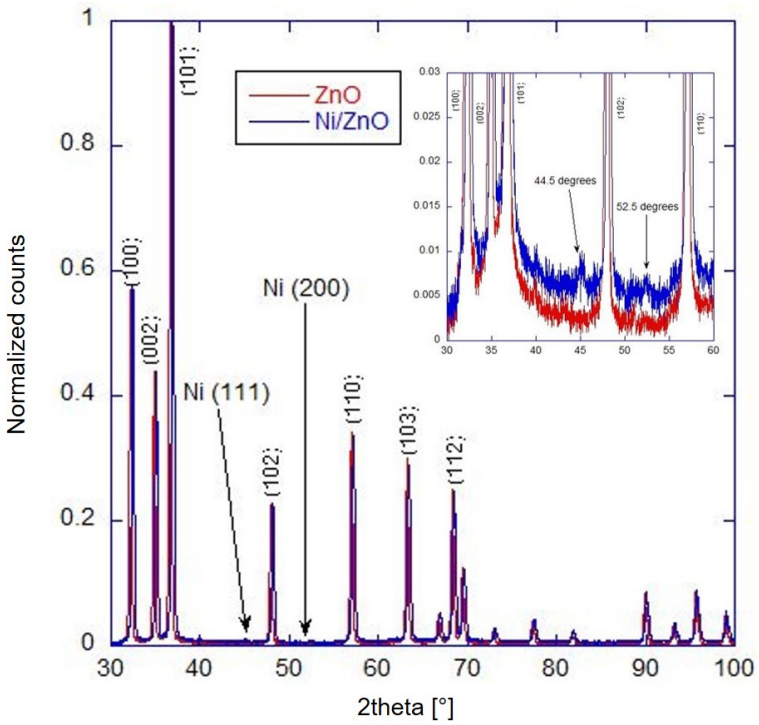

Figure B.32: Diffraction pattern of Ni/ZnO exposed to 10 W beam for 3 hours (heat-treatment before and after deposition at 250 °C). The Miller indices sets displayed on the pattern with no further specification represent crystalline phases of the bare ZnO structure.

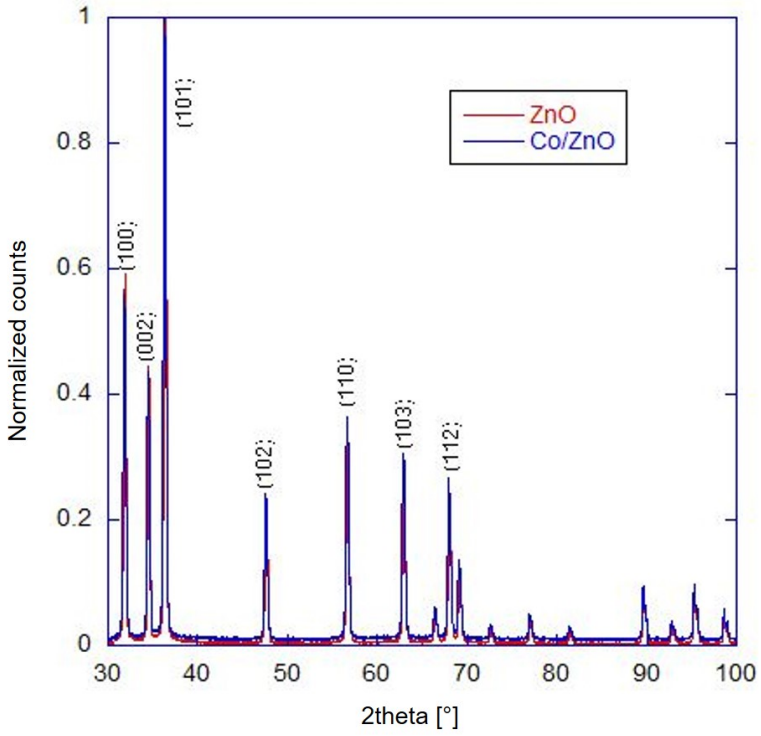

Figure B.33: Diffraction pattern of Co/ZnO exposed to 10 W beam for 3 hours (heat-treatment before and after deposition at 250 °C). The Miller indices sets displayed on the pattern represent crystalline phases of the bare ZnO structure.

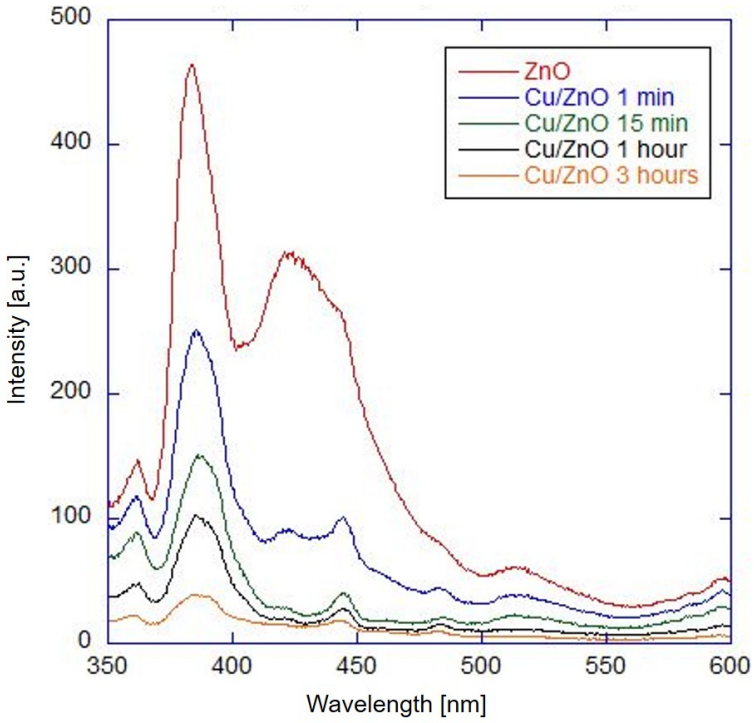

Figure B.34: PL spectra of Cu/ZnO for different deposition times; excitation at 325 nm (exposed to 10 W beam for 3 hours, heat-treatment before and after deposition at 250 °C).

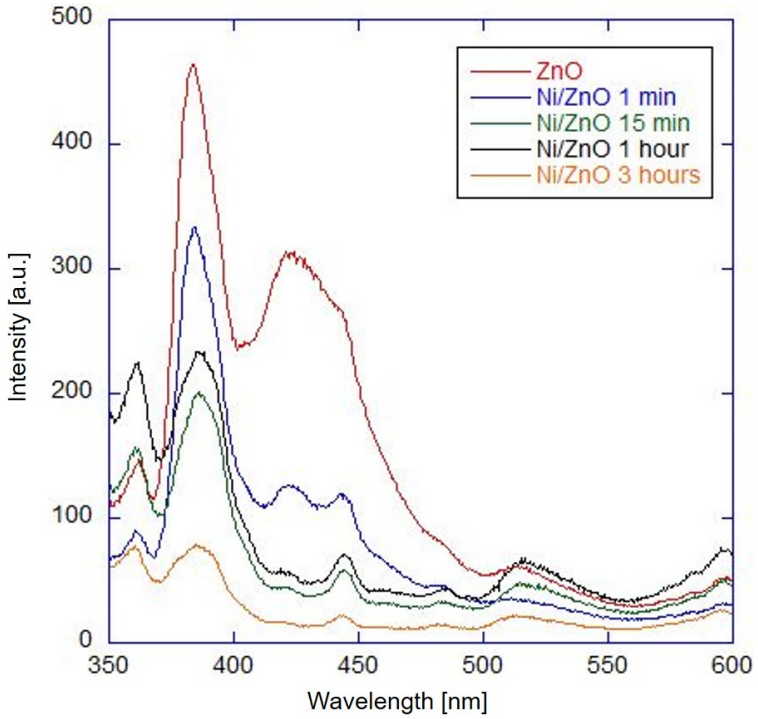

Figure B.35: PL spectra of Ni/ZnO for different deposition times; excitation at 325 nm (exposed to 10 W beam for 3 hours, heat-treatment before and after deposition at 250 °C).

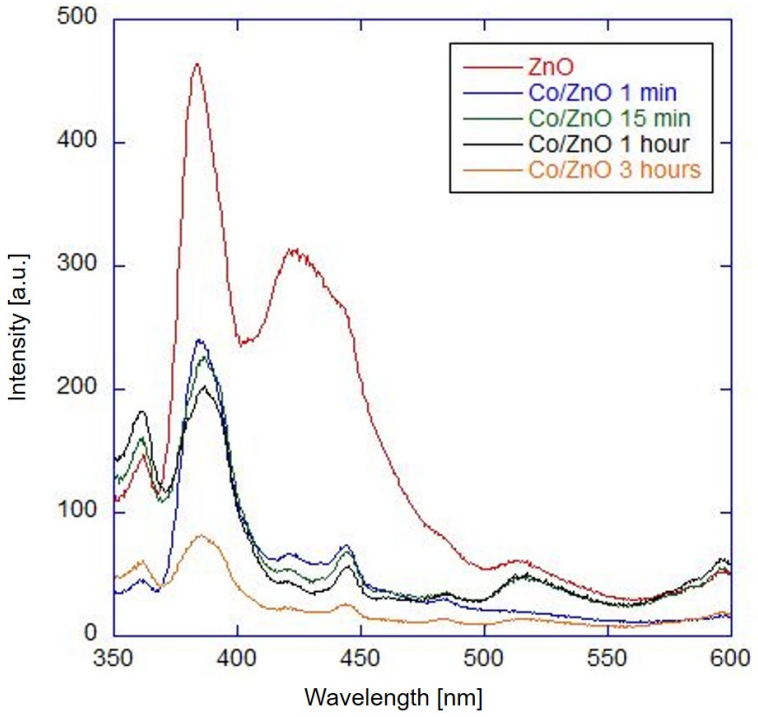

Figure B.36: PL spectra of Co/ZnO for different deposition times; excitation at 325 nm (exposed to 10 W beam for 3 hours, heat-treatment before and after deposition at 250 °C).

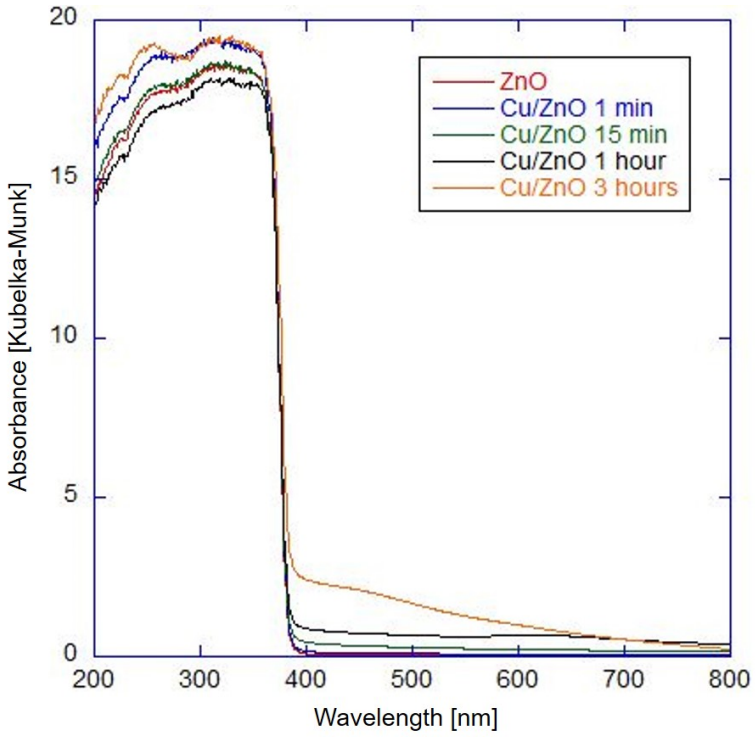

Figure B.37: Absorbance spectra of Cu/ZnO for different deposition times (exposed to 10 W beam for 3 hours, heat-treatment before and after deposition at 250 °C).

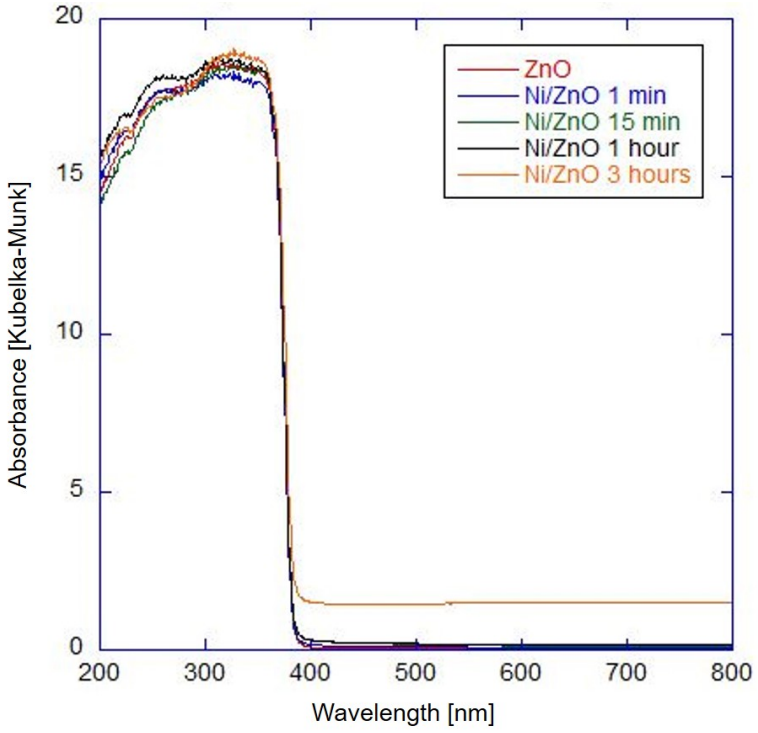

Figure B.38: Absorbance spectra of Ni/ZnO for different deposition times (exposed to 10 W beam for 3 hours, heat-treatment before and after deposition at 250 °C).

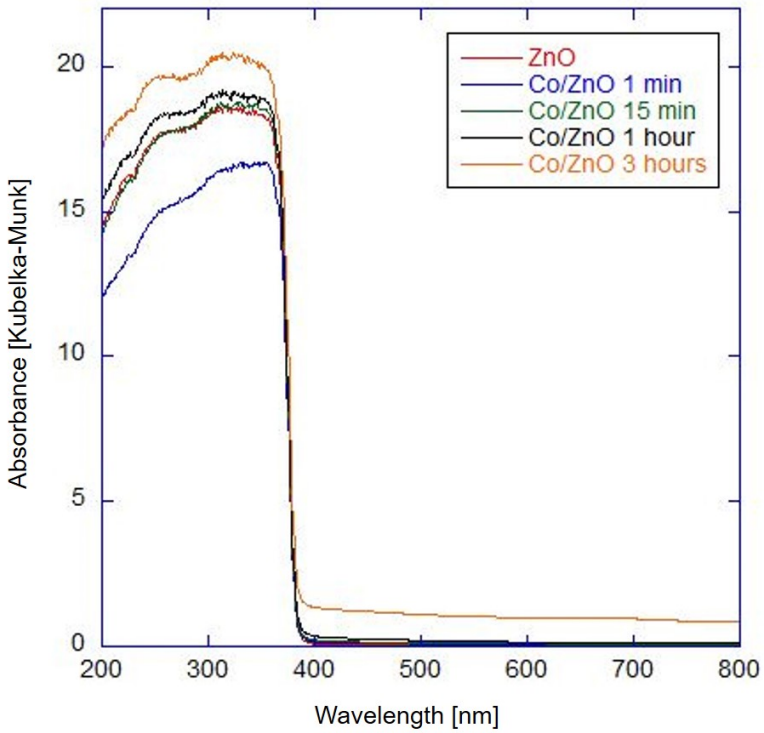

Figure B.39: Absorbance spectra of Co/ZnO for different deposition times (exposed to 10 W beam for 3 hours, heat-treatment before and after deposition at 250 °C).

C Description of code for pore size analysis

C.1 MATLAB code for PSD script

(Many code lines have been split in one or more lines to allow full visualization. A code line typically ends with a semicolon.)

```
prompt1 ='Type 1 for Methane, 2 for Argon, 3 for Nitrogen: ';
Gas = input(prompt1);
datafile = 'Adsorption.dat';
datafile2 = 'Desorption.dat';
T_init = readtable(datafile);
T_init2 = readtable(datafile2);
[m,n] = size(T_init);
[p,q] = size(T_init2);
sz = [m,38];
sz2 = [p,38];
varTypes = {'double','double','double','double','double',
    'double','double','double','double','double','double',
    'double','double','double','double','double','double',
    'double','double','double','double','double','double',
    'double','double','double','double','double','double',
    'double','double','double','double','double','double',
    'double','double','double'};
varTypes2 = {'double','double','double','double','double',
    'double','double','double','double','double','double',
    'double','double','double','double','double','double',
    'double','double','double','double','double','double',
    'double','double','double','double','double','double',
    'double','double','double','double','double','double',
    'double','double','double'};
varNames = {'p_final','SumdP','Void','delta_p_fin','p_p0',
```

```
    'n_ads','V_ads','V_liq','ln_p_p0','stat_t','r_p',
    'dV_ads_dr_p','r_p_mod','dV_ads_dr_p_mod','Void2',
    'delta_stat_t','r_k','r_k_mod','Void3','delta_V_liq',
    'V_liq_DESC','stat_t_DESC','r_p_DESC','r_p_mod_DESC',
    'delta_stat_t_DESC','r_k_DESC','r_k_mod_DESC',
    'delta_V_liq_DESC','BJH_Vol','c_j_A_j','c_j_A_j_run_sum',
    'BJH_Vol_run_sum','dV_BJH_dr_p','BJH_Vol_mod',
    'c_j_A_j_mod','c_j_A_j_run_sum_mod','BJH_Vol_run_sum_mod',
    'dV_BJH_dr_p_mod'};
varNames2 = {'p_final','SumdP','Void','delta_p_fin','p_p0',
    'n_ads','V_ads','V_liq','ln_p_p0','stat_t','r_p',
    'dV_ads_dr_p','r_p_mod','dV_ads_dr_p_mod','Void2',
    'delta_stat_t','r_k','r_k_mod','Void3','delta_V_liq',
    'V_liq_DESC','stat_t_DESC','r_p_DESC','r_p_mod_DESC',
    'delta_stat_t_DESC','r_k_DESC','r_k_mod_DESC',
    'delta_V_liq_DESC','BJH_Vol','c_j_A_j','c_j_A_j_run_sum',
    'BJH_Vol_run_sum','dV_BJH_dr_p','BJH_Vol_mod','c_j_A_j_mod',
    'c_j_A_j_run_sum_mod','BJH_Vol_run_sum_mod',
    'dV_BJH_dr_p_mod'};
T_fin = table
('Size',sz,'VariableTypes',varTypes,'VariableNames',varNames);
T_fin2 = table
('Size',sz2,'VariableTypes',varTypes2,'VariableNames',varNames2);
T_fin.p_final = T_init.Var10; T_fin.SumdP = T_init.Var11;
T_fin2.p_final = T_init2.Var10; T_fin2.SumdP = T_init2.Var11;
prompt2 = 'Insert value for dosing volume in cc: ';
prompt3 = 'Insert value for deadspace volume in cc: ';
prompt4 = 'Insert value for experimental temperature in K: ';
prompt5 = 'Insert value for sample mass in g: ';
prompt6 = 'Type 100 for 100 torr, 1000 for 1000 torr head: ';
```

```
Vdose = input(prompt2);
Vdead = input(prompt3);
Temp = input(prompt4);
sample_mass = input(prompt5);
torrhead = input(prompt6);
if Gas == 1
    Gamma = 33.986 - 0.18929*Temp;
    MolarMass = 16.043;
    DeltaRhoLiquid = 0.423;
    Sigma = 0.4;
elseif Gas == 2
    Gamma = 34.28 - 0.2493*Temp;
    MolarMass = 39.948;
    DeltaRhoLiquid = 1.395;
    Sigma = 0.4;
elseif Gas == 3
    Gamma = 26.42 - 0.2265*Temp;
    MolarMass = 28.013;
    DeltaRhoLiquid = 0.808;
    Sigma = 0.356;
end
R = 8.314;
p0 = max(T_fin.p_final);
T_fin.p_p0 = T_fin.p_final/p0;
T_fin.Void = circshift(T_fin.p_final,1);
T_fin{1,'Void'} = T_fin{1,'Void'}*0;
T_fin.delta_p_fin = T_fin.p_final - T_fin.Void;
T_fin.n_ads = (((T_fin.SumdP*Vdose)/(R*298)
-((T_fin.delta_p_fin*Vdead)/(R*Temp)))*0.001*133.322;
T_fin.V_ads = (T_fin.n_ads*22.4)/sample_mass;
```

```
if Gas == 1
    T_fin.V_liq = T_fin.V_ads*0.0018;
elseif Gas == 2
    T_fin.V_liq = T_fin.V_ads*0.00128;
elseif Gas == 3
    T_fin.V_liq = T_fin.V_ads*0.00155;
end
if torrhead == 100
    A = T_fin.p_p0(T_fin.p_p0 <= 0.05);
elseif torrhead == 1000
    A = T_fin.p_p0(T_fin.p_p0 <= 0.1);
end
a = size(A,1);
n_ads_mono = T_fin{a,'n_ads'};
disp('Number of moles adsorbed at the monolayer (mmol):');
disp(n_ads_mono);
surface_area = (n_ads_mono*(Sigma^2)*6.023*100)/sample_mass;
disp('Surface area per unit mass (m^2/g):');
disp(surface_area);
T_fin.ln_p_p0 = log(T_fin.p_p0);
T_fin{end,'ln_p_p0'} = T_fin{end,'ln_p_p0'} - 0.00001;
T_fin.stat_t = ((T_fin.n_ads/n_ads_mono)*Sigma);
T_fin.r_p =
-2./T_fin.ln_p_p0*((Gamma*MolarMass)/(R*Temp*DeltaRhoLiquid));
T_fin.r_p_mod =
-2./T_fin.ln_p_p0*((Gamma*MolarMass)/(R*Temp*DeltaRhoLiquid))
+ T_fin.stat_t;
DeltaV_ads = diff(T_fin.V_ads);
Delta_r_p = diff(T_fin.r_p);
Delta_r_p_mod = diff(T_fin.r_p_mod);
```

```
DeltaV_ads_Delta_r_p = DeltaV_ads./Delta_r_p;
DeltaV_ads_Delta_r_p_mod = DeltaV_ads./Delta_r_p_mod;
T_fin{1:(end-1),'dV_ads_dr_p'} = DeltaV_ads_Delta_r_p;
T_fin{1:(end-1),'dV_ads_dr_p_mod'} = DeltaV_ads_Delta_r_p_mod;
T_fin{end,'dV_ads_dr_p'} = T_fin{end,'dV_ads_dr_p'} + 0;
T_fin{end,'dV_ads_dr_p_mod'} = T_fin{end,'dV_ads_dr_p_mod'} + 0;
T_fin.Void2 = circshift(T_fin.stat_t,1);
T_fin{1,'Void2'} = T_fin{1,'Void2'}*0;
T_fin.delta_stat_t = T_fin.stat_t - T_fin.Void2;
T_fin.r_k = T_fin.r_p - T_fin.stat_t;
T_fin.r_k_mod = T_fin.r_p_mod - T_fin.stat_t;
T_fin.Void3 = circshift(T_fin.V_liq,1);
T_fin{1,'Void3'} = T_fin{1,'Void3'}*0;
T_fin.delta_V_liq = T_fin.V_liq - T_fin.Void3;
T_fin.V_liq_DESC = sort(T_fin.V_liq,'descend');
T_fin.stat_t_DESC = sort(T_fin.stat_t,'descend');
T_fin.r_p_DESC = sort(T_fin.r_p,'descend');
T_fin.r_p_mod_DESC = sort(T_fin.r_p_mod,'descend');
T_fin.delta_stat_t_DESC = sort(T_fin.delta_stat_t,'descend');
T_fin.r_k_DESC = sort(T_fin.r_k,'descend');
T_fin.r_k_mod_DESC = sort(T_fin.r_k_mod,'descend');
T_fin.delta_V_liq_DESC = sort(T_fin.delta_V_liq,'descend');
T_fin.BJH_Vol = (((T_fin.r_p_DESC).^2)./((T_fin.r_k_DESC
+ T_fin.delta_stat_t_DESC).^2)).*T_fin.delta_V_liq_DESC;
T_fin.BJH_Vol_mod
= (((T_fin.r_p_mod_DESC).^2)./((T_fin.r_k_mod_DESC
+ T_fin.delta_stat_t_DESC).^2)).*T_fin.delta_V_liq_DESC;
T_fin.c_j_A_j =
2*((T_fin.r_p_DESC- T_fin.stat_t_DESC)./T_fin.r_p_DESC)
.*(T_fin.BJH_Vol./T_fin.r_p_DESC);
```

```
T_fin.c_j_A_j_mod = 2*((T_fin.r_p_mod_DESC - T_fin.stat_t_DESC)
./T_fin.r_p_mod_DESC).*(T_fin.BJH_Vol_mod./T_fin.r_p_mod_DESC);
T_fin.c_j_A_j_run_sum = cumsum(T_fin.c_j_A_j);
T_fin.c_j_A_j_run_sum_mod = cumsum(T_fin.c_j_A_j_mod);
T_fin.BJH_Vol_run_sum =
T_fin.BJH_Vol - (((T_fin.r_p_DESC).^2)./((T_fin.r_k_DESC
+ T_fin.delta_stat_t_DESC).^2)).*T_fin.delta_stat_t_DESC
.*T_fin.c_j_A_j_run_sum;
T_fin.BJH_Vol_run_sum_mod = T_fin.BJH_Vol_mod
- (((T_fin.r_p_mod_DESC).^2)./((T_fin.r_k_mod_DESC
+ T_fin.delta_stat_t_DESC).^2)).*T_fin.delta_stat_t_DESC
.*T_fin.c_j_A_j_run_sum_mod;
DeltaBJH_Vol = diff(T_fin.BJH_Vol_run_sum);
DeltaBJH_Vol_mod = diff(T_fin.BJH_Vol_run_sum_mod);
Delta_r_p_DESC = diff(T_fin.r_p_DESC);
Delta_r_p_mod_DESC = diff(T_fin.r_p_mod_DESC);
DeltaBJH_Vol_Delta_r_p = DeltaBJH_Vol./Delta_r_p_DESC;
DeltaBJH_Vol_Delta_r_p_mod = DeltaBJH_Vol_mod./Delta_r_p_mod_DESC
T_fin{1:(end-1),'dV_BJH_dr_p'} = DeltaBJH_Vol_Delta_r_p;
T_fin{1:(end-1),'dV_BJH_dr_p_mod'} = DeltaBJH_Vol_Delta_r_p_mod;
T_fin{end,'dV_BJH_dr_p'} = T_fin{end,'dV_BJH_dr_p'} + 0;
T_fin{end,'dV_BJH_dr_p_mod'} = T_fin{end,'dV_BJH_dr_p_mod'} + 0;
writetable(T_fin,'PSD_Ads.dat');
T_fin2.p_p0 = T_fin2.p_final/p0;
T_fin2.Void = circshift(T_fin2.p_final,1);
T_fin2{1,'Void'} = p0;
T_fin2.delta_p_fin = T_fin2.Void - T_fin2.p_final;
T_fin2.n_ads = (((T_fin2.SumdP*Vdose)/(R*298)
-((T_fin2.delta_p_fin*Vdead)/(R*Temp)))*0.001*133.322;
T_fin2.V_ads = (T_fin2.n_ads*22.4)/sample_mass;
```

```
if Gas == 1
    T_fin2.V_liq = T_fin2.V_ads*0.0018;
elseif Gas == 2
    T_fin2.V_liq = T_fin2.V_ads*0.00128;
elseif Gas == 3
    T_fin2.V_liq = T_fin2.V_ads*0.00155;
end
T_fin2.ln_p_p0 = log(T_fin2.p_p0);
T_fin2{1,'ln_p_p0'} = T_fin2{1,'ln_p_p0'} - 0.00001;
T_fin2.stat_t = ((T_fin2.n_ads/n_ads_mono)*Sigma);
T_fin2.r_p =
-2./T_fin2.ln_p_p0*((Gamma*MolarMass)/(R*Temp*DeltaRhoLiquid));
T_fin2.r_p_mod =
-2./T_fin2.ln_p_p0*((Gamma*MolarMass)/(R*Temp*DeltaRhoLiquid))
+ T_fin2.stat_t;
DeltaV_ads2 = diff(T_fin2.V_ads);
Delta_r_p2 = diff(T_fin2.r_p);
Delta_r_p_mod2 = diff(T_fin2.r_p_mod);
DeltaV_ads_Delta_r_p2 = DeltaV_ads2./Delta_r_p2;
DeltaV_ads_Delta_r_p_mod2 = DeltaV_ads2./Delta_r_p_mod2;
T_fin2{1:(end-1),'dV_ads_dr_p'} = DeltaV_ads_Delta_r_p2;
T_fin2{1:(end-1),'dV_ads_dr_p_mod'} = DeltaV_ads_Delta_r_p_mod2;
T_fin2{end,'dV_ads_dr_p'} = T_fin2{end,'dV_ads_dr_p'} + 0;
T_fin2{end,'dV_ads_dr_p_mod'} = T_fin2{end,'dV_ads_dr_p_mod'} + 0;
T_fin2.Void2 = circshift(T_fin2.stat_t,1);
T_fin2{1,'Void2'} = T_fin{end,'stat_t'};
T_fin2.delta_stat_t = T_fin2.Void2 - T_fin2.stat_t;
T_fin2.r_k = T_fin2.r_p - T_fin2.stat_t;
T_fin2.r_k_mod = T_fin2.r_p_mod - T_fin2.stat_t;
T_fin2.Void3 = circshift(T_fin2.V_liq,1);
```

```
T_fin2{1,'Void3'} = T_fin{end,'V_liq'};
T_fin2.delta_V_liq = T_fin2.Void3 - T_fin2.V_liq;
T_fin2.BJH_Vol = (((T_fin2.r_p).^2)./((T_fin2.r_k
+ T_fin2.delta_stat_t).^2)).*T_fin2.delta_V_liq;
T_fin2.BJH_Vol_mod = (((T_fin2.r_p_mod).^2)./((T_fin2.r_k_mod
+ T_fin2.delta_stat_t).^2)).*T_fin2.delta_V_liq;
T_fin2.c_j_A_j = 2*((T_fin2.r_p
- T_fin2.stat_t)./T_fin2.r_p).*(T_fin2.BJH_Vol./T_fin2.r_p);
T_fin2.c_j_A_j_mod
= 2*((T_fin2.r_p_mod - T_fin2.stat_t)./T_fin2.r_p_mod)
.*(T_fin2.BJH_Vol_mod./T_fin2.r_p_mod);
T_fin2.c_j_A_j_run_sum = cumsum(T_fin2.c_j_A_j);
T_fin2.c_j_A_j_run_sum_mod = cumsum(T_fin2.c_j_A_j_mod);
T_fin2.BJH_Vol_run_sum
= T_fin2.BJH_Vol- (((T_fin2.r_p).^2)
./((T_fin2.r_k + T_fin2.delta_stat_t).^2))
.*T_fin2.delta_stat_t.*T_fin2.c_j_A_j_run_sum;
T_fin2.BJH_Vol_run_sum_mod = T_fin2.BJH_Vol_mod
- (((T_fin2.r_p_mod).^2)./((T_fin2.r_k_mod
+ T_fin2.delta_stat_t).^2)).*T_fin2.delta_stat_t
.*T_fin2.c_j_A_j_run_sum_mod;
DeltaBJH_Vol2 = diff(T_fin2.BJH_Vol_run_sum);
DeltaBJH_Vol_mod2 = diff(T_fin2.BJH_Vol_run_sum_mod);
Delta_r_p2 = diff(T_fin2.r_p);
Delta_r_p_mod2 = diff(T_fin2.r_p_mod);
DeltaBJH_Vol_Delta_r_p2 = DeltaBJH_Vol2./Delta_r_p2;
DeltaBJH_Vol_Delta_r_p_mod2 = DeltaBJH_Vol_mod2./Delta_r_p_mod2;
T_fin2{1:(end-1),'dV_BJH_dr_p'} = DeltaBJH_Vol_Delta_r_p2;
T_fin2{1:(end-1),'dV_BJH_dr_p_mod'} = DeltaBJH_Vol_Delta_r_p_mod2;
T_fin2{end,'dV_BJH_dr_p'} = T_fin2{end,'dV_BJH_dr_p'} + 0;
```

```
T_fin2{end,'dV_BJH_dr_p_mod'} = T_fin2{end,'dV_BJH_dr_p_mod'} + 0;
writetable(T_fin2,'PSD_Des.dat');
figure;
outliers = excludedata
(T_fin.r_p_mod,T_fin.dV_ads_dr_p_mod,'domain',[1 30]);
outliers2 = excludedata
(T_fin2.r_p_mod,T_fin2.dV_ads_dr_p_mod,'domain',[1 30]);
h(1) = subplot(3,1,1);
PSD_fit_1 = fit(T_fin2.r_p_mod,T_fin2.dV_ads_dr_p_mod,
'gauss3', 'Exclude', outliers2);
plot (PSD_fit_1,T_fin2.r_p_mod,T_fin2.dV_ads_dr_p_mod,outliers2);
title('Pore Size Distribution: cylinders');
xlim([0 30]);
ylim([0 2000]);
xlabel('Pore radius r [nm]');
ylabel('dV/dr [STP cc/(g*nm)]');
h(2) = subplot(3,1,2);
PSD_fit_2 = fit(T_fin.r_p_mod,T_fin.dV_ads_dr_p_mod,
'gauss3', 'Exclude', outliers);
plot (PSD_fit_2,T_fin.r_p_mod,T_fin.dV_ads_dr_p_mod,outliers);
title('Pore Size Distribution: spheres');
xlim([0 30]);
ylim([0 2000]);
xlabel('Pore radius r [nm]');
ylabel('dV/dr [STP cc/(g*nm)]');
h(3) = subplot(3,1,3);
PSD_fit_3 = fit(T_fin2.r_p_mod,T_fin2.dV_ads_dr_p_mod,
'gauss3', 'Exclude', outliers2);
plot (PSD_fit_3,T_fin2.r_p_mod,T_fin2.dV_ads_dr_p_mod,outliers2);
title('Pore Size Distribution: slits');
```

```
xlim([0 30]);
ylim([0 2000]);
xlabel('Pore diameter d [nm]');
ylabel('dV/dr [STP cc/(g*nm)]');
disp('Mean value for Gaussian distribution - cylinders (in nm):');
disp(PSD_fit_1.b1);
disp('Std. dev. value for Gaussian distribution
- cylinders (in nm):');
disp(PSD_fit_1.c1/sqrt(2));
disp('Rel. std. dev. value for Gaussian distribution
- cylinders (%):');
disp(((PSD_fit_1.c1/sqrt(2))/PSD_fit_1.b1)*100);
disp('Mean value for Gaussian distribution - spheres (in nm):');
disp(PSD_fit_2.b1);
disp
('Std. dev. value for Gaussian distribution - spheres (in nm):');
disp(PSD_fit_2.c1/sqrt(2));
disp('Rel.std. dev. value for Gaussian distribution
- spheres (%):');
disp(((PSD_fit_2.c1/sqrt(2))/PSD_fit_2.b1)*100);
disp('Mean value for Gaussian distribution - slits (in nm):');
disp(PSD_fit_3.b1);
disp('Std. dev. value for Gaussian distribution
- slits (in nm):');
disp(PSD_fit_3.c1/sqrt(2));
disp
('Rel. std. dev. value for Gaussian distribution - slits (%):');
disp(((PSD_fit_3.c1/sqrt(2))/PSD_fit_3.b1)*100);
disp
('Fit parameters including 95% confidence levels  cylinders:');
```

```
disp(PSD_fit_1);
disp('Fit parameters including 95% confidence levels - spheres:');
disp(PSD_fit_2);
disp('Fit parameters including 95% confidence levels - slits:');
disp(PSD_fit_3);
```

C.2 Directions on how to use MATLAB script

1. Obtain MATLAB © (e.g. OIT Software on UTK website using your university credentials).

2. MATLAB © script takes two files as input and gives two files as output. These are all *.dat files. The input files should be the adsorption and desorption isotherm data (in the usual IsoiMac LabView © program format, *.dat by default), and they need to be renamed Adsorption.dat and Desorption.dat, respectively (case sensitive names). Input files have to be in the same MATLAB © folder as PSD.m, i.e. the MATLAB © file with script code. The output files will have names PSD_Ads.dat and PSD_Des.dat, and they will be found in MATLAB © folder as well.

3. You will be asked to choose the gas used for measurements (Methane, Argon, or Nitrogen).

4. You will need to input the parameters which are specific to the isotherm station: dosing volume, deadspace volume (for data correction), experimental temperature (what you deem to be the most exact value for your data), and sample mass.

5. The script will then generate three plots according to as many different pore models used to interpret the PSD data from the two output files. These are: cylinders, spheres, or slits.

    - Cylinders: hysteresis (i.e. capillary condensation-like behavior, typical of porous materials) is expected from cylinders open at both ends. Desorption branch of hysteresis loop is used.

- Spheres: this actually refers to the interstitials between spherical particles, and the use of the adsorption branch is preferred over desorption, because network effects might play a role (i.e. desorption tends to increase PSD peaks intensity misrepresenting it - more peaked distribution than real).
- Slits: this is the case of, e.g. plate-like particles, where the pores happen to be slit-shaped. The desorption branch is again preferred over adsorption, and the pore radius actually represents the diameter of the slits (i.e. an average distance between plates).

The script uses a Gaussian fitting function, in particular it combines three Gaussian distributions to achieve the best fit. In fact, when one or two Gaussian distributions are used, MATLAB © may be unable to converge toward a smooth fitting function especially when single peaks are composite, and/or multiple peaks are present throughout the distribution. The number of Gaussian distributions used to fit the PSD curve can be changed modifying the argument of the functions "PSD_fit_1", "PSD_fit_2" and "PSD_fit_3" in the MATLAB © code from 'gauss3' to 'gauss4' for four distributions, up to 'gauss8' for eight distributions.

In general, it is important to keep in mind that Kelvin equation is used to pursue the calculations, and this relates relative pressure at which condensation in pores/evaporation occurs and the average radius of the pores (from geometrical arguments about radii of curvature of a pore).

However, what is actually measured (especially in desorption) is the so called "core" radius, hence the radius of the pore aperture with confined fluid in it. This aspect has to be taken into account when using this model and calculation script.

The plots generated by the script utilize the results from a modified Kelvin equation, therefore taking into consideration the statistical thickness of adsorbed liquid. The script calculates adsorbed quantity (in mmol) at the monolayer, as well as the surface area per unit mass, utilizing the molecular diameter of the chosen gas.

In both Adsorption.dat and Desorption.dat files, the user can find all the following quantities in order to generate other different plots:

- p_final: final pressure of equilibration of isotherm SumdP: sum of the DeltaP values in the isotherm;
- p_p0: reduced pressure;
- n_ads: number of moles adsorbed (related to SumdP);
- V_ads: adsorbed volume at STP conditions (related to SumdP);
- r_p: Kelvin radius;
- r_p_mod: modified Kelvin radius (takes statistical thickness "stat_t" into account);
- dV_ads_dr_p: variation of pore volume (with respect to pore radius);
- dV_ads_dr_p_mod: variation of pore volume (with respect to modified pore radius);
- dV_BJH_dr_p: variation of pore volume according to Barrett, Joyner and Halenda (1951);
- dV_BJH_dr_p_mod: variation of pore volume according to Barrett, Joyner and Halenda, 1951 (BJH) using modified Kelvin radius.

In order to plot a PSD graph, you may choose one of the following options:

- dV/dr vs. radius: plot "r_p" on X-axis and "dV_ads_dr_p" on Y-axis (this is what the script does to produce the plot on the base of chosen pore model, either from adsorption or from desorption data);
- dV/dr vs. modified radius: plot "r_p_mod" on X-axis and "dV_ads_dr_p_mod" on Y-axis;
- dV/dr vs. radius (BJH): plot "r_p" on X-axis and "dV_BJH_dr_p" on Y-axis;
- dV/dr vs. modified radius (BJH): plot "r_p_mod" on X-axis and "dV_BJH_dr_p_mod" on Y-axis.

When you open the output .dat files in KaleidaGraph, select "Other" as delimiter (comma), "Number" = 1, "Lines Skipped" = 0, and check the "Read Titles" box.

NOTE 1: the script will give a warning at the beginning with respect to DATETIME after reading from input files. This happens when month and day of the measurement can be read as MM/DD/YYYY or DD/MM/YYYY. This generates ambiguity. An example is the day 1/3/2019 (January 3rd, 2019) that could be interpreted by MATLAB © as 1st March 2019 in the other DATETIME format. This ambiguity, though, should NOT affect the correct performance of the calculations and generation of output files, because it has to do with DATETIME function which does not read any of the two columns of interest from input files, i.e. Column 10 (final pressure of equilibration) and Column 11 (sum of the Delta P).

NOTE 2: there might be some non-numerical entries in the output files. In fact, MATLAB © reports "Inf" or "-Inf" for extremely large positive and negative numbers, respectively. In order to overcome the problem of KaleidaGraph reading such entries as text, you can just substitute "Inf" character with a very large number. Usually, such large values come from numerical derivative calculations associated to the derivatives involved in the PSD (dV/dr).

D Additional information on the porous structure characterization

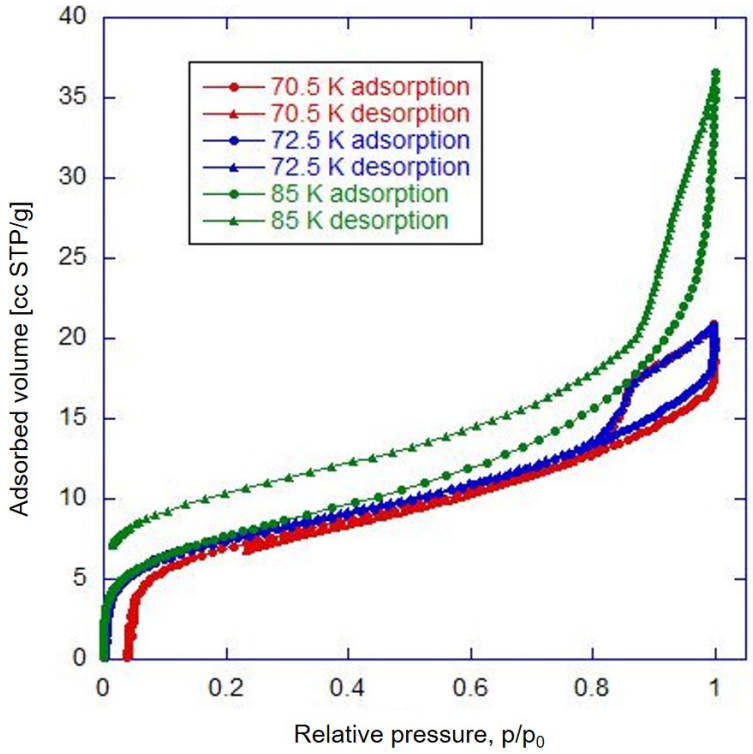

Figure D.40: Compilation of CH_4 isotherms (adsorption and desorption) on 100 nm size silica for several temperature values.

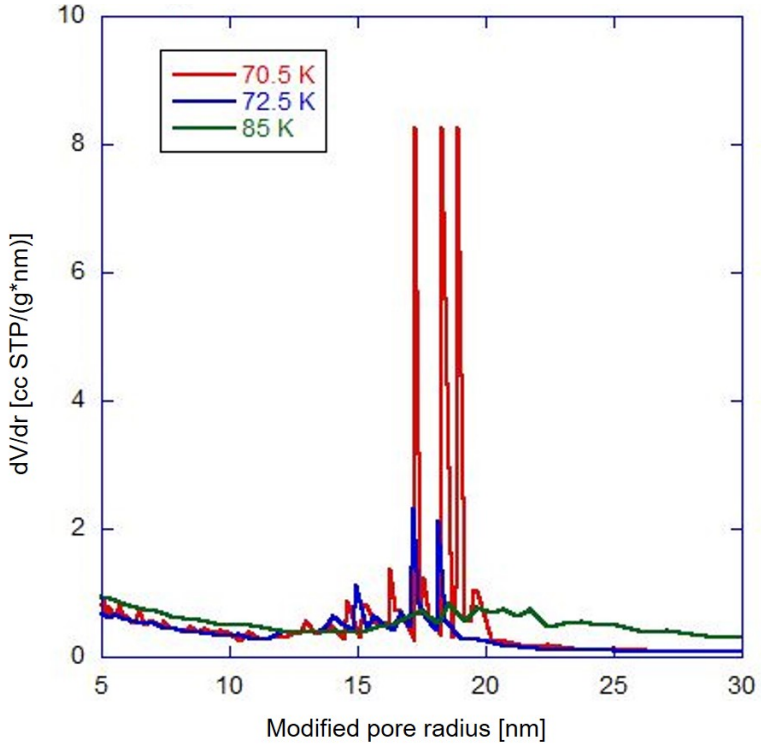

Figure D.41: Pore size distribution plots for the desorption branches of the isotherms in Fig. D.40.

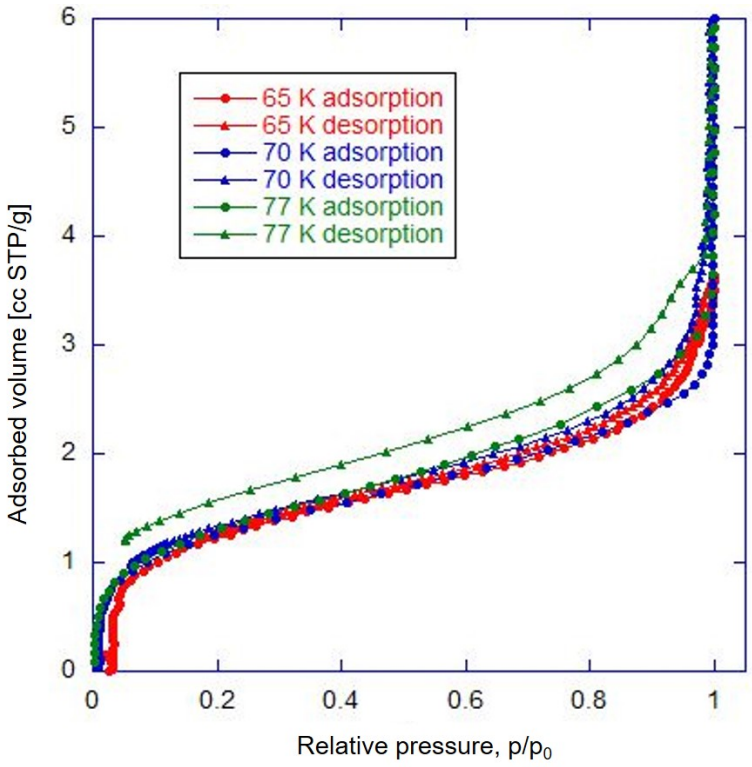

Figure D.42: Compilation of CH_4 isotherms (adsorption and desorption) on 600 nm size silica for several temperature values.

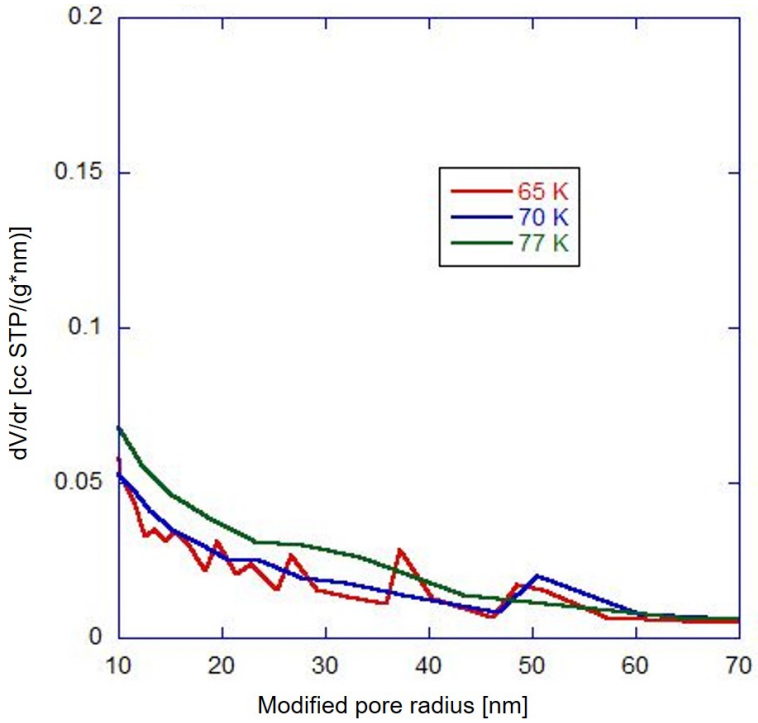

Figure D.43: Pore size distribution plots for the desorption branches of the isotherms in Fig. D.42.

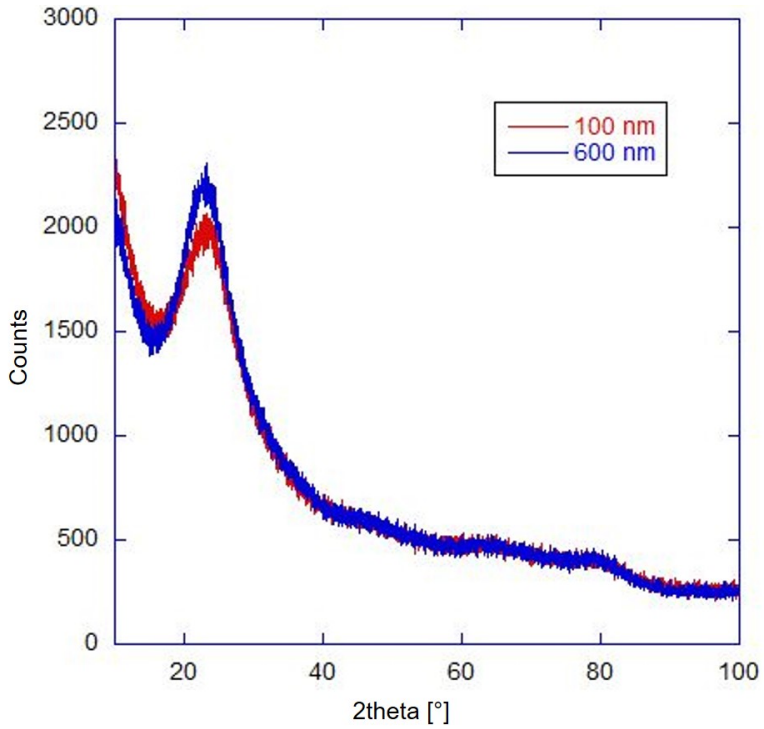

Figure D.44: Diffraction patterns of silica spheres (100 nm and 600 nm size) studied in this work.

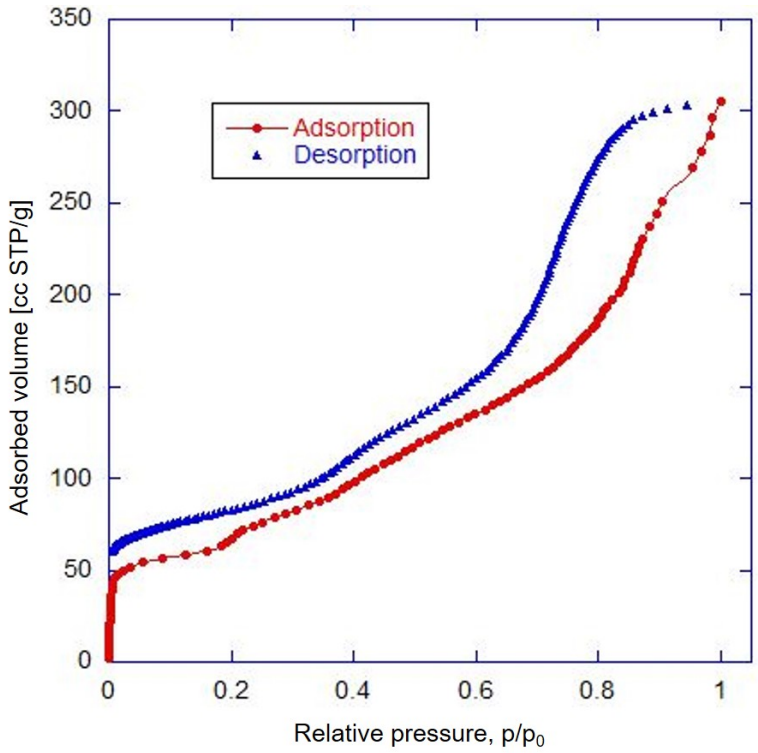

Figure D.45: Adsorption and desorption isotherms of CH_4/CNT at 77 K. The interpolating line is meant to guide the eye.

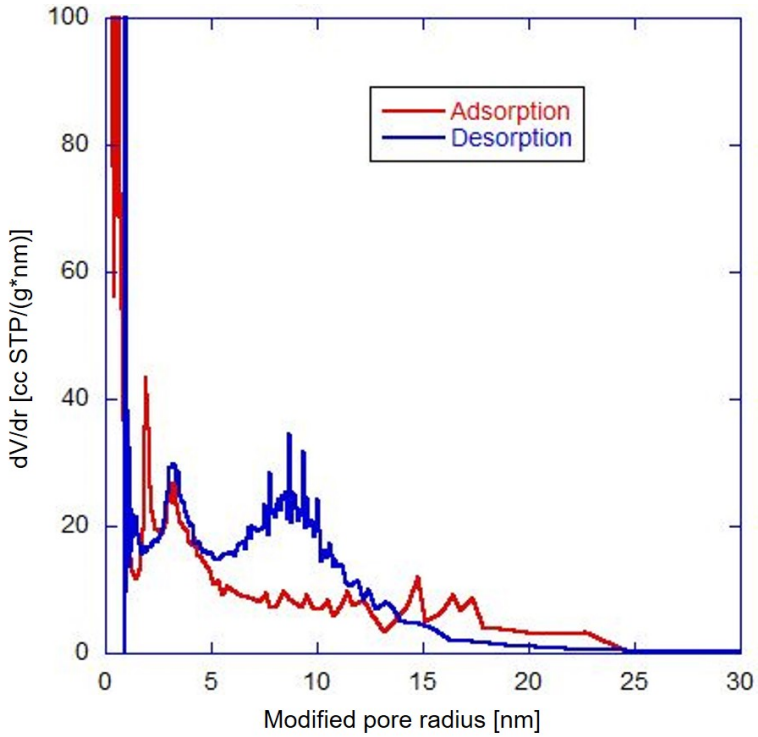

Figure D.46: PSD plot for the isotherms reported in Fig. D.45.

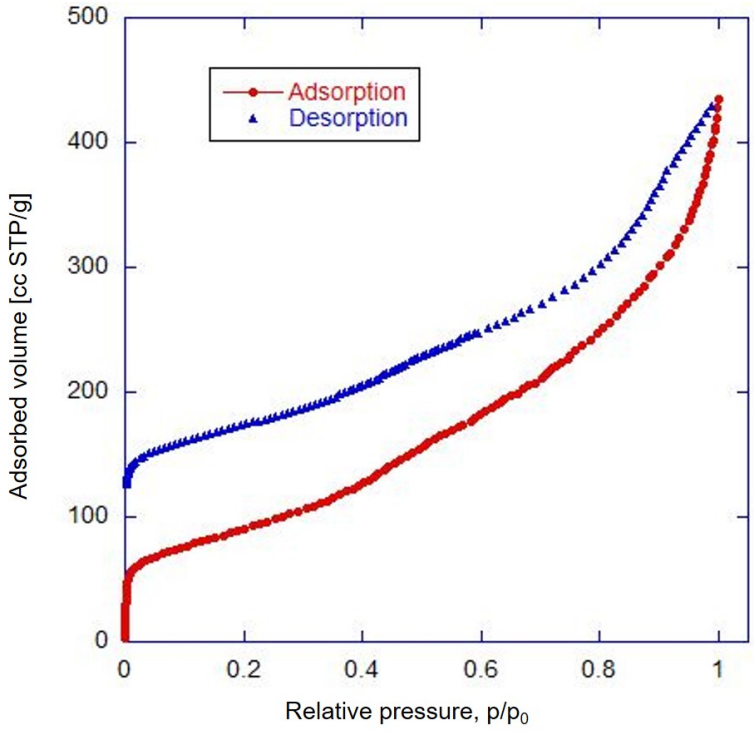

Figure D.47: Adsorption and desorption isotherms for Ar/CNT at 77 K. The interpolating line is meant to guide the eye.

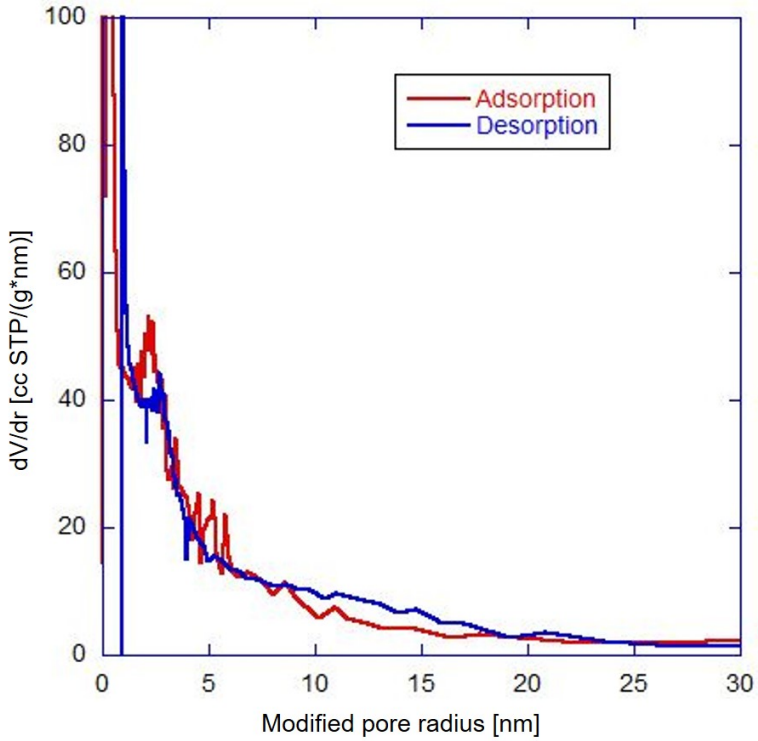

Figure D.48: PSD plot for the isotherms reported in Fig. D.47.

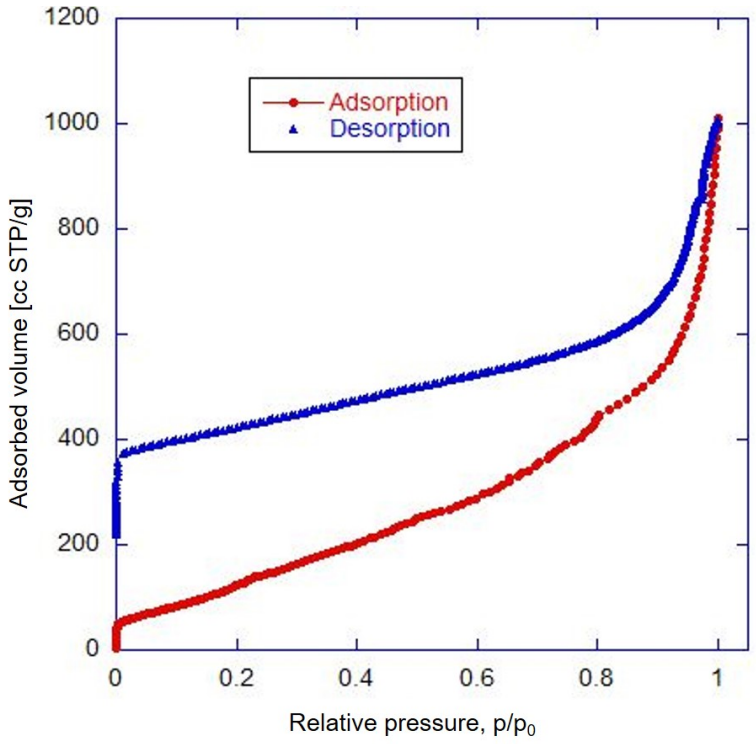

Figure D.49: Adsorption and desorption isotherms of N_2/CNT at 77 K. The interpolating line is meant to guide the eye.

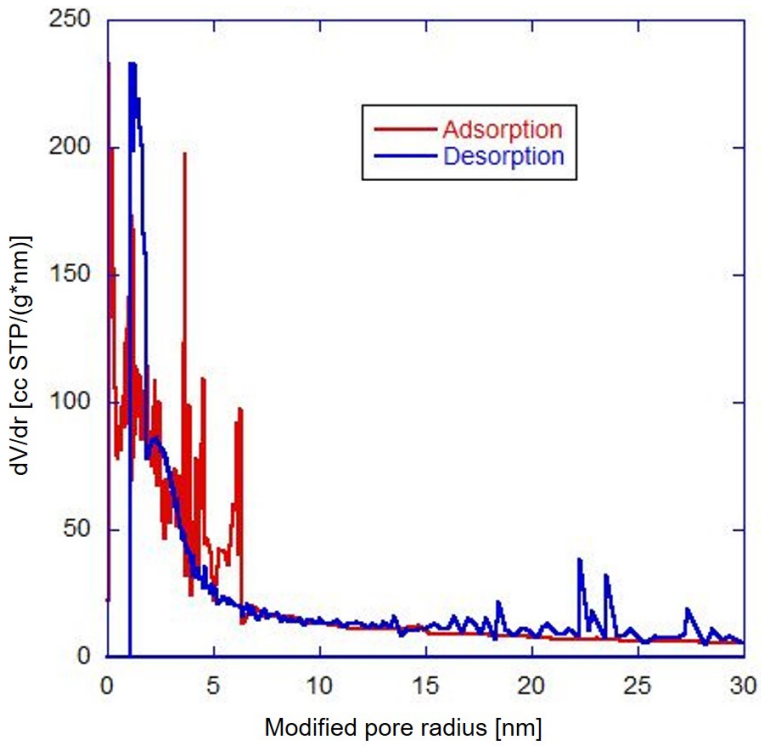

Figure D.50: PSD plot for the isotherms reported in Fig. D.49.

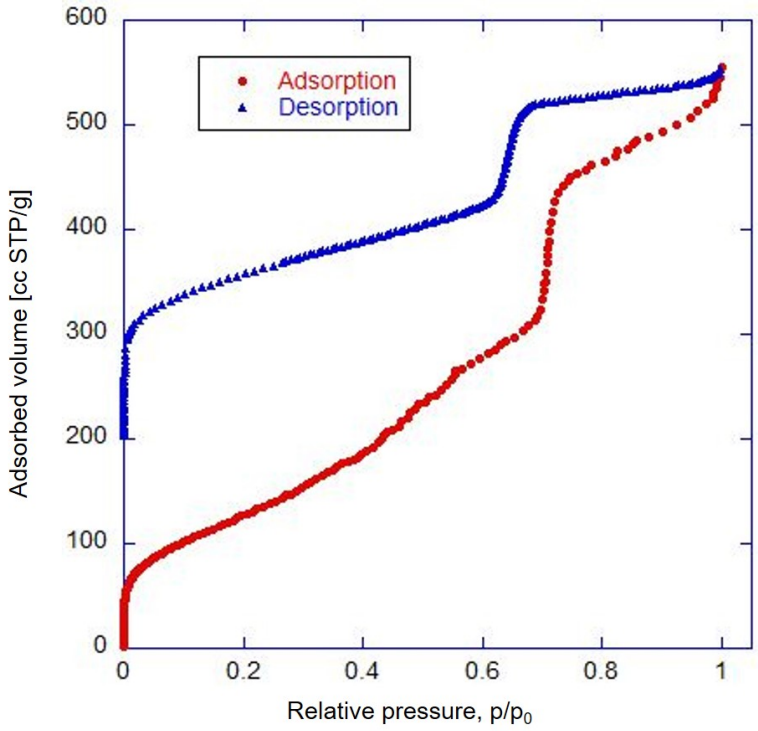

Figure D.51: Adsorption and desorption isotherms of N_2 on SBA-15 at 77 K.

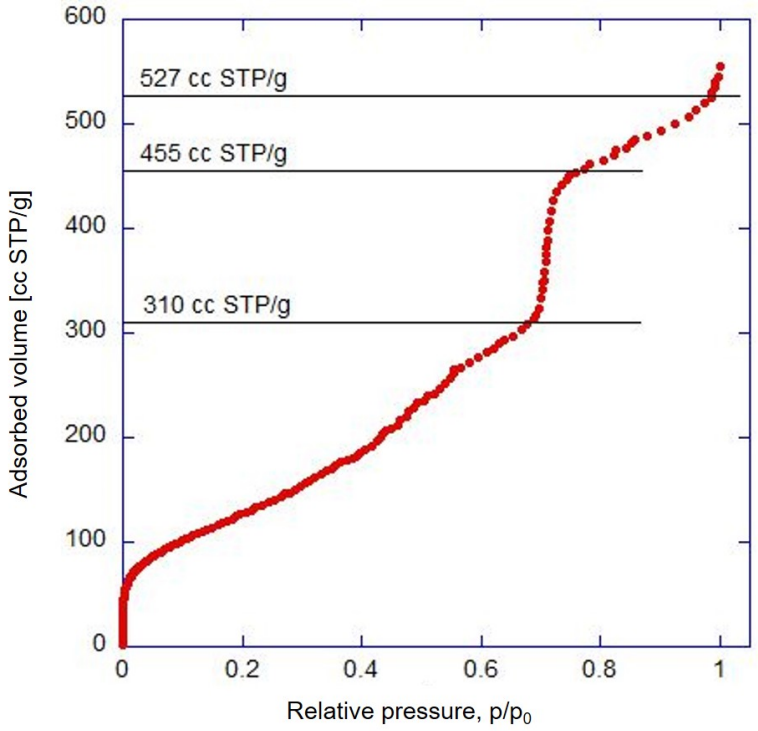

Figure D.52: Adsorption isotherm of Fig. D.51 with marks for adsorbed volume determination at inflection points.

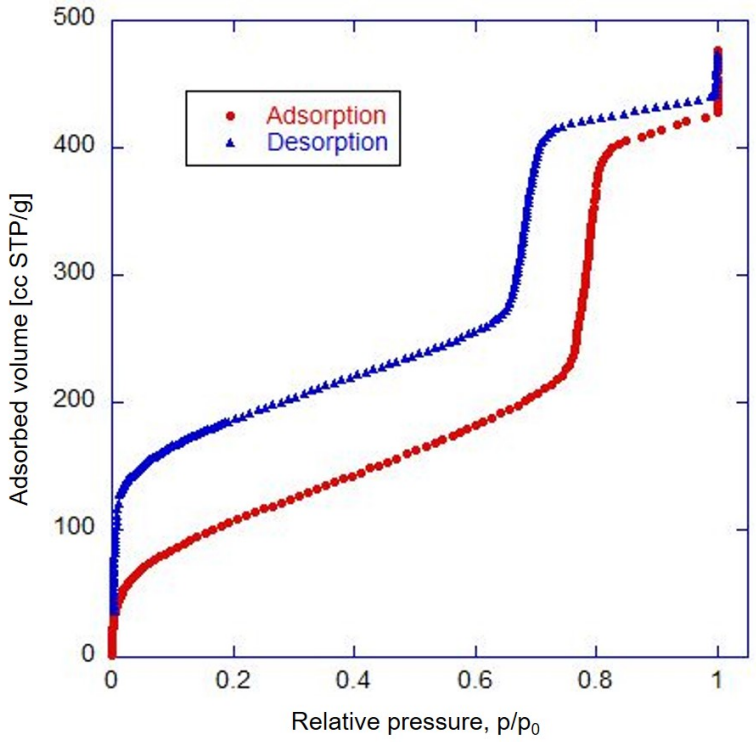

Figure D.53: Adsorption and desorption isotherms of Ar on SBA-15 at 77 K.

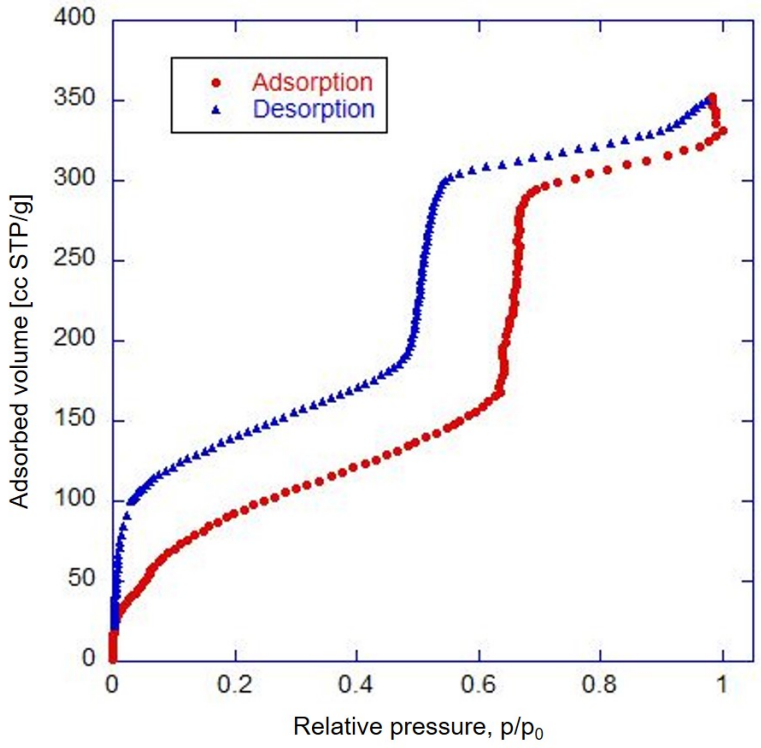

Figure D.54: Adsorption and desorption isotherms of CH_4 on SBA-15 at 93 K.

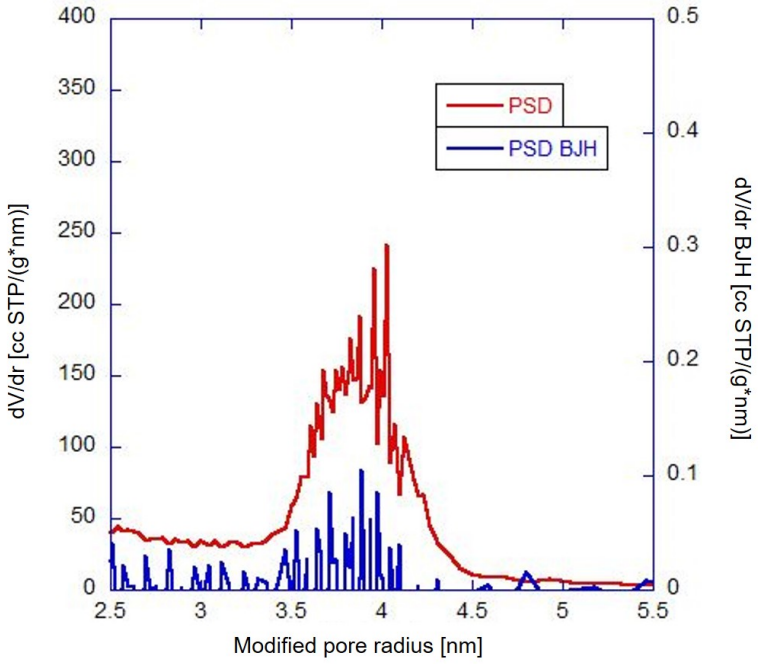

Figure D.55: PSD from adsorbed volume and BJH volume calculated from the desorption isotherm of Fig. D.51 (N_2/SBA-15).

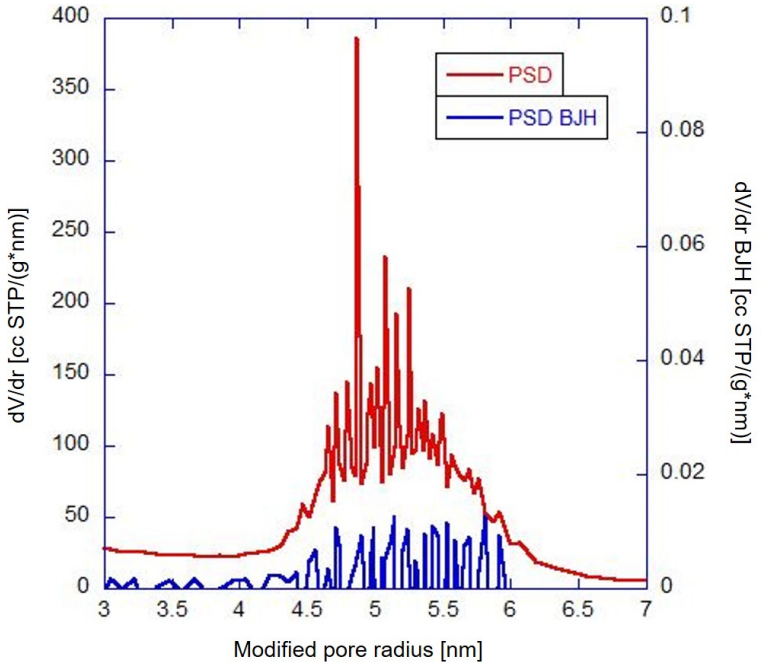

Figure D.56: PSD from adsorbed volume and BJH volume calculated from the desorption isotherm of Fig. D.53 (Ar/SBA-15).

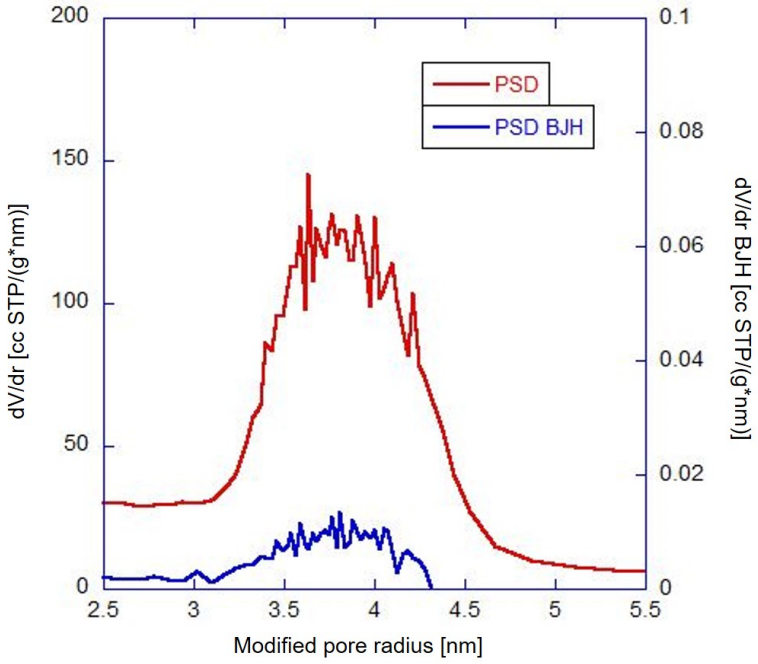

Figure D.57: PSD from adsorbed volume and BJH volume calculated from the desorption isotherm of Fig. D.54 (CH_4/SBA-15).

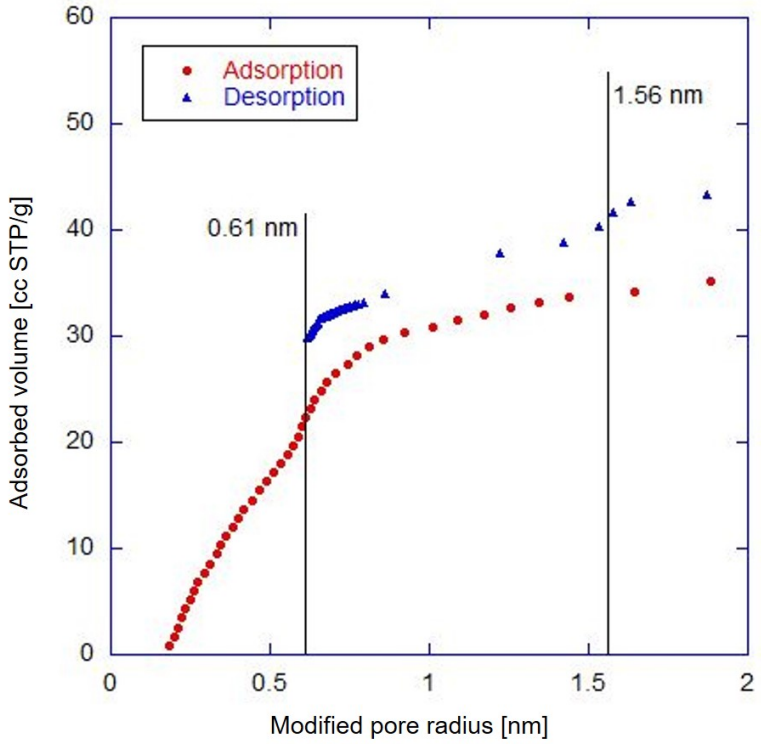

Figure D.58: Same plot as Fig. 5.8, where the adsorbed volume is instead expressed in terms of modified pore radius. The x-axis is zoomed on the lowest values of pore radius.

Vita

Daniele Paradiso was born in a small town named Lentate sul Seveso, located outside of the outskirts of Milan, Italy. The town of Lentate is also close to the area of the beatiful Como lake. He grew up and attended schools in the area: in particular, he attended high school with a concentration in the study of Latin and Ancient Greek.

After high school completion, he undertook university studies in the city of Milan. There he studied Physics both at the undergraduate and graduate level, pursuing a bachelor's and master's degree from the Università degli Studi di Milano.

During the time of his graduate studies in Milan, he had the opportunity to visit the University of Tennessee, Knoxville, in the Department of Chemistry, and the Oak Ridge National Laboratory (ORNL), to work under the guidance of Prof. John Z. Larese. While he was learning about volumetric adsorption isothermal techniques in Prof. Larese's laboratory, he pursued low-temperature studies of some biological dipeptide-based materials, along with some neutron scattering experiments at the Spallation Neutron Source (SNS) at ORNL.

He then continued his relationship with the Larese Research Group enrolling in the Chemistry graduate program to pursue a doctoral degree. He has been conducting research primarily on the experimental development of a deposition methodology to decorate metal oxide powders with metal clusters, along with the characterization of their properties. He has also spent effort in learning and optimizing gas adsorption/desorption techniques to determine the pore size distribution in some mesoporous silica and carbonaceous materials.